Microstructural characterisation and quantitative evaluation of nuclear graphite grades candidate for Generation-IV nuclear reactors

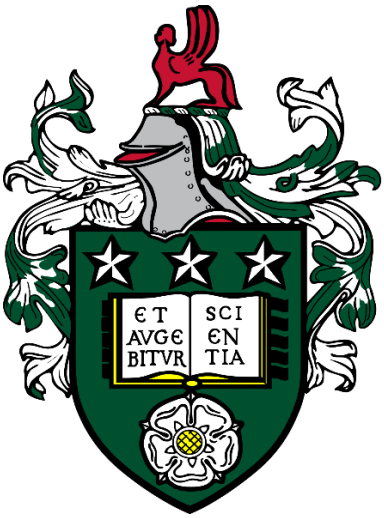

Marzoqa Mabrok H Alnairi

School of Chemical and Process Engineering

University of Leeds

Submitted in accordance with the requirements for the degree of

Doctor of Philosophy

November 2019

The candidate confirms that the work submitted is her own, except where work which has formed part of jointly authored publications has been included. The contribution of the candidate and the other authors to this work has been explicitly indicated below. The candidate confirms that appropriate credit has been given within the Thesis where reference has been made to the work of others. That is XRD and Raman's work undertaken by the author of this Thesis and obtained from Mironov (2014).

Chapter 5 and 7 were published in:

Freeman, H.M., Mironov, B.E., Windes, W., Alnairi, M.M., Scott, A.J., Westwood, A.V.K. and Brydson, R.M.D., 2017. Micro to nanostructural observations in neutron-irradiated nuclear graphites PCEA and PCIB. *Journal of Nuclear Materials*, *491*, pp.221-231.

The candidate wrote the Optical microscopy section of virgin nuclear graphite and added SEM micrographs of virgin nuclear graphite to this paper and also involved in the analysis of XRD data. Also, the candidate contributed to the overall writing and review of drafts of this paper.

©2018 The University of Leeds and Marzoqa Mabrok Alnairi

Acknowledgements

All praise and thanks be to my God, the Creator of all that exists. Prayers and peace be upon Prophet Muhammad, the last messenger sent to humanity.

I would like to thank the Ministry of Higher Education in Saudi Arabia and the Umm Al-Qura University branch, University College, in Al-leith for the scholarship.

The completion of this Thesis would not have been possible without considerable support, guidance, prayers, and love from many people. So, I would like to first thank my project supervisors, Prof. Rik Brydson, Dr Andrew Scott, and Dr Aidan Westwood. In particular, I would like to express my sincere gratitude to Rik who afforded a tremendous amount of help in bringing this Thesis to light. I would also like to thank Dr Brindusa Mironov for providing data regarding Raman and XRD of irradiated graphite. I am also grateful for the support and continual training during my studies of the rest of the University of Leeds staff, including Dr Helen Freeman, Diane Cochrane, Stuart Mickleth waite and Robert Simpson. My sincere thanks also go to Dr Tatiana Grebennikova for arranging the analysis of the irradiated material in Manchester.

My deepest thanks also go to my mother and father who always support and pray for me to fulfill my dreams and throughout my education as a whole, and to my sisters and brothers for encouraging me spiritually throughout. Last but not the least, to my loyal husband, Mr Suliman H. Alnarey, for his patience, motivation, and emotional and financial support, as well as to my lovely children Reema, Wellaf, and Ahmad for their love and patience with me.

Thanks for all your encouragement!

Abstract

Nuclear Graphite is a complex material, and its microstructure depends strongly upon the starting materials, manufacturing processes, and operating conditions (Aitkaliyeva, 2017; Heijna et al., 2017; Marsden et al., 2017; Zhou et al., 2017a). Nuclear graphite plays a critical role as a moderator, a neutron reflector, and a core structural component in the operation of old generation reactors, still it is the potential candidates for very high-temperature reactors ((V)HTRs), (Generation-IV reactor). The understanding of nuclear graphite behaviour under irradiation is critical in helping select nuclear graphite grades that offer an enhancement in the safe and economical operation of (V)HTR, and as a basis for core design and safety evaluation. Hence, the experimental work described in this Thesis was designed to quantitatively study the changes in the crystallinity and porosity of virgin and neutron-irradiated nuclear graphite. After neutron irradiation, highly damaged regions (defects) were observed in which the thicknesses reached a few hundred nanometres.

Various material characterisation techniques were used to characterise the nuclear graphite samples at various length scales (macroscale, microscale, and nanoscale), including X-ray diffraction (XRD), Raman spectroscopy, polarised light microscopy (PLM), Scanning Electron Microscopy (SEM), and Focussed Ion Beam–Scanning Electron Microscopy (FIB-SEM). PLM and SEM were used to study the changes in the shape and size of the filler particles and porosity in the whole structure, while PLM image analysis facilitated a qualitative and quantitative analysis of domains in different grades of virgin nuclear graphite (PGA, Gilsocarbon, PCEA, and PCIB).

For the first time, FIB-SEM was also adopted to study the porosity in 3D of two different virgin nuclear graphite grades (PCEA and PCIB), which are possible candidate materials for (V)HTRs. The data was then compared to the results obtained from PLM and used to build up a 3D view after progressive polishing. As for XRD, it was used to investigate the deformation of the crystal lattice and quantify the build-up of the lattice micro-strains. Raman spectroscopy was performed to evaluate the change in crystallite coherence lengths of virgin and neutron-irradiated graphite, which gave information on the accumulation of defects within the basal plane and the introduction of basal plane fragmentation.

The findings of this Thesis enhance current understanding of how the structure of nuclear graphite changes under neutron irradiation using a novel combination of techniques and by improving the use of existing techniques to study the changes in the porosity of nuclear graphite.

Abbreviations

AGR	The Advanced Gas-cooled Reactor in the UK
Magnox	Magnesium-Oxygen Reactor
NGNP	Next Generation Nuclear Plant
AGC	Advanced Graphite Creep
ATR	Advanced Test Reactor
(V)HTR	Very High-Temperature Reactor
UNGG	Uranium Naturel Graphite Gas Reactor (France)
PWR	Sizewell B Pressurised Water Reactor
CTE	Coefficient of Thermal Expansion
HTS	Heat-Transport System
AGX	Graphite electrode grade
PGA	Pile Grade A Nuclear Graphite used in Magnox Reactor
GILSO	Gilsocarbon Nuclear Graphite used in AGRs
PCEA	Nuclear Graphite Grade used in HTGRs
PCIB	Nuclear Graphite Grade used In HTRs
HOPG	Highly Oriented Pyrolytic Graphite
PLM	Polarised-Light Microscopy
SEM	Scanning Electron Microscopy
EBSD	Electron Backscattered diffraction
t-EBSD	Transmission Electron Backscatter Diffraction
FIB-SEM	Focussed Ion Beam Scanning Electron Microscopes
XRD	X-Ray Diffraction
TEM	Transmission Electron Microscopy
CVD	Chemical Vapour Deposition
dpa	Displacements per Atom
PKAs	Primary Knock-on Atoms
CLSM	Confocal Laser Scanning Microscopy
CT	X-Ray Computed Tomography
SE	Secondary electron
BSE	Backscattered electron
EDS	Energy Dispersive Spectroscopy

GIS	Gas Injection System
W-H	Williamson and Hall plot
BWF	Breit-Wigner-Fano
PECS II	Gatan Argon Ion Polishing System
PIPS	Precision Ion Polishing System
SiC	Silicon Carbide Grinding Paper
MaL	Major axis Length

Notations

a	The crystal lattice parameter
c	The crystal lattice parameter
L_a	coherence length in $\boldsymbol{a}$ direction
L_c	coherence length in $\boldsymbol{c}$ direction
Å	Angstrom (10^{-10}m)
ΔE	kinetic energy
GWe	Gigawatt of electricity
u	Atomic mass unit
dpa	displacements per atom
d	Crystal layer spacing
I_D	D band intensity
I_G	G band intensity
λ	wavelength
β	full width half maximum (FWHM)
K	shape factor
pV	Pseudo-Voigt function
C_ε	Strain
e	Eccentricity
y_h	voxel height

Table of Contents

List of Figures

List of Tables

Chapter 1

1.1 Introduction

1.1.1 The importance of nuclear graphite in Generation-IV reactors

In the late 1990s, 25% of the UK's electricity supply generated via nuclear reactors (WorldNuclearAssociation, 2018). The proportion of the UK's electricity supply that is generated by nuclear power reactors today is around 21%. By 2025, experts predict that the demand for electrical power will exceed the supply by more than 40% (WorldNuclearAssociation, 2018), as population growth will increase the demand for electricity used in transportation and heating. At present, there are 14 active nuclear reactors in the UK, with a combined net power capacity of 8 GW of electricity (WorldNuclearAssociation, 2018). However, half of these existing nuclear reactors are expected to be retired by 2025, as these reactors are reaching the end of their lifetime.

Researchers worldwide, therefore, focus on technologies that look to extending the lifetime of reactors currently in operation, in order to address this supply-demand gap. Hence, the current work is focusing on the development of Generation-IV reactors and how they can avoid the issues of old and current generation reactors. Generation-IV reactors are a set of theoretical nuclear reactor designs that have the nuclear graphite as the core moderator. The main target for each Generation-IV reactor design is to make improvements in sustainability, economics, safety, reliability, and proliferation-resistance (Aitkaliyeva, 2017; Marsden et al., 2017; Zhou et al., 2017a). At present, a few operational prototypes exist, most of these reactors are generally not expected to be available for commercial use until commencing in the 2030s or 2040s (Aitkaliyeva, 2017; Zhou et al., 2017a).

Nuclear graphite is an attractive material for Generation-IV reactors because it has been a moderator material, fuel matrix, and a major core structural component for past generation reactors. There is an array of reasons why nuclear graphite is an important candidate material that is related to its

intrinsic properties, such as high neutron moderating and reflecting efficiency, safety, physical and chemical stability at high temperatures. Specifically, nuclear graphite has a relatively low atomic weight (12.011u) which reduces the amount of energy removed from neutrons during each collision (Aitkaliyeva, 2017; Lewis, 2008; Marsden et al., 2017; Zhou et al., 2017a). By slowing down the energies of the fast neutrons during the fission reaction with a moderator, there is no need for high levels of fuel enrichment, a process that can be time-consuming and expensive (Taylor, 2016). Hence nuclear graphite a potential moderator for Generation-IV reactors.

Recent research by Zhou et al. (2017a) shows that during the (V)HTRs reactor operation, the nuclear graphite physical, mechanical, and thermal properties are significantly affected by the exposure to fast neutron irradiation. Consequently, this leads to the failure of nuclear graphite components (composing filler particles, binder matrix, and porosity) after a significant neutron dose (Marsden et al., 2017; Zhou et al., 2017a). This refers not only to these properties but also to the chemical stability in various environments (Contescu et al., 2014). Therefore, the parent materials (e.g., the coke source), the subsequent manufacturing method, impurity level, and the operating conditions have a significant influence in determining the structure, corresponding properties, and performance of nuclear graphite under neutron irradiation (Burchell, 2012; Aitkaliyeva, 2017). The microstructural and dimensional changes under neutron irradiation act as the fundamental mechanisms that alter most of the thermal and mechanical properties of graphite.

The understanding of the above changes is the key to designing radiation-tolerant materials for the (V)HTRs reactors and helps to predict their lifetime. Specifically, changes occur in porosity and crystallinity of the graphite material due to neutron irradiation. For instance, porosity has a major impact on thermal conductivity and Young's modulus, both of which are reduced by more than half for a 30% porous graphite (Berre et al., 2006). Additionally, the temperatures play a key role in determining the ultimate microstructure and properties of nuclear graphite. For example, the porosity dimensions are greatly affected by the operating temperature and the potential fission product release.

After neutron irradiation, highly damaged regions (defects) are observed. These defects can reach thicknesses of a few hundred nanometres. The defects are caused by a series of knock-on collisions, which lead to significant expansion and contraction in the crystal's c-axis and a-axis, respectively. The expansion is attributed to interstitial clusters, whereas the contraction is attributed to the collapse of vacancy defects with a partial contribution via the Poisson effect caused by the expansion in the c-axis (Aitkaliyeva, 2017; Kelly et al., 1966; Kelly, 1982; Marsden et al., 2017; Nightingale, 1962). The rate of damage to the graphite structure in terms of the a-axis contraction depends on the irradiation dose and temperature. With increasing irradiation dose, the rate of contraction in the a-axis decreases, and eventually, the graphite begins to experience net expansion. The critical point at which this reversal occurs (the turnaround point) varies with the operating temperature (Hall et al., 2006; Zhou et al., 2017a).

For these reasons, a stability analysis of the Generation-IV nuclear systems is needed, which will be used to verify the stability of the reactors following a reactivity change, as well as to identify any potential regions of instability. Particularly, the behaviour of the new graphite grades candidate for the Generation-IV nuclear reactors in normal operating conditions must be of great interest.

Consequently, this Thesis attempts to contribute to the structural characterisation of nuclear graphites; observations are made for both virgin and neutron-irradiated graphite. Nuclear graphite is the main component of the reactor core that is affected by irradiation. Emphasis is focused on nuclear graphite candidates for very high-temperature gas reactors ((V)HTRs), which is a part of Generation-IV nuclear reactors, and a combination of both novel and improved-upon existing techniques are employed to study the changes in the structure of graphite.

In the following section, the designs of reactors used in the UK, such as Magnox reactors, advanced gas-cooled reactors (AGRs henceforth) and two of Generation- IV reactors; thermal Molten salt reactor (MSR henceforth) and very high-temperature gas reactors (VHTRs) are discussed in terms of changes and improvements of each generation. In addition to the 14 active nuclear reactors in the UK, which represent ~3% of the total number of reactors in operation globally, the newest facility—the Sizewell B Pressurised Water Reactor (PWR),

uses water instead of graphite as the moderating material and therefore is not discussed here.

1.1.2 Old, current and future nuclear reactor generations

1.1.2.1 The Magnox gas-cooled reactors

The Magnox reactors were the first nuclear reactors to be operated commercially in the UK. A total of 26 reactors were built between 1956 and 1971, all of which have been shut down (WorldNuclearNews, 2015). The first Magnox reactor was built at Calder Hall, and the last opened reactor was at Wylfa (2 reactors) on the Isle of Anglesey in 1971. Wylfa 1 was the last operating Magnox reactor shut down in December 2015. Figure 1.1 shows a schematic of the Magnox nuclear reactor highlighting the flow of gas through the system.

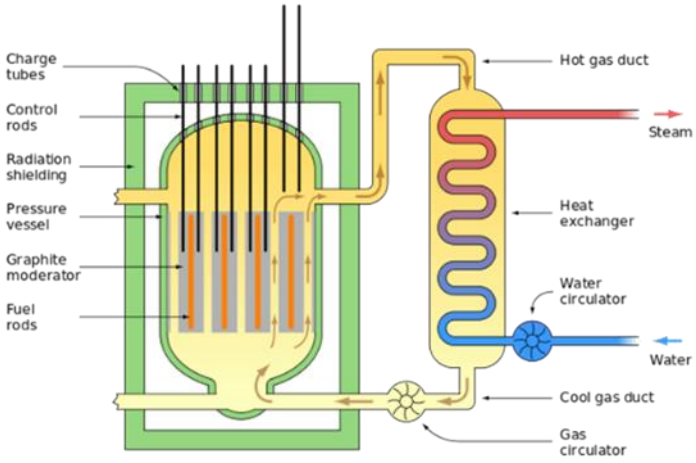

Figure 1.1: An early Magnox design with a cylindrical steel pressure vessel (WorldNuclearAssociation, 2018).

Outside the reactors are many heat exchangers with concrete shielding from radiation. The inlet gas temperature was 140 ˚C, and the outlet temperature was 336 ˚C (Anon, 1956; Jensen and Nonbøl, 1999). Magnox reactors used graphite as a moderator and required a large quantity of fuel due to the lack of any enrichment (i.e., only 0.7% fissile material in the fuel). Natural uranium metal was used as the fuel in these reactors, which ignites spontaneously with air; hence, it was clad in an alloy of magnesium with aluminium (from which the name 'Magnox' is derived) due to its low neutron capture cross-section and its

resistance to oxidation. They were cooled with CO_2 gas instead of liquid cooling because gases absorb relatively few neutrons. The graphite core was constructed from thousands of blocks, accommodating the fuel channels (Magnox sites had either 3,000 or 6,000 fuel channels). The fuel was stacked eight modules deep, and control rods (between fuel elements) were inserted to absorb the neutrons and stop the chain reaction or to shut down the reactor in the event of refuelling or an emergency (WorldNuclearAssociation, 2018).

The Magnox reactor generation naturally has many disadvantages in its design. For example, Magnox has a low operating temperature because the cladding restricts the maximum operating temperature to below 665 ˚C as when these temperatures exceeded, it would result in a phase change with associated swelling (Bodel, 2013). The tendency of uranium metal to ignite with air causes a potential plant operation risk, which could lead to fire such as, the accident which occurred at Windscale in 1957 and which proved terminal for the affected pile (WorldNuclearNews, 2015).

1.1.2.2 Advanced gas-cooled reactors (AGRs)

In the late 1970s, the UK government began to develop the next generation of nuclear power stations. The Magnox design was improved to form the AGRs. There is a total of 14 reactors of AGRs design currently in operation that also use graphite as moderator material. In the AGRs, the fuel cladding was upgraded to stainless steel instead of Magnesium alloy, and the gas coolant fills a larger pressure volume. The use of stainless-steel cladding is to resist higher operation temperatures. The disadvantage of this material is that it has a higher neutron capture cross-section than the material used in Magnox design, so the uranium fuel must be enriched to compensate. Therefore, uranium dioxide pellets enriched to 2.5–3.5% of U-235 was used instead of the natural uranium metal fuel with 0.7% of U-235 that was used in the Magnox reactors (Gill, 2014). In addition, AGRs increased the reactor's thermal efficiency to about 41%, which is an improvement over the typical Magnox efficiency of 32%. This improvement in thermal efficiency can be attained with higher coolant temperatures (CO_2 coolant in AGRs) that can operate in excess of 627 ˚C (Bodel, 2013). The graphite brick moderators in the operational gas are at 450 ˚C to prevent excessive

thermal oxidation (Gill, 2014; Nonbøl, 1996). Figure 1.2 shows a schematic of the AGR. Other disadvantages of the graphite core are weight-loss and cracking.

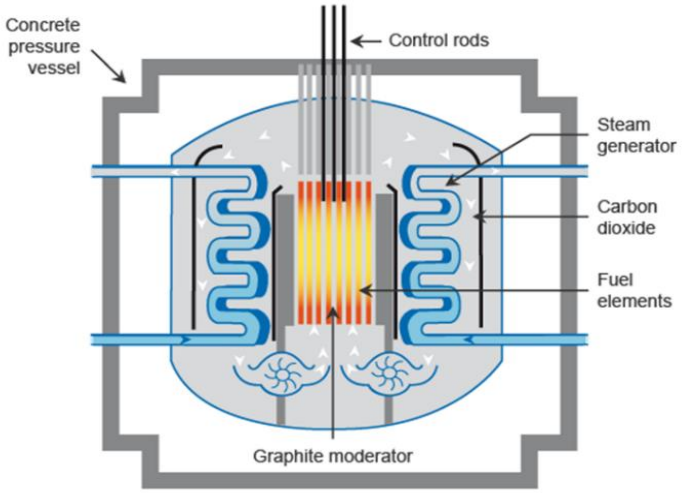

Figure 1.2: Schematic of AGR (WorldNuclearAssociation, 2018).

In the UK, France's EDF Energy company, who owns and controls 14 of the UK's reactors, successfully extended the life expectancy of the reactor by a minimum of seven years. (WorldNuclearAssociation, 2018). However, recently it has been reported that the EDF group has decided to take reactor 3 (of Hunterston B nuclear power station in Scotland; an Advanced Gas-Cooling Reactor (AGR)) offline for six months [possibly longer] after inspections showed a greater amount of cracks than normally expected in the graphite bricks of the reactor's core, which appears from changing the microstructure. Furthermore, approximately 370 hairline fractures have been discovered in the graphite bricks, which exceeds the operational limit by about 350 hairline fractures (Vaughan, 2018; Kevin Keane, 2019).

Consequently, this leads to potentially three issues; the first issue, as reported by Vaughan (2018), '*probably limit[s] the lifetime for the current generation of AGRs*' and therefore, could result in electricity shortages. The second issue is that of safety; to ensure that the nuclear reactors operate safely until new nuclear power stations are built, or a new form of an alternative energy technology becomes viable. If such safety is not ensured, the change in the whole bulk bricks could cause distortions in the graphite core's control channel and unintended shutdowns of the reactor, especially, in the event of natural disasters

(such as earthquakes) (WorldNuclearAssociation, 2018). The third issue is that these cracks in the graphite bricks may cause coolant leakage and consequently, a rise in fuel temperature (Marsden et al., 2017).

1.1.2.3 Generation-IV nuclear reactors

In order to combat such issues with current generation reactors mentioned above, Generation-IV reactors are being designed. Recently, the UK and other countries such as China, the USA, and other European countries have become interested in the development of this generation of nuclear reactors, which include six reactor systems proposed by the Generation-IV International Forum (WorldNuclearAssociation, 2018). The UK is interested in the development of two of the six systems; a thermal Molten salt reactor (MSR) and very high-temperature gas reactors ((V)HTRs), which both also use graphite as a neutron moderator and structural component. Generation-IV will be subjected to much higher irradiation doses at approximately 80–200 dpa, rather than the current generation irradiation doses of 25dpa. Similarly, irradiation temperatures of the new reactors (between 600-1000 °C) is higher than the old reactors (below 600 °C) (Aitkaliyeva, 2017). Thus, Generation-IV reactors have an excessive thermal efficiency which is approximately 60-80%.

Consequently, the effects of radiation will be more pronounced in Generation-IV reactor materials as compared to those in Magnox and AGR materials (Zhou et al., 2017a). The materials to be used in Generation-IV must to have good dimensional stability during irradiation, a high degree of chemical compatibility with the coolant and the fuel, and resilient mechanical properties such as strength and fracture toughness after aging (Marsden et al., 2017). These requirements need to be met under both normal operation and accident conditions.

The MSR uses molten salt as primary coolant flows through graphite moderator channels at high temperature and high radiation environment (Jing et al., 2016). Nuclear graphite in MSR must have a microstructural porosity that can achieve two requirements (Song et al., 2014). Firstly, it should preferably exclude the molten salt fuel to avoid local overheating within the porosity of nuclear graphite. Secondly, the nuclear graphite must allow the removal of Xenon (Xe) gas that helps to reduce the poisoning of the fission-product. This

requires the internal porosity of graphite to have pore diameters larger than 1 mm to allow for the removal of the gas. Also, a pore diameter of less than 100 nm is required to exclude the molten salt fuel (Song et al., 2014).

1.1.2.3.1 Very high-temperature gas reactors ((V)HTRs)

The development of (V)HTRs aims at a possible temperature operation of 1000 °C and uses helium as a coolant gas because it is a safe, non-reactive cooling medium with a low nuclear cross-section (Cervi et al., 2018; Hay et al., 2011). Due to the use of helium coolant, the radiolytic oxidation, which results in loss of moderator mass, is not a design issue in (V)HTRs (and MSR), unlike in old and current reactors (Magnox reactors and AGRs) (IAEA, 2019). However, due to the higher temperature operation in the (V)HTRs, graphite is still susceptible to thermal oxidation by oxygen, carbon dioxide, and water. Therefore, porosity evaluation with irradiation is essential in the development of Generation-IV, as this generation requires the development of the microstructure of graphite of very small pores, which are not inter-connected.

This interest in (V)HTRs is due to their ability to achieve very high fuel utilisation rates and operate at high temperatures allowing for hydrogen production (which can be extracted from water using thermo-chemical, electro-chemical or hybrid processes).

Moreover, there are two different types of (V)HTRs core that are under consideration: pebble-bed and prismatic core. The (V)HTRs include three main components: a helium-coolant system, a heat-transport system (HTS), and a cylindrical cross-vessel wherein the graphite bricks are stacked. The design configuration of each prismatic block and pebble bed is distinct. In a prismatic block of core configuration, hexagonal graphite blocks are stacked to fit in the cross-vessel. In contrast, the pebble bed reactor design is comprised of fuel in the form of pebbles stacked together in the cross-vessel. The cross-vessel routes the helium between the reactor and the HTS (Gill, 2014). Typically, a nuclear reactor core of graphite moderators contains several graphite bricks with holes drilled within each brick for fuel element placement (typically, this is the TRISO coated particle fuel, but alternative fuel cycles such as U-Pu, Pu, MOX or U-Th can also be used), as well as adding control rods. These control rods (made of materials such as cadmium, hafnium, or boron) are then used to absorb neutrons and are

designed to move vertically at varying rates (Garcia et al., 2009). A chain reaction can be stopped when the control rods are inserted inside the holes or accelerated upon withdrawing the control rods. More importantly, the position of control rods can be altered to ensure complete reactor shutdown, in the event of a prismatic core blockage.

In contrast, in the case of the pebble bed core design, the control rods are inserted into a surrounding graphite reflector. Due to the vast amount of heat energy present in the core, a coolant is used to circulate the fluid throughout the core, thus transferring the heat energy and converting it into electrical energy. Therefore, coolant plays an important part in nuclear reactor safety operations by maintaining core temperature within the established safe limits. Figure 1.3 shows a general schematic of the (V)HTR.

Also, in the pebble-bed design, the presence of more dust in the primary system can be predictable as a result of the refuelling procedure and pebble movement in the core vessel. Moreover, a pebble-bed core is comprised of less-graphitic graphite. A prismatic core contains primarily highly graphitic graphite with only a minor fraction of fuel-element matrix graphite. In terms of the power cycle, there is a slight difference between the two designs. The coolant flow instabilities can be an issue in prismatic (V)HTRs if the temperature rise in the core exceeds 400 K (Garcia et al., 2009).

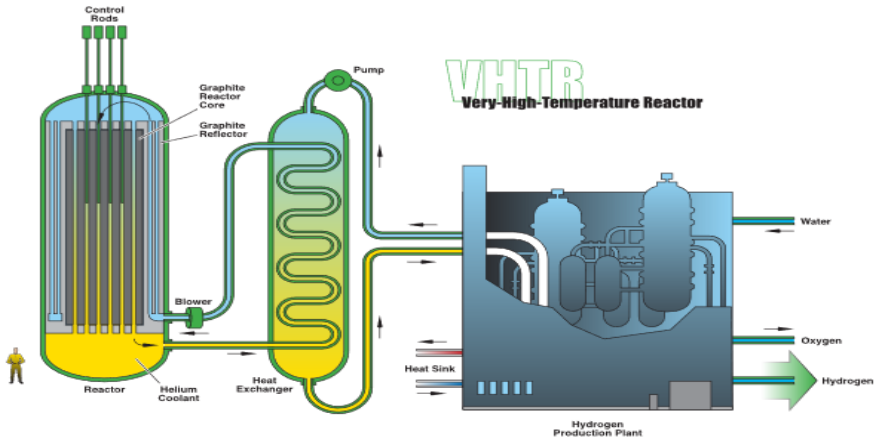

Figure 1.3: Schematic of VHTR (WorldNuclearAssociation, 2018).

1.1.3 Research questions and approach

The selection of appropriate heat-tolerant materials for the safe construction of reactors is a topic of utmost priority when it comes to research and development in the field of nuclear power. Thus, a fundamental understanding of the behavioural properties (e.g., mechanical) of the materials (both the structural and refractory materials themselves, as well as irradiated materials) at high temperature must be established to define the critical performance limitations and possible design alternatives. Nuclear graphite—which is used as a moderator, reflector, and structural support material—can evolve when exposed to radiation during high temperatures, causing changes such as the appearance of crystal growth or break up, porosity, and creep. These issues affect the entire reactor system.

Although extensive research has been conducted since the 1940s in order to better predict the behaviour of irradiated nuclear graphite, the microstructural effects of radiation damage remain unclear, especially in those new graphite grades candidates for (V)HTRs. The bulk properties of radiation-damaged graphite have been investigated (Marsden et al., 2017; Yvon, 2016), and theoretical models have been developed for the macro-scale structure of the irradiated material (Bacon and Warren, 1956; Delannay et al., 2014; Heggie et al., 2011). However, an understanding of the varying types of nuclear graphite moderators' structure at different length scales is of great interest for (V)HTRs design, particularly as the carbon graphitisation process leads to differences between nuclear graphites structure prepared from different raw materials (or some other formational process). The effects of neutron irradiation on graphite are strongly dependent upon graphite's structural properties. Adding to this, most of the historical data on irradiated graphite is from a low temperature of approximately <550 ˚C irradiations. Thus, these data on the effect of neutron irradiation on nuclear graphite material cannot be directly applied to the current-new build (V)HTRs.

Thus, structural characterisation of nuclear graphite will help to improve the current knowledge on the effect of neutron irradiation dose and temperature on nuclear graphite in order to design and select graphite material with improved resistance to irradiation damage. Accordingly, the outcomes of this

Thesis might be relevant in the evaluation of developmental graphite grades proposed for future generation reactors, mainly (V)HTRs.

Consequently, this Thesis attempts to address some gaps by answering the following research questions:

1. How does neutron irradiation affect the structure of nuclear graphite grades at micro and nanoscale? How are these changes affected by neutron radiation dose and temperature?
1. What measurement techniques help to quantitatively evaluate these changes for both virgin and irradiated nuclear graphite?

In order to answer the above research questions, the author of this Thesis follows four objectives. The first objective is to study the variation between different virgin nuclear graphite microstructures in terms of filler and binder phases, porosity and crack microstructure focusing on the following nuclear graphites: PGA (used in Magnox reactors), Gilsocarbon (used in AGRs), PCEA and PCIB (which are both candidates for (V)HTRs). These components can significantly influence the dimensional change, as well as the mechanical and thermal properties of the graphite. This is due to the strong correlation between neutron irradiation-induced changes and the virgin graphite component microstructure (Burchell et al., 2007; Kane et al., 2011). Consequently, this evaluation will potentially establish a good understanding of the fundamental mechanisms that affect the material properties and dimensions of nuclear graphite. This task was achieved using PLM and SEM-based techniques via digital image analysis, allowing for the study of the material in 2D.

The second objective was to use FIB-SEM methods to develop a 3D microstructural analysis of porosity in virgin nuclear graphite grades (PCEA and PCIB) that are candidates for (V)HTRs (Generation-IV reactor). The data was then compared to the results obtained from PLM, which was also used to build up a 3D view after progressive polishing. This allows for a detailed statistical description of the features of interest, which will aid in the analysis of neutron-irradiated graphite.

The third objective was to examine physical changes in the crystal structure in terms of coherence lengths (crystallite sizes) in the a and c directions, interlayer spacing along the c direction, the in-plane lattice parameter along the a direction, micro-strain and the lattice disorder of similar virgin

graphite samples (PGA, Gilsocarbon, PCEA and PCIB) using XRD and then compare the results to Raman data.

The final objective was to evaluate the neutron irradiation-induced changes by using two different nuclear graphites (PCEA and PCIB, candidates grades for Future (V)HTRs (Generation-IV reactor) irradiated at different temperatures and doses (at the Advanced Test Reactor at the Idaho National Laboratory, USA; see Appendix A for more information) using PLM, SEM, XRD and Raman spectroscopy.

1.1.4 Outline of Thesis

This Thesis is divided into eight chapters and two appendices. Chapter 2 provides a general overview of the structural properties of various grades of graphite, including how they are produced for use as neutron moderators. The nuclear fission reaction is then detailed to give an understanding of how nuclear graphite changes over its service life. Chapter 3 comprehensively reviews the literature about radiation damage in nuclear graphite with a focus on the experimental techniques applied in the Thesis. Chapter 4 outlines the different material characterisation techniques that were used to characterise graphite samples, including XRD, Raman spectroscopy, PLM and SEM, and Focussed Ion Beam–Scanning Electron Microscopy (FIB-SEM). The results from each set of measurements are discussed in chapters 5, 6, and 7. Finally, chapter 8 summarizes the overall results and outlines future research directions.

Chapter 2

2.1 General background

Graphite can be used as a neutron moderator and a structural component in nuclear reactors. During reactor operation, there are two main events that influence the graphite material properties; neutron irradiation and radiolytic oxidation. However, the latter is not an issue in the (V)HTRs (Generation-IV reactors) designs due to the use of helium as a coolant. The extent of the irradiation-induced damage is dependent on neutron fluence and irradiation temperature which are investigated in this Thesis. Therefore, this chapter begins with an introduction to the crystallographic structure of graphite and discusses the effect of neutron irradiation on nuclear-grade graphite and single-crystal graphite. The virgin and irradiated nuclear graphite properties are also outlined.

2.1.1 Introduction to graphite

Graphite is an extremely versatile and naturally occurring allotrope of carbon. It is widely available in mineral form. The structure of single-crystal graphite comprises of layers of carbon atoms bonded covalently in-plane to form a honeycomb lattice with atoms separated by an angle of 120° and C–C bond lengths of 1.42 Å (Figure 2.1). The flat parallel layers are separated by a distance of 3.35 Å and are held in place by weak van der Waals interactions (Liu and Zhou, 2014). Within a plane, the graphene layers are bound by sp^2 sigma (σ) bonds and pi (π) bonds. The carbon atoms bond through sp^2 hybridisation, creating a planar trigonal structure (Klein, 2010; Liu and Zhou, 2014; Tipler and Mosca, 2007), while the remaining fourth electron is delocalised within the plane, which explains the graphite's conductivity (Klein, 2010). The structure of sp^2 graphene (i.e., single plane) hybridisation is shown in Figure 2.2, with the σ bonds and the 2p delocalised electrons marked. The graphene layers can be arranged in hexagonal or rhombohedral stacks.

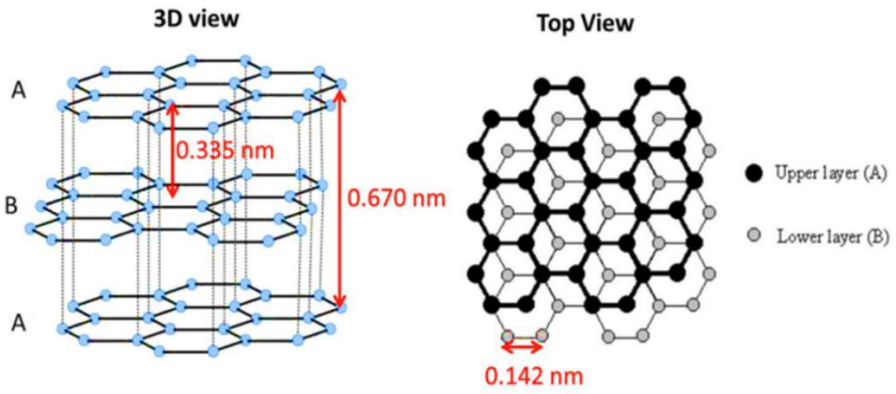

Figure 2.1: Crystal structure of graphite unit cell and ABAB stacking sequence reprinted from (Liu and Zhou, 2014).

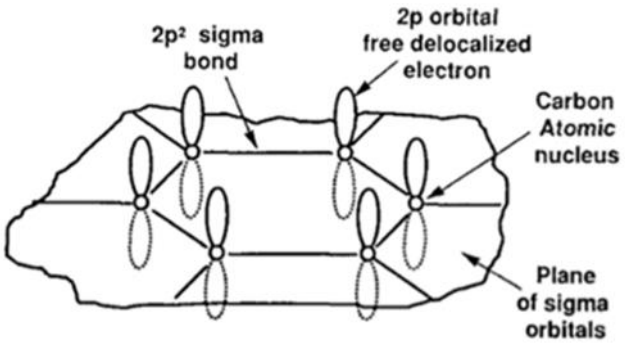

Figure 2.2: The structure of the sp^2 hybridisation of graphite with the σ bonds and the 2p delocalised electrons marked (above and below the σ orbital and plane) (Thrower, 1964).

In graphite, the atoms form a two-dimensional hexagonal lattice (Figure 2.3 (a)) with layers held together through Van der Waals attraction with an ABAB stacking sequence (Nightingale, 1962; Simmons, 1965). The crystal lattice parameters in this case are: a_0 = 0.245 nm and c_0 = 0.6708 nm. Rhombohedral graphite (Figure 2.3 (b)) has another stacking sequence in addition to the hexagonal one, but less frequent one. The ABCABC stacking sequence gives rise to a rhombohedral structure (Simmons, 1965). The crystal lattice parameters in this case are a_0 = 0.2256 nm and c_0 = 1.006 nm.

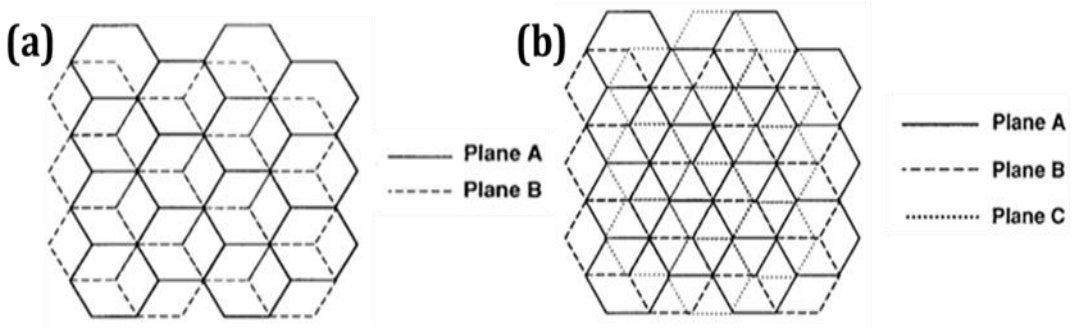

Figure 2.3: Schematic of (a) hexagonal; (b) rhombohedral graphite crystal (Thrower, 1964).

These perfect planar networks of hexagons of carbon atoms may be displaced from the ideal stacking sequence (hexagonal or rhombohedral) due to the presence of dislocations, stacking faults, vacancy, and interstitial defects. The stacking faults have been assumed to occur due to the weak interlayer binding and accommodation of basal dislocations (Evans, 1978; Telling and Heggie, 2003).

2.1.1.1 Graphitising and non-graphitising carbon

Some forms of carbon cannot be transformed into crystalline graphite, or graphitised, even when treated at temperatures of 3000 ˚C or more. Non-graphitising carbons are usually low-density, hard substances that are isomorphic and microporous (Harris, 2005). Initial models of the graphitisation process were suggested by Franklin, who defined the basic units of carbon material as small graphitic crystallites containing very few plane layers joined together by cross-links (Radovic, 2004). The thermal expansivity of these crystallites is very much like single crystals, but the cross-links restrict the volume of the bulk material. These cross-links, together with internal hydrogen and the viscosity of the material, play an important part in preventing the stacking of incipient graphene sheets during carbonisation. As a result, char forms at 1000 ˚C or above, with randomly ordered crystallites that are held together by van der Waals forces and the remaining cross-links. These links may break at higher temperatures, but the activation energy required to order all the crystallites is too high, and graphitisation is thus prevented. On the other hand, graphitising carbon is soft, non-porous, and much denser (closer to that of

crystalline graphite, so it crystallises readily at higher temperatures (Harris, 2005; Radovic, 2004).

In the Harris model, non-graphitising carbon includes discrete fragments of curved carbon sheets, with pentagonal and heptagonal structures distributed randomly, along with micropores 0.5–1.0 nm in diameter. On the other hand, graphitising carbon contains only hexagonal structures. Non-hexagonal fullerene structures prevent graphitisation (Kelly, 1981).

Mrozowski classified carbon into two broad groups: 'soft' carbons that are graphitisable and 'hard' carbons that are non-graphitisable. The material is classified according to the orderliness of the arrangements of crystallites at micro-scales. Soft carbons are formed from organic materials that melt on heating and solidify at temperatures higher than 673 K. Hard carbons are formed from organic materials that do not melt at all, such as polymers, or that solidify at lower temperatures (Evans, 1978).

Graphitisation, or the thermal ordering of disordered carbon into graphite, proceeds in two stages. The first stage is very short-lived and consists principally of displacement of intermediate carbon atoms to their nearest equilibrium positions. As a result, some of the crystallographic planes are straightened out, the curvature is decreased, and the planes thicken perpendicular to the basal plane due to texture growth. The proportion of layer defects decreases while lattice dimensions increase. This stage is controlled by diffusion, and ends once the packet edges contact each other, usually around 2300–2500°C (Nightingale, 1962). The second stage begins at a higher temperature of 2500–3300°C, at which some of the remaining planes straighten and the crystal size increases. The ordering process, however, slows down greatly with time, so that the second stage lasts longer. This stage is essentially a transformation in the solid phase and is like recrystallisation (Arai, 1993; Nightingale, 1962; Trefilov, 2012). The number of impurities must be reduced before graphitisation. Figure 2.4 is a schematic diagram of the graphitisation process for the model of carbon fibers, while Figure 2.5 is a schematic diagram of the process of graphitisation in general.

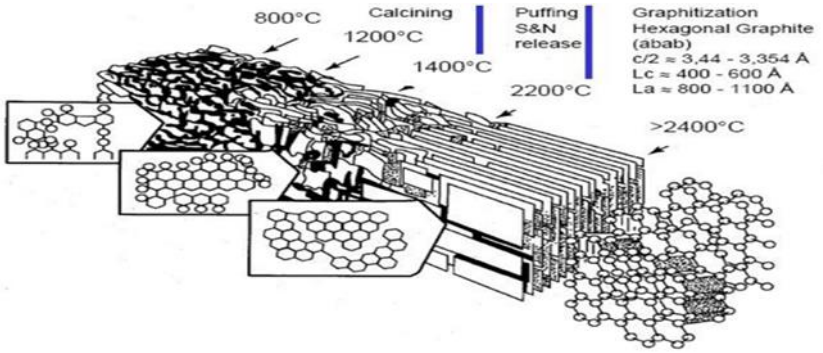

Figure 2.4: Graphitization process for carbon fibers showing the different stages of heating treatment (Marsh and Reinoso, 2006).

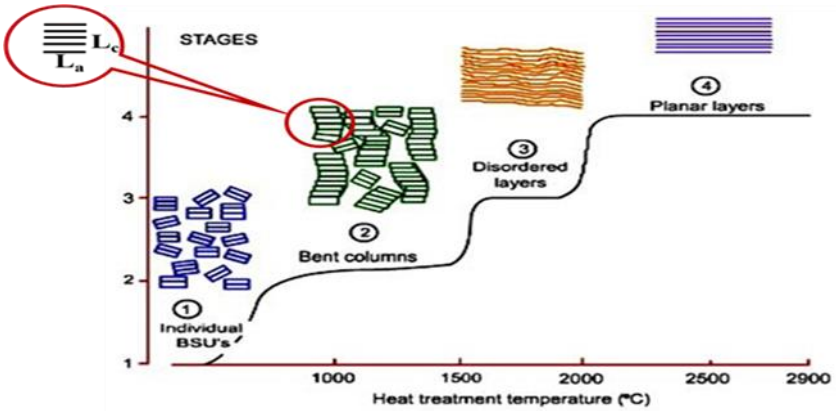

Figure 2.5: A schematic diagram demonstrating the general graphitisation process (NPTEL, 2009).

2.1.2 Types of graphite

There are three principal types of graphite; natural, pyrolytic, and synthetic bulk graphite. Each of these sources of graphite has different properties and occurrences which are discussed below:

2.1.2.1 Natural graphite

Natural graphite is very abundant, although the quality of ores may differ substantially from one region to another. High-purity graphite ore with up to 100% carbon content, the type that is used in reactors, is mined in Sri Lanka. Lower-grade ores that need to be refined are found in Germany, Russia, Korea, Norway, Mexico, China, and Austria. Ticonderoga in the United States has been used as a source of high-quality flakes of natural graphite for crystallographic and nanoscale studies (Gogotsi, 2006; Simmons, 1965). Bulk deposits are found

often in the form of flakes, and sometimes in the form of columns. These columns contain a polycrystalline form of graphite that exhibits a high degree of preferential orientation of the crystalline c-axes parallel to the columns (Gogotsi, 2006).

Natural graphite is used principally in foundries, refractories, and the fabrication of electrical components. It is usually not used in nuclear reactors because of its impurity content. However, it is used for analysis and experimental studies because it can be used to approximate the properties of ideal single-crystal graphite (Simmons, 1965). Small regions of the nearly ideal structure occur in natural graphite and are bounded by a twist or twin boundaries. The single crystals occurring within these ideal regions have been found to have diameters of a few millimetres and thicknesses of a few tenths of millimetres (Simmons, 1965).

2.1.2.2 Pyrolytic graphite

Pyrolytic graphite is manufactured using chemical vapour deposition (CVD), whereby a graphite plate or rod is heated in a stream of hydrocarbon at high temperatures to deposit carbon on the substrate. The deposition of carbon is highly sensitive to CVD parameters, such as the partial pressures of the hydrocarbon and inert gas streams, total pressure, and the substrate temperature (Pierson, 2012). The polycrystalline deposits are highly oriented under optimal conditions. For example, a crystal density of up to 2.24 g/cm^3 can be achieved if CVD is initially applied at 2100 ˚C followed by annealing at 2800 ˚C. Some material properties are altered during this formation process, including resistivity, hardness, and toughness. As a result, pyrolytic carbon can be fabricated as a thick coating on many types of substrates including moulded graphite, carbon fibers, and porous carbon-carbon structures (Pierson, 2012).

Depending on the specific manufacturing process and the parameters used, pyrolytic graphite may have columnar, laminar, and isotropic structures. The columnar structure consists of basal planes formed parallel to the deposition surface, and the cone-like formation is a result of uninterrupted grain growth towards the reactant source (Simmons, 1965). The laminar structure, on the other hand, usually appears as concentric shells deposited on particles or fibers. Although both structures are optically active to polarised light, the third

structural type, isotropic, shows no optical activity because it is formed from fine grains that lack orientation (Pierson, 2012; Simmons, 1965; Thrower, 1964). The three structures found in pyrolytic graphite are shown in Figure 2.6.

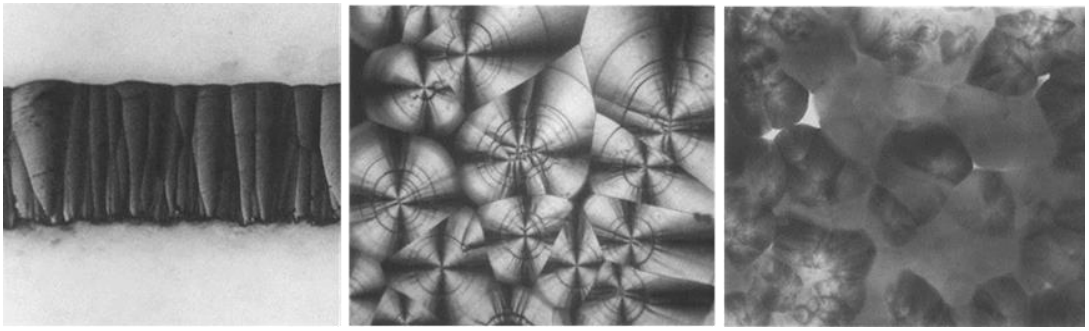

Figure 2.6: Different structures of pyrolytic graphite: columnar (left), laminar (middle), and isotropic (right) (Thrower, 1964).

2.1.2.2.1 Highly oriented pyrolytic graphite (HOPG)

HOPG grade is the most common deposited pyrolytic material. It is a highly pure and ordered material, which is produced under pressure by thermal cracking of hydrocarbon and subsequent heat treatment that improves the quality of the c-axis orientation of the crystallites (Wen et al., 2008). HOPG has been used as an approximant for single-crystal graphite to measure the irradiation-induced dimensional change in the nuclear graphite core. The dimensional instability under irradiation is one of the critical issues in the nuclear graphite core; hence, intensive efforts have been made to understand the mechanism behind it.

However, HOPG is considered an unsuitable material for nuclear applications due to two reasons. Firstly, although HOPG is inherently anisotropic on the nanoscale, graphite material to be used as a moderator must have a highly isotropic property on larger length scales, which HOPG does not meet (Wen et al., 2008). This is due to the fact that isotropic materials exhibit much longer irradiation lifetimes than anisotropic materials. Hence isotropic graphite has better dimensional stability (Burchell et al., 2007; Neighbour, 2012). The dimensional change in anisotropic graphite could distort graphite components, resulting in interference with control rod operation or coolant leakage (Shen et al., 2015). Secondly, HOPG cannot be used due to its size because the graphite moderator is required to be a bulk material, whereas HOPG is a thin film

(Burchell et al., 2007). Thus, HOPG can be deemed as unsuitable for use as a moderator material in nuclear reactors.

2.1.2.3 Bulk synthetic graphite

Synthetic graphite is manufactured by heating solid hydrocarbons as raw materials to encourage graphitisation (>2800 ˚C) and crystal growth (Simmons, 1965). The final product has significant properties such as low neutron-absorption cross-section, high scattering cross-section, physical and chemical stability at high temperatures, etc. These important properties make synthetic graphite the perfect candidate as a moderator and structural support material in nuclear reactors. Thus, in the following section, the general steps of the manufacturing process of nuclear graphite grades suggested for Generation-IV reactors, its microstructure and properties are discussed.

2.1.3 Nuclear graphites manufacturing processes, microstructure and properties

Nuclear graphite is a highly crystalline synthetic material. Synthetic graphite differs in their properties, such as optical texture, density, electrical resistivity, mechanical strength, pore shape, and size distributions. These properties are controlled by the method of manufacture and source materials. Most manufactured nuclear graphite uses isotropic petroleum coke as a filler particle and coal-tar pitch as a binder matrix, thus being formed in a manner to make the graphite near-isotropic or fully isotropic (Marsden et al., 2017; Nightingale, 1962; Simmons, 1965). The process used to manufacture new types of graphite (candidates for Generation-IV reactors) is almost similar to that used to produce conventional graphite (Marsden et al., 2017; Nightingale, 1962; Zhou et al., 2017a). A schematic of the manufacturing process of nuclear graphite is shown in Figure 2.7.

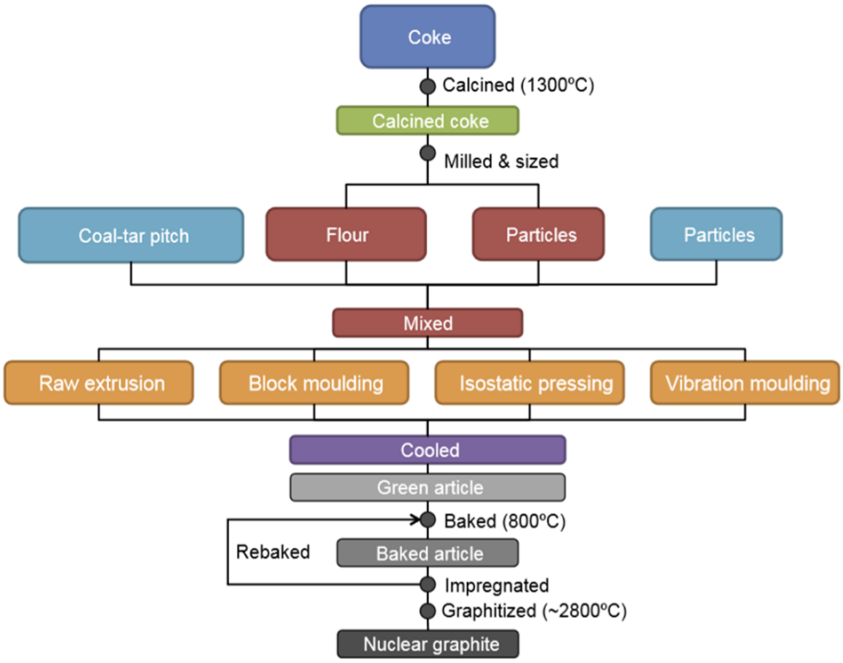

Figure 2.7: Manufacturing process of nuclear graphite (Marsden et al., 2017).

The first and most critical step of the manufacturing process is the selection of the appropriate raw materials. This step ensures the desired comprehensive properties of nuclear graphite. In particular, the goal of this step is to attain high chemical purity of nuclear graphite, which helps to minimise the neutron absorption via impurities (e.g., Boron) (Contescu et al., 2014; Nightingale, 1962).

The coke is calcined to remove volatiles, then the mixture of calcined coke (at temperature range 1000-1300 ˚C) is crushed and sieved to achieve various particle sizes (Holt, 2008). The coke particles are then blended with hot tar pitch binder. In most cases, a coal-tar pitch is preferred because of its high carbon content and low manufacturing cost (Zheng et al., 2017). However, crushed graphite flour (finer material) will be included in the binder mixture in instances where the component is particularly large. This mixture is then formed into solid blocks (billets) referred to as 'green articles', which may consist of approximately 80% coke/flour and 20% binder (Marsden et al., 2017).

The final product's properties are then affected by the forming method since this determines the preferred orientation of crystallites and subsequent anisotropy within the nuclear graphite. For example, graphite with a high degree of anisotropy exhibits high internal stresses, cracking, and shortened irradiation

lifetimes as a result of anisotropic irradiation-induced dimensional changes (Marsden et al., 2017; Nightingale, 1962; Simmons, 1965; Zhou et al., 2017a).

Isotropic coke is preferred in the forming process of nuclear graphite cokes (such as Gilsonite coke). However, this type of coke is no longer available in amounts large enough to manufacture isotropic nuclear graphite (Zhou et al., 2017a). Secondary coke is used to attain the anticipated isotropic irradiation response. Essentially, anisotropic cokes are manufactured into graphite and then ground to become the starting 'isotropic' filler in the conventional process. This makes the entire manufacturing process much longer (Holt, 2008; Zhou et al., 2017a). During the isostatic moulding procedure, the pressure is applied to the mixture from one or two directions at once. This is done through a rubber membrane in a liquid-filled chamber, subsequent in a material with great uniformity and isotropic properties. Other moulding practices utilise vibration techniques to increase the density of the mixture. Extrusion is the most popular formational method, where the mixture is forced through a dye under pressure in order to align filler particles (Marsden et al., 2017).

The green article is then immersed in water for cooling, which causes internal cracking. Crushed graphite flour is added to the mixture to minimise cracking. After cooling, the green article is baked for several days at 800 ˚C. The billets now are referred to as baked carbon, which is unsuitable for nuclear applications but can be used in the steel industry as a furnace liner. During baking, gas-evolution pores are formed throughout the material, particularly during the binder phase. Therefore, successful manufacturing requires that porosity be reduced while increasing the density of the blocks. This can be achieved by impregnating the green article with a coal-tar pitch under vacuum in an autoclave. Several cycles of re-baking and impregnation may be needed to achieve the required density (Marsden et al., 2017; Nightingale, 1962; Simmons, 1965).

The following step is graphitisation, where the baked green blocks are graphitised either by applying a relatively low voltage and large amount of electrical current to the coke (which has been covered with an electrically conducting coke), or by covering the block with an oxidation-protection coke and applying current directly to the block (Marsden et al., 2017). Graphitisation usually requires temperatures of ~2800-3000 ˚C, over a one- or two-day period

(Zhou et al., 2017a). This is usually carried out in an Acheson graphitisation furnace or a longitudinal graphitisation furnace. The process removes impurities and improves electrical and thermal conductivity as the graphite crystals grow (Holt, 2008; Nightingale, 1962). If high-purity graphite is required there may be another cycle of chemical purification via the use of halogens in which the stack is heated to around 2400 ˚C during the manufacture of coke and/or graphite. Halogens can be used to penetrate both bulk graphite and graphite crystals. This process causes a reaction involving the impurities, allowing for their subsequent removal using volatile halide salts.

The final product is a highly pure (quantified in volume-per-million), polycrystalline graphite, consisting of three main components: filler coke, binder pitch and voids of ~20% of the total volume (Zhou et al., 2017a). The voids include gas-evolution pores and cracks of various dimensions. It has been reported that the initially closed pores range from approximately 25 to 75% of the total porosity (Paul & Morral, 2018; Zheng et al., 2014). The typical nuclear graphite has a density of 1.7–1.85 g/cm^3 that is lower than the theoretical density of graphite 2.265 g/cm^3. Mrozowski (1956) suggested that the low particle density is due to the presence of micropores, which form during the cooling process after graphitisation.

The manufacturing process affects the shape, size, and distribution of the nuclear graphite pores. Porosity affects properties such as strength, thermal conductivity, and Young's modulus of the polycrystalline material; this is especially true when the graphite undergoes radiolytic oxidation in a reactor, such as in Magnox and AGR graphite moderator reactors (Zhou et al., 2017a).

Open gas-evolution pores are introduced as a result of the removal of volatiles during manufacturing. These open pores are relatively large, which means that they do not accommodate thermal expansion (Freeman et al., 2016; Zhou et al., 2017a). In addition to open gas-evolution pores, two other types of pores have been observed in nuclear graphite: bulk or inter-particle pores and filler-particle pores. The former is caused by the incomplete filling of inter-particle packing voids due to both shrinkage and gas evolution during binder pyrolysis. Filler-particle pores are caused by basal plane delamination due to local stresses that arise as the material expands and contracts with temperature during manufacturing (Kane et al., 2011). Hagos et al. (2010) simulated these

porosities using finite element methods and found that the dimensions of pores within the material depend on the dimensions of the filler particles. Mileeva et al. (2013) reported that around 70% of the porosity is open pores.

In contrast, cracks are introduced during the high-temperature graphitisation process for a number of reasons: firstly, due to gradients in temperatures; secondly, the anisotropy in the coefficient of thermal expansion (CTE) of crystallites in the material causes cracking; and thirdly, internal stresses crack the material (Freeman et al., 2016). Researchers have classified microcracks into intra-granular and inter-granular microcracks. Intra-granular microcracks, such as Mrozowski cracks (>5 nm to 200 nm wide and <10 μm long), develop within crystallites and lie perpendicular to the crystallographic c direction, see Figure 2.8. This is due to the very large anisotropy of the thermal expansion of the crystallites, which causes the formation of Mrozowski cracks that can be seen using electron microscopy (Baskin and Meyer, 1955; Haag, 2005). Inter-granular microcracks are found between crystallites at grain boundaries (Shi et al., 2008).

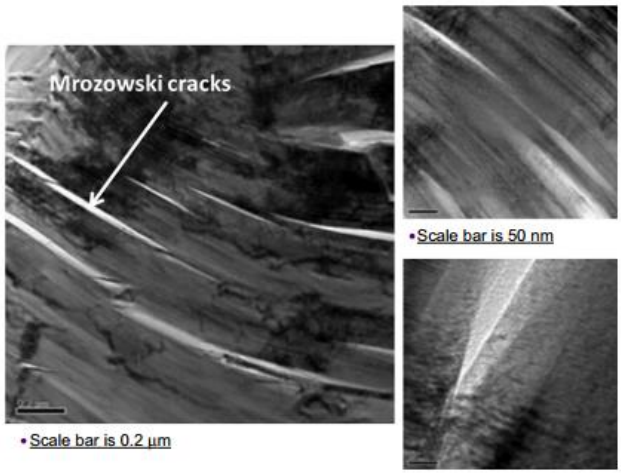

Figure 2.8: TEM images show Mrozowski cracks (Mrozowski, 1954) and the basal planes. Images reprinted from (Marsden et al., 2017).

Thus, the nuclear graphite used in Generation-IV reactors must have high purity, low contamination, minimal isotropic changes in material dimension, and an irradiation database that has validation. The anisotropic purity, microstructure orientation, method of formation, the concentration of material defects, and the size of grain determine the response of different nuclear

graphite grades to irradiation (Zhou et al., 2017a). It is important to note that nuclear graphite billets exhibit different material properties, which are commonly imparted in the microstructure by thermal processes and formation. Moreover, the anisotropic nature of a graphite crystal causes material properties to vary between different nuclear graphite grades. For example, the c-axis and a-axis have modulus of elasticity equivalent to 3.46 x 10^{10} N/m^2 and 106 x 10^{10} N/m^2, respectively, in a graphite crystal. Therefore, the orientation of the crystallites in graphite's microstructure together with crystal distribution are the main factors that determine the major properties of graphite. Marsden et al. (2017) define isotropic and near-isotropic nuclear graphite as graphite in which the isotropy ratio based on the coefficient of thermal expansion measured over the range (25- 500 ˚C) are 1.00-1.10 and 1.10-1.15 respectively. While, graphite in which the isotropy ratio is >1.10 is called anisotropic graphite (Shen et al., 2015). Nuclear graphite grain size is medium, fine grain, superfine, or ultrafine grain. However, superfine graphite has been considered for Molten Salt Reactor applications.

2.1.3.1 Properties of the grades of nuclear graphite used in this Thesis

Table 2.1 summarises the properties of the different types of nuclear graphite that were tested in the present Thesis research. The data were gathered from several sources (Béghein et al., 2012; Brocklehurst and Kelly, 1993; Heijna et al., 2017; Marsden et al., 2008; Marsden et al., 2017; Neighbour, 2012; Preston and Marsden, 2006). Figure2.9 shows polarised optical images of nuclear graphite grades microstructure outlined here.

Table 2.1: Virgin Polycrystalline graphite properties.

Graphite	**GILSO**	**PGA**	**PCEA**	**PCIB**
Filler	Gilso-coke	Petroleum coke	Petroleum coke	Petroleum coke
Filler shape	spherical filler particles	Needle-shaped	Needle-shaped & spherical filler particles	Ultrafine grains make it hard to distinguish
Binder	Coal tar pitch	Coal tar pitch	Coal tar pitch	Coal tar pitch
Used in	AGRs, UK	Magnox, UK	VHTR, USA	HTR
Process	Molded (pressing)	Extrusion	Extrusion	Iso-molded
Filler particle size (μm)*	Medium ~500	Medium ~1000	Medium 360–800	Ultrafine ~10 μm in length
Experimental Bulk density (g/cm^3)	1.81	1.74	1.84	1.75–1.85
Flexural strength (N/mm^2)	⊥26.7, // 26.9	⊥12, // 19	⊥32, // 32	30–45
Tensile strength (N/mm^2)	⊥19.9, // 20.3	⊥11, // 17	⊥17, // 22	20–30
Compressive strength (N/mm^2)	74.7	⊥27, // 27	⊥68, // 61	70–90
Thermal conductivity (W/mK)	⊥137.9, // 137.9	⊥109, // 200	⊥159, // 162	120–150
CTE (10^{-6}/°C)	⊥4.9, // 4.7	4.35	⊥3.7, // 3.5	3.5–4.5

*⊥= perpendicular (against) grain orientation; // = parallel to (with) grain orientation
*****Medium size: Comprising fillers in the starting mix of size generally are less than 4 mm (Marsden et al., 2017).
*Ultrafine size: Comprising filler in the starting mix of size generally is less than 10 μm (Marsden et al., 2017).

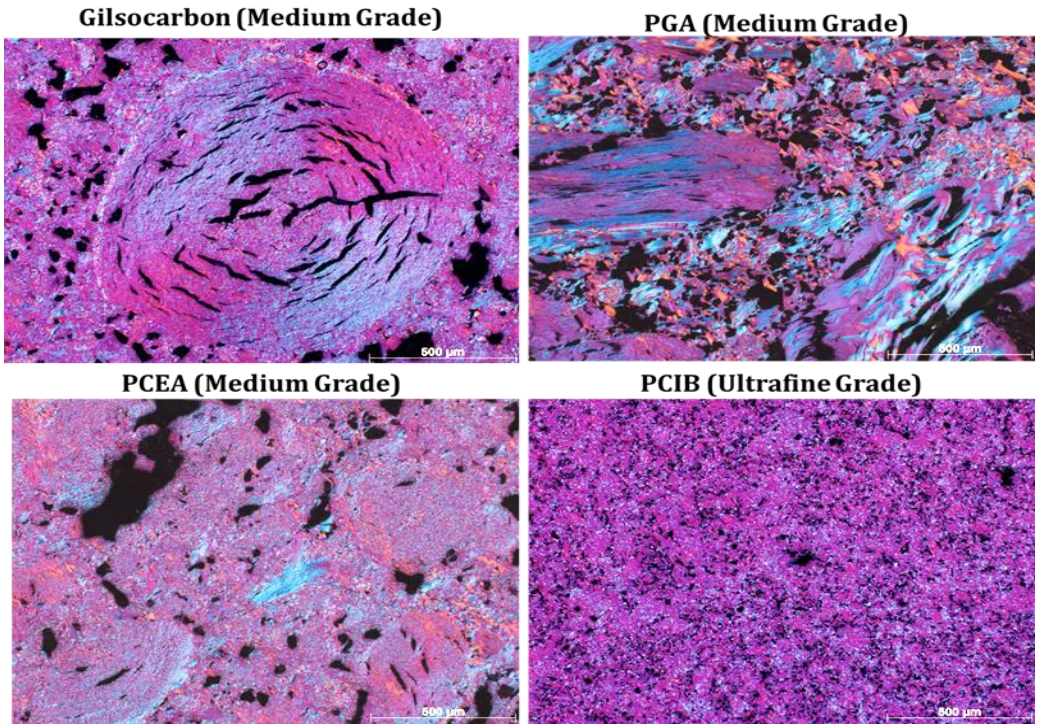

Figure2.9: Polarised optical micrographs of Gilsocarbon, PGA (top), and the candidate VHTRs graphite grades; PCEA and PCIB used in this Thesis. Scale bars are 500 μm.

2.1.4 Radiation damage in graphite

Graphite as a core material used in nuclear reactors undergoes significant property changes due to irradiation (mainly fast neutron bombardment), temperature changes, and radiolytic oxidation. The radiolytic oxidation causes the loss of graphite mass; however, this issue is not relevant to Generation-IV nuclear reactors since the proposed coolant is inert.

The radiation-induced changes in the graphite structure have been studied extensively; these changes are complex and affect several parameters. Ballistic or radiolytic events can damage any solid microstructure. The former are kinetic collisions at atomic or subatomic scales, while the latter occurs when electronic excitations caused by radiation are converted into kinetic energy. The principal result of these events is the disruption of the crystalline lattice, and the extent of the disturbance depends on the binding energies between the carbon atoms (Jones et al., 2008). Ballistic events cause further damage with each compounding event; therefore, ballistic events usually account for the limits on the radiation damage sustained by neutron moderators (Kelly, 1971). Irradiation

affects properties of graphite, including strength, thermal conductivity, coefficient of thermal expansion, Young's modulus and electrical resistivity (Burchell, 2012). Thus, a thorough understanding of the radiation damage mechanisms is essential to evaluate the viability of Generation-IV reactor systems.

2.1.4.1 Damage mechanisms

Atomic displacements arise when energetic charged particles such as electrons, ions, or neutrons collide with carbon atoms, and the transfer of kinetic energy (ΔE) exceeds the local binding energy. This displacement mechanism can only be modelled with relativistic equations, as the bombarding neutrons are moving at extremely high velocities (Kelly, 1982). The fast neutrons involved in the process are products of fission reactions, possessing mean energy of at least 0.18 MeV (Johns et al., 2018). The transfer of energy is modelled as follows (2.1):

$$\Delta \mathrm{E} = \frac{4\mathrm{A}}{(\mathrm{A}+1)^2}\,\mathrm{E_n} \tag{2.1}$$

where ΔE is the transferred energy, E_n is the total energy of the incident particles and A is the mass number of the bombarded atom.

The cascade displacement rate caused by high-energy neutrons is measured in displacements per atom (dpa) and is usually of the order 10^0 to 10^2 (Haag, 2005). The initial displacement of carbon atoms is referred to as primary knock-on atoms (PKAs). These displaced carbon atoms act as energetic projectiles. These PKAs then collide with neighbouring carbon atoms, which results in further displacement of carbon atoms in a cascade that is known as secondary knock-on atoms, as shown in Figure 2.10 (Simmons, 1965). Many of these carbon atoms recombine with previously produced lattice vacancies, while some diffuse between graphite layer planes and others coalesce to form linear molecular chains of C-C and C-C-C bonds (Fletcher, 2008; Tipler and Mosca, 2007). These linear chains usually generate new dislocation loops and new planes where the material may fracture. The dislocation loops also generate basal plane defects when the displaced interstitial carbon atoms combine into less-mobile agglomerates (Fletcher, 2008).

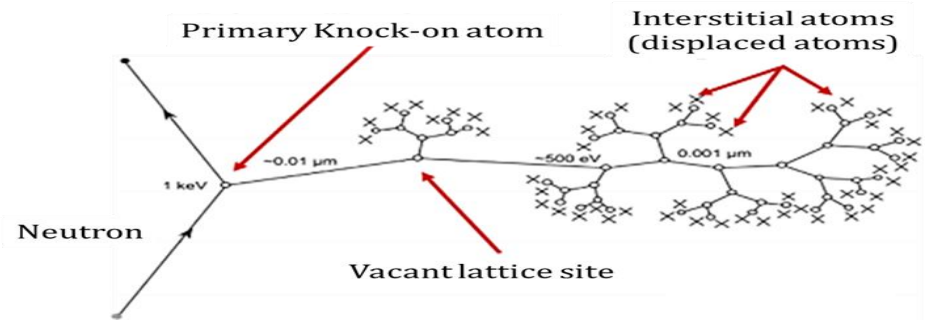

Figure 2.10: Schematic diagrams of the displacement cascade caused by high-energy neutrons (Tipler and Mosca, 2007).

2.1.5 Point defects and dislocation

Fast neutron bombardment is a key cause of defects in the crystal lattice of graphite, although some of these defects also occur in virgin graphite. The simplest defects are interstitial atoms and vacant lattice sites (Telling and Heggie, 2003). More information about point defects and dislocations are discussed in the following sections.

2.1.5.1 Point defects

Upon generating defects in graphite, the energetic neutrons created through reactor fission, transfer some energy to the nuclei of carbon (C) atoms available in the moderator. (Li et al., 2005). The energised C atoms break from the lattice and, consequently, become energetic projectiles that displace the remaining C atoms in series from the lattice. Therefore, every collision produces numerous displaced C atoms (interstitials) and vacant lattice sites (Kelly, 1981). Practically, one out of ten atoms displace after every second, and the displacements are random.

The interstitial (displaced) atoms do not occur within the hexagonal lattice as the energy required to do so is significantly higher than an inter-planer location. Therefore, locating between the planes layer is an energetically favourable process (Li et al., 2005). Although the formation energy of the interstitial atoms studied both theoretically and experimentally, the findings in both cases vary to some extent (Li et al., 2005).

Kelly (1971) derived a simple model to discuss the effect of interstitial atoms on the interlayer properties of a graphite crystal. Kelly (1971) tests his model empirically, in which he concluded that interstitial atoms do not form covalent bonds with the adjacent layers, due to the irradiation above the room temperature. The Kelly model discusses the dimensional changes following neutron irradiation, which suggests that collisions between interstitial atoms yield two groups of displaced atoms. The first group grows in size by capturing the displaced, diffusing atoms, while the second one stabilises and attains the size of 4 ± 2 atoms. The latter is regularly attenuated by the displacement cascades (irradiation annealing). At low doses, the interstitial atoms form a linear group between defect layers, as Figure 2.11 illustrates. Kelly studied the dimensional changes of graphite crystallites and polycrystalline graphites to observe irradiation effects. Thus, Kelly (1971) examines the highly oriented pyrolytic graphite over a wide range of irradiation temperatures and neutron doses. At relatively lower doses (0.6-1.2 dpa), the data illustrated an expansion in c-axis and shrinkage in a-axis at temperatures between 150 and 700 ˚C. The former associated with loop interstitials accumulated between basal planes and the latter linked to the migration of vacancies to crystal boundaries as temperature vacancies become mobile above a certain temperature. The findings revealed a constant change in total volume as the crystallite changes dimensions. Kelly explained this behaviour as a result of the combination of interstitial loop growth and complete vacancy collapse parallel to the basal planes. This suggestion is in agreement with experimental data (Kelly, 1981). Although the crystallite dimensional changes can be reversed by annealing at temperature, the changes will continue to occur under further radiation (Kodsi, 2017).

Kelly (1981) proposed that vacancies can disappear without the annihilation of an interstitial. Instead of forming the expected vacancy loops, random atomic displacements can produce linear vacancy groups, which can collapse parallel to the basal planes, preventing interstitial annihilation. New vacancies created near to the dislocation core disappear almost instantly, and therefore, the interstitial can only contribute to a small group of interstitials or a dislocation loop.

Kelly (1981) also explained pore formation in both crystalline and polycrystalline forms of graphite. The existing porosity decreases by the shrinkage; hence, the expansion is essential on volume grounds. The expansion in the c-axis occurs due to the formation of the new pore by the crystallite strains. This formation of the pore changes at all irradiation doses and temperatures as the internal strains exceed a critical value. The formation process proceeds until the graphite collapses. The newly established porosity affects the mechanical properties of graphite, including Young's modulus, strength, thermal conductivity, and thermal expansion coefficients. These properties alter throughout the radiolytic oxidation, which targets the pore volumes.

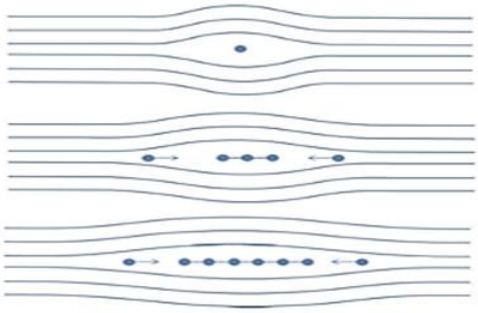

Figure 2.11: Kelly model of interstitial aggregation (Kelly, 1971).

More recently, a new model discusses (Latham et al., 2008; Telling et al., 2003; Teobaldi et al., 2010) the atomic structural behaviour when the interstitial carbon atoms move in between basal planes. This model suggests inter-planar interstitials form strong covalent bonds with its neighbouring planes to cause deformation. Figure 2.12 illustrates the possible arrangements of extra atoms that can form: grafted (G), Spiro (S), Y-lid (Y), migrated Spiro (S′), and dumbbell (D). Grafted (G) is a simple triangular arrangement of interstitials due to the bonding of two atoms in one of the neighbouring planes. Spiro (S) clusters have two atoms in both top and bottom layers (four atoms in total), which is the most stable state (Gulans et al., 2011; Telling et al., 2003). In contrast, the least-stable configuration of interstitials refers to a dumbbell (D), in which the triangle shape alters slightly to allow the formation of an extra bond between an interstitial and another atom in the same plane (Gulans et al., 2011). The calculated formation energies of each interstitial arrangement vary between 5.5 to 7.5 eV (Gulans et

al., 2011; Ma, 2007; Telling and Heggie, 2003). When shear forces are introduced to the basal plane, the Spiro-interstitial becomes mobile and travels across the lattice structure to a new position (S′), while breaking and reforming bonds. The Y-lid (Y) bonding arrangement makes the movement possible. The migration energies of Spiro-interstitials vary between 0.1 and 2.12 eV (Gulans et al., 2011; Ma, 2007; Telling and Heggie, 2003; Zhang et al., 2010).

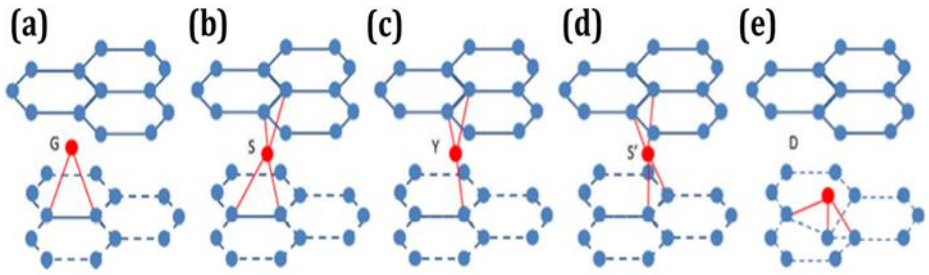

Figure 2.12: A schematic. (a) is grafted (G), (b) is Spiro (S), (c) is Y-lid (Y), (d) is the migrated Spiro (S′), and (e) is dumbbell (D) of the interstitial arrangement. Reprinted from (Freeman, 2016).

Latham et al.'s (2008) model of irradiation damage in graphite appears to discredit the classical view of dimensional changes, where the aggregation of interstitial atoms promotes the existing ones (Latham et al., 2008). Changes in the dimensions of the lattice begin at temperatures that are insufficient to induce the mobility of interstitial atoms. As demonstrated in Latham's work, the first phase of aggregation stimulates the formation of strongly-bonded di-interstitial states. Immediately, dimensional changes that conflict with measured values induce immobile anomalies. The two forms of low energies that neither migrate nor disintegrate with ease (Latham et al., 2008), which is associated with di-interstitial defects. Going by the author's interpretation, the classical model, which describes the Wigner energy in the low-temperature profiles, is misleading. It then follows that di-interstitial defects do not account for graphite damage by irradiation (Latham et al., 2008).

From Latham's theory, the energies associated with bridging defects are reduced considerably when the layers shear in the basal plane direction. Since basal plane displacements feature prominently in graphite, they are unlikely to cause defects in bridging layers. The layers in graphite could further buckle due

to basal distortions, thereby, causing dimensional change, especially after irradiation. Such distortions are more pronounced in the grafted bridge of the graphite interlayer (Latham et al., 2008).

Single vacancy (holes) formed due to the removal of an atom from its atomic site, leaving three dangling bonds on the adjacent atoms. The vacancy does undergo a spontaneous Jahn–Teller distortion after relaxation, since two of the atoms bond neighbouring move closer to form a 5-fold ring, leaving one dangling bond to attach to the closest neighbour (labelled as the 5–9 structure) (Ma et al., 2004; Trevethan et al., 2014). This results in a pentagon-and a nonagon like structure (Figure 2.13). Ma et al. (2004) stated that the process of relaxation reduces the formation energy of vacancies and therefore increase stability.

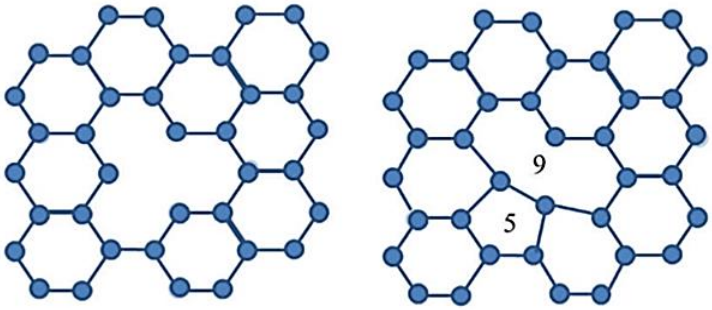

Figure 2.13: Single vacancy (left) relaxation of carbon atoms around a single vacancy (reprinted from Freeman, 2016).

While Di-vacancies occur due to either the removal of two carbon atoms at the same time or due to the migration of two vacancies together, resulting in the formation of two new bonds as a result of the linking of four dangling bonds (Ma et al., 2004), this process results in the formation of the stable pentagon–octagon–pentagon (5–8–5) structure (Figure 2.14) (Trevethan et al., 2014). The di-vacancies have higher migration energy than single vacancies as the di-vacancy has two missing atoms; each atom has lower energy, which makes the di-vacancies more thermodynamically stable (Trevethan et al., 2014).

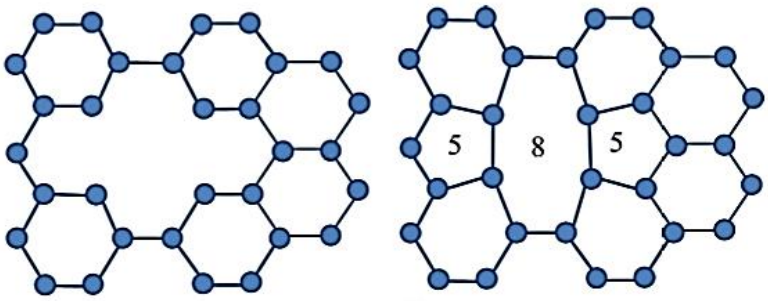

Figure 2.14: Di-vacancy (left); relaxation of carbon atoms around di-vacancy (reprinted from Freeman, 2016).

New theory: Buckle, ruck and tuck

While referring to the classical theory of radiation damage in graphite, which invokes that the formation of Frenkel pair was the principal cause of changes in the physical properties of the lattice, Heggie et al. (2011) argued that is insufficient and proposed different mechanisms for irradiation at different temperatures. Heggie et al. (2011) model suggested that when two sheets of graphene of different lengths links at two places with single interstitial atom, the result is buckling, as it is energetically favourable for compression buckling of the longer sheet than stretching of the shorter sheets, which tends to stay close to its unstrained length. Heggie et al. (2011) estimated that nearly one-third of the energy stored in the supercell is due to buckling. At irradiation temperature below 250 ˚C, the authors calculated the dimensional changes in the c-axis (expansion) and a-axis (shrinkage) were 63% and 5% respectively, the latter in agreement with experimental data of Kelly et al. (2000). At irradiation temperature above 250 ˚C, this gives rise to the folded or "*ruck and tuck*" graphite, and the interlayer expansion continues. The formation of this process occurs when the single interstitial inter-planer connectors become loose, which means the edge dislocations become free to interact, and the 'pile-up' of dislocations causes the accumulation of matter that is "*ruck and tuck*", as shown in Figure 2.15.

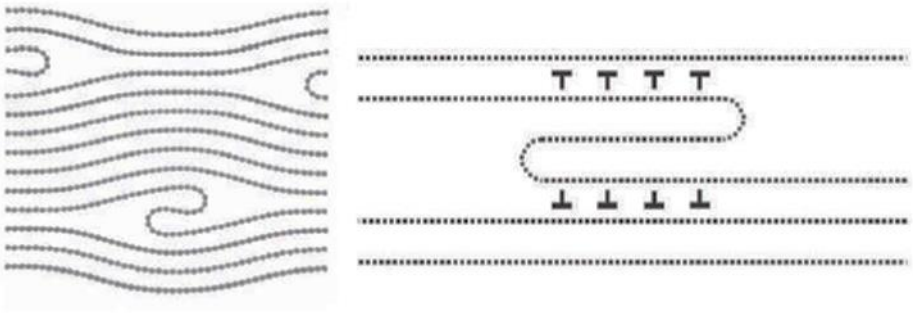

Figure 2.15: Basel dislocation; ruck and tuck (Heggie et al., 2011).

Overall, the standard model adopted by Kelly proposed the aggregation of displaced interstitial carbon atoms that form additional basal layers. This leads to pre-existing basal planes opening for the purpose of accommodating the new interstitial atomic planes as well as their corresponding defects; for example, di-vacancies and spiro-interstitials, etc. Then the corresponding shrinkage parallel to the layer plane results from the vacancy lines which collapse. Heggie et al., (2011) argued this concept for number of reasons: firstly at low temperatures below 250 ˚C interstitials are immobile and cannot aggregate to form new graphene sheets which suggested that the standard model is insufficient for neutron irradiation at lower temperature (< 250 ˚C); secondly, the small interstitial defect clusters that would form would be unable to have a major impact on the interlayer spacing; thirdly, the standard model fails to consider the movement of basal dislocations. Thus, Heggie et al. (2011) suggested the mechanisms of buckling and "*ruck and tuck*" to describe these behaviours at different temperatures. Nevertheless, all discussed models are agreeable to the fact that the most obvious observations in irradiated graphite pertain to dimensional changes.

2.1.5.2 Dislocations in nuclear graphite

Deformations within a graphite lattice can be elastic or inelastic; the lattice may or may not return to its initial state once the stress is removed. In an inelastic deformation, the lattice has undergone some plastic deformation and can be described by dislocation theory. During the migration of interstitial atoms or vacancies, they coalesce together, and their energy decreases, so the cluster is less mobile. These clusters of interstitials are postulated to vary in size, from di-

interstitial atoms or vacancies of a few nanometres wide up to clusters of multiple interstitial atoms or vacancies. The largest clusters of interstitial atoms or vacancies are referred to as dislocations.

Dislocations can be considered as either basal or non-basal dislocations. The former is responsible for glide between successive layer planes in directions parallel to the layers that usually includes stacking faults. Basal dislocations do not involve breaking the strong covalent bonding, but only the weak van der Waals bonding between the layer planes. Non-basal dislocations have three different types; Edge/basal plane dislocations are held parallel to the graphene layers because of the weak van der Waals interaction between layers; screw dislocations and dislocation loops also occur which have very low mobility, because of their movement would need the breaking and restoration of the covalent bonds. Dislocations were investigated widely in the 1960s (Eiichi and Izui, 1961; Reynolds and Thrower, 1965; Williamson, 1960) as well as more recently modelled (Banhart, 2002; Telling and Heggie, 2003).

2.1.5.2.1 Edge dislocations

An edge or basal dislocation is a simple type of dislocation caused by shear stress on the graphite core that results from the splitting of the lattice. The edge dislocation is modelled as a semi–infinite cylinder of elastic material. In graphite, an edge dislocation corresponds to a half-plane of atoms in the infinite case which may become stationary between full planes at several layering positions, marked as B in Figure 2.16 (Hull and Bacon, 2011; Panyukov and Subbotin, 2008; Simmons, 1965; Telling and Heggie, 2007). The base of the half lattice is marked as ⊥ in Figure 2.16. The movement of planar dislocations through the lattice structure is known as glide. Figure 2.16 illustrates that when shear stress is applied, the dislocation gliding starts with a change in the position of the top half-plane of the atoms relative to the bottom half-plane of atoms. This causes the C-C bonds to be broken and reformed, which affects the graphite's mechanical properties. When the shear stress is removed, the structural changes do not revert to their previous state due to the motion of the atoms into a thermodynamically stable state, which results in a permanent dislocation (Latham et al., 2015). This mechanism is defined as a slip by the authors.

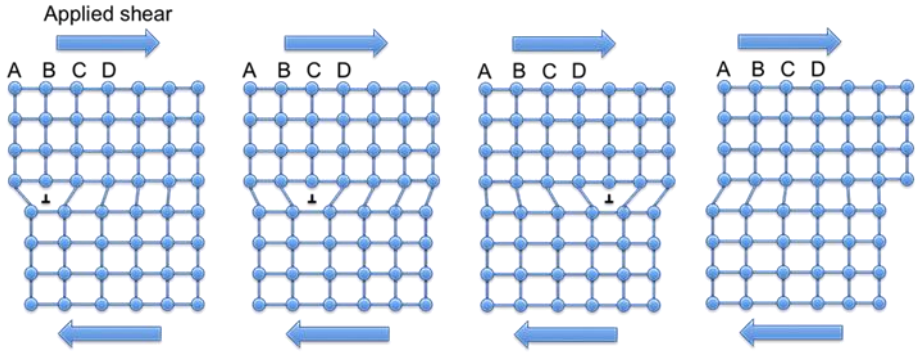

Figure 2.16: Edge dislocation with dislocation glide. Reprinted from (Sparky, 2013).

2.1.5.2.2 Screw dislocations

Screw dislocations occur when the defect movement is perpendicular to the applied shear stress, as well as the atom displacement, as opposed to parallel, as is the case for edge dislocations (Hull and Bacon, 2011; Wirth, 2007). Figure 2.17 shows shear stress applied across one end of a block of material, which then begins to tear, as shown in Figure 2.17 (a). Figure 2.17 (b) shows the plane of atoms just above the tear and the atoms represented using different colours (blue, green and red); the blue atoms have not yet moved from their original position, the red atoms have moved to a new position and have formed bonds, and the green atoms are in the process of moving. This kind of movement requires a much smaller force than what is required to break all the bonds across the middle plane simultaneously (Crouse,2011). Therefore, only a small portion of the bonds tend to break. The atoms may also slip to the right, thereby increasing the shear force. Thus, the green atoms return to an appropriate lattice position and change to red. Then the blue atoms start to slip out of position and change to green. These movements are usually referred to as a helix (Hull and Bacon, 2011).

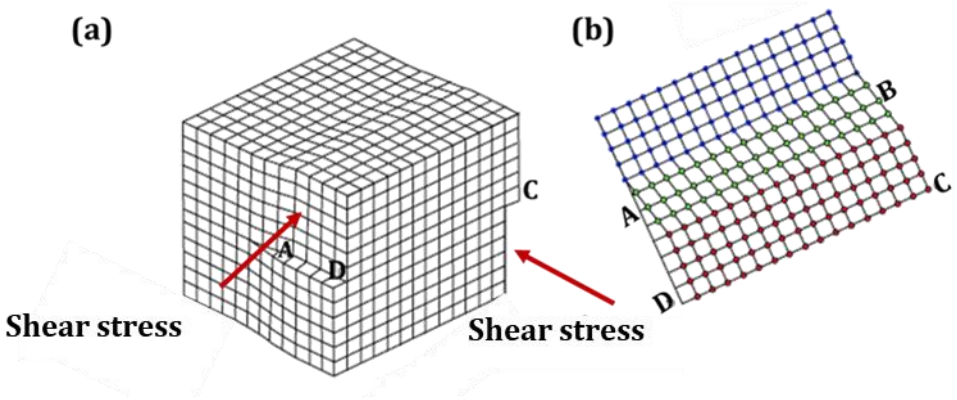

Figure 2.17: Screw Dislocations (NDT, 2014).

As the edge and screw dislocations progress and interact, they start to hinder the movement of adjacent dislocations, which causes an increase in the level of embrittlement (Crouse,2011; Hull and Bacon, 2011). It is often challenging to examine the nature of dislocations in such boundary conditions (Butz et al., 2013). Bilayer graphene is often the best material for such a study, as it is capable of confining linear defects that come with screw dislocations. Figure 2.18 illustrates the results of screw dislocations in bilayer graphene. The figure shows a dense network of dislocation (Butz et al., 2013; Lin et al., 2013). The dislocations are restricted between two graphene sheets and are represented by the sharp dark lines in Figure 2.18 (Butz et al., 2013).

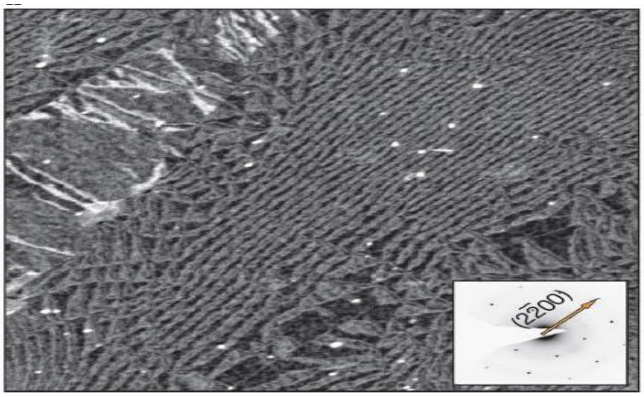

Figure 2.18: TEM image of a screw dislocation in graphite (Butz et al., 2013).

According to Butz et al. (2013), screw dislocations in graphite results in two size effects. The first effect comes as a result of the lack of stacking-fault energy in bilayer graphene. This results in a special pattern of dislocations resembling an alternating change in stacking order. The second effect is the

major buckling of the membrane of bilayer graphene. This is caused by strain accommodation. Screw dislocations, together with their role in electronic, mechanical, and structural properties of graphite, can be understood using these two size effects.

2.1.5.2.3 Dislocation loops

Dislocation loops are formed by the addition or removal of a portion of a plane, and both are often observed in irradiated materials. These dislocations can be further categorised into interstitial and vacancy loops. The former occurs between basal planes and cause an expansion in the c direction, while the latter happens when a portion of a plane is removed: when vacancies collapse, the adjacent planes can cause two similar planes to become close neighbours (Hennig, 1962; Telling and Heggie, 2003). This situation results in a stacking fault with very high energy.

2.1.6 Properties of graphite

During reactor environment exposure, nuclear graphite properties will be affected. Thus, the characterisation and irradiation of newly fabricated grades of nuclear graphite must be considered to prove that the current grades of graphite display acceptable behaviour before and after irradiation. Subsequently, the thermomechanical design of nuclear graphite grades for the Generation-IV can be validated. In this section, dimensional changes due to neutron irradiation in nuclear graphite and the changes in nuclear graphite properties such as thermal conductivity, coefficient of thermal expansion, Young's modulus, and electrical resistivity are discussed.

2.1.6.1 Dimensional changes due to neutron irradiation in nuclear graphite

The alterations that occur in nuclear graphite link with atomic displacements, which take place within the crystal structure and lead to the formation of interstitial and vacancy loops. During irradiation, the crystallites of graphite expand in the c-axis direction and contract in the a-axis direction due to the anisotropic crystallite structure of graphite (Zhou et al., 2017a). Mrozowski cracks (containing defects), which align in the crystallographic a-axis direction.

This provides a ready volume of space to accommodate the c-axis expansion during irradiation (Marsden et al., 2017; Zhou et al., 2017a). This causes the graphite to undergo net volume shrinkage due to the a-axis contraction throughout the graphite volume. With increasing irradiation, more cracks close and eventually, the c-axis expansion is no longer accommodated (Fugallo et al., 2014). New pores oriented parallel to the basal planes also form because of the disparity of crystallite dimensional changes. Consequently, the volume contraction rate reduces and finally reaches zero. The graphite then begins to expand at an increasing rate as the irradiation dose increases. This point is known as the turnaround point, which occurs due to the combined effect of c-axis expansion and the generation of new porosity or cracks (Freeman et al., 2016; Zhou et al., 2017a).

Irradiation of a particular temperature in the Generation-IV system, which varies between 300 to 1200 ˚C, would cause shrinkage of semi-isotropic nuclear graphite followed by expansion (Marsden et al. 2017). The rate of shrinkage and expansion is dependent on the temperature and fluence of the irradiation (Zhou et al., 2017b). Marsden et al. (2017) reported the behaviour of three different types of nuclear graphite; MG-2 with medium grains and FG-1 with fine grains, which irradiated recently as part of the EU Raphael and Archer programs, and Gilsocarbon graphite in response to irradiation at a temperature range of 430-1430 ˚C for a Gilsocarbon graphite and at 750-950 ˚C for MG-2 and and FG-1 nuclear graphites, illustrated in Figure 2.19 and Figure 2.20. The authors stated that inspite of having different properties from those of Gilsocarbon, both types of nuclear graphite; MG-2 and FG-1 have similar dimensional changes as Gilsocarbon (Marsden et al., 2017).

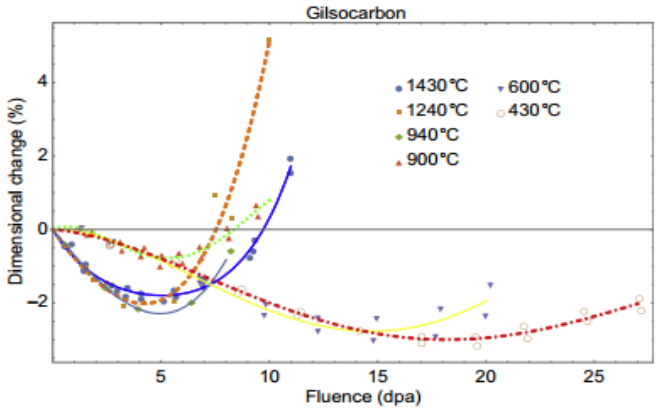

Figure 2.19: Irradiation-induced dimensional changes at a temperature range of 430-1430 ˚C for Gilsocarbon graphite (Marsden et al., 2017).

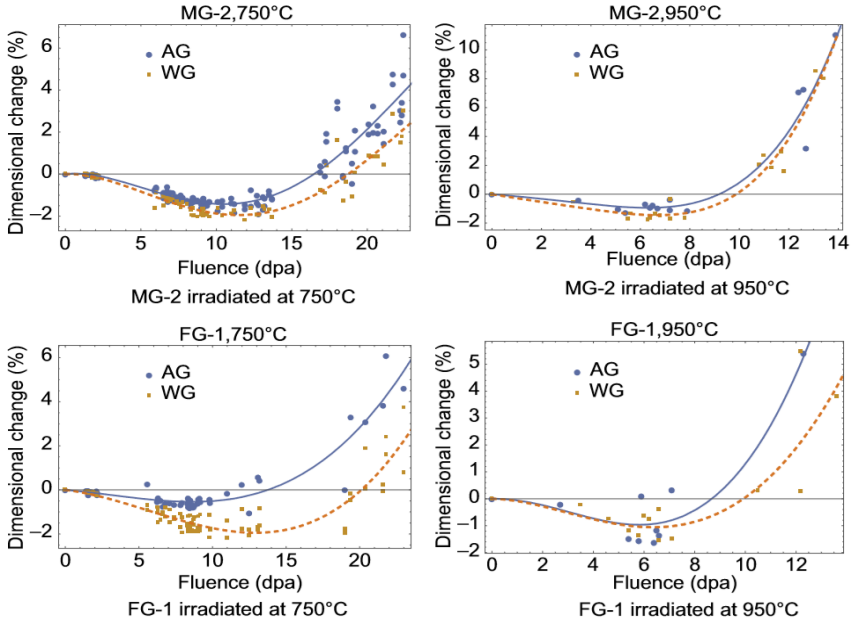

Figure 2.20: Irradiation-induced dimensional changes at a temperature range of 750-950 ˚C for MG-2 and fine-grained and FG-1 nuclear graphites (Marsden et al., 2017).

During the operation of (V)HTR, differential strains and resultant stresses develop in the graphite microstructure occur because of local differences in neutron fluence and temperature within large graphite components (Marsden et al., 2017). These variances should be large enough to induce crack growth and final failure of the component within a short in-reactor time. However, within irradiated graphite microstructures, strain relief of induced stresses (irradiation creep) helps to avoid premature failure (Heijna et al., 2017; Zhou et al., 2017b). This allows the nuclear graphite to withstand irradiation damage causing by irradiation-induced dimensional changes. Heijna et al. (2017) investigated the

dimensional changes of the neutron irradiation (up to 25 dpa) in PCEA and PCIB graphite grades (candidate grades for (V)HTRs) at irradiation temperatures 750 ˚C and 950 ˚C. The authors concluded that both PCEA (medium-grained) and PCIB (fine-grained) show that dimensional changes are highly anisotropic in with and against grains directions. However, PCEA graphite exhibits low dimensional anisotropy compared to PCIB, which makes it more favourable to be used in (V)HTRs.

2.1.6.2 Coefficient of Thermal Expansion (CTE)

CTE is the ratio of the amount of expansion that follows a change in temperature. As in any material, the temperature influences the interatomic spacing between the carbon atoms of graphite. Researchers typically use thermomechanical analysis (TMA) to measure the initial dimension of the sample and record the finite changes caused by changes in temperature (Heijna et al., 2017; Zhou et al., 2017)

The bulk thermal expansion of a single crystal in both the a and c directions are different and have average values of $<1.5\times10^{-6}$ K^{-1} along the a-axis and $\sim20\text{-}40\times10^{-6}$ K^{-1} along the c-axis, respectively (Hacker et al., 2000; Marsden et al., 2017). As temperature increases, changes in the CTE along the c-axis occurs due to the weakening Van der Waals forces (Baskin and Meyer, 1955; Haag, 2005). At lower temperatures (<150 ˚C), the change in a is relatively small; c is positive above 150 ˚C and negative below 150 ˚C because of strong in-plane bonding (Haag, 2005).

Nuclear graphite has a very small thermal expansion coefficient compared to the single crystal structure due to the high volume of porosity in its structure (Haag, 2005; Simmons, 1965). Nuclear graphite has an average CTE value of $\sim-1.5\times10^{-6}$ K^{-1} (20-120 ˚C) along the a-axis and $\sim27\times10^{-6}$ K^{-1} (20-120 ˚C) along the c-axis, respectively (Hacker et al., 2000; Marsden et al., 2017). The smaller CTE of graphite is beneficial to decrease the thermal stresses in graphite and provides excellent thermal shock resistance. The measurement of linear CTE is complicated to determine and requires careful sample preparation and temperature control.

The CTE of nuclear graphite is important. Firstly, to ensure their dimensional tolerances as the temperature increases during reactor operation

(Zhou et al., 2017a). Secondly, the determination of the CTE is critical to avoid the occurrence of diverted coolant flows because of the large gaps between reflector blocks, subsequent in hot spots, and potential damage to the fuel (Haag, 2005). Thirdly, the CTE and its changes to nuclear graphite properties are vital to guarantee that the automatically interlocked nuclear graphite core components will not experience increasing stresses resulted from the binding of the components (Zhou et al., 2017a). Lastly, the CTE of graphite is controlled by the thermal closure of aligned internal porosity (Marsden et al., 2017).

During irradiation, the CTE of irradiated graphite will commonly increase slightly first, then reach a peak, and decrease well below the virgin graphite value as the neutron dose increases. Also, the irradiation temperature influences the CTE values. Marsden et al. (2017) reported the changes in CTE of three different nuclear graphite grades (MG-2 with medium grains and FG-1 with fine grains, and Gilsocarbon graphite) during irradiation at different temperatures, as illustrated in Figure 2.21 and Figure 2.22. It is apparent from Figure 2.21 that the rapidity of CTE change is more pronounced when the irradiation temperature is high. MG-2 with medium grains and FG-1 with fine grains have similar CTE changes as Gilsocarbon (Figure 2.22). As noted from these figures, CTE increases slightly then falls, reaching a saturation state where the original CTE has reduced by half as compared to that of virgin nuclear graphite (Marsden et al., 2017; Zhou et al., 2017a). The CTE changes occur due to variations in graphite structure that results from porosity modifications.

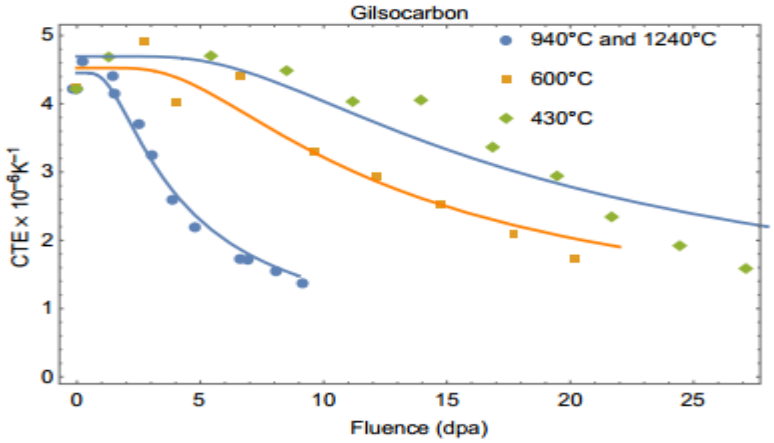

Figure 2.21: Irradiation-induced CTE changes for Gilsocarbon graphite at various temperatures (Marsden et al., 2017).

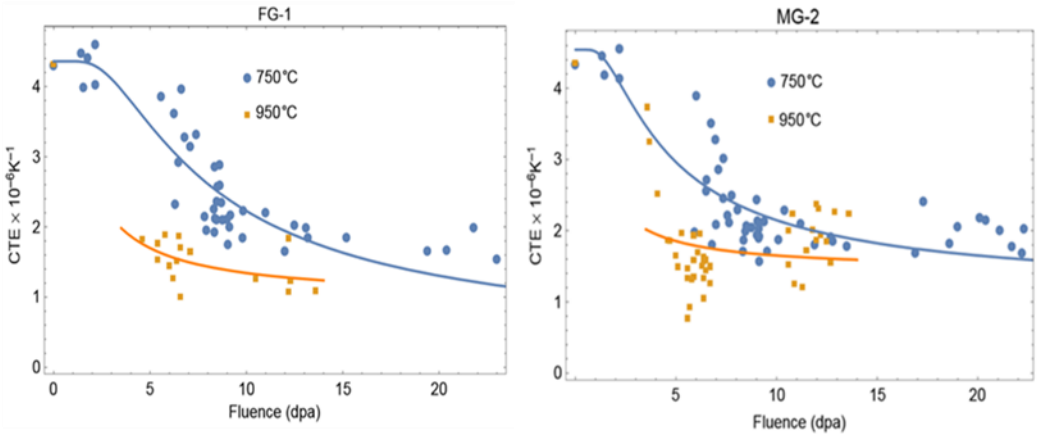

Figure 2.22: Irradiation-induced CTE changes in FG-1 and MG-2 nuclear graphite grades at 750 and 950 ˚C (Marsden et al., 2017).

2.1.6.3 Thermal Conductivity

The thermal conductivity is critical to determine the rate of heat transfer from the fuel through the graphite, which is important for safe reactor design. The temperature and radiation dose in the reactor affect the thermal conductivity of nuclear graphite. Heat is primarily conducted by lattice vibrations, with phonons as the main heat carrier, instead of electrons and holes (Zhou et al., 2017a). The mean free paths of these phonons can reach hundreds of micrometres (Fugallo et al., 2014). The Debye equation relates the thermal conductivity to this phonon mechanism (2.2):

$$K = bC_\rho vL \tag{2.2}$$

Where K is the thermal conductivity, b is a constant, C_p is the specific heat per unit volume of the crystal, v is the speed of the phonon, and L is the mean free path for phonon scattering. During the manufacturing process, a high graphitization temperature (> 2700 ˚C) is essential to ensure sufficient thermal conductivity (Zhou et al., 2017a). Generally, with increasing treatment temperature, the thermal conductivity of graphite decreases. Phonon scattering occurs in single-crystal graphite: the mean free path L is high which is the dominant factor above room temperature, more than offsetting the increase in specific heat, C_p, and therefore thermal conductivity is high particularly along the a-axis because of the strong covalent bonds (Aitkaliyeva, 2017; Marsden, et al., 2017; Zhou, et al., 2017a). The thermal conductivity of single crystals varies

between 1660–1900 $Wm^{-1}K^{-1}$ and ~0.013 $Wm^{-1}K^{-1}$ at 25 ˚C along with the a and c-axes, respectively (Fugallo et al., 2014; Sun et al., 2009).

In virgin polycrystalline graphite, the thermal conductivity of virgin nuclear graphite is relatively high, ranging from approximately 60 to 170 $Wm^{-1}K^{-1}$ at 25 ˚C (Pierson, 2012; Sun et al., 2009; Zhou et al., 2017a). The thermal conductivity decreases with increasing porosity (Pierson, 2012). For highly crystalline, stress-annealed pyrolytic graphite, the thermal conductivity is around 4180 $Wm^{-1}K^{-1}$ in the a direction (Pierson, 2012). The thermal conductivity of commercial pyrolytic graphite, such as HOPG grade, is lower, at approximately 390 $Wm^{-1}K^{-1}$ (Pierson, 2012).

The change in thermal conductivity during neutron irradiation follows a similar trend in nuclear graphite grades (Figure 2.23). At relatively low temperatures, the thermal conductivity changes significantly under irradiation. At higher temperatures of approximately 1000 ˚C, the irradiation-induced changes are minimal as point defect damage in nuclear graphite is annealed out of the microstructure (Burchell et al., 2000). Under irradiation, especially at low neutron fluences, the thermal conductivity of nuclear graphite experiences a fast decrease from the original values. This fast decrease saturates quickly, and slight thermal conductivity changes occur over this intermediate level (Heijna et al., 2017; Zhou et al., 2017a). If the neutron fluence levels past the turnaround, the thermal conductivity of the nuclear graphite will start to decrease further (Burchell et al., 2000; Zhou et al., 2017a), this is possibly due to the generation of pore and cracks induced by the irradiation (Zhou et al., 2017a). The decrease of thermal conductivity within nuclear graphite can influence the passive heat removal rate in the nuclear reactor core, and therefore the peak temperature which the nuclear reactor core and, subsequently, the fuel particles will encounter during off-normal events. Therefore, determining changes to the conductivity during irradiation is vital for safety analyses of Generation-IV reactors.

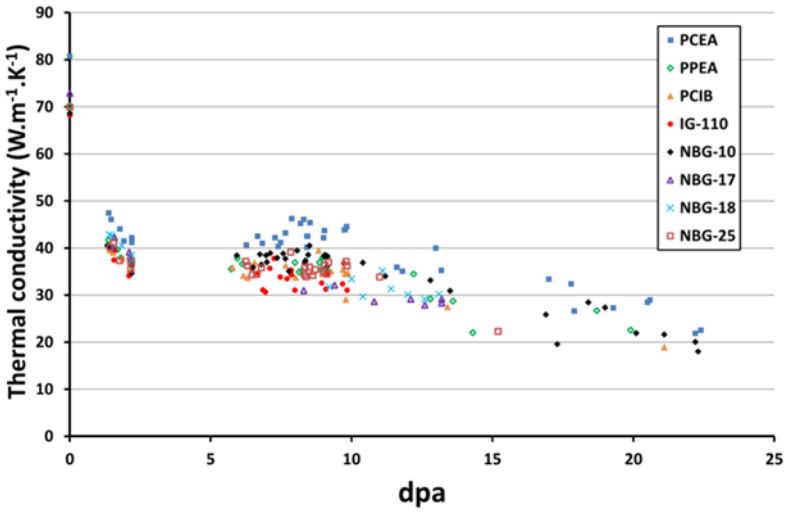

Figure 2.23: Thermal conductivity for different types of nuclear graphite irradiated to fluence up to 25 dpa at 750 ˚C (Heijna et al., 2017).

2.1.6.4 Young's Modulus

The mechanical Young's modulus is critical to determine the structural integrity of the graphite core components, which is one of the aspects to assess and predict the lifetime of graphite moderator. The measurement of Young's modulus (also known as the elastic modulus or stiffness) is critical to monitor stresses and their impacts on the operation of nuclear reactors.

The Young's modulus is a numerical application of Hooke's Law, which enables the measurement of material resistance to elastic deformation. Liu and Zhou (2014) found that single graphite crystals are stiffer in the a direction than in the c direction because of extremely strong in-plane bonding. Young's modulus for nuclear graphite at room temperature, as measured by Baker (1970), ranges from 0.7–1.5 × 10^6 psi in the parallel direction and from 0.6–1.2 × 10^6 psi in the transverse direction for a moulded H4LM graphite of maximum particles size ~838 μm, 1.72 g/cm^3 density (Baker, 1971). More recently, Marsden et al. (2017) reported the typical values of three different virgin nuclear graphite grades; MG-2, FG-2, and Gilsocarbon, which are 1.5 × 10^6 psi, 1.4 × 10^6 psi and 1.5 × 10^6 psi respectively in the parallel direction. However, the authors reported Young's modulus value of 1.5 × 10^6 psi in the transverse direction for Gilsocarbon only.

Baker (1971) stated that Young's modulus increases with increasing irradiation dose and temperature. However, Hall et al., (2006) and Haag, (2005)

reported that neutron flux is the dominant factor that affects the value of Young's modulus, and few changes the authors observed with changes in irradiation temperature. At higher neutron flux, Young's modulus shows an initial increase followed by a decrease. Conversely, at lower neutron flux Young's modulus increases to threefold the original value (Haag, 2005; Hall et al., 2006).

A recent study by Heijna et al. (2017) studied the effect of irradiation on the microstructure of different nuclear graphite grades suggested the following candidates for (V)HTRs; PCEA, PCIB, NBG-10, NBG-17, NBG-18, NBG-20, NBG-25, PPEA, and IG-110, which are irradiated at 750°C. At lower doses, Young's modulus values increase to a plateau of 2.2-2.9 × 10^6 psi compared to the original values (1.4-2.1 × 10^6 psi), as can be seen in Figure 2.24. At higher doses between 10-15 dpa, these values increase further to reach maximum values between 4.3-5.9× 10^6 psi, after which Young's modulus decreases, as shown in Figure 2.24. The authors proposed that closure of Mrozowski cracks has a partial effect on the stiffening in the later stages of irradiation. This result emphasises previous work by Hall et al. (2006) that reported a secondary increase in Young's modulus after the plateau which was attributed to the closure of larger-scale porosity.

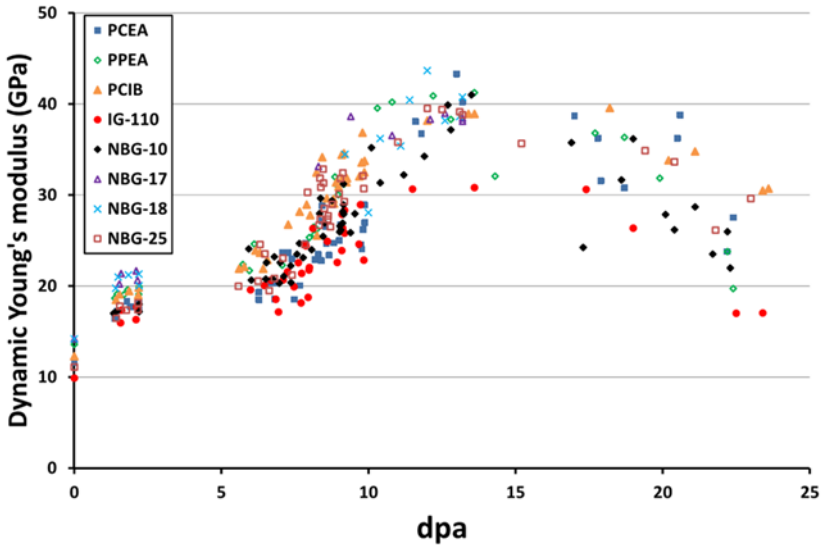

Figure 2.24: Young's modulus changes due to neutron irradiation at irradiation temperatures of 750 °C (Heijna et al., 2017).

2.1.6.1 Electrical Resistivity

Electrical resistivity is a measure of how strongly a material opposes an electric current. The electrical resistivity of graphite is important as it provides information on the degree of crystallinity (Haag, 2005). Generally, the Eddy-current-technique measures the electrical resistivity of the graphite (Dekdouk et al., 2012).

The measurements of electrical resistivity of single crystals are most conveniently made in the a-direction along the graphite planes due to the small size and the platelet shape of single crystals (Nightingale, 1962; Baker, 1970; Haag, 2005). At room temperature, the electrical resistivity of almost perfect single crystals is 0.040×10^{-3} ohm-cm in a direction and 5×10^{-3} ohm-cm in the c direction. As the temperature increases, this increases the resistivity of single crystal as the amplitude of the lattice vibrations increases (Telling et al., 2003).

The electrical resistivity of virgin graphite has a value between 7×10^{-4} - 15×10^{-4} ohm-cm at room temperature. The electrical resistivity varies due to the raw materials, the manufacturing process, and the degree of graphitisation (Haag, 2005). For instance, the electrical resistivity of extruded graphite is almost double in the parallel direction than in the transverse direction. During neutron irradiation, the electrical resistivity of graphite increases in a-axis and decreases in the c-axis (Haag, 2005; Telling et al., 2003). Then a level of saturation is quickly reached, where the changes become extremely slow (Haag, 2005). The change in electrical resistivity is usually independent of irradiation temperature. However, at low neutron doses, electrical resistivity increases remarkably (Baker, 1970; Telling et al., 2003). Figure 2.25 displays the change in electrical resistivity of IG-110 nuclear graphite (fine-grained isotropic graphite) irradiated to a neutron dose of 25 dpa at 600 ˚C (Ishiyama et al., 2008). The electrical resistivity of IG-110 nuclear graphite increased by a factor of 2. However, a small decrease was detected with increasing neutron dose (Ishiyama et al., 2008).

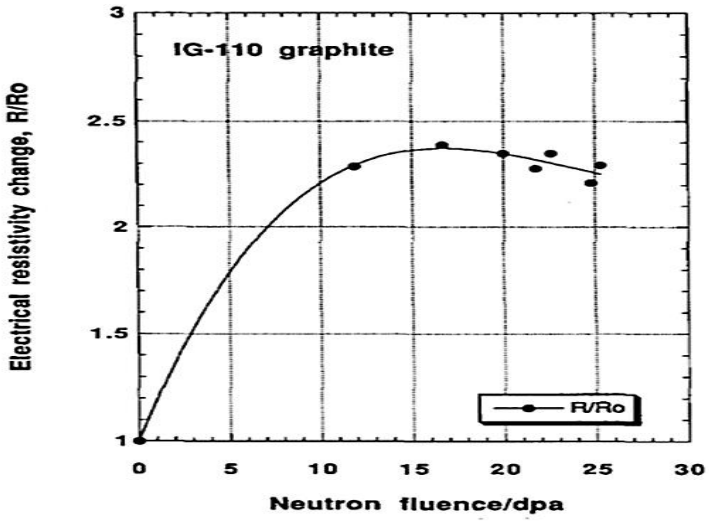

Figure 2.25: Change in electrical resistivity of IG-110 nuclear graphite due to neutron irradiation (Ishiyama et al., 2008).

Chapter 3

3.1 Literature review of nuclear graphite analysis methods

This chapter reviews the methods used to examine both virgin and irradiated graphite, especially those conducted in types of graphite candidates to be used in Generation-IV nuclear reactors. This review provides further context for the findings of more recent studies in this area of research, which are also discussed.

3.1.1 Nuclear graphite microstructure

Various techniques have been used to investigate the microstructure of different kinds of nuclear graphite (Arregui-Mena et al., 2018; Bodel, 2013; Gallego et al., 2006; Hagos et al., 2010; Kane et al., 2011; Krishna et al., 2015; Krishna et al., 2017; Marsden et al., 2017; Metcalfe and Tzelepi, 2014; Nightingale, 1962; Taylor, 2016; Wen et al., 2008; Zheng et al., 2014; Zhou et al., 2014). Polarised-Light microscopy (PLM) and scanning electron microscopy (SEM) are the most frequently applied techniques for understanding the shapes, sizes and distribution of filler particles, binder phase pores within the microstructure. The graphite properties are inherently based on its microstructure. Therefore, the microstructure of graphite provides a significant connection between manufacture and material properties.

The manufacturing process and nature of the filler particles influence the microstructure of nuclear graphite drastically. For instance, PGA is an anisotropic graphite grade used in British Magnox reactors. PGA with petroleum-based coke has needle-shaped filler particles, which contain lenticular cracks that are oriented parallel to the filler's longitudinal axis (Figure 3.1). The filler particle is responsible for the anisotropic behaviour of PGA. During production PGA forms by an extrusion process, which causes the alignment of the filler particles parallel to the extrusion direction (Hagos et al., 2010; Taylor, 2016; Wen et al., 2008). In contrast, pores in binder regions exhibit no preferential orientations (Figure 3.1).

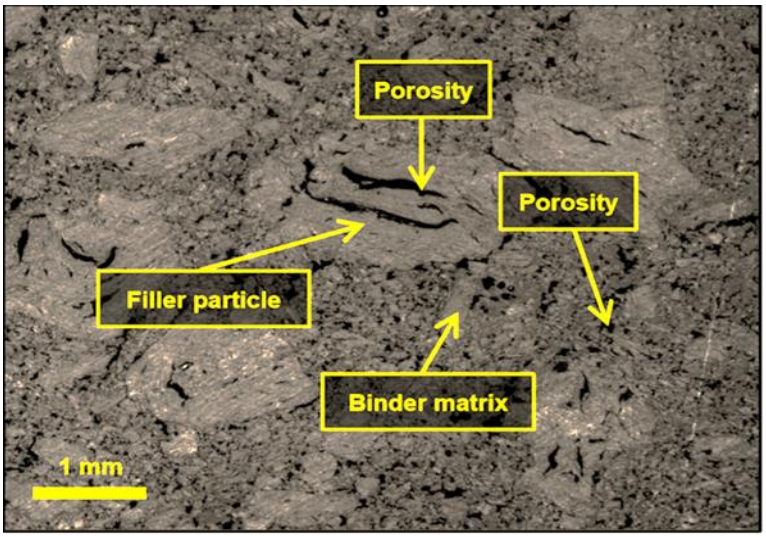

Figure 3.1: Optical micrograph of the microstructure of PGA graphite (Bodel, 2013).

Conversely, the filler particles in Gilsocarbon, which include pitch coke, are spherical with a lower degree of crystallite alignment with an onion-like structure (Figure 3.2), which differs from the shape of the filler particle of PGA. (Bodel, 2013; Marsden et al., 2008; Taylor, 2016; Wen et al., 2008). The manufacturing process has a great influence on the shape of the filler particle, Gilsocarbon graphite undergoes moulding process rather than extrusion to form it into a suitable geometry for nuclear reactor core, resulting in random distribution and orientation of filler particles. Hence, Gilsocarbon graphite can be considered to be quasi-isotropic.

Gilsocarbon filler particles include two different kinds of cracks: circumferential cracks and radial cracks through the filler. This diversity of cracks separates the outer onion-skin structure from the central mass of the filler particles. Quantitative measurements of the size of cracks and pores have assessed how cracks are affected by irradiation of Gilsocarbon graphite (Bodel, 2013). Whereas, pores in binder regions have no preferential orientations

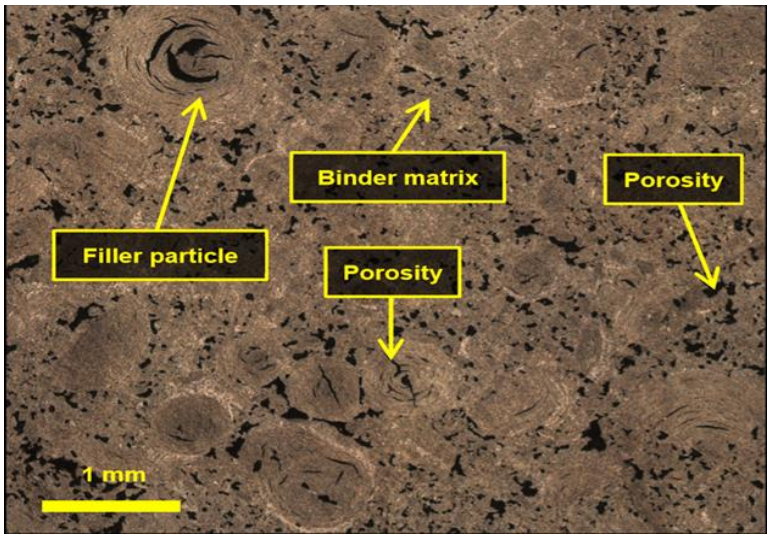

Figure 3.2: Optical micrograph of the microstructure of Gilsocarbon graphite (Bodel, 2013).

Another type of nuclear graphite is PCEA that is anisotropic and has a medium filler particle (grain) size of approximately 0.8 mm (density ~ 1.8 g/cm^3), which may use in the fourth generation of high-temperature graphite-moderated nuclear reactors (Jones et al., 2008). It is manufactured via the extrusion process using petroleum-based coke and hosts a wide variation in filler particle size and degree of crystalline alignment (regions of uniform colour in a PLM). In contrast, the binder phase exhibits a more chaotic distribution (regions of sparkled colour in a PLM). Almost 70% of the filler is needle-shaped, and 30% is spherical; see Figure 3.3 (Kane et al., 2011). The crystallites visible in Figure 3.3 (b) have a high degree of crystalline alignment (needle-shaped), while the spherical filler particles in Figure 3.3 (c) have a low degree of crystalline alignment. These crystallites, which are visible at the centre of the filler particles, are relatively small and are oriented randomly. Furthermore, the shrinkage cracks in the PCEA are narrow, with randomly oriented small cracks and preferential orientation of large cracks along the needle filler particles' long axis; see Figure 3.3 (a) and Figure 3.3 (d) (Kane et al., 2011).

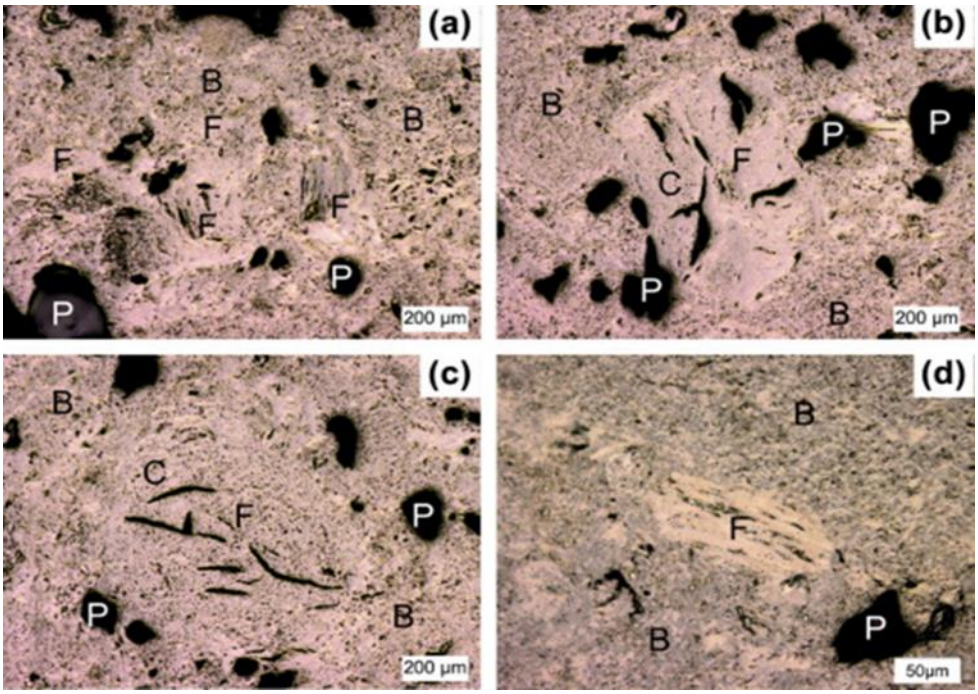

Figure 3.3: Optical micrographs of PCEA graphite. P = porosity; F = filler; B = binder; C = shrinkage crack (Kane et al., 2011).

Although SEM is used often to study nuclear graphite, this technique is still limited by the difficulty of sample preparation (Bodel, 2013; Jones et al., 2008). The necessary polishing process negates the principal advantage of SEM, which is its large depth of field. This depth of field allows for the observation of the microstructure and the types and distribution of micropores on the graphite surface, as well as the relative arrangement of structural features. The only benefit of using SEM over PLM is the increased resolution.

SEM studies of irradiated polycrystalline nuclear graphite have shown that volume changes and dimensional changes are introduced by heavy nuclear bombardment. Hagos (2013) compared the microstructure and pore distribution of virgin and irradiated NBG-10 nuclear graphite, which were suggested for future HTRs. That data is reprinted in Figure 3.4 and Figure 3.5. A considerable change in the topography and size of the graphite after neutron irradiation is evident. Figure 3.5 (a) and (b) show irradiation damage to the microstructure of the graphite, which is less homogeneous than the virgin sample. The microstructure before neutron irradiation includes areas of oriented morphology, with the graphite crystals aligned and roughly equal in size. After irradiation, the graphite crystals are fragmented and are smaller. In

addition, a high degree of cracking inside the pores was observed in both virgin and irradiated nuclear graphite (Figure 3.5 (d)) The frequency and size of these cracks increased significantly after irradiation.

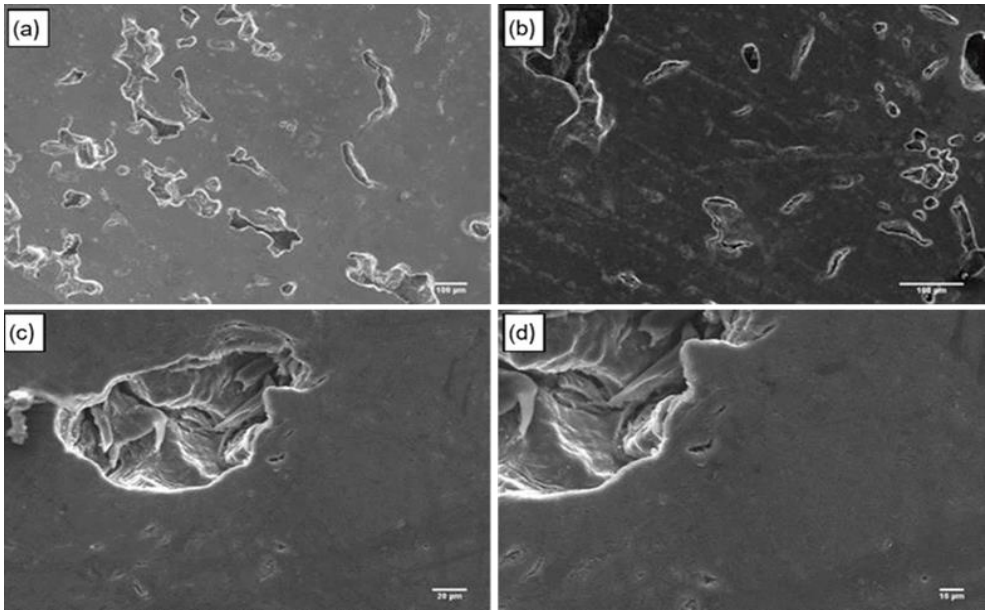

Figure 3.4: SEM micrographs showing cracks inside pores and voids in virgin NBG-10 nuclear graphite (Hagos, 2013).

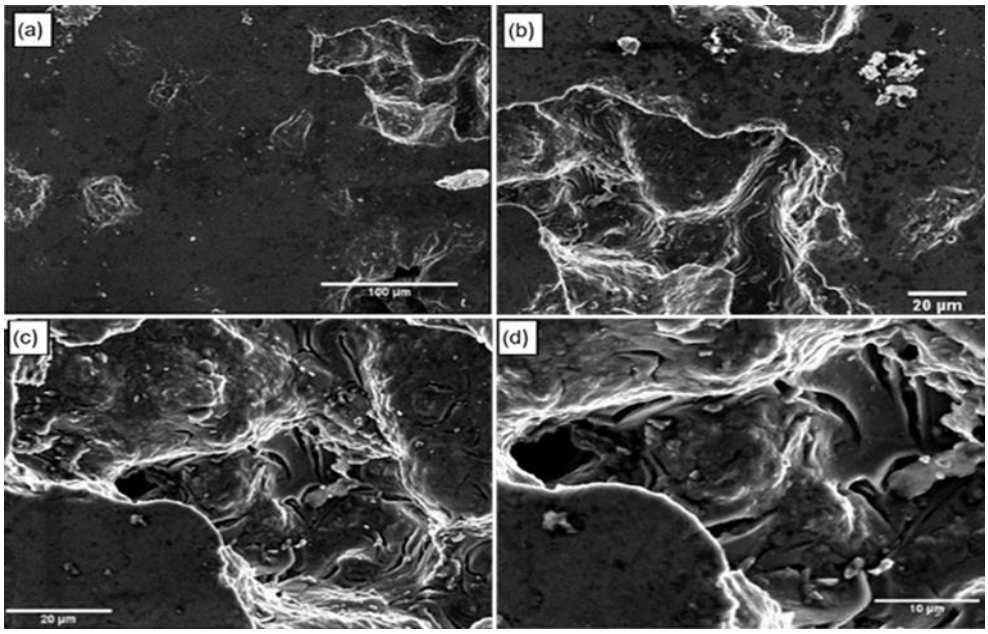

Figure 3.5: SEM micrographs showing the development of cracks and voids in the crystal lattices of NBG-10 graphite irradiated at 9.16 dpa (Hagos, 2013).

Mironov (2014) studied two nuclear graphite (Generation-IV candidates) grades; PCEA and PCIB, which were exposed to neutron irradiation doses ranging from 1.5 to 6.8 dpa and irradiation temperatures varying between 350 °C and 670 °C. Figure 3.6 and 3.7 show SEM images for both unpolished virgin and irradiated PCEA (medium-grained) and PCIB (an ultrafine-grained) nuclear graphite. Virgin PCEA graphite (Figure 3.6 (a)) does not exhibit filler or binder regions clearly but reveals some information about porosity compared to virgin PCIB graphite (Figure 3.7 (a)). After neutron irradiation, significant changes in the surface morphology were observed. It has been also reported qualitatively that both PCEA and PCIB graphite showed an increase in total porosity; with no preferential pore shape and orientation.

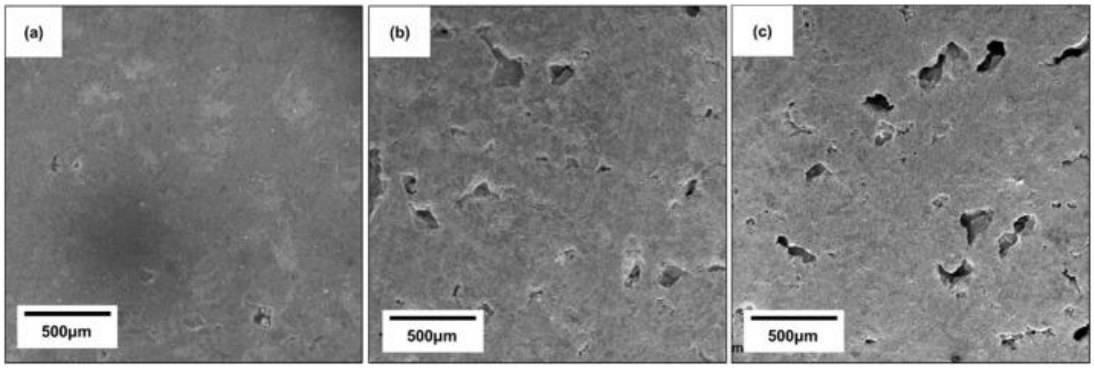

Figure 3.6: SEM micrographs of PCEA graphite (a) virgin sample (b) PCEA irradiated to 1.5 dpa and (c) PCEA sample irradiate to 6.8 dpa (Mironov, 2014).

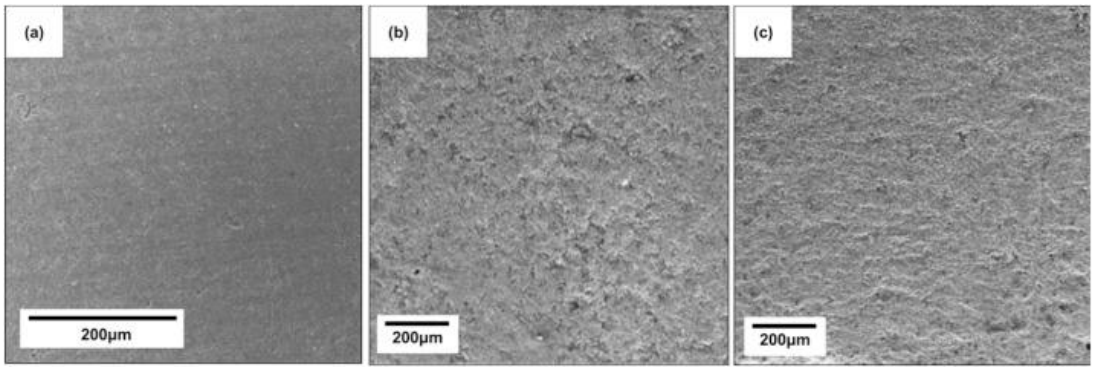

Figure 3.7: SEM micrographs of PCIB graphite (a) virgin sample(b) PCIB irradiated to 1.5 dpa and (c) PCIB sample irradiate to 6.8 dpa (Mironov, 2014).

3.1.2 Serial sectioning methods

Since stresses are generated throughout the whole of the graphite components during reactor operation, it is desirable to employ three-dimensional techniques to evaluate internal as well as external changes to the graphite material. Therefore, this section reviews the current state of the art techniques for the experimental collection of microstructural data in three dimensions (3D). 3D imaging is an essential aspect of the study of microstructure. This Thesis will focus on the use of serial sectioning methods to prepare samples for focussed ion beam–scanning electron microscopy (FIB-SEM) and conventional PLM, as these are the most widely available and accessible techniques for the observation of microstructure. First, this section will highlight the manual and automated systems that can be used for such experiments. Then, the present-day limitations and possible future improvements in this area of research are detailed.

3.1.2.1 Manual serial sectioning instrumentation for PLM

PLM allows for the distinction of the distribution of various constituents of the sample, such as binder and filler particles, and the types and distribution of pores within the microstructure, as mentioned in section 3.1.1. PLM can also be used with serial-sectioned samples to assemble 3D data from a series of 2D images. Each section is polished to different depths below the surface, which may allow a more accurate estimation of the structural changes of voids.

This method has advantages and disadvantages, and one advantage is that the measurements are easy and cost-efficient if the samples are prepared manually. Another advantage is that PLM offers a large field of view, which greatly eases the identification and classification of the microstructural features. The primary disadvantage of this technique is that image alignment between serial sections is very difficult. Another disadvantage is that the need to polish each slice limits the quality of the optical sectioning. Serial sectioning is also a time-consuming process; it takes around 30 minutes to produce one slice. However, this technique is still preferable to investigate the microstructure of nuclear graphite pre and post-irradiation as it allows estimation of the damage of neutron radiation throughout the body of nuclear graphite using a large field of view technique.

Evans, (1978) studied six different types of virgin nuclear graphite samples under an optical microscope attached to a Quantimet (an image analysing computer that performs stereological analyses) with 200,000 picture points. Evans used this method to distinguish the microstructure of each graphite and to follow the porosity through the body of samples of a range from 500 μm to 5 nm, which was considered at the time to be the best way to quantify porosity within nuclear graphite.

3.1.2.2 Automated serial sectioning instrumentation

In this section, a review of the most common techniques used to obtain a raw 3D image through serial sectioning is discussed: Confocal Laser Scanning Microscopy (CLSM) and FIB-SEM. CLSM has been used in some studies of nuclear graphite and is therefore reviewed to compare with the FIB-SEM used in this work.

3.1.2.2.1 Confocal laser scanning microscopy (CLSM)

CLSM is commonly referred to as 'optical sectioning,' as it captures a series of two-dimensional images at different depths in a sample. The series of images are combined into a 3D model of the sample's structure. When taking CLSM images, the laser beam is passed through an aperture before it is focussed onto a specific area of dimension ~1μm. The sample stage of the laser is scanned to provide a 2D point by point image. The projected image includes numerous pixels that are imprinted by photons scattered from the features within the sample. After sectioning, light passes through another aperture in the confocal plane before reaching the detector. CLSM allows a range of magnifications from 5x to 250x. These magnifications represent a compromise between image quality and image size, which can show enough detail of the surface microstructure of the materials.

The constructed 3D map of the sample facilitates the definition of properties of the pores based on geometric and topological attributes. The specific size, shape, and distribution of the microscopic components can thus be evaluated (Bodel, 2013). Ultimately, CLSM can be coupled with other equipment to obtain information from samples in controlled environments such as radiation chambers. Bodel (2013) studied the relationship between the microstructure

and Young's modulus of graphite using CLSM. This study shows a qualitative analysis of the microstructural deformation and cracks propagation in axially stressed graphite. Figure 3.8 is an example of Bodel's data, which shows the closure of microcracks in filler particles of PGA graphite sample compressed by a compression rig. Although crack growth and propagation were evident in his results, the benefits of CLSM is still limited. This is because it is difficult to distinguish between changes in the pore structure and bending of the sample caused by compression from visual analysis only. Bodel (2013) shows no attempt to quantify the behaviour of pore structure in his work.

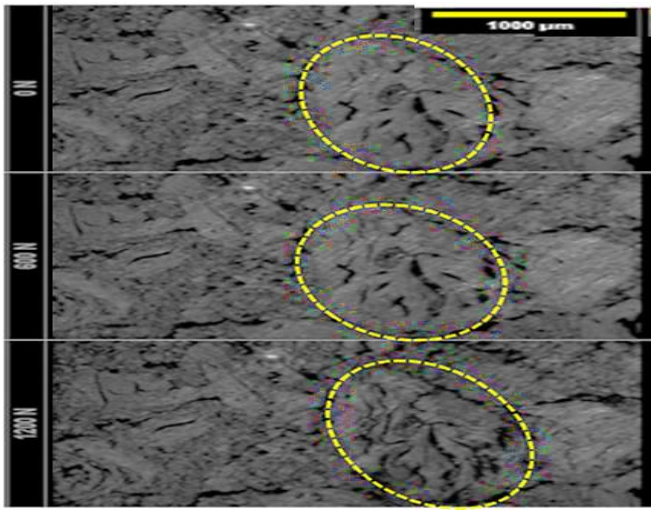

Figure 3.8: CLSM micrographs of PGA graphite, where the sample is axially loaded, showing critical deformation in the near elliptical filler particle (yellow dashes). Image adapted from (Bodel, 2013).

Another study by Taylor (2016) investigated the stress-induced deformation of open pores at the surface of PGA and Gilsocarbon graphites using CLSM and X-ray tomography. It was found that the average pore volume was four times less responsive to loading-induced contraction than the average pore area. The average pore area decreased linearly as the applied load increased because of the stiffness and preferential pore orientation in both samples of graphite (Taylor, 2016).

CLSM faces several limitations. The resolution of the microscope is limited (~1µm), and the pixel size of the images is rather large, the latter of which makes it difficult to quantify the behaviour of the small pores within graphite

precisely. Second, CLSM can only detect open pores near the surface of the sample, because of the 3D nature of graphite X-ray tomography can be used as a supplement. Third, studying the surfaces of the samples cannot provide accurate information about the stresses within the whole sample (Taylor, 2016).

3.1.2.2.2 Focussed ion beam–scanning electron microscopy (FIB-SEM)

FIB-SEM is generally considered one of the best techniques for characterising small-scale structures of grains and precipitates with serial sectioning (Dunn and Hull, 1999; Uchic, 2006; Uchic et al., 2007). FIB-SEM is applicable to structures smaller than 10 μm in one dimension; new plasma FIBs have increased this to 100 μm. Each step in this method typically begins with the repeated removal of a thin slice of material using a focussed ion beam. Then an electron beam is used to image the exposed material in cross-section. The dual-beam setup of FIB-SEM machines facilitates iterative sectioning and imaging, eliminating the need to move specimens between sectioning and imaging machines (Bansal et al., 2006). This high-level automation reduces the time required for testing and hence increases the efficiency of the overall procedure. Improved efficiency means that several stacks of images can be processed concurrently and reconstructed to provide a 3D overview of the microstructure (Schaffer et al., 2007).

FIB columns focus high-energy ions (typically Gallium [Ga^+]) on small spots of dimensions on the order of 0.005–0.02 μm. Interactions between these ions and the target remove material locally through ion sputtering. FIB microscopy is the best-known technique for serial sectioning via cross-section milling, with an average serial section thickness of around 10–15 nm made possible by the very fine resolution of the ion beam (Bansal et al., 2006; Holzer et al., 2004). This value is at least ~10 times smaller than the section thickness possible with traditional mechanical methods for removing material, such as polishing.

Another advantage of FIB-SEM microscopy is how cross-sectional ion milling is almost universally applicable for preparing planar surfaces, with reported success in imaging metallic alloys and biological materials. FIB-SEM has only merely been used for imaging nuclear graphite, as low beam currents are needed to prevent alteration of the microstructure. Ion sputtering causes relatively little structural damage when compared with polishing or cutting

methods because the damage layer is shallow. To quantify this damage, image analysis using software such as Fiji, Amira usually adapted. Ion sputtering also preserves the details of hard-to-prepare microstructures that contain significant porosity, such as nuclear graphite (Groeber et al., 2006; Zaefferer et al., 2008). During the slice and view process, many issues were raised, such as the presence of artefacts, shading, and charging defects. The issue of artefacts, such as curtaining can cause by the ion beam milling step. While charging effects can cause by a large number of secondary electrons being emitted from the sample due to local topological effects, and the lack of a conductive path by which excess electrons can be removed, causing bright areas in the images (Arregui-Mena et al., 2018).

Krishna et al. (2015) examined a range of neutron-irradiated graphite samples taken from the British experimental pile zero (BEPO) facility using FIB as a sample preparation technique for transmission electron microscopy (TEM), which usually requires specimens of approximately 100 nm in thickness. Arregui-Mena et al. (2018) used FIB-SEM to characterise the porosity of AGX graphite an electrode material. They selected two different regions (filler and filler-binder regions). The voxel resolutions achieved were between 20 and 50 nm, which allowed the intricate porosity structure of graphite to be captured. Figure 3.9 shows the 3D reconstruction of region 1 and 2 pore structures. Their data shows an important and interesting contribution to study the pore structure of AGX graphite. However, most of the calculated pores appeared to be located around the edges of images, which is a limitation of using FIB-SEM. Consequently, the measurements of the size of the pore still need further investigation for more accuracy.

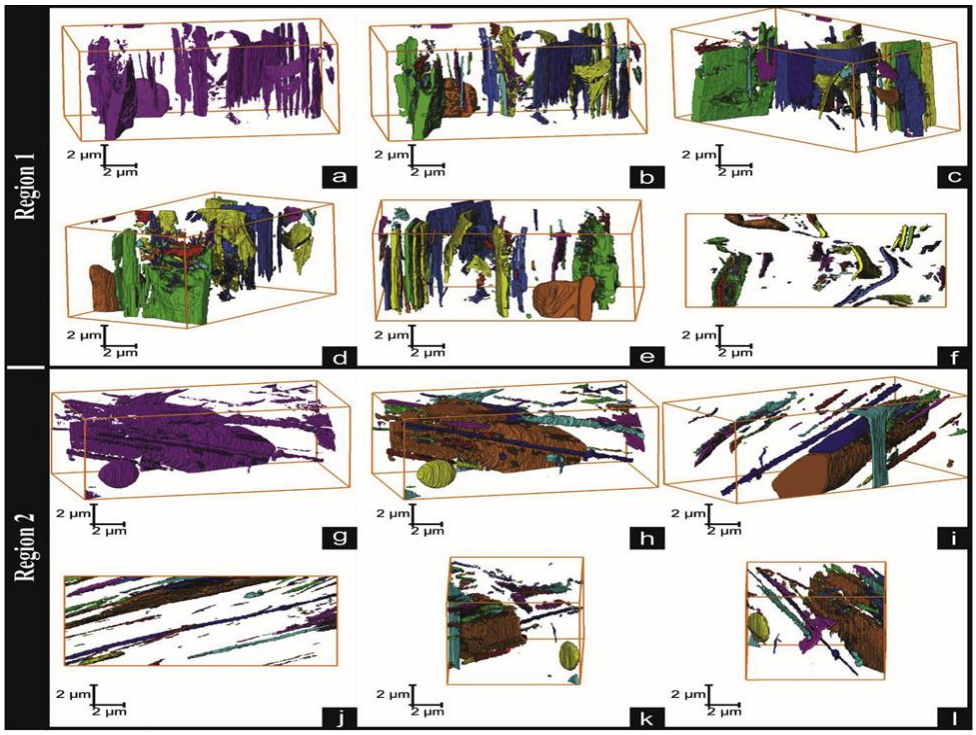

Figure 3.9: 3D reconstruction of the pore structure of AGX graphite of two different regions, Colours are used to ease the identification of each pore. For more information, images adapted from (Arregui-Mena et al., 2018).

3.1.3 X-ray tomography

X-ray tomography, also known as X-ray, computed tomography (CT), was not used in the present research but is included here in order to highlight the main differences and important considerations in general compared to FIB-SEM techniques. CT is a powerful technique for three-dimensional imaging of nuclear graphite structure, particularly the characterisation of porosity, which is a topic that merits much more attention and is vital to any structural modelling of nuclear graphite. CT is used to investigate the size, shape, spatial connectivity and structure of nuclear graphite morphologies. Babout et al. (2008) demonstrated the use of CT characterisation to study macro-porosity in modelling the thermal conductivity of radiolytically oxidised nuclear graphites.

Compared with FIB-SEM techniques, they are quite different in terms of system operation and capabilities. CT imaging exploits the differing absorption of X-rays by regions of different density to acquire volumetric microstructural data. In general, CT produces a series of 2D images oriented at slightly different angles. Once enough images are produced, computer software then reconstructs these images into a 3D object (Berre et al., 2008).

One of the key differences between these two techniques is that CT is a non-destructive technique to graphite samples compared to FIB-SEM. This is because slices of the graphite samples are physically milled away by the FIB to reveal successive cross-sections, which are imaged with the SEM (Arregui-Mena et al., 2018). Besides, CT does not require vacuum conditions, whereas FIB-SEM must be conducted under vacuum. This feature, combined with the non-destructive nature of CT, makes it a promising technique for imaging the microstructure of nuclear graphite (Arregui-Mena et al., 2018; Babout et al.,2008). Moreover, the maximum resolutions of CT are ~32 nm/voxel, while FIB-SEM systems are ~ 10 nm/voxel, which enables to observe smaller pores size.

3.1.4 Crystalline structure measurements

3.1.4.1 X-ray diffraction (XRD)

XRD can quantify the effects of neutron damage in nuclear graphite at any stage of irradiation. Because nuclear graphite is highly crystalline, the degree of crystallinity must be considered when comparing samples of different grades. XRD analysis is used to calculate crystallinity in terms of the following significant parameters: d_{002} interlayer spacing along the c direction, the in-plane lattice parameter along the a direction, and crystallite coherence lengths along the c and a directions. Several researchers have measured these parameters from a range of grades of graphite from various reactors (Babu and Seehra, 1996; Freeman et al., 2017; Goggin et al., 1964; Hagos et al., 2010; Henson et al., 1968; Howe et al., 2007; Nightingale, 1962; Krishna et al., 2015; Zheng et al., 2014; Zhou et al., 2014). These authors all agree that the XRD peaks of irradiated graphite can be analysed to quantify neutron damage when compared in unirradiated samples and single-crystal samples. Neutron damage is evidenced by changes in diffraction-peak position and widths and the disappearance of certain peaks.

The lattice parameters a and c are calculated from the peak positions in the XRD profiles that are related to the reflections of the (100) and (110) planes for the a direction and the (002) plane for the c direction. These measurements show an increase in lattice parameters with increasing dose and temperature; a reduction in both L_c and L_a has also been observed, which confirms an increase

in lattice disorder. Different grades of graphite vary widely in coherence lengths (L_c and L_a), but L_a is always smaller than L_c in unirradiated graphite because of the anisotropic nature of the crystals (Hagos et al., 2010; Howe et al., 2007; Krishna et al., 2015; Zheng et al., 2014; Zhou et al., 2014).

Goggin et al. (1964) studied several types of graphite, including pile grade A (PGA) and single-crystal Ticonderoga graphite. Samples were subjected to an irradiation dose of 2 dpa at temperatures of 200 and 650 ˚C. The authors used the model proposed by Simmons and Reynolds (1962) to analyse the behaviour of the graphite. The authors did not provide details about the changes in diffraction-peak widths. The authors believed that the lattice-parameter measurements were of single-crystal material. Their observations revealed significant changes in c-axis spacing: a change in c spacing of approximately 4% occurred at 200 ˚C, and at 650 ˚C, the change was approximately 0.15%. The changes observed at 200 ˚C were fully recovered after annealing to around 1850 ˚C, but the detailed changes at 650 ˚C were not reported (Goggin et al., 1964). Henson et al. (1968) investigated PGA and Gilsocarbon graphite samples subjected to a very high dose of ~30 dpa, with temperatures ranging from 300 ˚C to 1350 ˚C. The strong irradiation dose resulted in dimensional changes (Henson et al., 1968). A contraction in the a-axis and an expansion in the c-axis for irradiation between 300 and 650 ˚C was observed (Figure 3.10 and 3.11). The lattice parameter changes show a tendency of asymptotic/saturation behaviour between 6-7 dpa (~ 50×10^{20} n.cm^{-2} Ni), which is more obvious in a-axis lattice parameters than c-axis lattice parameters. The data did not indicate any significant differences between the PGA and Gilsocarbon graphite grades and the data for both grades were plotted together without distinction (Henson et al., 1968).

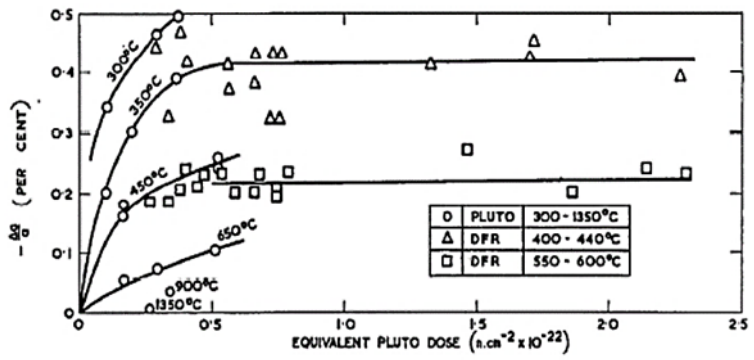

Figure 3.10: Changes in the a-axis lattice parameter as a function of irradiation temperature (Henson et al., 1968).

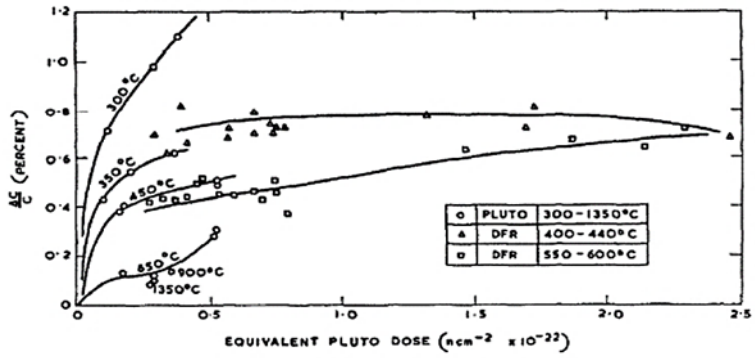

Figure 3.11: Changes in the c-axis lattice parameter as a function of irradiation temperature (Henson et al., 1968).

Gallego et al. (2003) studied HOPG reference samples subjected to doses between 3–7 dpa, with irradiation temperatures ranging from 619 to 751 ˚C (Figure 3.12 and Figure 3.13). The authors found that with increasing dose and temperature, the c-axis lattice parameter increases, and the a-axis lattice parameter reduces, with a significant decrease in coherence lengths (crystallite sizes L_c and L_a), compared to virgin HOPG, as shown in the Tables in Figure 3.12 and Figure 3.13. Asthana et al. (2005), with a study of HOPG irradiated at low doses 10^{-3} dpa and a temperature of ~333 K. Their results showed an average increase of ~3% in the c-axis lattice parameter and degradation of the crystalline structure (Asthana et al., 2005). This data provides evidence that the static displacement of atoms leads to fragmentation of the crystal lattice into nano-crystallites. Displacement also causes breaking, bending and displacement of the basal planes due to loss of layer stacking efficiency. However, changes in the L_c value were not included.

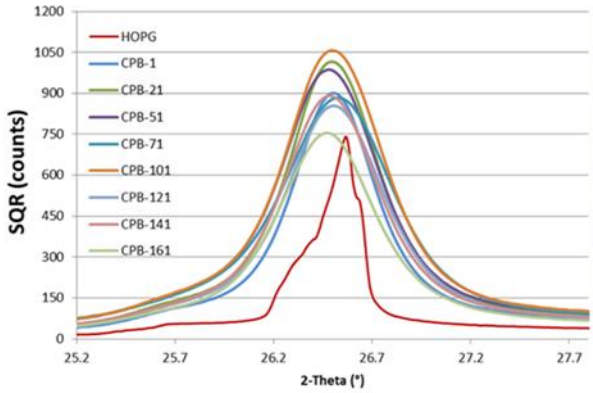

Sample	T_{irr} [°C]	Dose [dpa]	d(002)	Lc
HOPG unirrad	-	-	3.3508	702
CPB1	619	3.41	3.3651	294
CPB21	678	5.06	3.3658	260
CPB51	744	6.49	3.3673	235
CPB71	751	6.82	3.3614	202
CPB101	726	6.62	3.3650	231
CPB121	690	6.01	3.3649	231
CPB141	622	4.88	3.3676	238
CPB161	511	3.09	3.3699	236

Figure 3.12: Changes in the (002) peak with irradiation of HOPG. Inset Table lists data obtained from c-axis lattice parameters with L_c (right) (Gallego et al., 2013).

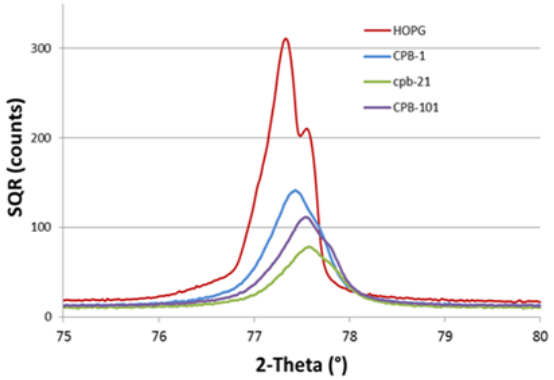

Sample	T_{irr} [°C]	Dose [dpa]	d(110)	La
HOPG unirrad	-	-	1.2323	544
CPB1	619	3.41	1.2318	337
CPB21	678	5.06	1.2300	307
CPB101	726	6.62	1.2302	321

Figure 3.13: Changes in the (110) peak with irradiation of HOPG. Inset Table lists data obtained from a-axis lattice parameters with L_a (right) (Gallego et al., 2013).

Vreeling et al. (2012) have reported studies done by the Nuclear Research and Consultancy Group (NRG, Petten, Netherlands) on a range of irradiated polygranular nuclear graphites of high dose and irradiation temperatures at 420, 750 and 950 ˚C. Samples were irradiated under the EU-framework-funded INNOGRAPH and EdF Energy-funded 'Blackstone' programmes for the development of high-temperature reactor (HTR) technology. There were some similarities to previous studies of a continual broadening of the (002) peaks as well as broadening in the (110) peaks. However, these results are important since samples pass through a turnaround point in bulk growth because there are two areas of significant departure from previous studies: first, the change in c-axis lattice parameter shows a decrease as the neutron dose increases (Figure 3.14). It then expanded when cracks had closed up. Second, a continuous decrease in the a-axis lattice parameter was observed (Figure 3.15). Hence, the

increase in lattice disorder leads to a decrease in coherence lengths (L_c and L_a) as neutron fluence increased (Vreeling et al., 2008). However, measurements reported by Henson et al. are different, which show in the a-axis lattice parameter asymptotic/saturation behaviour as mentioned above. The NRG measurements are consistent across several samples studied over several temperature ranges over an extended period and have been produced under procedures that include reference material checks. The key difference between the two sets of studies, which may affect the results, is that Vreeling et al. (2012) used intact polycrystalline specimens, while Henson et al. (1986) used powdered specimens.

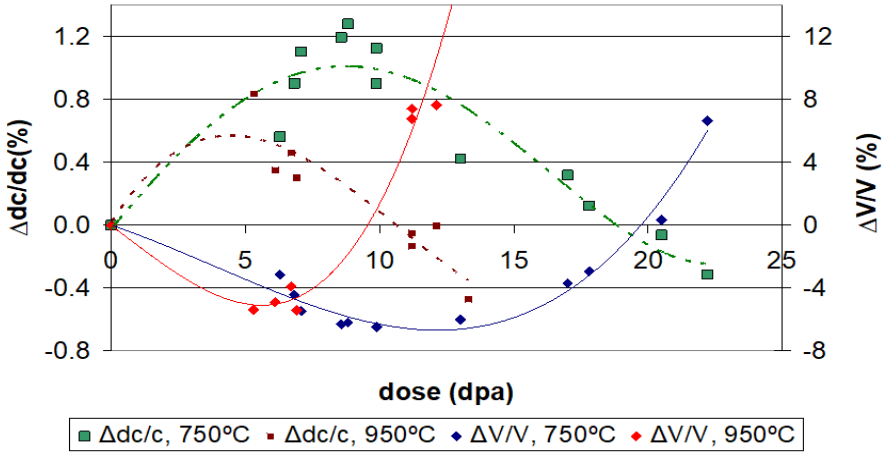

Figure 3.14: Bulk dimensional change and the change in c-axis lattice parameter versus neutron doses. Adapted from (Vreeling et al., 2012).

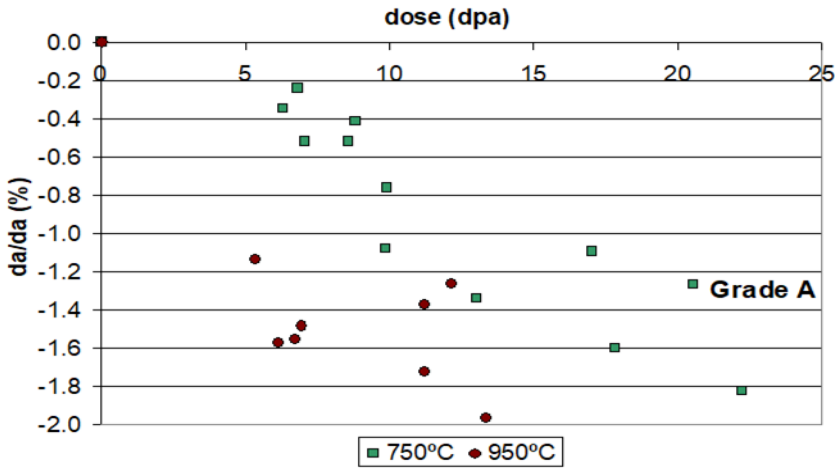

Figure 3.15: Change in a-axis lattice parameter versus neutron doses. Adapted from (Vreeling et al., 2012).

Zhou et al., (2017b) used XRD to quantify neutron irradiation effects on the atomic structure of virgin and low dose (~1.3 dpa and ~2.2 dpa), high temperature (750 ˚C) irradiated nuclear graphite samples. Samples were also irradiated at Nuclear Research and Consultancy Group (NRG). In this study, two refinement procedures were applied and yielded fairly good fits: the single-layer model and the two-layer model. Due to the X-ray form factor of carbon, the intensities of diffraction peaks reduce at extreme angles of 2θ, and thus the strong (002) peak dominates the diffraction pattern. It is this peak that highly determines the standard deviation ruling out standard deviation as the best indicator for how good the fit is. Each model reproduces the peaks accurately in a different manner. The single-layer model is appropriate for high dose irradiations as they have a very disordered structured. However, the two-layer model produces the best description for both measurements and fits of the irradiations for XRD patterns of low doses (~ 1:3 and ~ 2:2 dpa) and high temperature (750 ˚C). The finding of refined parameters against irradiation doses, the average in-plane lattice parameter, varies weakly with irradiation for all the specimens. Both the interlayer spacing (d_{002}) and the in-plane coherent lengths were found to be both directly proportional to the irradiation dose. The increase in (d_{002}) is explained using a mechanism involving the presence of displaced carbon atoms between carbon layers; and is caused by interstitial defects stacking faults, vacancies/dislocations, and crosslinks. The change in coherent lengths shows an increase at low irradiation dose caused by the formation of interstitial dislocation loops and closing of micro-cracks within the layers. High temperature and low dose irradiation modify, to a great extent, the structure of nuclear graphite, resulting in disorders such as stacking faults. From the findings, it is possible to quantify the effects of neutron irradiation on the atomic structure.

Krishna et al. (2017) performed XRD analysis on different samples of nuclear graphite; a virgin PCEA (Generation-IV candidate nuclear graphite sample) graphite, PCEA sample irradiated at 900 ˚C to 6.6 dpa, PCEA graphite irradiated at 900 ˚C to 10.3 dpa, and a BEPO (sample from British experimental pile zero reactor) whose irradiation is at 100 – 120 ˚C to 1.6 dpa. The observation recorded is that unlike the irradiated ones, the virgin sample of PCEA resulted in sharper, slender, yet more intense Bragg peaks. The broadened Bragg peaks with

relatively lower intensity in irradiated samples could be associated with the displacement of carbon atoms in the lattice structure during irradiation. This translates to an increased lattice disordering, dislocations, and micro-strain in the graphite structure. BEPO had a significant broadening of the diffraction peaks with irradiation that could be associated with its poor graphitization during manufacture or the exposure to fast-neutron irradiation (Krishna et al., 2017).

Considering the lattice structure, the values of the lattice parameter (a) was found to decrease with respect to the irradiation dose. In PCEA irradiated to 6.6 dpa and 10.2 dpa, there is a reduction in percentages of these parameters by 0.52% and 1%, respectively. The reduction was lowest (0.37%) in BEPO exposed to 1.6 dpa. Similarly, the magnitude of reduction in lateral size, the stack height of the lattice structure and the change in lattice dimension was found to be dependent on the temperature and irradiation dose, see Figure 3.16. In particular, it was observed that there was a significant change in the crystallite size, dislocation density, and micro-strain in BEPO and irradiated PCEA compared to the virgin PCEA (Krishna et al., 2017). The micro-strain was found to be 6-times higher in irradiated PCEA and 10-times higher in BEPO than in virgin PCEA. Generally, the micro-structure got deteriorated as the dose of irradiation increased leading to increased interplanar spacing, smaller crystallite size, reduced lattice parameter, and loss of crystallinity. A full amorphisation of the lattice structure is predicted at very high irradiation doses.

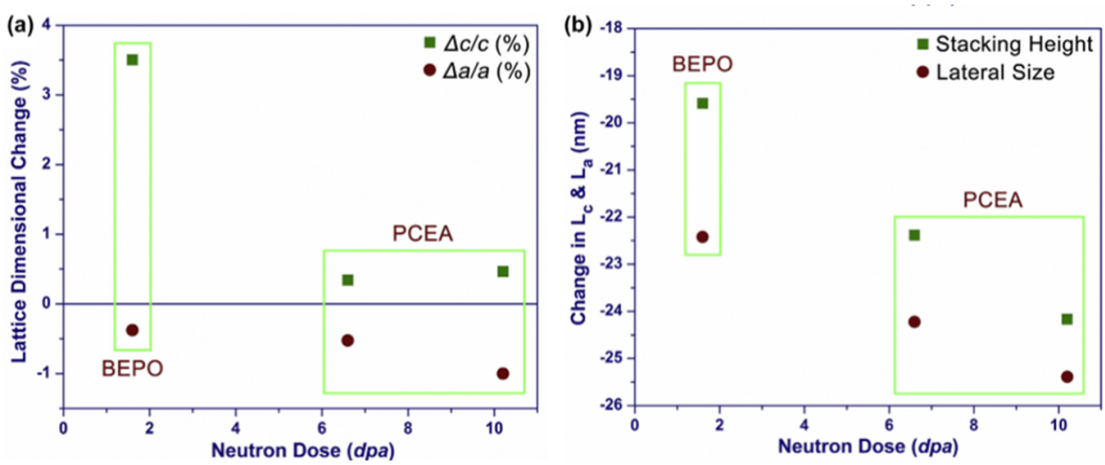

Figure 3.16: Change in lattice properties due to irradiation of two nuclear graphite grades; BEPO and PCEA: (a) dimensional change, and (b) stacking height and lateral size reprinted from (Krishna et al., 2017).

Mironov (2014) also used XRD to study both virgin and irradiated graphite of the same samples, as discussed earlier. Compared to virgin specimens of the same grade, XRD diffractograms of the two graphite samples showed that the crystallite size decreased by roughly 35% (for both L_a and L_c) in low-dose (PCEA1.5/PCIB1.5), low-temperature samples. In high-dose, high-temperature samples (PCEA 6.8/PCIB6.8), the crystallite size reduced by roughly 50% (for both L_a and L_c). Although these findings seem to agree with the literature (Gallego et al., 2003; Krishna et al., 2017), PCIB sample irradiated to 4 dpa with irradiation temperature at ~538 ˚C shows different behaviour under irradiation. At this dose and temperature (4 dpa, ~538 ˚C), the L_a crystallite size increased from its virgin values by roughly 8%.

To sum up, there seems to be a consistent observation that an increase in the irradiation dose results in changes in the microstructure of nuclear graphite. The changes are proportional to the dose. To some extent, the irradiation temperature affects the microstructure of the graphite too. For instance, the stack height and the lateral size of a nuclear graphite crystallites are found to vary depending on the temperature and irradiation dose with un-irradiated samples experiencing insignificant changes. However, each study follows a different analysis approach on varying graphite sample compositions, which influence not only the accuracy of the results but also the ability to compare the findings effectively.

3.1.4.2 Raman spectroscopy

Raman spectroscopy allows both qualitative and quantitative investigation of a sample (Larkin, 2011). Nuclear graphite shows a peak at approximately 1580 cm^{-1} (the G band), as shown in Figure 3.17. This peak arises from the double degenerate phonon mode that is involved in in-plane vibrations: the stretching of sp^2 atoms that occurs in chains and rings. The G band is observed in all polyaromatic hydrocarbon materials, of which nuclear graphite is an example (Ferrari, 2007; Malard et al., 2009).

The D band, which is the second-most important peak, occurs at approximately 1357 cm^{-1} (Figure 3.17). It appears only in small particles of crystallised graphite and does not arise in perfect crystals (Willmott, 2011). The

main cause of the D band is double-resonance Raman scattering (Mironov, 2014; Nemanich and Solin, 1979). The D band is also related to lattice disorder, such as vacancies and interstitials, and the D band can be evidence of any defect (Freeman et al., 2017).

The third peak present in the Raman spectrum of graphite is D', which occurs at approximately 1620 cm^{-1} (an overtone of the D band), as shown in Figure 3.17. Some researchers have argued that the D' band is caused by a second phonon mode and not by a defect (Reich and Thomsen, 2004). Others have attributed its presence to disordered carbon atoms, and therefore to imperfect graphite (Gouadec and Colomban, 2007; Nemanich and Solin, 1979). The 2D (an overtone of the D peak) and 2G (an overtone of the G peak) bands have also been detected at 2710 cm^{-1} and 3250 cm^{-1}, respectively. The final observed peak is the D+G band, which occurs at approximately 2950 cm^{-1} and is related to the E_{2g} and D modes. Table 3.1 lists the most common naming system used for the Raman bands present in a graphite spectrum.

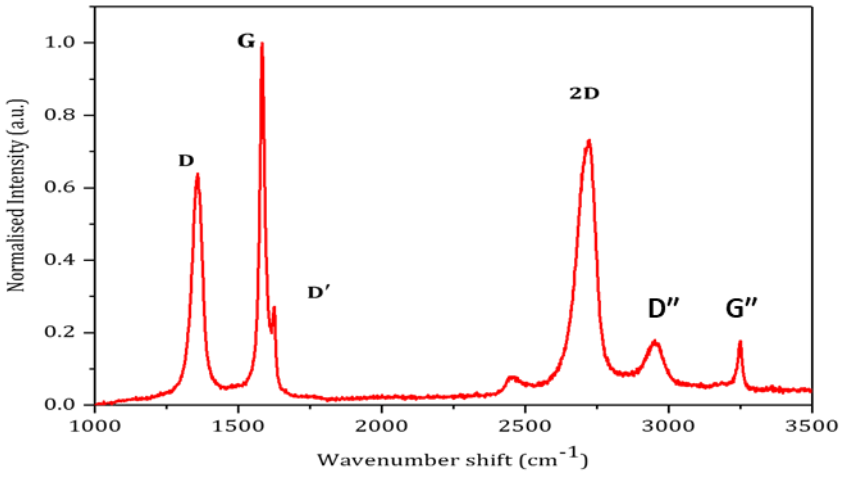

Figure 3.17: Raman spectrum for nuclear graphite (PGA).

Table 3.1: Raman vibrational modes for graphite (Krishna et al., 2015).

Raman order	Raman rules	Raman Active peaks	Raman frequency (cm^{-1})	Origin
First	Disorder Induced A_{1g} line	D	1350	Breathing oscillation of defected C–C sp^2 hexagonal rings and possible sp^3 rings
	E_{2g} C–C scattering from sp^2 hybridized sites	G	1580	sp^2 hybridized bond stretching mode
	E'_{2g} scattering	D'	1620	Nature of defect
Second	Structural information	$G'(2D)$	2700	$2D$ and $3D$ graphitic structure
	E_{2g} + D	$D''(D+D')$	2950	Overtones of fundamental first modes
	$2 \times E'_{2g}$	$G''(2D')$	3240	

Measurements of the intensity ratio of the D and G bands can provide information about the coherence length L_a. The position and FWHM of the G band can also provide evidence about the extent of lattice disorder. Tuinstra and Koenig (1970) carried out a systematic comparison between data obtained from Raman spectra and XRD patterns. They suggested an inverse relationship (roughly a linear relationship) between the I_D/I_G ratio and the crystallite size L_a. As the crystallite size L_a becomes smaller, this relationship will no longer be linear because of the width variations. The I_D/I_G ratio multiplied by the coherence length L_a, or $1/L_a$, depending on the magnitude of L_a (Tuinstra and Koenig, 1970). This value was found later to be ~4.4 nm, as stated in (Knight and White, 1989), which was considered to be similar for both Raman spectra at 0.488 μm (blue excitation wavelength) and 0.514 μm (blue excitation wavelength) (E_l=2.41 eV). Mernagh et al. (1984) demonstrated that the I_D/I_G ratio depends on the excitation energy (E_l), which revealed the Knight and White empirical formula was valid when the experiment was only done using these two values. Because this ratio is controversial, XRD measurements should be considered as a first tool for acquiring data about crystallite size (Cuesta et al., 1998). Ferrari and Robertson (2001) carried out measurements on disordered and amorphous carbons showing a linear trend for the I_D/I_G ratio versus L_a for very small crystallite sizes (L_a < 2 nm). Thomsen and Reich (2000) demonstrated the origin of the D band and found it to be related to a double resonance process;

this model was used in several physical processes such as multiple scattering (Barros et al., 2011) and active defects (Venezuela et al., 2011). Experimentally (Beams et al., 2011) and theoretically (Basko, 2009), the mean free path l_D of the excited photoelectron interacting with the D phonon was measured to be adjacent to 3 nm at room temperature.

Consequently, the ratio of D and G bands was not measured in a similar way in all the published literature. While Tuinstra and Koenig measure the height of the peaks and not the peak area, several authors diverged from this methodology. For instance, to obtain a good fit for the spectra, numerous bands (up to five) were added (Zickler et al., 2006), which is strongly modifying the ratio of D and G bands. Recently, an empirical law has been widely adopted to estimate the crystallite size, L_a, for any excitation laser energy in the visible range (Cançado et al., 2006; Krishna et al., 2017; Pimenta et al., 2007; Zheng et al., 2014).

$$L_a\ (\mathrm{nm}) = \frac{560}{E_l^4}\left(\frac{I_D}{I_G}\right)^{-1} \tag{3.1}$$

Where E_l is the excitation laser energy in eV units and the laser line wavelength in nm units, Eq. 3.1 can be rewritten as:

$$L_a\ (\mathrm{nm}) = (2.4 \times 10^{-10})\lambda_l^4\left(\frac{I_D}{I_G}\right)^{-1} \tag{3.2}$$

The constant of proportionality between the crystallite size L_a and the ratio of D and G bands is obtained from Eqs. (3.1) and (3.2) by using E_l=2.54 eV (13.5 nm). This value is higher than the value stated by Knight and White (4.4 nm).

Compressive residual stress shifts the Raman G peak to a higher frequency, while tensile stress moves G peak to a lower frequency. The splitting of the G band (E_{2g} optical mode) into two components G+ and G− is because of anisotropic stress. The anisotropic stress causes changes in the crystallographic symmetry of the materials. Nevertheless, hydrostatic stress within the microstructure of graphite only produces a shift, and the original symmetry remains intact (Tuinstra and Koenig, 1970). Krishna et al. (2015) investigated the compressive residual and tensile stresses distribution in the constituents of

nuclear-grade polygranular graphite using Raman micro-spectroscopy (Figure 3.18). Their analysis of G peaks showed that the binder phase in Gilsocarbon graphite had very high stresses based on the shifting of G peaks. The authors also found that cracks in the filler and binder phases were under compressive and tensile forces, while the pores were mostly under compression. These data could enable the design of a more durable nuclear graphite that could withstand higher radiation doses because, within irradiated graphite microstructures, strain relief of induced stresses help to avoid premature failure, as mentioned earlier. Moreover, through the correlation between the I_D/I_G ratio and the FWHM of G peaks, three different stages of damage to the nuclear graphite were identified: the accumulation of defects within the basal plane, crystal fragmentation and increasing tortuosity, and graphitisation.

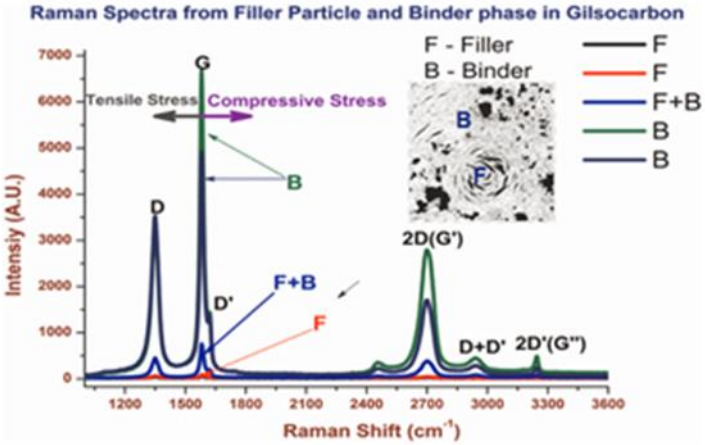

Figure 3.18: Raman spectra of Gilsocarbon graphite (shown in inset). The plot shows the Raman spectra from both the filler and binder regions (Krishna et al., 2015).

More recently, Krishna et al. (2017) carried out another study using Raman spectroscopy to investigate similar samples discussed earlier in the XRD section (PCEA and BEPO graphite grades). Raman data were used to quantify the crystallite size (L_a), micro-strain and dislocation density for irradiated PCEA and BEPO graphite samples. The findings show a rapid change in the intensity, wavenumber shift and the FWHM of G peaks as radiation dose increases. This is because neutron exposure results in a reduction in sp^2 hybridised hexagonal carbon networks. While the increase in D-peak with increasing neutron flux, confirms the presence of defects in the layered structure. At higher wavenumber

(> 2500 cm^{-1}), a decrease in intensity and symmetrical broadening of the peaks were observed, which suggests the tilting and bending of basal layers (Cançado et al., 2008; Krishna et al., 2017). Moreover, the crystallite size (L_a) reduces and the micro-strain increases with increasing radiation dose. Dislocation density observations show an increase in both samples; two orders of magnitude in PCEA graphite, and three orders of magnitude in BEPO graphite. A similar observation was reported by Mironov (2014), who studied Raman spectra of virgin and irradiated PCIB and PCEA.

3.2 Summary

A number of techniques including XRD, Raman spectroscopy, SEM and PLM have been used to observe neutron-induced damage to nuclear graphite under a range of doses and temperatures and at different length scales (Bodel, 2013; Evans, 1978; Gallego et al., 2006; Goggin et al., 1964; Hagos et al., 2010; Henson et al., 1968; Kane et al., 2011; Metcalfe and Tzelepi, 2014; Nightingale, 1962; Taylor, 2016; Wen et al., 2008; Zheng et al., 2014; Zhou et al., 2014). Some of these studies are outdated, and many are incomplete due to gaps and inconsistencies in the irradiation temperature schedules. The models also fail to address real-time performance inside nuclear reactors and do not provide information about the structure of nuclear graphite at different length scales. Serial sectioning using FIB-SEM is used widely in other fields such as biology. Although biologists have found the technique to be very useful for obtaining high-resolution 3D data over relatively large material volumes with nanoscale characteristics, in the case of nuclear graphite, very few studies have been conducted using FIB-SEM. For instance, FIB sectioning has been used to prepare samples for TEM (Krishna et al., 2015) and a study of pore structures in AGX graphite, an electrode material (Arregui-Mena et al., 2018).

Furthermore, while, PLM is proved to be one the best ways to distinguish the microstructure to quantify the porosity graphite before and after irradiation, only study by (Evans, 1978) using progressive polishing method to investigate irradiated graphite in 3D, and (Kane et al., 2011) to examine porosity of virgin graphite in 2D has been reported. The effect of neutron irradiation on nano-micro scale porosity of Generation-IV nuclear graphite is still unclear, and only a

few qualitative studies conducted on irradiated graphite exist using SEM (Hagos, 2013; Mironov, 2014). Thus, to better understand the structural changes of virgin and neutron-irradiated graphite, different characterisation methods (e.g., XRD, Raman, PLM, SEM, and serial sectioning methods using PLM and FIB-SEM) are needed to asses both crystallinity, and porosity of nuclear graphite grades suggested for Generation-IV reactors. This Thesis reports on such studies, the results of which can be found in chapters 5, 6 and 7.

Chapter 4

4.1 Materials and methodology

This chapter first presents the materials studied and their sample preparation. Second, it discusses the experimental and data analysis techniques in detail, and third, it demonstrates how these methods have been employed to examine various material properties.

4.1.1 Materials used

4.1.1.1 Virgin graphites

Four different coke sources were examined, as given in Table 4.1. HOPG has been used also in this project as reference material.

Table 4.1: Characteristics of virgin nuclear graphites investigated in this work.

Graphite	Provider	Used in	Source coke	Forming method	Density (g/cm^3)
PGA	NNL-UK	Magnox	Needle-coke	Extrusion	1.74
GILSO	University of Manchester	AGRs	GILSO-coke	Moulding	1.79
PCEA		HTR	Petroleum coke	Extrusion	1.81
PCIB		HTR	Petroleum coke	Iso-molding	1.83

4.1.1.2 Irradiated graphite

Two graphite samples (Generation-IV candidates) were examined in this project. Samples were irradiated at the Advanced Test Reactor at the Idaho National Laboratory (grades PCEA and PCIB both based on petroleum coke) and subjected to neutron irradiation doses ranging from 1.5 - 6.8 dpa with the irradiation temperature varied between 350 ˚C – 670 ˚C, see Appendix A for more information and Table 4.2.

Table 4.2: Characteristics of Irradiated nuclear graphites investigated in this work.

Graphite Grade	Specimen ID#	Est. Temp, °C	Est. DPA	Activity (KBq)	Current mass
PCIB	P2**C03**	350	1.5	30	1.5 g
	P1**B02**	534.47	4.04	330	1.5 g
	P3**B05**	655	6.8	175	1.5 g
PCEA	DW14C01 (3P**B17**)	670	6.8	15	1.5 g
	DW15C01 (3P**B25**)	350	1.5	30	1.5 g

4.1.2 Virgin sample preparation

Several techniques were used to examine virgin samples, including X-ray diffraction (XRD), polarised-light microscopy (PLM), and Raman spectroscopy. Electron microscopy techniques, such as scanning electron microscopy (SEM), and focussed ion beam–scanning electron microscopy (FIB-SEM) were also employed. Each experimental technique requires samples to undergo a specific series of appropriate preparation processes before characterisation, which includes cutting samples into suitable shapes and sizes, treating the surfaces, and performing chemical cleaning. The following sections provide details of these processes.

4.1.2.1 Preparation of PLM and Raman samples

The preparation of samples for testing followed a polishing route initially proposed by (Mogire, 2015) and subsequently developed by the author of this Thesis. Samples were prepared in similar dimensions that were approximately 30 mm (length) x 30 mm (width) x 10 mm (height). In general, the three main steps to prepare virgin graphites started with mounting and followed by grinding and polishing, see Table 4.3. Mounting was carried out using a compression mounting machine with EpoMet F (offers good edge retention) and backed by Phenocure (cheaper compared to EpoMet F). However, EpoMet F can also be used for SEM work, using KonductoMet resin as it contains conductive

fillers eliminating the need to coat samples to prevent charging effects, see Figure 4.1.

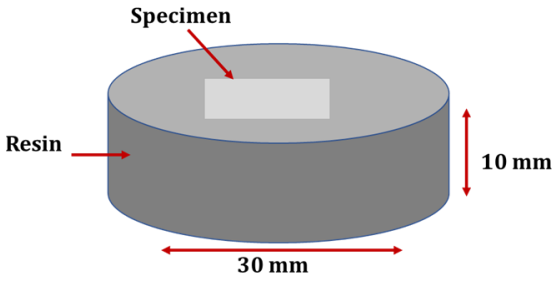

Figure 4.1: a schematic of a mounted specimen.

Grinding/Polishing

The following procedure was carried out on EcoMet/AutoMet 250 grinder polisher. Four steps were used as shown in Table 4.3 starting with Apex DGD Yellow – with 35µm abrasive diamonds ideally suited for brittle materials like graphite. The machine was run in single force mode with the individual force on each specimen set at 22N (5lbs). The first step used water as a lubricant with subsequent steps using MetaDi Fluid as the lubricant. Cleaning was carried out between each stage to prevent cross-contamination between the steps before continuing with the next polishing stage.

Step 4 was the final step with polishing using a micro cloth and master prep suspension for two minutes, with the last 10-15 seconds using water only. After this step, samples were rinsed in running tap water with gentle swabbing using cotton wool with a final rinse using Isopropanol or ethanol and dried using a hand dryer before observation under an optical microscope.

Table 4.3: shows details of sample preparation route followed in this work.

No	Surface	Abrasive	Lubricant/ Extender	Force (Per Specimen)	time (min:sec)	Platen speed (rpm)	Head speed (rpm)	Rotation*
1	Apex DGD Yellow	35µm dimond	Water	22N	Until Planar	300	60	>>
2	TexMet C	9µm MetaDi supreme water based	MetaDi Fluid	22N	5:00	150	60	><
3	Trident	3µm MetaDi supreme water based	MetaDi Fluid	22N	4.00	150	60	>>
4	Micro-Cloth	0.06 µm MasterPrep Alumina suspension	Water	22N	2.00	150	60	><

*Samples rotation with >> or opposite to the platen direction ><

4.1.2.2 Preparation of SEM samples

Graphite is typically prepared for SEM by following a similar polishing process explained above for Raman and PLM. The samples' dimensions were slightly different to fit the machine holder; 30 mm (length) x 30 mm (width) x 5 mm (height). In the final step, samples were stuck on stubs suitable for SEM, using a double-stick electrically conductive carbon tape. The SEM conducted in this project has indicated that polishing preparation methods can provide better results under observation than unpolished samples. Although graphite is a soft material, its surface can easily be damaged by polishing - this route provided a smooth surface and thus a better imaging and accurate presentation of the microstructure, see Figure 4.2.

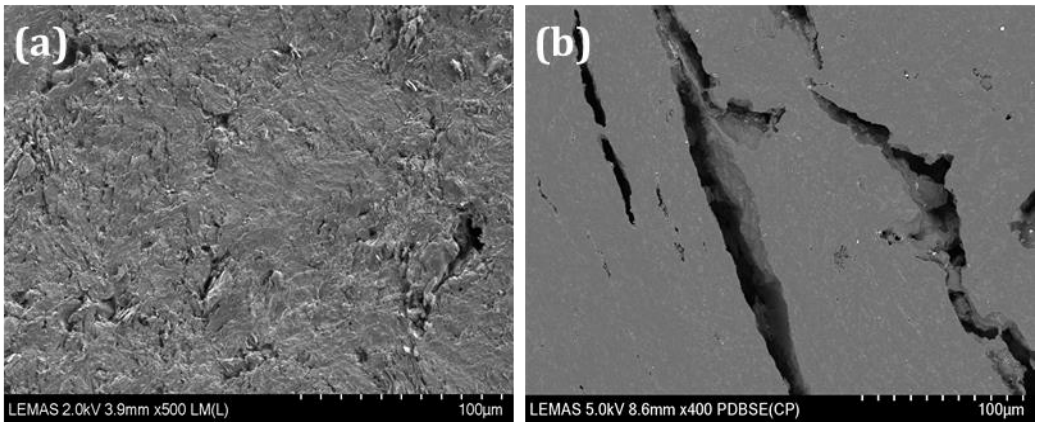

Figure 4.2: SEM micrographs of Gilsocarbon graphite samples show both filler and binder particles areas (a) unpolished sample, (b) polished sample.

4.1.2.3 Preparation of XRD samples

All measurements were taken using the same configuration. All solid samples had a cubic shape, with dimensions of 10mm in diameter and a height of 5mm cut from the respective raw block materials using a Struers Accutom-2 cutting machine at a speed of 1200 rpm/sec. The samples were then placed on a sample holder and subjected to XRD measurement. Some of the measurements were performed using a thin powder, which provided sufficiently intense (0 0 2) reflections that could then be used to measure the lattice in the c direction. This step was performed by grinding solid samples. For each nuclear graphite material, four separate samples were extracted. Each sample was measured by XRD in four different sample orientations. Finally, the sample was powdered, measured independently, and all results were averaged. This gave a total of 80 XRD measurements overall, see Table 4.4.

4.1.2.4 Summary of the virgin samples' analysis

Table 4.4: A summary of the measurements undertaken for each virgin graphite samples using PLM, SEM, XRD, and Raman spectroscopy.

Virgin Samples	No. of specimens per grades	PLM images	SEM images	XRD		Raman
				Solid	Powder	
PGA	4	80 (20 images per specimen)	100 (25 images per specimen)	16	4	60 (15 images per specimen)
Gilso-carbon	4	80 (20 images per specimen)	100 (25 images per specimen)	16	4	60 (15 images per specimen)
PCEA	4	80 (20 images per specimen)	100 (25 images per specimen)	16	4	60 (15 images per specimen)
PCIB	4	80 (20 images per specimen)	60 (15 images per specimen)	16	4	60 (15 images per specimen)
HOPG	4	-	-	20	-	40 (10 spots per specimen)
Total	16	320 images	360 images	100 measurements		280 measurements

4.1.3 Irradiated sample preparation

The as-received irradiated PCEA and PCIB specimens were ~6mm (height) × 12mm (diameter) cylinders (for more information on sample irradiation, see Appendix A). The XRD and Raman data of the irradiated specimens were collected by Mironov (2014), but the data were re-analysed by the author of this Thesis. While for the PLM and SEM samples, they were prepared and examined by Grebennikova (2018), but the author of this Thesis conducted the analysis.

Appropriate microstructural preparation of irradiated nuclear graphite is critical to maintain the structure of the material and to allow physical surface visualisation when using the SEM, particularly information about the distribution of pores, which is the main concern of this Thesis. Thus, three different steps were followed to achieve a highly polished scratch-free surface akin to the virgin samples; mounting, grinding, and polishing. However, for irradiated samples, different parameters and consumables were used. This is accomplished by first mounting graphite specimens on a mounting jig with the help of glue, which minimised any damage likely to be caused to the samples and

allowed easy handling of the samples. The samples were then ground manually with a series of Silicon Carbide (SiC) papers (800, 1200, and 4000 grit) using 5 µm and subsequently 1 µm diamond lubricant. The samples were then rotated by 90° before each pass until the original surface was entirely removed. This step aims to eliminate all sectioning damage and establish a flat surface with a uniform scratch pattern. The samples were then cleaned in an acetone bath and dried. A series of polishing tables ranging from 5 µm to 0.25 µm (diamond paste) were used for polishing for less than five minutes per step, and the samples were then cleaned and dried. The polishing steps were applied to produce progressively finer scratch patterns and lesser depths of subsurface damage. Finally, the samples were removed from the jig by dissolving the glue in warm ethanol/acetone and were then rinsed to remove the solvent. The samples were dried on a filter paper and placed on a clean glass slide, ready for observation. Table 4.5 shows a summary of total measurements undertaken using different techniques to investigate neutron irradiated samples.

Table 4.5: A summary of the measurements undertaken for each irradiated graphite samples using PLM, SEM, XRD, and Raman spectroscopy.

Irradiated Samples	No. of specimens per grades	PLM	SEM	XRD	Raman
PCEA 1.5 dpa/350 ˚C	1	10	5	4	60
PCEA 6.8 dpa/670 ˚C	1	10	5	4	60
PCIB 1.5 dpa/350 ˚C	1	10	5	4	60
PCIB 4.0 dpa/535 ˚C	1	-	-	4	60
PCIB 6.8 dpa/655 ˚C	1	10	5	4	60
Total	4	40 images	20 images	20	280

4.1.4 Experimental methodology

4.1.4.1 Microscopic examination

4.1.4.1.1 Optical microscopy

An optical microscope is best understood as a device comprising of one or more lenses, that produces a magnified image of an object placed in the focal plane of the lens. This technique has some limitations which can image only dark or strongly refracting objects. The diffraction effects and the wavelengths of

transmitted light are the main factors that limit the resolution of an optical microscope to roughly 200 nm, and out-of-focus light issues reduce image clarity (Mukhopadhyay and Gupta, 2012). There are two main techniques in optical microscopy. The first is transmission microscopy, which involves the passage of a light beam through a transparent object or thin section. The second type of optical microscopy, where incident light gets reflected off a solid sample's surface, is called reflected-light microscopy. The additional development and enhancement involved the employment of plane-polarised light. In particular, this technique allowed the study of anisotropic materials, of which graphite is an example (Daniels, 2003).

4.1.4.1.1.1 *Polarised-Light microscopy (PLM)*

Normal white light usually comprises of all visible wavelengths, with light waves undergoing electromagnetic oscillation in all possible directions perpendicular to the direction of the propagation of light. When light is passed through a polarisation filter, plane-polarised light in the form of a wave with a single electromagnetic oscillation direction parallel to the polariser emerges. In instances where two such polarisers are positioned back-to-back, no light is propagated if the polarizers are placed at 90° angles to each other (Mukhopadhyay and Gupta, 2012). In addition to this, the initial plane-polarized light gets propagated, if both polarisers are positioned in a way that their orientation is in a similar direction.

It is worth noting that anisotropic materials, such as nuclear graphite, are characterised by an extremely ordered arrangement of atoms in the crystal lattice. This form of arrangement is what determines the crystal's optical properties, which vary with direction. When this kind of material is illuminated with plane-polarised light, the incident light orientation is changed because of the orientation of the impinged surface, which assumes a crystallographic orientation.

For hexagonal crystals such as those of graphite, the anisotropic direction orientations respond differently to the polarised light. They eventually produce different reflected beams, that when combined, have the ability to form a beam comprised of diverse colours and intensities, which occur due to either constructive or destructive interference of diffracted wavelengths of light. These

effects can be used to reveal information about a sample's character, along with quantitative and qualitative data about the material's anisotropic nature (i.e., the crystallographic orientation of grains, strain, etc.). These steps form the primary foundation on which reflected PLM is based (Mukhopadhyay and Gupta, 2012).

During the operation of such microscopy, a light is generated by the use of an epi-illuminator and then directed through a polariser, from which it emerges as plane-polarised light. This light is directed to a half-mirror and then redirected to the tube, and finally to the sample. Upon hitting the sample, the light is reflected back via the objective lens and the eyepiece. The light then passes to the eyepiece through the half-mirror, where it is viewed by the operator. In order to vary the crystalline orientation with respect to the plane of light, the stage can be rotated. During the course of this operation, colour changes will be observed in the sample. Normally, the solid sample is positioned in an epoxy. This step is coupled with the polishing of the sample surface to attain optical flatness (Mukhopadhyay and Gupta, 2012).

When this technique was employed to observe nuclear graphite, interference patterns were generated due to the presence of graphitic layers on the sample surface. Depending on the layer orientation, the colours observed will range from purple to yellowish-blue (Mukhopadhyay and Gupta, 2012). A schematic diagram of a PLM configuration is shown in Figure 4.3.

The nuclear graphite sample observations were conducted using a standard bench-top Olympus BX51 optical microscope. To investigate graphite samples, a 5x objective lens was used and set to a pixel resolution of approximately 0.7 μm while analysing the pores.

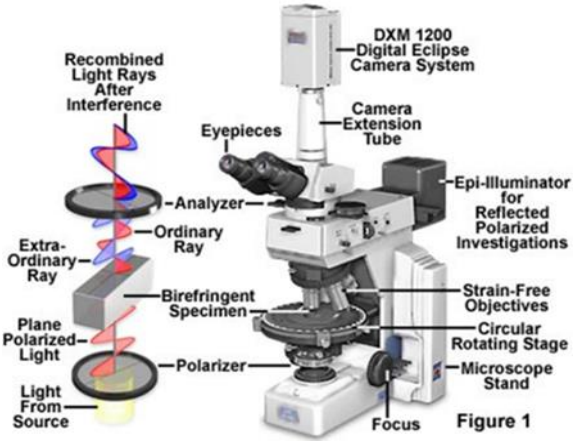

Figure 4.3: Schematic diagram showing PLM configuration reprinted from (Mukhopadhyay and Gupta, 2012).

4.1.4.1.2 Electron microscopy

4.1.4.1.2.1 *Scanning electron microscopy (SEM)*

SEM is an important morphological technique that is employed to study graphite samples. In SEM, an accelerated beam of electrons is focussed into a small beam by using a system of electrostatic and magnetic fields, the beam is then scanned across a particular sample's surface (Mukhopadhyay and Gupta, 2012). During SEM operation, incident electrons interact with atoms within the sample and then scatter elastically or inelastically. Consequently, various types of signals for imaging are produced.

The main imaging signals utilised in SEM are the backscattered and secondary electrons. When studying samples such as nuclear graphite, the secondary electrons are used to provide information about the surface topology of the graphite sample (Milev et al., 2008; Mironov, 2014). Secondary electrons are low-energy electrons (<50 eV) produced when electrons are ionised from the inner shells of the atoms in the sample, by inelastic scattering interactions with beam electrons. De-excitation of ionised atoms can generate characteristic X-rays. This, in turn, provides information about the elemental composition of a sample.

SEM was performed on a Hitachi SU8230 high-performance cold field emission (CFE) with Oxford Instruments Aztec EDX detector for virgin samples, and a FEI Nova 200 Nanolab dual-beam FEG-SEM/FIB for the irradiated samples.

In both cases, secondary electron images were captured using an in-lens detector at operating voltages of 2-5 kV.

Conventional Electron Back-Scatter Diffraction (EBSD) and Transmission electron backscatter diffraction (t-EBSD) were used in this Thesis, which usually measure the crystallographic properties of materials (e.g., grain orientations). However, both techniques are extremely difficult to apply to nuclear graphite because the samples' polishing has never appeared to be sufficient in providing a completely flat surface. Hence it is impossible to get any EBSD/t-EBSD patterns at all, and there were very few backscattered electrons detected.

4.1.4.1.3 Image analysis for PLM/SEM micrographs

To analyse the Polarised-Light Microscopy (PLM)/ Scanning electron microscopy (SEM) micrographs, Fiji software was used in order to identify and analyse the binder and filler particles and the porosity distribution. Fiji is an open-source platform for biological-image analysis (Schindelin et al., 2012). It is usually compatible with most user-created plug-ins, thus making it particularly favourable with quantitative analysis of microscopy. It is an improvement of ImageJ (Schneider et al., 2012), and it contains many more features than its predecessor, with its base software having the capabilities for image analysis, and the ability to apply user-created software to deal with any errors or gaps. In this work, the analysis of porosity within nuclear graphite was conducted in two parts: (i) most of the 2D analysis of PLM/ SEM microscopy data was conducted using tools in the base programme and (ii) serial sectioning data (3D) analysis using user-created plugins, which will be explained in chapter 6.

The analysis procedure began by first importing the images from the microscope into Fiji, in JPEG format for compatibility, and calibrating images by setting a scale on them using data from the microscope. It was necessary to separate the pore structure from the binder and filler phases to make it possible to quantify the pore structure from these images. For this purpose, segmentation was performed where the image was split into different and distinct phases, making it possible to define the physical properties of each region.

Greyscale segmentation techniques were used in this work, and it uses greyscale thresholding. An image is split into two distinct phases separated by a specific pixel intensity. The pixels are classified as either black or white pixels depending on whether their intensity is lower or higher than the threshold intensity. During the segmentation of the pore structure, pores are defined as white pixels and non-pores black. The conversion of the images to binary image matrices required an increased sensitivity of the threshold parameter, which was attained by stretching the contrast. There exists a narrow peak at low brightness, which corresponds to pore regions. The other parts represent the binder and filler regions. The typical threshold parameter values were between 0–255.

Figure 4.4 (a) is an example of an image analysis for Gilsocarbon graphite, which shows the original micrographs formatted as RGB colour files. The images were then converted to 8-bit greyscale images. Hue elimination and information saturation while retaining the colour image's luminance, led to the accomplishment of greyscale transformation, as shown in Figure 4.4 (b). The contrast was stretched to reference points of approximately 50 and 220 in all greyscale images, as can be seen in Figure 4.4 (c). Figure 4.4 (d) displays the final segmented image which used to measure pores within the microstructure of nuclear graphite.

A near-identical intensity histogram was produced for Gilsocarbon, PGA and PCEA graphite grade. However, Figure 4.5 shows the intensity of PCIB graphite grade; in this histogram, there is no well-defined distinction between pore and non-pore regions due to the smaller pore size and the fact that pores often appear inter-connected. This makes it difficult to define an accurate thresholding level. This is the situation in all PLM images of PCIB, thereby subjecting the calculations of pore properties to systematic error. Therefore, manual measurements of pore size were adopted in this case by selecting each pore and measuring it. In contrast, SEM micrographs enable the calculation of porosity in PCIB graphite, which gives more accurate results than PLM micrographs.

A single PLM/SEM image was thresholded at different values in order to quantify the systematic errors in this experiment. This ensured that the best thresholding limits were used. The mean pore area was calculated from the

thresholded data using the “analyse particles” tool in Fiji. For each image, an upper and lower limit was defined by eye for the region where the thresholding seemed reasonable, and the middle value was taken to be the thresholding value. Therefore, the error was the difference between the thresholding value and the lower and upper limits, which was converted to a percentage to be used to calculate the errors of other images. This was done for PGA, Gilsocarbon, PCEA, and PCIB; the thresholding limit was defined at 45 for PGA, Gilsocarbon, and PCEA, and at 77 for PCIB and the errors introduced during thresholding were calculated to be +8.8% and -7% for all nuclear graphite materials.

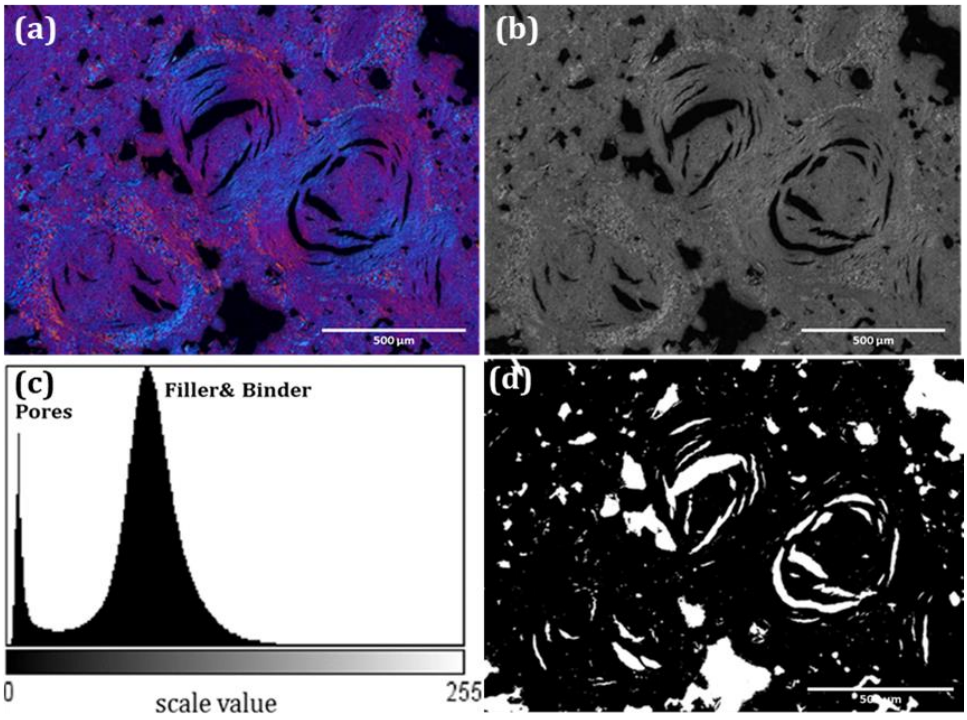

Figure 4.4: Nuclear graphite image analysis process; (a) original micrograph, (b) grayscale micrograph of original micrograph after removing the saturation and hue, (c) histogram of grayscale image before thresholding; lower intensity peak corresponds to pores region, and higher intensity peak corresponds to filler and binder regions, (d) final image that helped in extracting the quantitative analysis of pores within the microstructure of nuclear graphite.

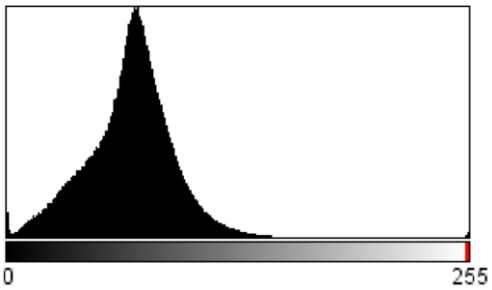

Figure 4.5: Histogram of a grayscale image before thresholding for PCIB graphite samples.

The difference in variation of mean pore volume with increasing thresholding limit for PGA, Gilsocarbon, and PCEA was unexpected. In Gilsocarbon and PCEA, an increase in the thresholding limit resulted in a reduction in the mean pore area. However, increasing the limit for the PGA sample resulted in an increase in the mean pore area. With PGA graphite increasing the thresholding limit, new small pores were formed. However, this effect was reduced because the pores are more closely together in PGA than in Gilsocarbon and PCEA. Raising the threshold limit resulted in separate pore merging and a reduction in the number of pores, but an increase in their mean size. In Gilsocarbon and PCEA, the effect was reversed as the pores are much further apart; raising the thresholding limit resulted in new small pores without merging, thus, reducing the mean pore area. Figure 4.6 shows an example of the segmentation process.

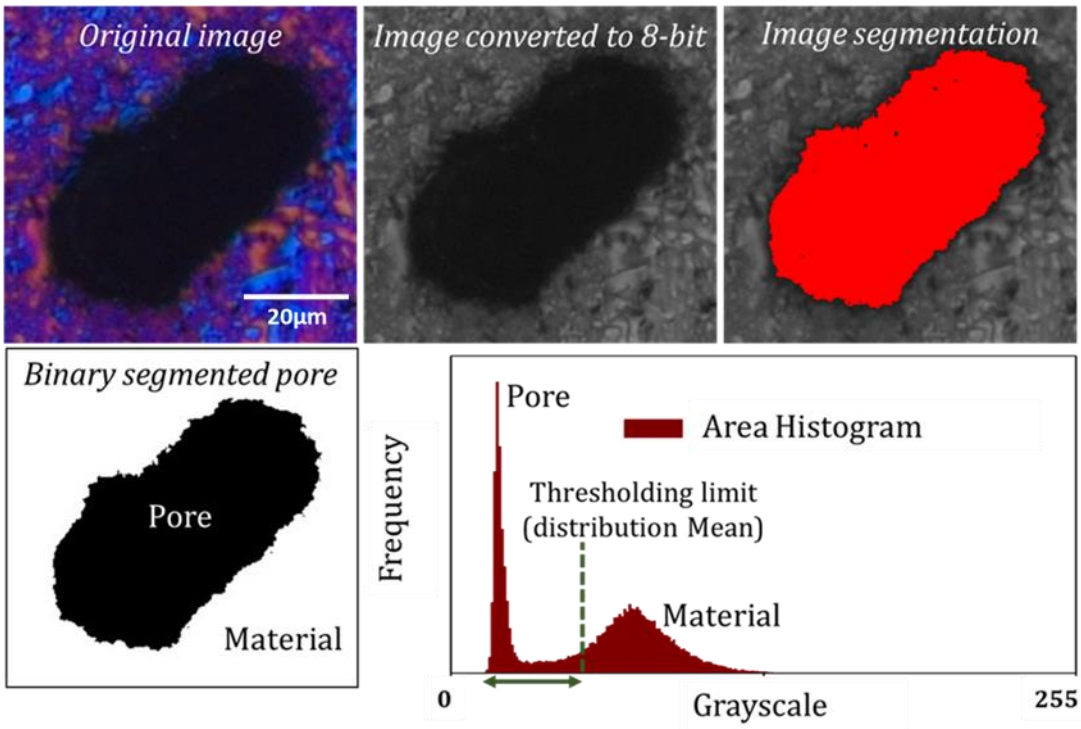

Figure 4.6: Simple example of a segmentation process for one pore, 'realistically' imaged. Image Resolution = 2.97 µm.voxel^{-1}.

Quantitative analyses were then conducted on each pore, once the images had been successfully segmented. Fiji enables this by providing various tools that make it possible to obtain numerical data from the images and quantify pore properties. In this Thesis, image analysis was used to quantitatively determine the variation of pore structure, area, size, shape, and orientation within and between nuclear graphite grades.

So, the area of each pore and the size of the pore were calculated after the scale of the sample had been defined from the microscope. Although the smallest pore size identified was 3 µm^2, a cut-off size of 50 µm^2 was selected to represent a suitable compromise between (i) eliminating very small features to represent the pore structure and (ii) keeping data loss at a minimum. This only applied to image analysis of irradiated samples, while the chosen cut-off size for image analysis of virgin samples was 10 µm^2, due to a very good surface finish. This resulted in errors due to the thresholding and image resolution (pixel size). The best method for calculating errors on pixel size is an approximation of the shapes of the pores. An ellipse, having a definite shape, was fitted to each pore through the ellipse fitting function in Fiji, and the errors due to pore size were calculated. These errors were combined with errors due to the thresholding in quadrature

and to get the total error in the pore area. This was done for all nuclear graphite samples using the following equation (4.1):

$$\sigma_{area} = \pi \sqrt{\left(\frac{\sigma_a}{a}\right)^2 + \left(\frac{\sigma_b}{b}\right)^2} \quad (4.1)$$

Where σ_{area} is an error in the pore area, a is the semi-major axis length, and b is semi-minor axis length. At a magnification of 5x, each pixel has a diameter of 1.47 μm, so the error on a and b is double the pixel size, 2.94 μm.

The density was then measured using [pore count/total area]. Although pores smaller than these cut-off values for both virgin and irradiated samples were excluded from further study, the smallest pore size values were reported in chapter 5 to show the differences between samples.

Pore eccentricity is a determinant of how much something 'moves away' from circularity on a scale of 0 to 1. Eccentricities were calculated by fitting ellipses (automatically by Fiji) to individual threshold regions. The eccentricity was then calculated from the semi-major and semi-minor axes. The fitting process is not entirely accurate; hence, a check is needed. The perimeter of the actual pore was calculated and compared to that of the fitted ellipse calculated using Ramanujan's equation, following equation (4.2):

$$e = \sqrt{\frac{M^2 - m^2}{M}} \quad (4.2)$$

Where M is the major axis length and m is the minor axis length ($0 \leq e < 1$; e=0 is a circle and e=1 is a line). The ratio of the two perimeters were calculated with a perfect fitting ellipse giving a ratio of 1. The further the ratio deviated from this, the poorer the fit of the ellipse. A fit of between 0.75-1.25 was accepted with pores having poor fits eliminated.

Aspect ratio (AR) ($0 < AR \leq 1$) was another measure for the particle shape, which was also calculated to compare with the ellipse fitting, as not all pores' shapes are ellipsoidal. A high aspect ratio (AR) gives an indication for the elongation of the particle. It is the ratio of the minimum to the maximum Feret diameter (xF), using the following equation (4.3):

$$AR = \frac{xF_{min}}{xF_{max}} \tag{4.3}$$

Feret's Diameter is the averaged distance between any two points along the selection boundary. Additionally, FeretAngle (0-180 degrees) was varied between 80-95˚ for all measured samples, which was the angle between the Feret's diameter and a line parallel to the x-axis of the micrograph.

In order to measure domain and filler particles, images were calibrated then the particle size selected and measured manually using the 'analyse particles' tools. In this case, there was no need for image segmentation. The data for both porosity and filler particle size were analysed further using Excel and the error quantified by the standard deviation of the measurements.

4.1.4.1.4 Serial Sectioning

4.1.4.1.4.1 *Polarised-Light microscopy (PLM)*

When conducting the serial sectioning in PLM, a specific procedure was followed. First, graphite samples were mounted, grinded, and polished to obtain the first layer, following similar procedures discussed in section 4.1.2.1. The sample then was ready for observation under the microscope to acquire the first 2D image. Note that during this step, the alignment in the PLM had to be considered. Therefore, the first sample was divided into the following four directions: north, south, east, and west. This helped to select the area of interest. In the present work, all images were taken from the northeast (NE) direction, which represented porosity in both filler and binder regions. After the images were taken, a number of indents are marked and put into the resin adjacent to the required sample, as shown in Figure 4.7.

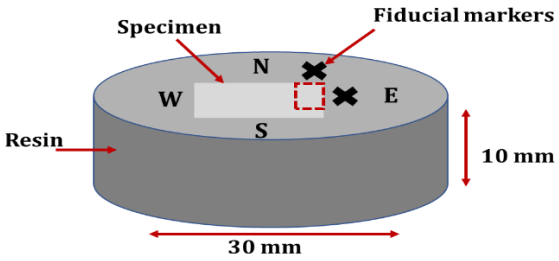

Figure 4.7: Schematic of the experimental set for serial sectioning alignment process; N: North, S: South, W: West, and E: East. Red square dots show the area selected to study porosity in 3-D. Cross marks represent regions of indenters.

These indents are used as fiducial markers as the process of polishing down the samples continued. This step was essential as it helped in aligning the images with the centre of the indents. It is also the means of knowing how far down the samples have been polished from the indent diameter or area. To achieve this, A Vickers hardness tester was used to add a number of indents using a Wilson hardness tester TUKON 1202 with a diamond indenter. These indents took the shape of an upside-down pyramid with a square base and an angle of 136° between opposite faces. This sample was subjected to a test force of 1kg applied (this force was chosen to make it easy to identify fiducial markers after each slice) for 10 seconds, see Figure 4.8.

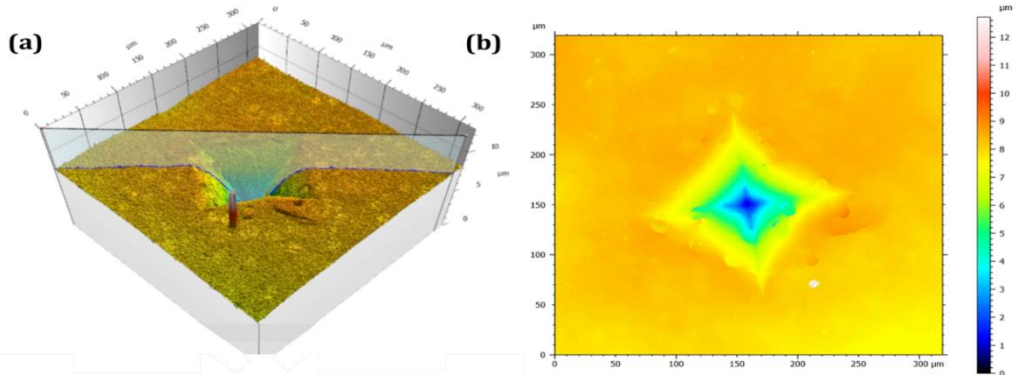

Figure 4.8: Shows a 3D view of (a) an indentation in the resin that was used as a fiducial marker; (b) shows the depth of the indentation.

The two diagonals of each indentation remaining in the resin were then measured using the PLM. Their average was calculated after imaging each slice

under a microscope. The depth of the indentation was determined using the following Equation (4.4):

$$h = \frac{d}{2\sqrt{2}\ \tan\frac{\theta}{2}} \tag{4.4}$$

Where h is the indentation's depth, d is the diameter of the indentation and θ is the Vickers angle (136°). For example, a diameter of 162.1 μm implied a depth of 23.2 μm.

To prepare the second slice, the samples were returned to the automated polisher (EcoMet/AutoMet 250 grinder polisher). At this stage, only the last step of polishing was applied because the aim was to polish down a few microns. The samples were polished using the micro cloth. They were then set in a master prep suspension for 4 minutes, using water only for the last 30 seconds. The samples were then rinsed in running water, gently wiped using cotton wool, sonicated in a bath of ethanol, and lastly dried using a dryer. The samples were then observed under an optical microscope. The new depth of the indentation was then calculated from the diameter of the indent. It was concluded that the difference of depth, in reference to the consecutive polishing steps was 1 micron. The process was repeated until 10 images were obtained. The diameter of each indentation was measured for each slice until an adequate number of slices were produced. Nevertheless, after a few slices, the fiducial markers disappeared and become difficult to distinguish. Therefore, new indentations were added, and the polishing time was set for 4 minutes to manage the depth of each slice.

4.1.4.1.4.2 *Focussed Ion Beam–Scanning Electron Microscopy (FIB-SEM)*

The dual-beam FIB-SEM instrument consists of a gallium ion beam mounted at 52° to the beam path of a conventional scanning electron microscope, as shown in Figure 4.9. The ion beam can be used to remove material from the volume of interest slice by slice at the microscale to the nanoscale in a controlled manner. After each slice, the freshly prepared surface is exposed to the electron beam for imaging. Software control scripts are then used to move the sample between the sectioning and imaging steps (Uchic, 2011). During milling, the stage tilt is kept constant at 52° so that the ion beam will be vertical to the smoothed surface.

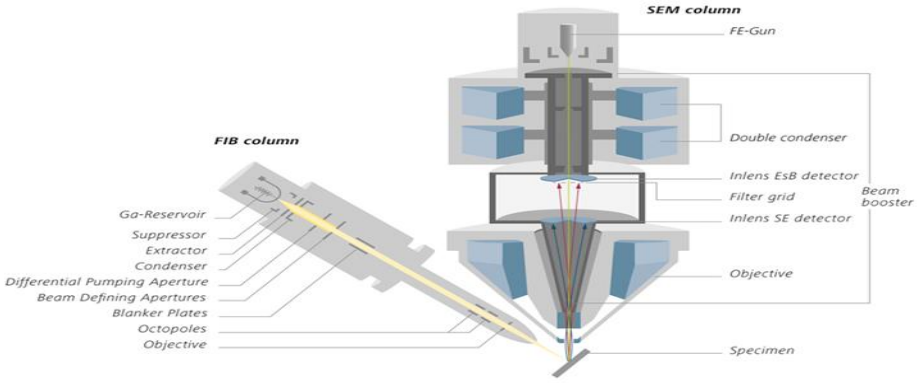

Figure 4.9: Schematic of the experimental setup for FIB-SEM experimentation (Uchic, 2011)

The slice thickness was controlled by the size of the structure, which needs to be reconstructed, as does the type of signal used for imaging. The signal depth ranges from SE ~5nm, BSE ~20nm to 100nm, and for EDS ~50nm to several µm. Figure 4.10 (a) demonstrates the schematic of the experimental setup for the slicing and viewing process, while Figure 4.10 (b)shows a cubic voxel SEM image prior to sectioning; this image was treated as pixels to obtain a 3D image. In Holzer et al. (2004), the authors suppose a so-called U-pattern, where the cross-sectioned surface area is exposed by three trenches; see Figure 4.10 (b). The surrounding trenches allow the electron beam to image the cross-sectional surface and to prevent sputtering and the re-deposition of material from obscuring the surface of interest. These experimental procedures require significant instrument time, depending on the size of the volume and the type of data that is examined (Zankel et al., 2014).

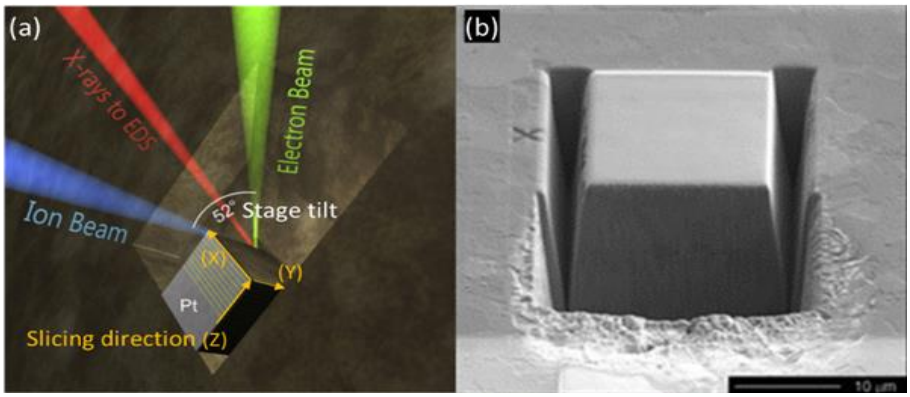

Figure 4.10: (a) Schematic of the experimental setup for serial sectioning; (b) SEM image of a sample volume prior to sectioning showing a fiducial mark reprinted from (Zankel et al., 2014).

Alignment

During serial milling, FIB alignment is required to ensure that the same surface area is imaged each time. A fiducial marker needs to be set, which then is recognised by the software to set the imaging parameters according to resolution, dwell time, and autofocussing. In FIB-SEM, cross-marking is used as a fiducial marker to ensure that all these parameters are controlled before the slicing and viewing begin, see Figure 4.10 (b) above.

Preparation of FIB-SEM samples

Similar specimens to those used for 2-Dimensional SEM analysis were also investigated using dual-beam FIB/SEM. Prior to observation, the samples were first mounted on standard SEM stubs and coated with a layer of carbon and iridium using an Agar brand high-resolution sputter coater of few hundreds of nanometres thickness. FIB-SEM was performed on FEI Helios G4CX DualBeam - High-resolution monochromated FEGSEM with precise Focused Ion Beam (FIB).

Experimental procedure

Before beginning the slicing and viewing process, a volume of interest was separated in each sample, the FIB was positioned perpendicular to the block surface. On top of this volume, a layer of platinum of ~1–2µm thickness was deposited by an ion beam deposition using a gas injection system (GIS). This layer helps to protect the area of interest and prevents rounding of the top edges of the cross-section during milling. The SEM column was positioned at an angle of 54° to the FIB column; the distal face of the selected area (trench) was imaged with the SEM after each milling cycle. A rectangular area of 22.3 µm (width) x 23.1 µm (height) was then milled to a depth of 73.00 µm for PCEA (Figure 4.11), and 40.4 µm (width) x 23.4 µm (height), which was then milled to a depth of 16.00 µm for PCIB. Both with a slice thickness of 100nm milled at 30 kV, 2.5 nA probe current and 300µs scan speed. Table 4.6 gives a summary of the conditions used for FIB-SEM experiments.

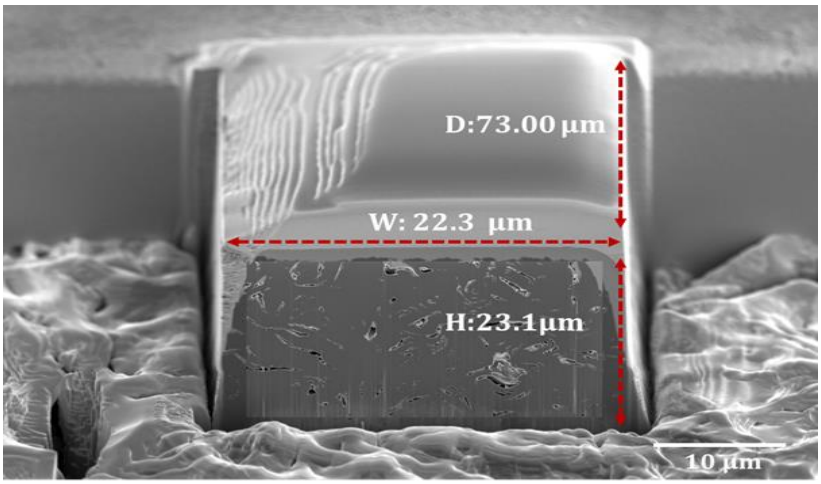

Figure 4.11: SEM image of PCEA sample volume prior to sectioning showing the selected area dimensions.

Table 4.6: Conditions used for FIB-SEM experiments.

Milling Parameters		**Imaging Parameters**	
Accelerating voltage	30kV	**Accelerating voltage**	2kV
Current	2.5nA	**Current**	0.8nA
slice thickness	100nm	**mode**	2
scan speed	300µs	**Detector**	TLD BSE
fiducial marker	~20 µm	**scan speed**	10µs
		line integrate	2x

The milling/imaging cycle was then set to remove 100 nm of material from the distal face of the trench. After removing each slice, the milling process was paused, and the freshly exposed surface was imaged with a 30-kV acceleration potential using the in-column energy selective backscattered electron detector. This helps to minimise any obstacles between the surface and the EDS detector. In addition, these trenches reduce the slicing and viewing time and protect the surface from any problems caused by redeposition and shadowing effects from the surrounding area. The milling and imaging processes were sequentially repeated to acquire a long series of images by means of a fully automated procedure, outputting a stack of images that represented a three-dimensional image of the sample. The total number of serial sections per sample ranged from 160 to 730. Fiji software was used to stack and align the images before the area of interest was cropped and thresholded to produce the final image stack.

Using CASINO software, it has been found that at 10 kV, the beam penetrates about 50 nm into the sample surface and the Backscattered electrons are produced from about 20 nm depth. So, the accelerating voltage of the SEM leads to a slight undersampling.

4.1.4.2 X-ray diffraction (XRD)

X-ray diffraction (XRD) analysis is a comprehensive tool used for characterising, quantifying, and identifying the atomic structures of crystals by utilising the property of diffraction of incident x-ray beams by planes of atoms and molecules into specific directions. High-energy X-rays are produced in a synchrotron or more simply in a laboratory X-ray tube. Metals such as copper or molybdenum are used as targets and are bombarded by high energy focused electron beams in order to produce X-rays with energies between 8-14 keV and wavelengths between 0.8-1.54 Å (Oku and Ishihara, 2004).

Essentially, X-ray diffraction (XRD) involves the scattering of X-rays by parallel planes of atoms that have similar Miller indices, which is equivalent to reflection (without any change in phase) occurring at a certain angle. The result is the creation of intense peaks, which happens because of constructive interference that relates to interplanar distances. This is illustrated in Figure 4.12. This Figure is an exemplification of Bragg's law, which can be mathematically expressed as the following (Equation (4.5)):

Bragg's law:

$$n\lambda = 2d_{hkl} \sin\theta \qquad (4.5)$$

Where: λ represents the wavelength of the reflected beam; *n* is an integer corresponding to the diffraction order; *d* represents spacing between the *hkl* planes, corresponds to the Miller indices; *2θ* represents the beam scattering angle (the Bragg angle).

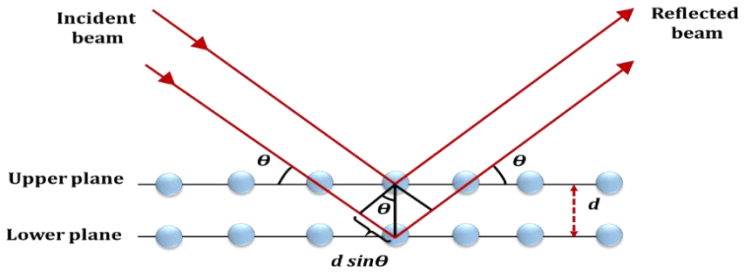

Figure 4.12: Diffraction on parallel crystalline planes separated by a distance d, explaining Bragg's law.

One particularly important function of XRD is that it can provide information regarding the coherence lengths of crystallites (indicative of the 'degree of order'), which can be obtained via Scherrer's equation by using the line broadening at a half-maximum intensity of the analysed XRD peak:

Scherrer's equation:

$$L = \frac{k\lambda}{\beta \cos\theta} \tag{4.6}$$

Where: L is the coherence length of crystallite, K is the shape factor, λ is the X-ray's wavelength, θ is the diffraction angle (Bragg angle), and β is the full-width half maximum of the peak intensity (FWHM) measured in radians. Many X-Ray diffractometers are semi-circle diffractometers, whereby the detector and X-ray tube move simultaneously, as illustrated in Figure 4.13 (a). In contrast, Figure 4.13 (b) shows an example of a calculated diffractogram obtained from hexagonal nuclear graphite. XRD also gives information about both of the unit cell and symmetry of materials.

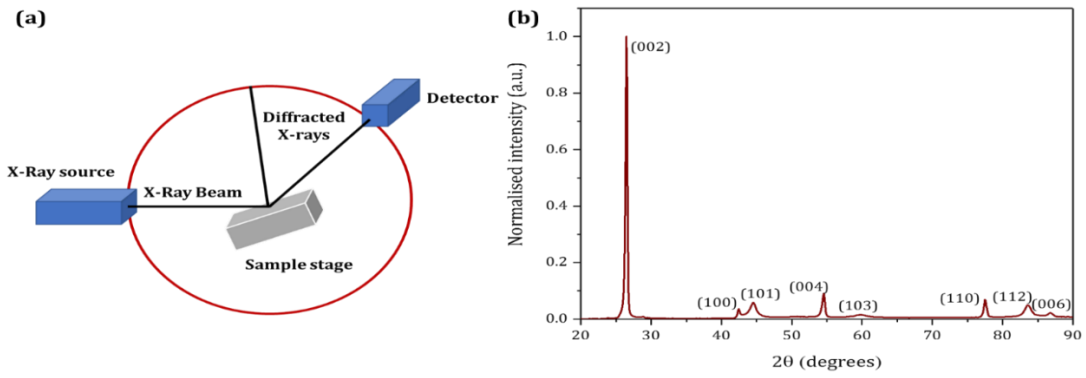

Figure 4.13: X-ray Diffractometer (a), calculated diffractogram from a hexagonal graphite powder (b).

4.1.4.2.1 XRD experimental details and data analysis

The XRD measurements in this project were obtained with a Philips Analytical X'pert MPD and a Brucker D8 diffractometers, which work in 2θ Bragg geometry (Figure 4.14 (a) and (b)). Samples were scanned from 20 to 90°, at an interval of 0.066° at 3 minutes/step using CuKα radiation (λ = 0.15406 nm) at room temperature. Samples were manually rotated by scanning each face of the cubic solid samples. This step was done to ensure that the same area of filler or binder was not collected.

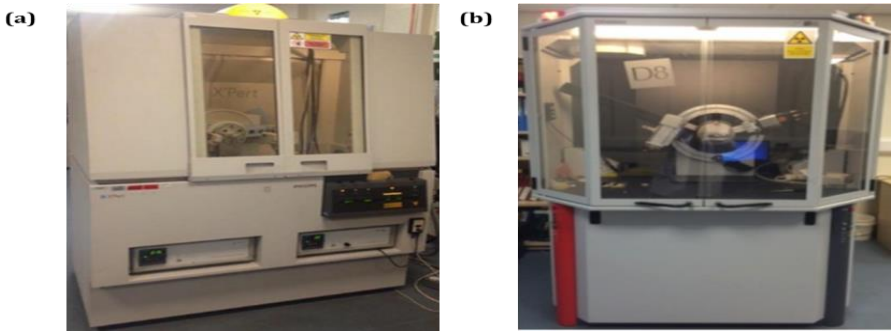

Figure 4.14: XRD machines used in this work: (a) Philips Analytical X'pert MPD diffractometer and (b) Bruker D8 X-ray diffractometer, University of Leeds.

To ensure that only the higher angle diffraction lines were used for subsequent peak analysis, the diffracted beam was measured using a parallel slit analyser and a K_β filter. Then as part of the analysis, the experimental diffraction profiles were modelled using a Pseudo-Voigt (pV) shape function in the software program X´pert High Score Plus. In accordance with the Rietveld refinement (Rietveld, 1969), the fitting involved a non-linear least-squares refinement of deconvoluted theoretical line profiles until they matched a measured diffraction line profile. The d-spacings, crystallite size, and micro-strain were then measured from the fitted peak parameters. All the diffraction peaks were assigned to the hexagonal phase with space group (P63/mmc), JCPDS file number 00-056-0159, and unit cell parameters a = b = 2.4617 Å and c = 6.7106 Å. For nuclear graphite, the lattice parameters for the c were obtained by (4.7):

$$c = 2d_{(002)} \tag{4.7}$$

While the correction factor was applied to obtain the a constant of $d_{(100)}$ and $d_{(110)}$, which can be calculated from (4.8) and (4.9):

$$d_{(100)} = \frac{\sqrt{3}}{2}\, a \tag{4.8}$$

$$d_{(110)} = \frac{a}{2} \tag{4.9}$$

The coherence lengths (crystallite size) in the a- and c-directions were calculated using the Scherrer equation as follows (4.10) and (4.11):

$$L_a = \frac{1.48\lambda}{\beta_a \cos\theta_a} \tag{4.10}$$

$$L_c = \frac{K_c\lambda}{\beta_c \cos\theta_c} \tag{4.11}$$

The shape factor, K, has a range of values depending upon several factors. To measure the crystallite size L_c from the (002), (004) and (006) peaks, a value of approximately 0.91 is recommended. For random layer structures where only 2D lattice reflections of the type (h k 0) are detected, a value of 1.84 was used to calculate the lattice planes of (100) and (110) for the a-direction, L_a. Nuclear graphite (Polycrystalline) lies somewhere between an oriented 3D and a completely random 2D structure (Chartier et al., 2018; Gallego et al., 2013; Krishna et al., 2017; Zheng et al., 2014). However, the value selected for K is not always stated in the literature.

For nuclear graphite, several previous studies have used the (002) peak to derive the L_c and (110) peak for L_a rather than (100), such as Nightingale (1962) and Simmons and Reynolds (1962). This is because the cross lattice (101) reflection overlaps with the (100) line on the large angle side of the latter, making it difficult to provide an accurate measurement to estimate the FWHM of the (100) peak. However, some research suggested that the (100) peak is more appropriate to calculate the lattice constant in carbonaceous materials (Delannay et al., 2014; Fang et al., 2012). Thus, in this work, the lattice dimensions in the a-direction were measured from both the (110) and (100) peaks. The instrumental broadening was measured from the line profile of a

standard silicon specimen (Figure 4.15), and each peak was corrected using the values shown in Figure 4.15 and estimated as (4.12):

$$\beta_{\text{corrected broadening}} = \sqrt{\beta^2_{\text{measured}} - \beta^2_{\text{Instrumental}}} \tag{4.12}$$

The peak widths increase as crystallite size decreases, and lattice strain increases. Where possible, the separation of size and strain broadening analysis was obtained using a Williamson and Hall plot (W-H) (Figure 4.15). In a W-H plot, the following equation (4.13) is used:

$$\beta \cos\theta = 4C_\varepsilon \sin\theta + \frac{K\lambda}{L} \tag{4.13}$$

Where β is the total broadening, C_ε is the strain, and L is the coherence length. βcosθ is plotted versus sinθ to obtain the strain from the slope ($4C_\varepsilon$) and the crystallite size from the intercept ($K\lambda/L$).

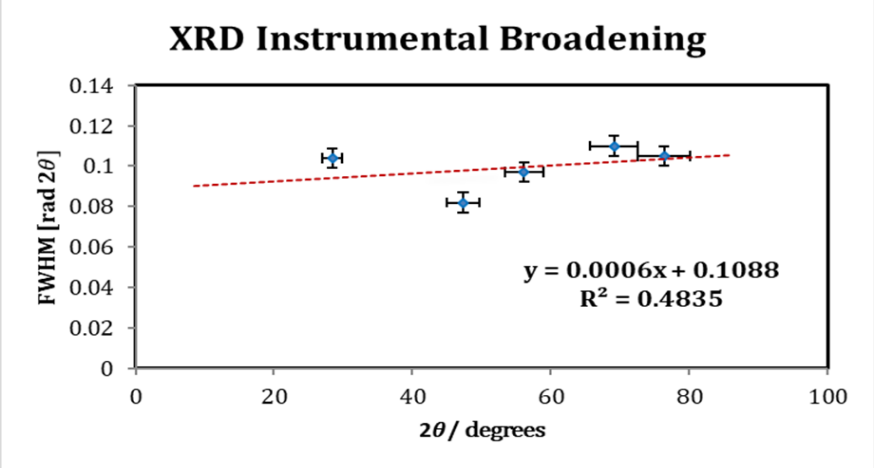

Figure 4.15: FWHM of the Silicon peaks obtained from the XRD pattern.

Figure 4.16 shows an example of a W-H plot of virgin nuclear graphite (Gilsocarbon). The average crystallite size calculated using the W-H plot was found to be larger compared to the calculated crystallite size using just Scherrer's equation, as shown later in this Thesis. The average microstrain was found to be around 0.01. Finally, for error estimation, the measurements were repeated a small number of times and the error quantified by the standard deviation of the measurements.

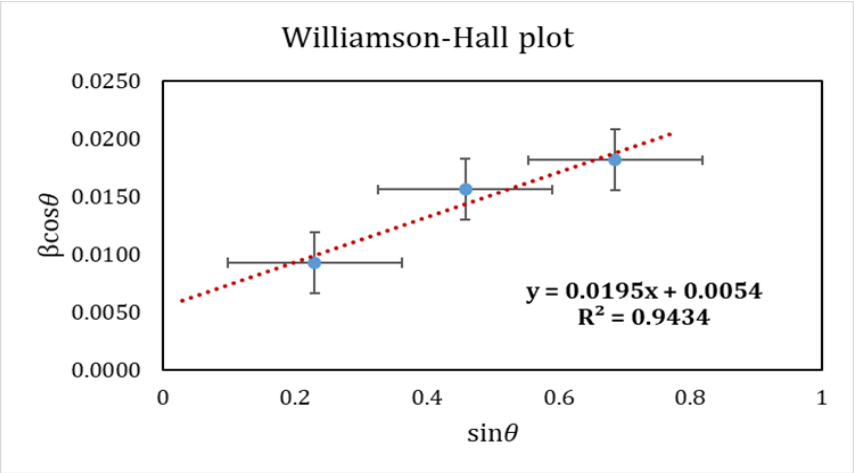

Figure 4.16: W-H plot of a virgin Gilsocarbon graphite sample collected.

4.1.4.3 Raman spectroscopy

The principle of this technique is to analyse different modes of excitation, including characteristic vibrational and rotational excitations of chemical bonds via the absorption and scattering of photons from a monochromatic laser. The photons that are scattered in the process assume various forms. The first form is Rayleigh scattering, whereby all scattered photons have the same energy as the incident photons. In the second form, the photons can take the form of Stokes and anti-Stokes scattering lines. Here, the photons are inelastically scattered, and they can have lower or higher energy compared to the incident photons (Mcdermott, 2012). The photons are conditioned by energy transfer between an illuminated system and an incident photon, which can be initiated in the ground or an excited state, as seen in Figure 4.17. The photons depend on the initial states of the analysed materials. Therefore, the proportion of Stokes transitions from the lower to the upper state will be greater than in anti-Stokes transitions, which is in the opposite direction. Correspondingly, anti-Stokes scattering is weaker than Stokes scattering.

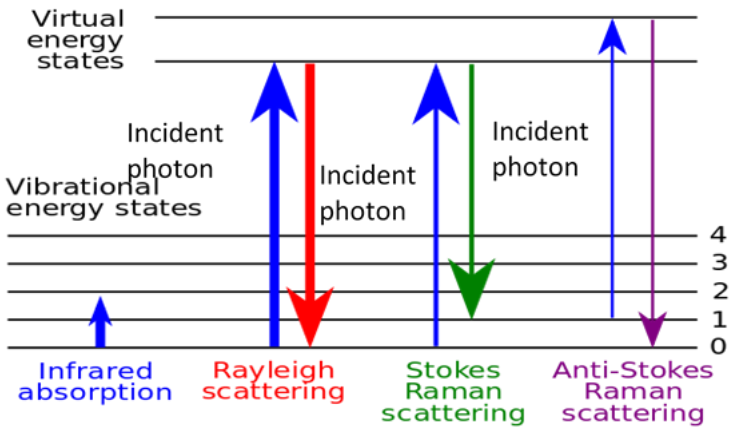

Figure 4.17: Raman scattering energy levels diagram. Taken from (Uskoković-Marković et al., 2013).

In operation, the Raman spectroscopy technique makes use of a laser beam for illuminating a sample. The laser can either emit light in the visible or near IR range and UV regions of the electromagnetic spectrum, producing inelastic sidebands on a very intense elastically scattered peak. The beam produced by the laser reaches a sample through a lens system of an optical microscope, and then the scattered beam bounces back through the same system. Finally, the filtered signal is quantified by high sensitivity, multichannel energy detector and transformed into a Raman spectrum.

Figure 4.18 shows the experimental set-up. The method has the advantage that it can be employed to analyse samples in bulk as well as in microscopic quantities over a wide range of physical states (gaseous, liquid, powder form, films, embedded layers, and others) as well as at different temperatures. IR spectroscopy can be used to analyse the asymmetric vibrations of polar groups, while its complementary Raman spectroscopy can be used to analyse the symmetric vibrations of non-polar groups (Larkin, 2011).

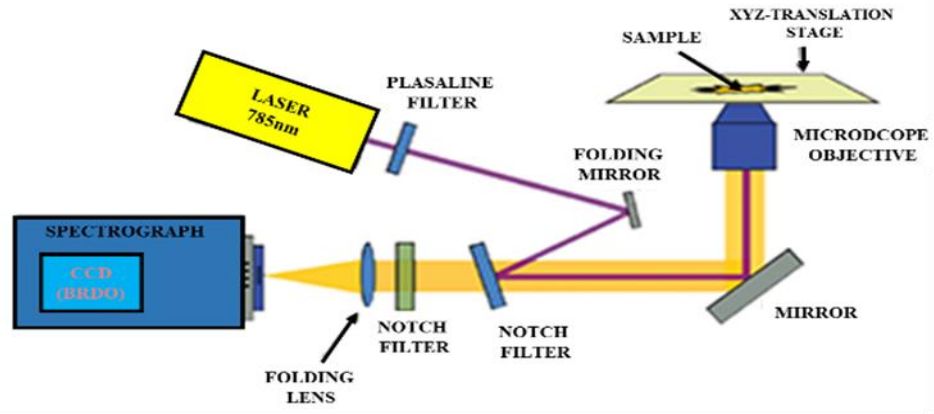

Figure 4.18: Schematic of Raman spectroscopy measurement set up. Source: (Andor, 2016).

4.1.4.3.1 Experimental details and data analysis

Virgin nuclear graphite samples were investigated at room temperature using a commercial Renishaw Raman Spectrometer equipped with a CCD detector and an optical microscope. The spectra were detected through using an Ar/Kr ion laser at a wavelength of 514.5nm and to focus the laser light onto the centre of the measured spot, and a 50x objective was used with a laser spot size of 10µm. The laser power was adjusted to 50%, and the spectral exposure time was 30sec with one spectrum per accumulation. The Raman spectra ranged from 1000 - 3200 cm^{-1}. The agreed procedure in the case of nuclear graphite was to use the Breit-Wigner-Fano (BWF) function to fit the G band and Lorentzian function for both the D and D′ bands (Ferrari and Robertson, 2000; Dillon et al., 1984), which was undertaken using Origin pro software, as shown in Figure 4.19. Highly ordered pyrolytic graphite (HOPG) was used as a reference to compare with the polycrystalline nuclear graphite. Finally, the crystallite size (L_a) was determined by using the following equation (4.14):

$$L_a\ (\mathrm{nm}) = (2.4 \times 10^{-10})\lambda_l^4 \left(\frac{I_D}{I_G}\right)^{-1} \qquad (4.14)$$

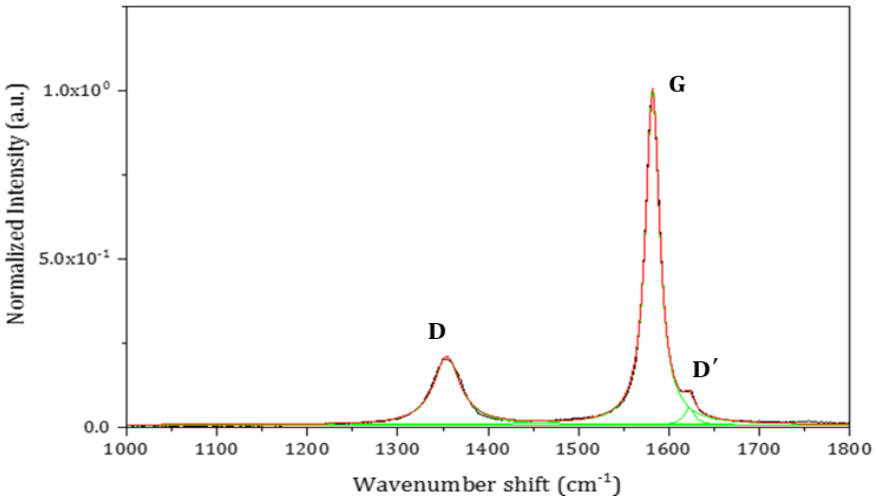

Figure 4.19: An example of the fitting procedures followed in this section to interpret Raman spectra; the green line represents the individual peak fitting, whereas the red line was a cumulative peak fitting when the fit converged.

4.2 Summary

This chapter summarised materials preparation and techniques that have been used, such as XRD, Raman spectroscopy, PLM, SEM, and FIB-SEM. XRD provided information regarding the integrity of the characteristic AB stacking sequence along with coherence lengths of crystallites (L_c and L_a) and the d-spacing of basal planes, whereas, Raman spectra was used to measure the changes in the FWHM of G peaks and the changes of I_D/I_G ratios before and after irradiation and the level of disorder within the lattice. PLM was used to distinguish between filler and binder particles and the shape and size of porosities of nuclear graphite. SEM was applied to examine the microstructure and types and distribution of micro-porosities, which were examined at a high resolution of the virgin graphite samples. This examination will also be performed on irradiated nuclear graphite for a better understanding of the damage evolution of the microstructure before and after neutron irradiation. Finally, PLM and FIB-SEM were used to acquire 3D data from 2D images, which were shown to be beneficial in studying the overall microstructure of nuclear graphite. The following three chapters of this Thesis (chapter 5, 6, and 7) are dedicated to the description and discussion of the results of the porosity and crystallinity of virgin and irradiated nuclear graphite.

Chapter 5

5.1 Microstructure and pore structure analysis of different types of virgin nuclear graphite

In this Thesis, the microstructure and pore structure analysis in both virgin graphite grades (PGA, Gilsocarbon, PCEA, and PCIB) and neutron-irradiated graphite grades (PCEA and PCIB) were examined using PLM and SEM techniques. This combined characterisation has never been applied to study both virgin and irradiated PCIB nuclear graphite grades (candidate grade for (V)HTRs). As discussed in chapter 3, only a few studies have applied the PLM technique to investigate the virgin graphite grades candidate for Generation-IV. For example, Kane et al. (2011) have applied the PLM technique to investigate the microstructure of virgin PCEA graphite quantitatively. Similarly, Mironov (2014) examined the grades using SEM. However, the latter was more of a qualitative analysis compared to the findings of this Thesis. Hence her results did not provide precise measurements of the filler particle, domain, and porosity.

As mentioned previously, the present Thesis uses quantitative analysis; hence, it provides precise measurements of the filler particle, domain, and porosity. The present chapter shows a great variation of filler shape and size, pore shape and size distribution between the grades of nuclear graphite. Such an in-depth quantitative analysis of the comparison between virgin and irradiated samples revealed that neutron irradiation causes significant damage to the structure of PCEA and PCIB nuclear graphites compared to virgin samples.

5.1.1 Polarised-Light microscopy (PLM)

5.1.1.1 Shape and size analyses of filler particles

The shape of the filler particles includes needle and spherical shapes, as shown in Figure 5.1. In general, the shape distribution of filler particles is affected significantly by the pitch source and the manufacturing methods used to prepare the graphite. PGA, petroleum-based graphite is relatively heterogeneous since

the filler particles are distributed within a matrix of coke flour and pitch binder. This material has mixed morphology, with many pores of different shapes and sizes. PGA tends to have needle-shaped filler particles with a mean length of 977±23 μm and an aspect ratio of 2.3±0.7. These elongated particles result from the highly aligned crystallites in the material, as confirmed by XRD patterns and reported in the literature (Hagos et al., 2010; Kane et al., 2011; Nightingale, 1962). The c-axes of the needle-shaped filler crystallites lie perpendicular to the direction in which the material was extruded. Conversely, Gilsocarbon tends to be more isotropic and spherical, with the average particle size in Gilsocarbon is 356± 21 μm with the circularity of ~0.85± 0.1. These results also agree with the literature (Jones et al., 2008; Marsden et al., 2008; Wen et al., 2008).

The filler particles observed in PCEA nuclear graphite, with petroleum-based coke, varied widely (Figure 5.1). Almost 60% of the particles were needle-shaped with an average length size of 565±12μm and an aspect ratio of 3.4±0.3, and the spherical particles had an average diameter of 322±20 μm with the circularity of ~0.75± 0.1. The needle-like particles in PCEA are slightly smaller than those in PGA. PCEA filler material had varying degrees of crystalline alignment, and these results are confirmed in the literature (Kane et al., 2011).

In contrast, from the PCIB micrographs (Figure 5.1), it was difficult to distinguish whether an area contained filler or binder particles due to the very fine microstructure (~20 μm, as reported in the literature (Freeman et al., 2017)). Table 5.1 shows a summary of the average size of filler particles calculated from virgin nuclear graphite samples. Filler particle size measured from 80 images for each virgin nuclear graphite grades (PGA, Gilsocarbon, and PCEA). Due to the difficulties in defining exact particle boundaries in some of the images, results for PGA, Gilsocarbon, and PCEA may vary from those reported in the literature (Table 2.1 (chapter 2 (section 2.1.3.1))).

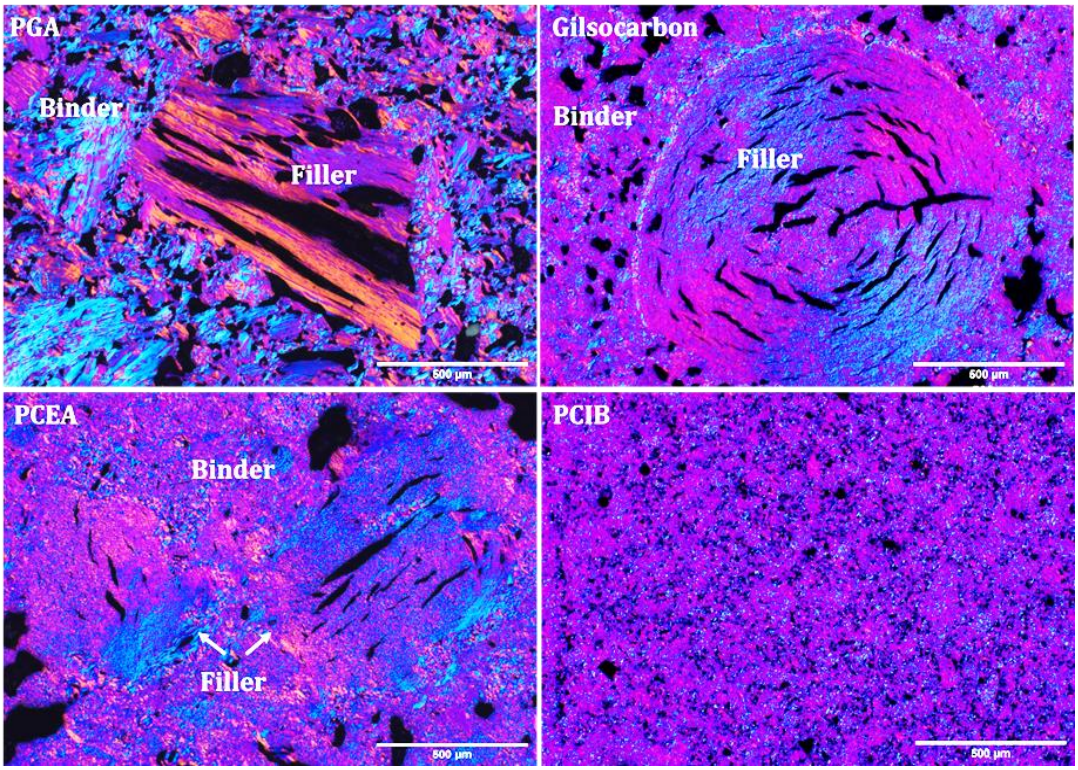

Figure 5.1: Optical micrographs of virgin nuclear graphites, showing both filler and binder phases in PGA, Gilsocarbon and PCEA graphites.

Table 5.1: Statistical summary of the average of filler particles size in three virgin nuclear graphite grades. Measurements collected from 80 images for each virgin.

Grade	Filler shape	Filler size (µm)	MaL (µm)
PGA	Needle-like	977±23 (L)	1136
Gilsocarbon	Spherical	356± 21(D)	1050
PCEA	Needle-like	565±12(L)	920
	Spherical	322±20(D)	772

*Major axis Length (MaL) is the maximum length size; L: Average length of needle particles; D: average diameter of spherical particles

Figure 5.1 also observed a series of colour changes (yellow, purple, blue and pink) when the sample was rotated 90° in plane-polarised light. These colours reflect different crystal and domain (mesocrystal) orientations with various shapes and sizes. Such colours appear in anisotropic samples (such as crystalline graphite) that have more than one refractive index, which allows for different degrees of light absorption when the crystal is oriented differently. The isochromatic regions (those of a single colour), indicate the optical texture that forms within graphitic carbon made from pitch-type precursors. This formation

depends on the growth of the liquid-crystal phase, also referred to as the mesophase. The analysis and description of this optical texture can be used to assess the microstructure of nuclear graphite. The isochromatic regions range in size from <0.1 μm to 500 μm. This range can be divided into two parts. First, 'mosaics' of size <0.1– 5 μm were observed around the edge of filler particles in Gilsocarbon and PCEA and were aligned to neighbouring filler particles, as seen in Figure 5.2, 5.3 and 5.4. Second, 'domains' of size <5– 500 μm were observed within the filler particles, and these had elongated structures. Separate domains have large angles of misorientation, while within domains, the corresponding crystallites are connected with low angles of misorientation.

Figures 5.2 to Figure 5.5 also present optical micrographs of Gilsocarbon graphite, PGA, and PCEA, which have domain textures of varying shape and size. The domains are larger within the coke filler particles than they are in the binder matrix, as they are in PGA, Gilsocarbon, and PCEA nuclear graphite. The round filler particles of Gilsocarbon have an oriented spherical shape with lamellae running around the boundary. This leads the domain texture to have a spherical shape that runs around the exterior regions of the filler particles with a preferred orientation, while the centre of the domains is more randomly oriented, forming a mosaic texture. The fine-mosaic texture was observed in the outer regions of the samples (Figure 5.2) with low angles of misorientation; therefore, most of the domains have a degree of preferred orientation. These regions in the binder are aligned with domains in the filler, as seen in graphite sheets in pitch-based carbon fibre (Roche et al., 1988). PGA graphite features larger domains within the coke filler particles, which often consist of a single large domain since the extrusion process forms needle-shaped filler particles with well-aligned crystallites (Figure 5.3). The elongated needle-coke filler particles of PGA nuclear graphite have parallel cracks, which indicate elongated domains in the direction perpendicular to the basal plane (Hagos et al., 2010). In PCEA (Figure 5.4 and 5.5), the domains appear to include varied shapes and sizes of spherical particles, and these domains are similar to those observed in Gilsocarbon graphite, but with less orderly orientations. In the elongated filler particles, the domains appear to be larger, as they are in PGA. The domain structure of PCIB is different because of its ultrafine microstructure, and it has a fine-mosaic structure with an average domain diameter of ~5 μm (Figure 5.6).

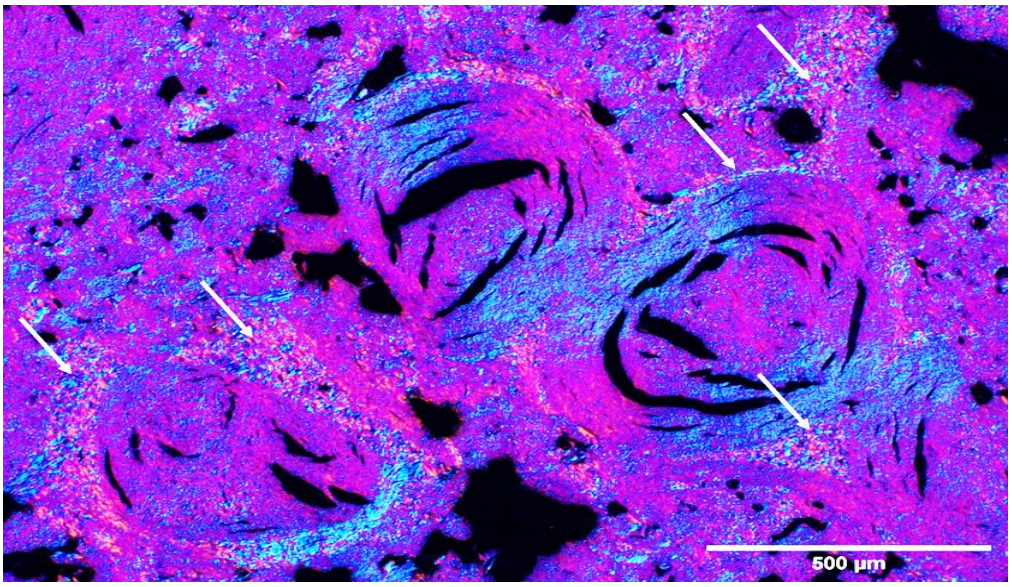

Figure 5.2: (a) Optical micrograph of virgin Gilsocarbon graphite, showing that there are numbers of mis-oriented domains within the more general preferred orientation of the domains (blue and pink colour represent domains within filler particles; white arrows highlight mosaic areas observed around filler particles.

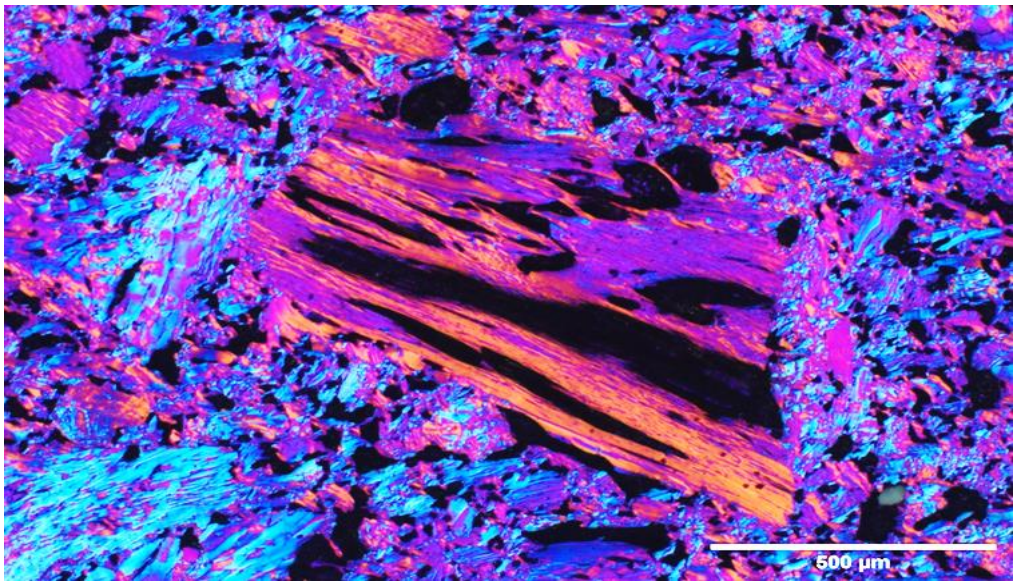

Figure 5.3: Optical micrograph of virgin PGA graphite, showing the needle-coke filler particles consist of elongated domains.

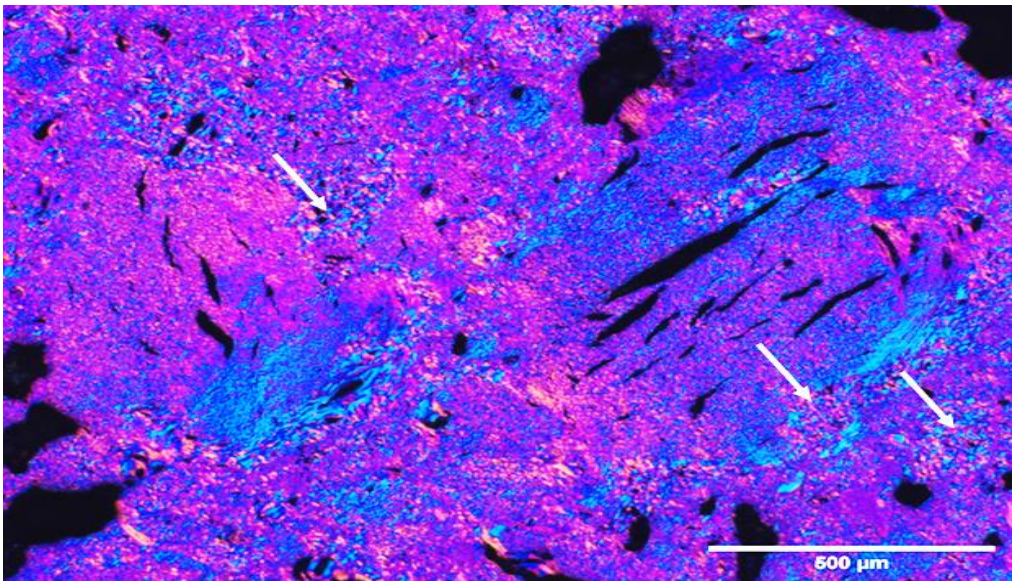

Figure 5.4: Optical micrographs of virgin PCEA graphite, showing white arrows highlight area of mosaic structure; the needle-coke filler particles consist of elongated domains which are twisted with respect to each other in the direction perpendicular to the plane similar to that observed in PGA.

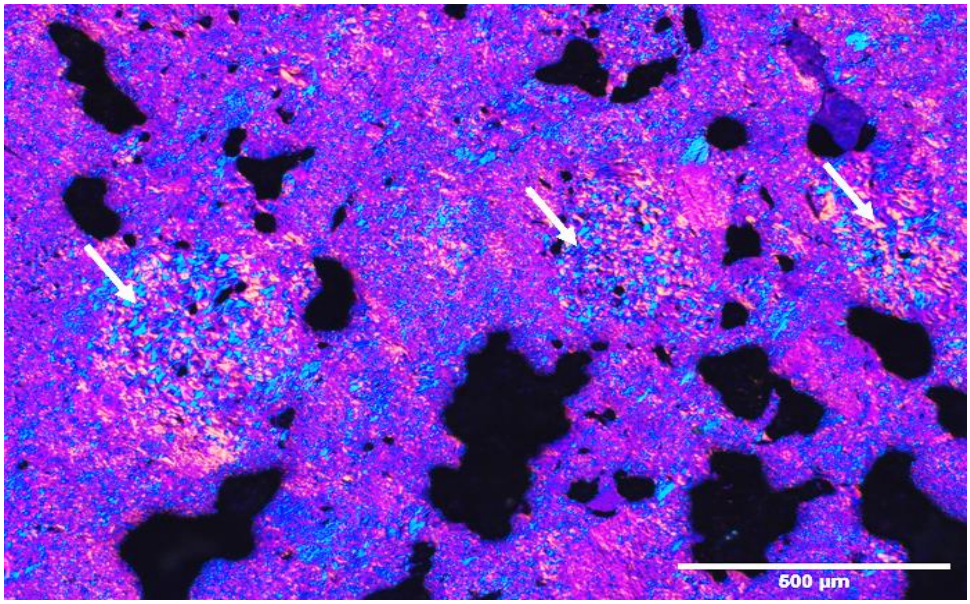

Figure 5.5: Optical micrographs of virgin PCEA graphite, showing white arrows highlight area of mosaic structure within the binder phase.

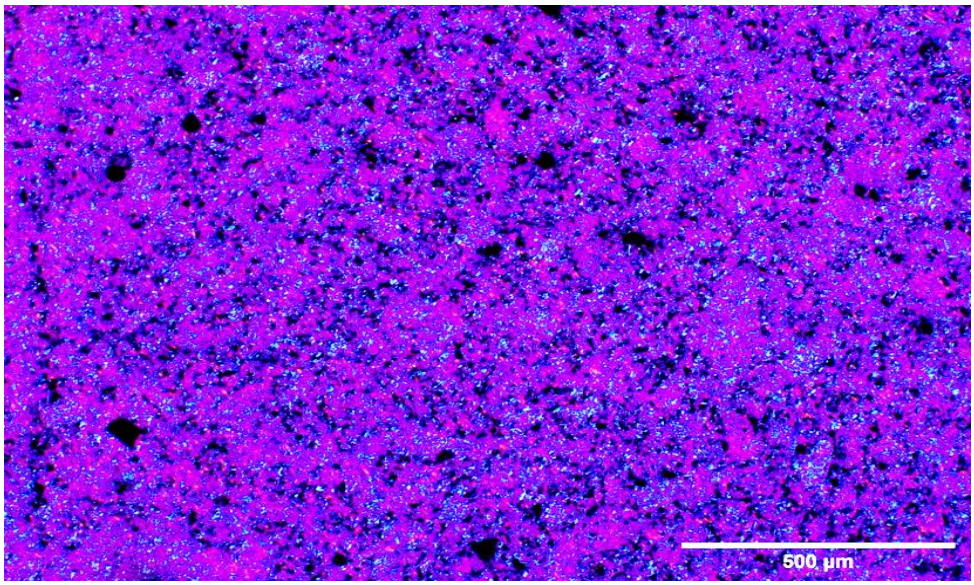

Figure 5.6: Optical micrograph of virgin PCIB graphite, showing the fine-mosaic structure.

5.1.1.2 Pore structure analysis

Figure 5.7 to Figure 5.10 show that each type of nuclear graphite has a characteristic pore structure due to differences in the manufacturing processes and precursor materials. Three major pore types have been observed in nuclear graphite: gas-evolution pores, shrinkage cracks, and micro-cracks (Jones et al., 2008; Kane et al., 2011; Nightingale, 1962). Gas-evolution pores and shrinkage cracks were observed using PLM, while micro-cracks were revealed using SEM and FIB-SEM. These figures illustrate the significant variation in pore shape, size, and distribution between the grades of nuclear graphite. Note that the pore shape and orientation can indicate whether the pores are within the filler particles or the binder matrix.

Furthermore, pores were more prevalent in the binder regions than they were in the filler particles in all graphite samples. Gas-evolution pores were particularly evident in the binder regions of PGA nuclear graphite (Figure 5.7 (a)). The removal of volatiles during the manufacturing process causes the formation of these pores, which are open and do not accommodate thermal expansion at low doses because of their relatively large dimensions. Instead, the accommodation of thermal expansion is associated with the c-direction of the crystal lattice and is attributed to the presence of cleavage micro-cracks that form during cooling after graphitisation.

Micrographs in Figure 5.7 (a) and (b) show pores of different shapes, sizes, and orientations in the binder and filler particles in PGA. Some crushed flour was also observed in the binder phase. Gas-evolution pores in Figure 5.7 (a) have an average area of 100 μm^2 to 700 μm^2. Some of these are spheroidal or of irregular shape. Long, thin acicular (crack-like) pores ~5 μm to 30 μm wide were also observed. Figure 5.7 (b) illustrates the longitudinal porosity within the filler particles in PGA, between ~200 μm to 944 μm in length.

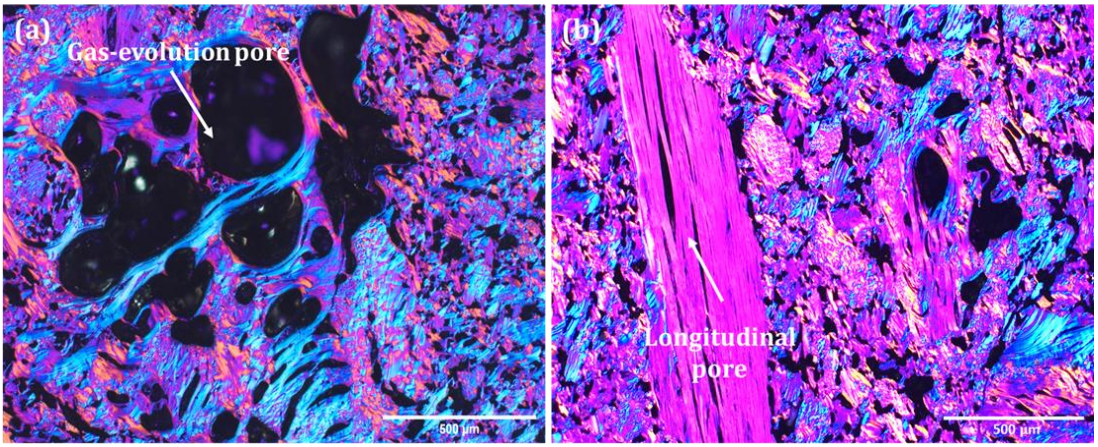

Figure 5.7: Optical micrographs of virgin PGA nuclear Graphite, showing the variation in porosity within binder (a) and filler (b) regions.

Figure 5.8 (a) shows the porosity of binder particles of Gilsocarbon graphite. As in PGA graphite, the pore shapes and sizes vary greatly, though the pore-size distribution differs slightly. Figure 5.8 (a) also illustrates macro-porosity both open (dark blue in open white circles), which is accessible to fluids (filled with resin during preparation for polishing), and the black regions, which are closed inaccessible pores. The average pore area in the binder region is between ~5 to 490 μm^2 in diameter, with pores of irregular shape. Conversely, the filler particles of Gilsocarbon graphite (Figure 5.8 (b)), showing macropores of maximum size ~449 μm^2 in diameter, exhibit crack-like pores arranged concentrically around a central pore with pore walls parallel to the basal planes of the graphite. The pores are surrounded by many layers of oriented graphitic sheets, highlighted in blue and purple in Figure 5.8 (b). In places, it does appear that these cracks have joined together to form a 2D network.

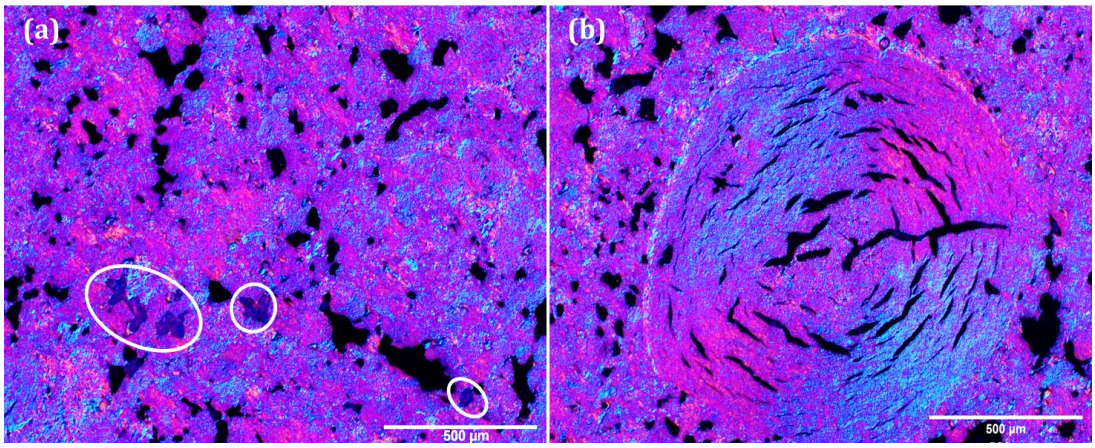

Figure 5.8: Optical micrographs of virgin Gilsocarbon nuclear Graphite, showing the variation in porosity within binder (a) and filler (c) regions.

Figure 5.9 (a) and (b) illustrate the porosity present in PCEA in both the binder and the filler particles. The statistical analysis suggests that the porosity is less than the porosity observed in PGA and Gilsocarbon. PCEA also exhibits pores of various shapes, including near-circular, elliptical, and acicular shapes, such as those observed in PGA and Gilsocarbon. The average pore sizes in binder regions of PCEA tend to be larger than those observed in PGA and Gilsocarbon samples, while the pores in the filler regions are relatively smaller, as summarised in Table 5.3. The average pore size is between 5 to 395 μm^2 in the filler regions and is between 5 to 462 μm^2 in binder regions. Conversely, the pore-size distribution PCIB graphite (Figure 5.10 (a) and (b)) exhibits a nearly uniform structure with pores of an average area of 25 μm^2.

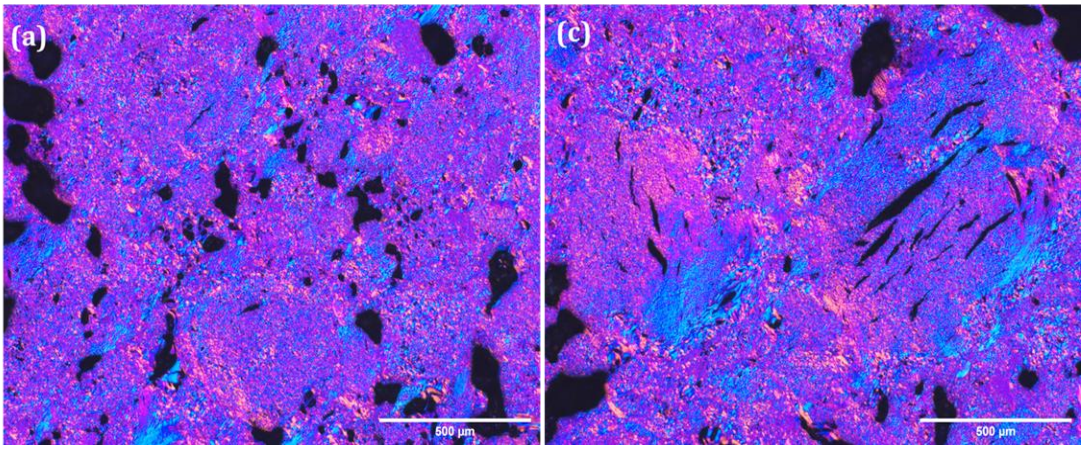

Figure 5.9: Optical micrographs of virgin PCEA nuclear Graphite, showing the variation in porosity within binder (a) and filler (b) regions.

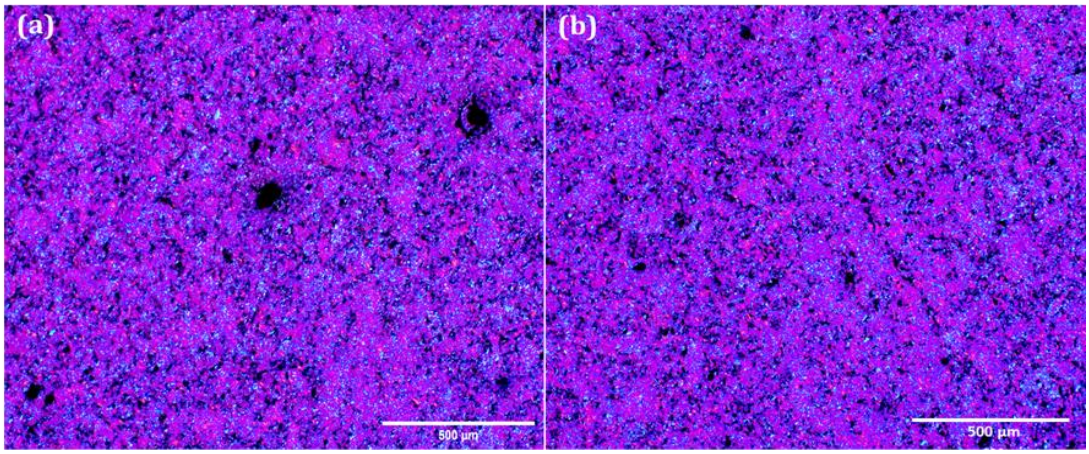

Figure 5.10: Optical micrographs of virgin PCIB nuclear graphite.

Table 5.2 gives a summary of the total average porosity in PGA, Gilsocarbon, PCEA, and PCIB, covering areas of approximately 10 cm^2 such area was sufficient to observe variation within a grade which measured from 80 images per sample. Table 5.3 is a summary of the porosity calculated for both filler and binder particles of PGA, Gilsocarbon, and PCEA virgin nuclear graphite. Figure 5.11 shows a visual comparison of pore size distribution between PGA, Gilsocarbon, PCEA, and PCIB nuclear graphite in both binder and filler regions. Compared to a normal distribution, the histograms are skewed greatly towards the minimum pore size, and a similar observation was recorded by Kane et al. (2011).

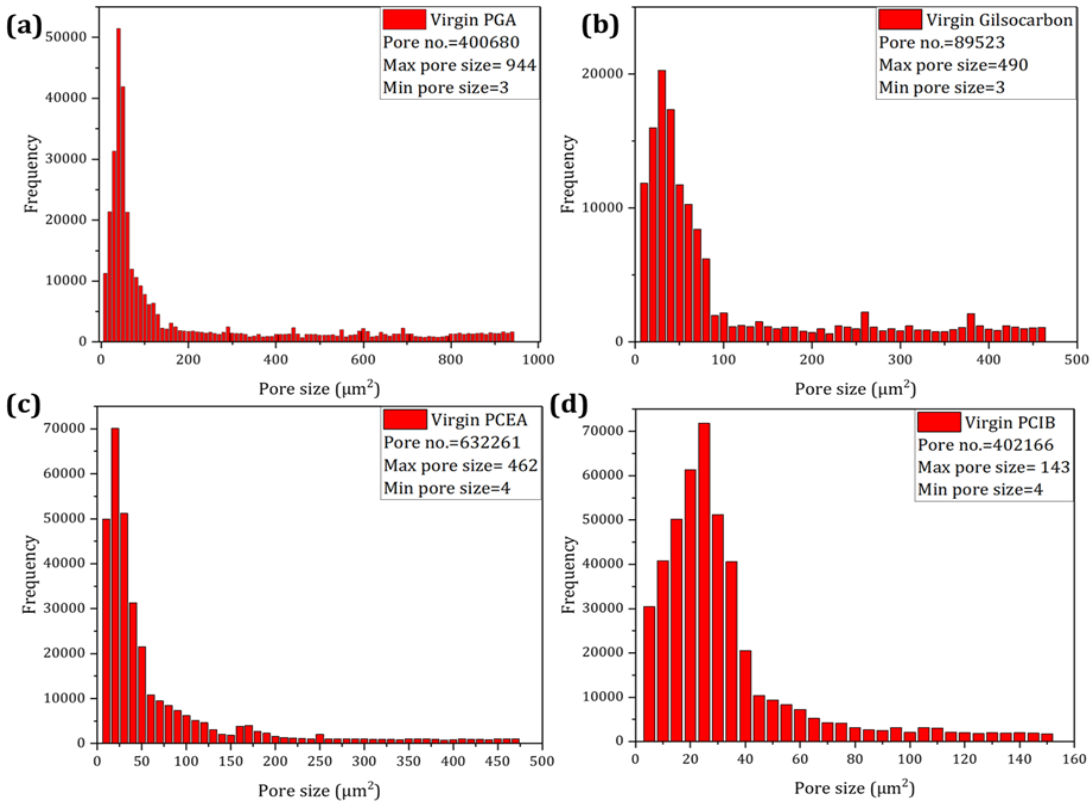

Figure 5.11: Histograms of the frequency of pore size distribution measured from 80 images for each virgin nuclear graphite grades.

Table 5.2 presents the results for the average pore size, eccentricity, and total porosity. The mean calculated the eccentricity of the pores varied between 0.81 to 0.84 for nuclear graphite grades, which shows they are of a relatively similar shape distribution. While, aspect ratio values were 1.81±0.1, 1.75±0.2, 1.66±0.2, 1.62±0.1 for PGA, Gilsocarbon, PCEA, and PCIB respectively. In comparison, the PGA samples had an average porosity of 20.3 %, which is higher than that of Gilsocarbon, PCEA, and PCIB graphite. The observed porosity within filler particles was higher in Gilsocarbon than in PGA or PCEA nuclear graphite (11.3%, 12.5%, and 9.5%, respectively). Meanwhile, the calculated porosities in PCIB graphite indicate a total porosity of ~15%. Therefore, this material is less porous than other grades according to this analysis.

Table 5.2: Statistical summary of calculated porosity within four grades of virgin nuclear graphite; σ represents standard deviation; Porosity percentage is the area fraction of the measured pores. Measurements collected from 80 images for each sample.

Grade	Pore size μm^2				Eccentricity		No. pores	Porosity %
	Average	σ	Max	Min	Average	σ		
PGA	47.4	20.4	998.5	3	0.84	0.12	400680	20.3±3
GILSO	68.4	31.3	490.3	3	0.82	0.12	89523	18.2±3
PCEA	50.4	18.8	461.5	4	0.81	0.12	632261	15.9±3
PCIB	25	6	143	4	0.84	0.12	402166	15.3±2

1-The areas imaged were randomly selected across samples.
2- Individual images were analysed from a set of images, and a standard deviation is quoted. This was the case for all measurements undertaken in this Thesis.

Table 5.3: Statistical summary of calculated porosity within both filler and binder area of PGA, Gilsocarbon, and PCEA virgin nuclear graphites. Porosity percentage is the area fraction of the measured pores. Measurements collected from 80 images for each sample.

Grade	Filler pore size μm^2			Porosity	Binder pore size μm^2			Porosity
	Average	Max	Min	%	Average	Max	Min	%
PGA	61.8±19	943.5	4	11.3	32.9±18	762.7	3	23.2
GILSO	83.4±69	449.1	4	12.5	53.3±13	490.3	3	19.4
PCEA	37.1±11	395.1	4	9.5	63.7±10	461.5	5	18.7

Table 5.4 summarises the bulk densities values for virgin nuclear graphites. This Table is a comparison made to show the relative accuracy of measurements via image analysis. Values for PGA, Gilsocarbon, and PCEA were more than those listed by the manufacturer and the errors relative to the manufacturer's value, which were 1.8%, 1.7%, and 4.5 %, respectively. While PCIB was less than the value reported by the manufacturer by 2.1%. These positive and negative errors may occur due to the choice of thresholding parameters. For instance, in PCIB nuclear graphite, size and proximity of the porosity affected the thresholding due to the size and connection of the pores, which lead to this negative error (for more information see chapter 4 (section 4.1.4.1.3)). Such error cannot be minimized, however, some of the literature reported density value for PCIB in the range of 1.75-1.85 g/cm^3 Another possibility is the manufacturer's values were derived from different methods

which lead to an underestimation and overestimation of the apparent (bulk) densities.

Table 5.4: Summary of Experimental, Manufacturer values for apparent (bulk) density compared with theoretical density.

Samples	Experimental (g/cm^3)	Manufacturer (g/cm^3)	Theoretical (g/cm^3)
PGA	1.771±0.02	1.74	2.265
Gilsocarbon	1.821±0.01	1.79	2.265
PCEA	1.892±0.01	1.81	2.265
PCIB	1.773±0.01	1.83	2.265

5.1.2 Scanning electron microscopy (SEM)

5.1.2.1 Pore size measurement of virgin graphite

The nuclear graphite samples were also observed via scanning electron microscopy (SEM). SEM was used to study the type, size and distribution of micropores with high resolution. This allowed examining pore sized from 100 nm to several hundred micrometres. These voids are micro-cracks that are lenticular in shape, running parallel to the graphite basal plane. Figure 5.12 (a) and (c) show micrographs of virgin PGA graphite, showing both filler and binder particles. Figure 5.12 (a) shows pores in the binder region of PGA graphite with an average size of 27.9 ±16 μm^2. The needle-like filler particles (Figure 5.12 (c)) have many long cracks with an average size of 15±22 μm^2. The pore distribution within the structure is heterogeneous. Thin cracks inside the pores in the binder are also observed and are between 1 μm to 10 μm long and 50 nm to 500 nm wide (Figure 5.13).

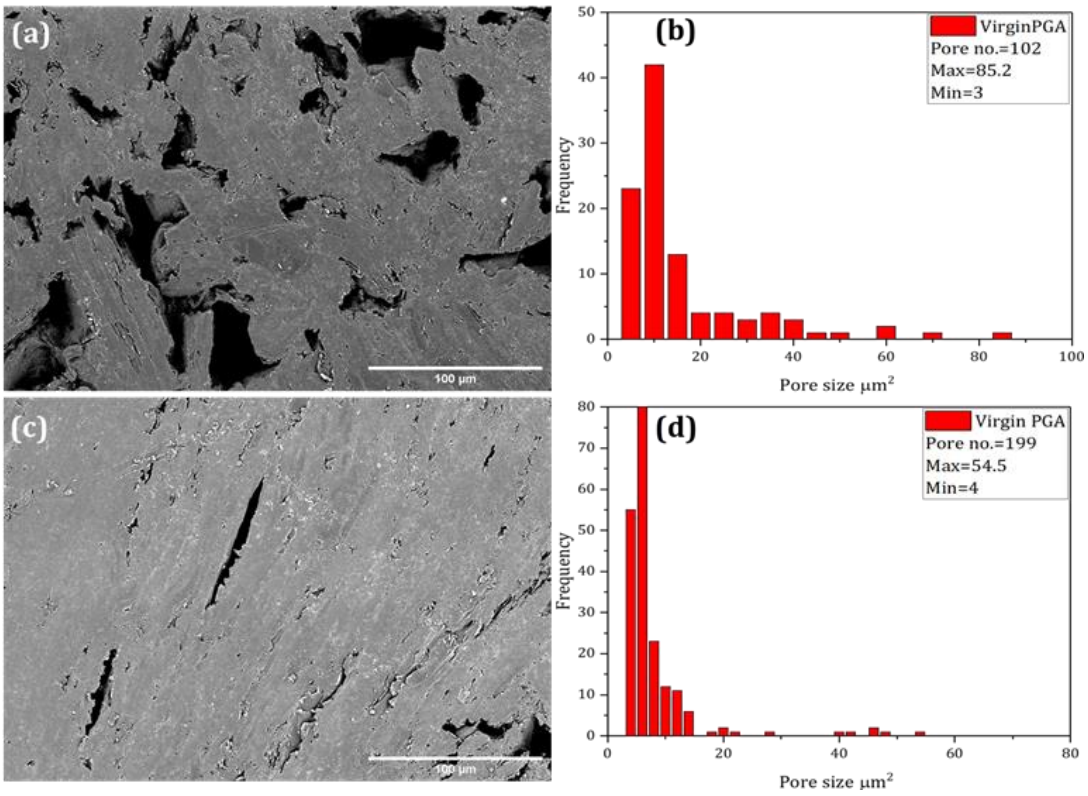

Figure 5.12: Secondary electron SEM micrographs of virgin PGA; (a) pores of various shape and size within binder phase; (c) crack-like pores within filler particle; (b) and (d) are histograms of pore size distribution measured from image (a) and(c) respectively.

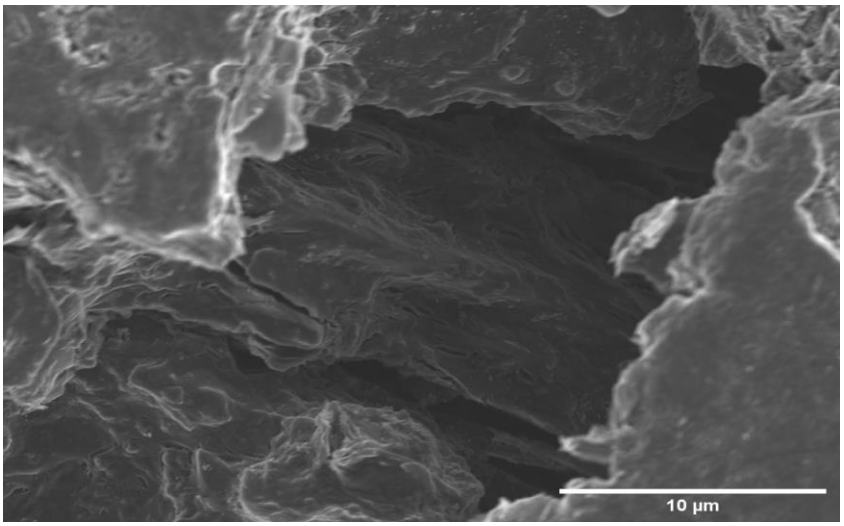

Figure 5.13: Secondary electron SEM micrographs of virgin PGA, showing crack-like pores inside larger pores in the binder phase.

Figure 5.14 (a) and (c) show SEM micrographs of virgin Gilsocarbon filler and binder regions, including several shapes of pores with different sizes. Figure 5.14 (a) shows pores in the binder with sizes from 25 µm to 150 µm. Figure 5.14

(c) shows a long crack in the filler, which was observed with PLM. The SEM images help to reveal the long, thin voids in the walls of the macropores that are 2-10 μm in length and 1-5 μm in width. Shrinkage cracks likely arise from the change in density of the material during cooling, and these cracks help to relieve internal stresses. The internal stress is generated by the interaction between the restraining effect of strong, inter-crystalline C-C bonds, and the anisotropic contraction of the crystal lattice. Also, gas evolves from the binder during heat treatment (such as those observed in PGA graphite), leaving large spherical macropores, after which shrinkage cracks are formed.

Figure 5.15 shows an example of long, thin cracks inside a pore in the binder between 500 nm to 35 μm in length and 100 nm to 5 μm wide. In addition, a pore 1 μm in length and 200 nm wide can be seen inside some of these thin pores. Several of these long narrow pores appear, and they may connect with other macros- and mesopores throughout the graphite body. Similar observation reported in (Hagos, 2013).

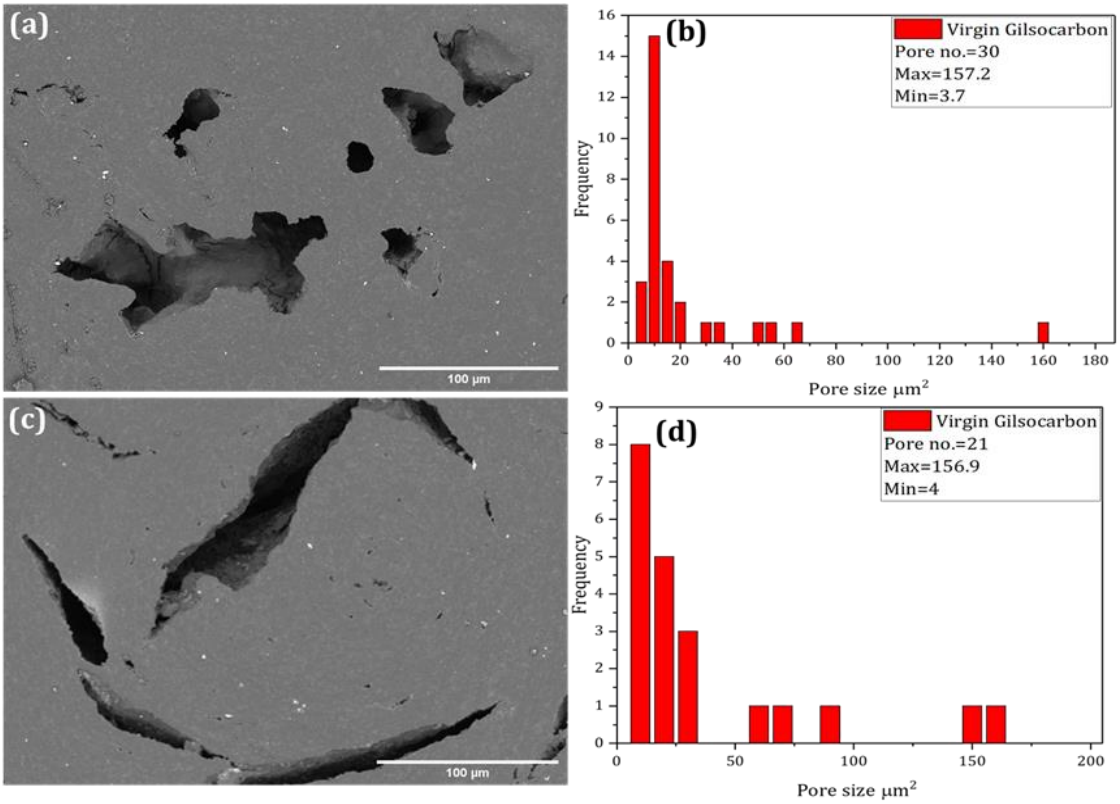

Figure 5.14: Secondary electron SEM micrographs of virgin Gilsocarbon; (a) pores within binder phase; (b) crack-like pores within a filler particle; (b) and (d) are histograms of pore size distribution measured from images (a) and(c) respectively.

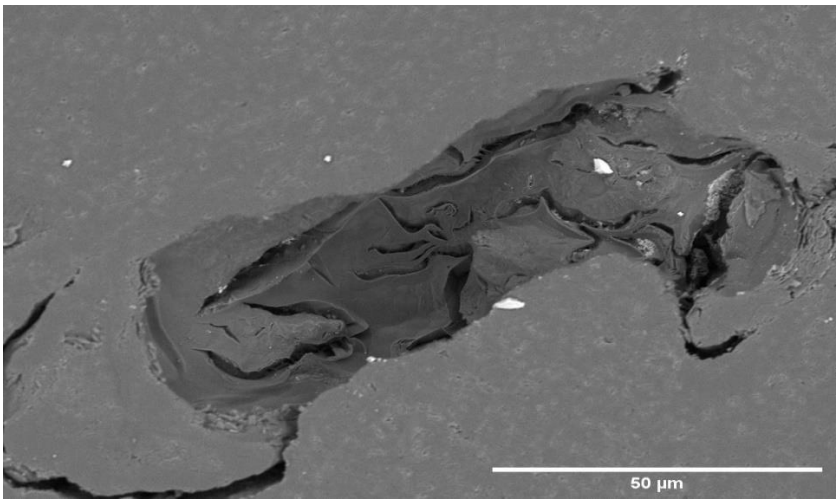

Figure 5.15: Secondary electron SEM micrographs of virgin Gilsocarbon, showing crack-like pores inside pores in the binder phase.

Figure 5.16 (a) shows an SEM image of virgin PCEA graphite, including voids in the binder that are both open and closed (some pores are partially closed) along with cracks inside the pores (Figure 5.17). These cracks are 300 nm to 22 µm in length and 100 nm to 3 µm in width, which they are more than the cracks in PGA and Gilsocarbon graphite (Figure 5.17). Figure 5.16 (b) shows long, thin cracks in the filler particles of a maximum are 96.7 ± 13 µm^2.

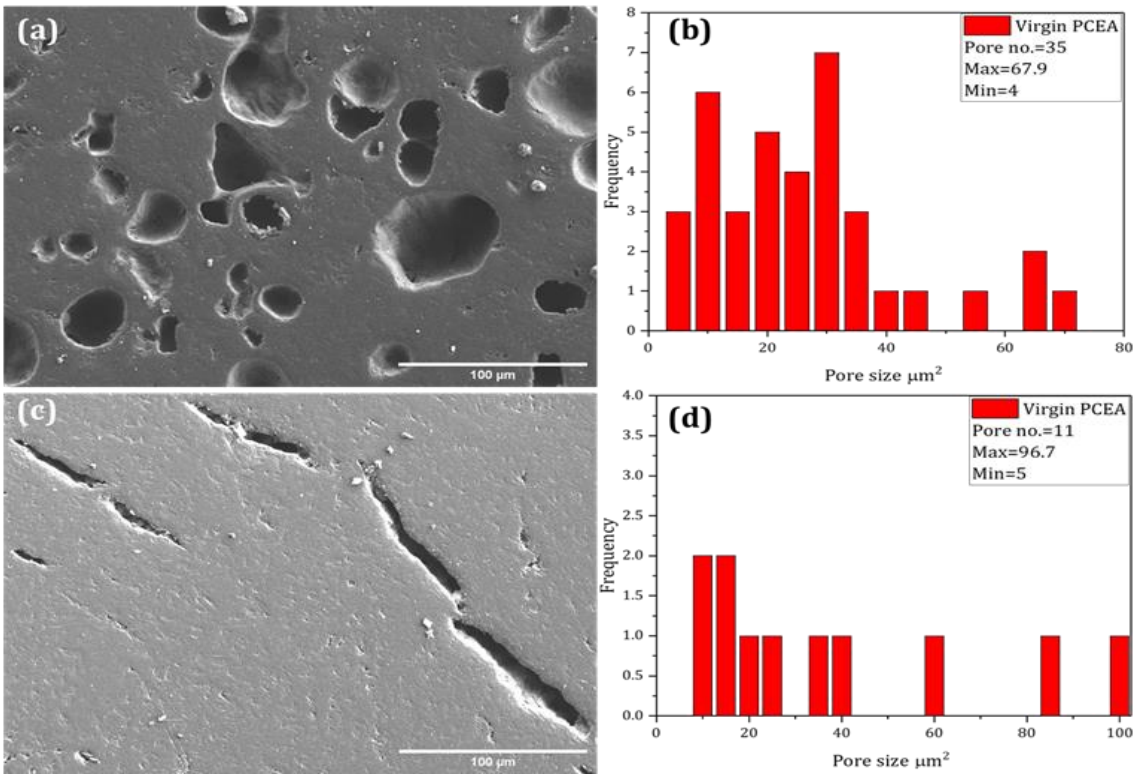

Figure 5.16: Secondary electron SEM micrographs of virgin PCEA; (a) showing pores of various shapes and sizes within the binder phase; (c) crack-like pores within a filler particle; (b) and (d) are histograms of pore size distributions measured from images (a) and(c) respectively.

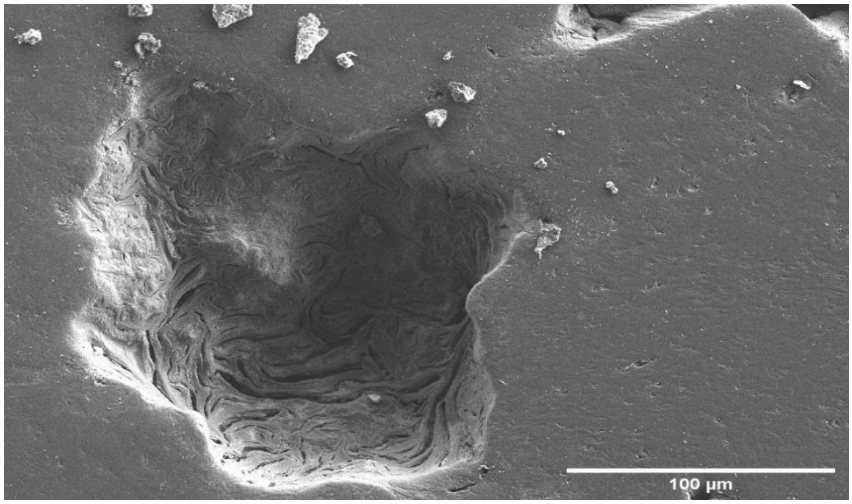

Figure 5.17: Secondary electron SEM micrographs of virgin PCEA, showing crack-like pores inside pores in the binder phase.

Figure 5.18 shows an SEM micrograph of virgin PCIB graphite, showing the 2D shape and size and the distribution of voids within the material. As in the PLM images, the fine microstructure of PCIB made it difficult to distinguish whether an area contained filler or binder particles. SEM allowed the measurement of pore sizes to be more precise; the pores were calculated to have an area between 1.5 µm^2 to 29.4 µm^2. Figure 5.19 shows an example of crack-like pores that were also observed in the inside wall of larger more-spherical pores; these were between 2 µm to 12 µm in length and 300 nm to 1 µm wide.

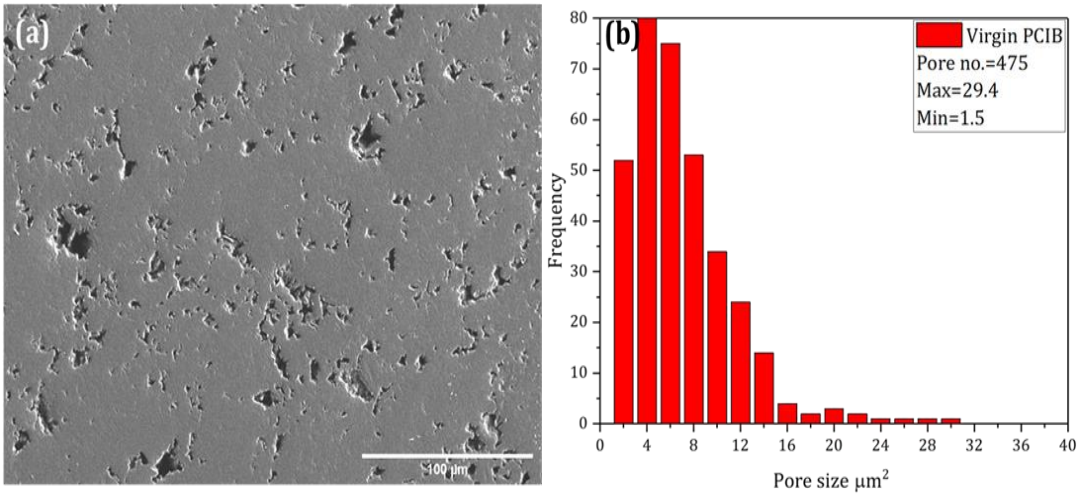

Figure 5.18: Secondary electron SEM micrographs of virgin PCIB; (a) showing different pores shapes and size; (b) is the histogram of the area of the measured pores.

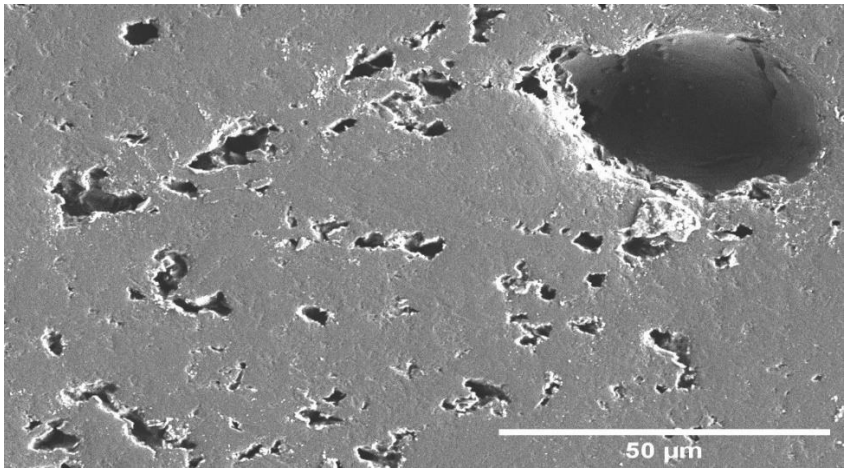

Figure 5.19: Secondary electron SEM micrographs of virgin PCIB, showing crack-like pores in the wall and of larger pores.

Figure 5.20 shows higher-magnification SEM images of PGA, Gilsocarbon, PCEA, and PCIB virgin graphite, which demonstrates thousands of folded graphitic sheets form the domains within the structure. The interconnected domains form a bent and twisted network.

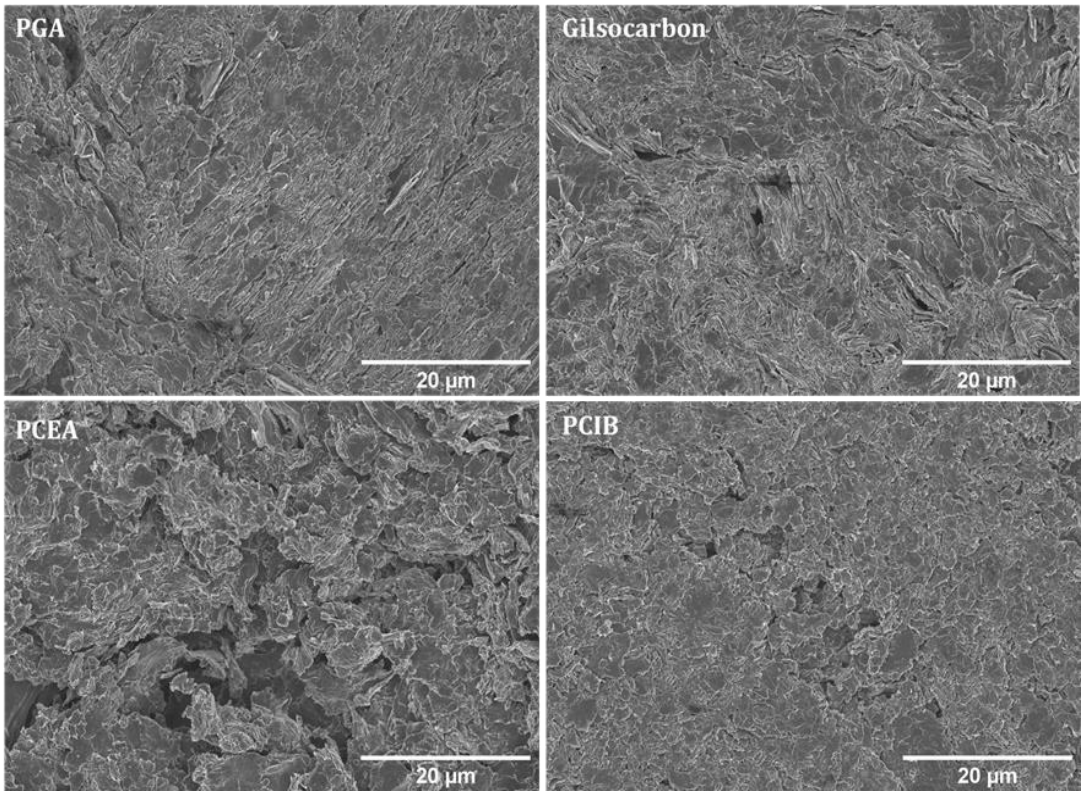

Figure 5.20: Secondary electron SEM images of virgin graphites, showing the structure of several thousands of folded graphitic sheets and the domains in Graphitic structures.

5.2 The effect of neutron irradiation on the microstructure of nuclear graphite

The changes in the topography and pore structure of nuclear graphite caused by neutron irradiation were also examined using PLM and SEM images. This section discusses and compares the structure of polished virgin and neutron-irradiation samples (PCEA and PCIB nuclear graphite, which are possible candidates for the next-generation nuclear reactors) with respect to their filler particle shape and size and porosity shape and size distribution. In comparing the virgin sample to the irradiated sample preparation process, the latter was restricted in working in the active materials. Hence there were not as many steps in the virgin sample preparation process.

As for the irradiated samples, there were prepared for PLM and SEM, by polishing the surfaces manually. The preparation was started by mounting the samples and then grounded to produce a flat surface, but this step possibly caused subsurface damage that was not removed in subsequent polishing steps. During the preparation procedure, it is important to check the samples after each step to ensure flatness, clean edges, and there are no artefacts, such as cracks and scratches on the surface, as it can be misinterpreted as microstructural features. The artifacts usually occur due to some external factors such as cross-contaminated cloths, improper cleaning of samples and sample holders between steps. Also, it can be due to the applied parameters such as pressure and insufficient time; hence, the finish of the sample surface was not ideal. Consequently, it was hard to ensure an ideal sample surface. Regardless of this, the samples analysed allowed for conclusions to be made.

5.2.1 PLM results

5.2.1.1 Shape and size analyses of filler particles

Figure 5.21 shows that irradiation causes significant damage to the structure of PCEA nuclear graphite compared to virgin samples. After irradiation, the graphite crystals fragmented and become smaller as the dose increases. In irradiated specimens, only the spherical filler particles remained easily observable. Because of the complexity in detecting the edges of filler particles, measurement of the sizes of spherical filler particles under lower dose/temperature conditions (1.5 dpa and 350 ˚C) was difficult. However, under higher dose/temperature conditions (6.8 dpa and 670 ˚C) the filler particles were found to have an average diameter of about 288 ± 18 μm, which is slightly smaller than the filler in the virgin material, and the filler particles became more elliptical rather than spherical in shape, as shown in Figure 5.21 (b). These changes could be caused by the closure of pre-existing micro-cracks, as these voids can accommodate thermal expansion in the c- direction. This may cause by the formation of interstitial and vacancy defects during neutron irradiation, which can accumulate as clusters. Table 5.5 shows a summary of the average of filler particle sizes calculated from virgin and irradiated PCEA samples. Due to the sub-optimal sample polishing of the irradiated samples studied here, it is difficult to draw any conclusions about the domain texture. However, to a first approximation, the domain texture of the coke filler and pitch binder at lower doses seem unchanged, when compared to the changes seen at higher doses and temperatures.

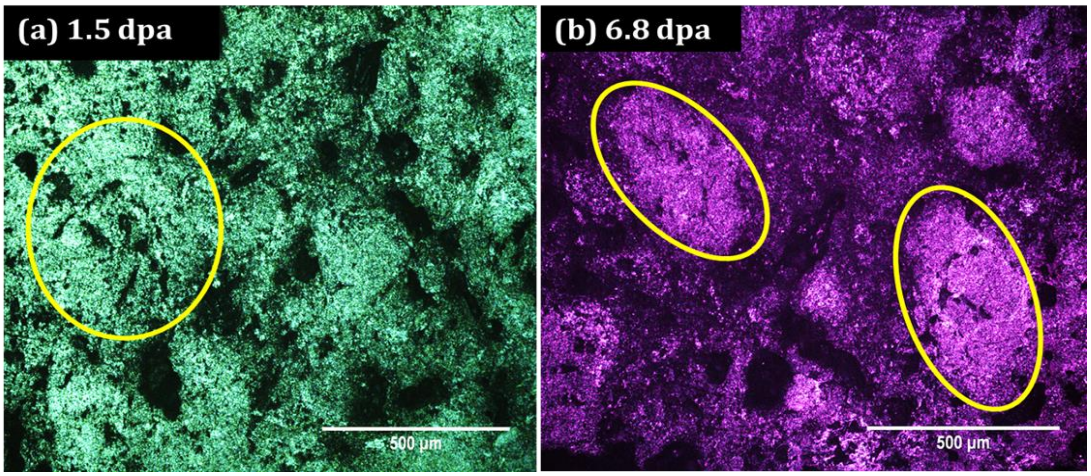

Figure 5.21: Optical micrograph of irradiated PCEA nuclear graphites, showing both filler and binder phase, yellow circles showing observed filler particles.

Table 5.5: Statistical summary of the average of spherical filler particle size in virgin and irradiated nuclear graphite grades. Measurements collected from 80 images for virgin PCEA samples and 10 images for irradiated samples are presented in this Table.

Grade	Dose dpa	Irr. Temp.˚C	Filler size (µm)	MaL (µm)
PCEA	NA	NA	322±20	722
	1.5	350	-**	-**
	6.8	670	288±18	371±13

*Major axis Length (MaL). ** there were no needle-like filler particles observed. Statistically could be around an average size of 300-500 µm.

5.2.1.2 Pore structure analysis

In both the filler and binder phases of PCEA and in the general microstructure of PCIB graphite irradiated to 1.5 dpa and 6.8 dpa respectively, there is no significant changes in the average size of voids were observed. However, there was a noticeable increase in the number of pores. Since the poor surface finish may have introduced additional porosity, the apparent increase in porosity in the irradiated materials should be interpreted cautiously. Furthermore, the limited size of image dataset (10 images per irradiated sample compared to 80 images per virgin sample) may have led to sampling problems such that the images are not representative of generalisable trends.

Table 5.6 gives a statistical summary of pore analysis for PCEA and PCIB grades both virgin and irradiated samples. At both lower and higher doses, the PCEA graphite specimen shows a general shrinking of the micro-cracks, especially within the filler particles. Here, new pores in the binder phase appear with different shapes and sizes; the average pore areas are 50.4 μm^2 ±19, 55.5 ±12 μm^2 and 49.5±16 μm^2 in virgin PCEA, PCEA dosed at 1.5 dpa and PCEA dosed at 6.8 dpa, respectively. The mean eccentricity of the pores was 0.81 for virgin PCEA, 0.59 for PCEA dosed at 1.5 dpa and 0.67 PCEA dosed at 6.8 dpa, corresponding to aspect ratios of 1.66±0.2, 1.11±0.1 and 1.23 ±0.1, respectively. The calculated porosities of the PCEA were found to have an overall porosity of

15.9% followed by PCEA (1.5dpa/350 ˚C) with 20.2% and PCEA (6.8 dpa/670 ˚C) with 22.5%. The calculated porosity for irradiated PCEA samples at 1.5 dpa compared to the theoretical porosity of PCEA nuclear graphite (~20%) was very close. At low dose and temperature, the errors relative to the theoretical porosity was 1% while for higher dose and temperature was 13%. Furthermore, in Figure 5.22; there some scratches in (a) and (b) on the surface after polishing, as it was difficult to remove the scratches completely. This is because the polishing process can introduce more damage to the surface and result in an overestimation of the final porosity.

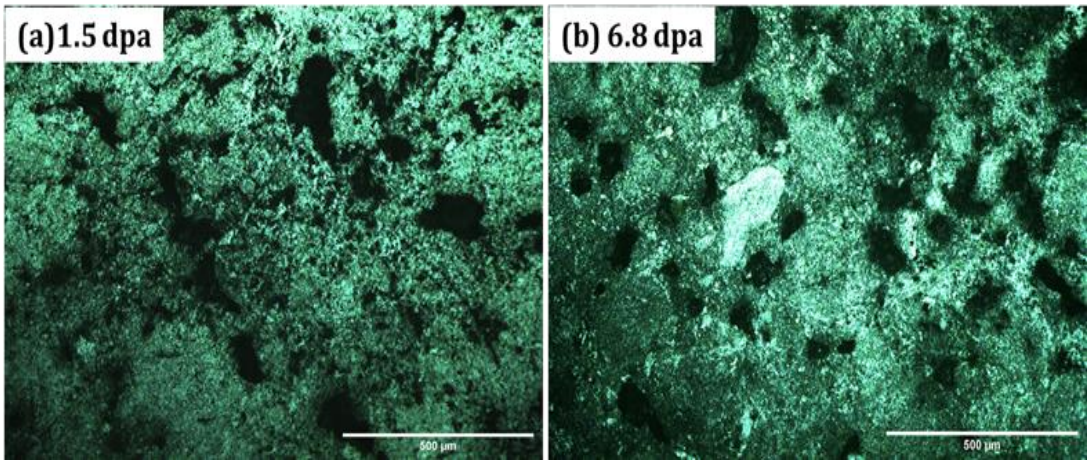

Figure 5.22: Optical micrographs of irradiated PCEA nuclear Graphite, showing the porosity within binder particles (a and b). (a) shows more damage to the surface due to the preparation process.

In Figure 5.23, optical micrographs of the irradiated PCIB samples demonstrate some changes to the surface of the samples compared to the virgin samples. Irradiated PCIB had a relatively inhomogeneous structure with some heavily porous regions, which were not seen in the virgin samples. These heavily poured regions of PCIB had a large average pore size in comparison to the other regions of the same PCIB sample. Examination also shows that the average pore size compared to the virgin samples were nearly the same for PCIB dosed at 1.5 dpa and PCIB dosed at 6.8 dpa.

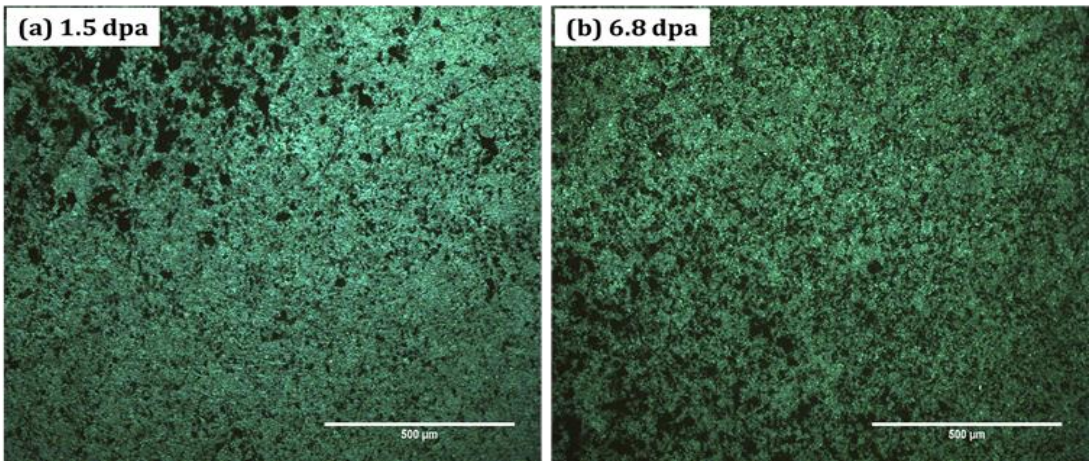

Figure 5.23: Optical micrographs of irradiated PCIB nuclear Graphite (a and b).

In Table 5.6, the mean eccentricity of the pores was 0.84 for virgin PCIB, 0.63 for PCIB dosed at 1.5 dpa and 0.61 PCIB dosed at 6.8 dpa, corresponding to aspect ratios of 1.62±0.1, 1.02±0.1 and 1.13±0.1 respectively. At the higher dose and temperature (6.8 dpa, 655 ˚C), statistical analysis indicated the total porosity was more than the lower dose; ~15% for virgin PCIB, ~20% for both PCIB dosed at 1.5 dpa and for PCIB dosed at 6.8 dpa, as summarised in Table 5.6. The calculated porosity of PCIB at lower and higher doses and temperatures agreed well with the theoretical porosity of PCIB nuclear graphite (~20%). Figure 5.24 illustrates a normal distribution of the total pore size measured from both binder and filler regions of PCEA nuclear graphite and general structure of PCIB nuclear graphite, both at lower and higher doses and temperatures.

Moreover, the calculated density of irradiated PCEA samples showed a slight reduction compared to the virgin value following neutron irradiation; 1.892±0.01 g/cm^3, 1.83±0.02 g/cm^3 and 1.81±0.02 g/cm^3 for virgin PCEA, PCEA dosed at 1.5 dpa and PCIB dosed at 6.8 dpa, respectively. Whereas, the density of irradiated PCIB samples was decreased from 1.773±0.01 g/cm^3 to 1.72±0.01 g/cm^3 for both PCIB samples irradiated at 1.5 and 6.8 dpa.

Table 5.6: Statistical summary of calculated porosity within four grades of irradiated nuclear graphite; σ represents standard deviation. Measurements collected from 80 images for each virgin samples and 10 images for each irradiated sample are presented.

Grade	Pore size µm^2				Eccentricity		AS	No. pores	Porosity %
	Average	σ	Max	Min	Average	σ			
PCEA virgin	50.4	19	461.5	5	0.81	0.12	1.66	632261	15.9±3
PCEA 1.5dpa, 350˚C	55.5	12	515.3	10	0.59	0.06	1.11	10954	20.2±2
PCEA 6.8dpa, 670˚C	49.5	16	487.2	10	0.67	0.04	1.23	16477	22.5±1
PCIB virgin	25	6	143	4	0.84	0.12	1.62	402166	15.3±2
PCIB 1.5dpa, 350˚C	32.6	9	137.7	10	0.63	0.04	1.02	10197	19.9±1
PCIB 6.8dpa, 655˚C	31.4	10	231.3	10	0.61	0.02	1.13	12115	20.3±1

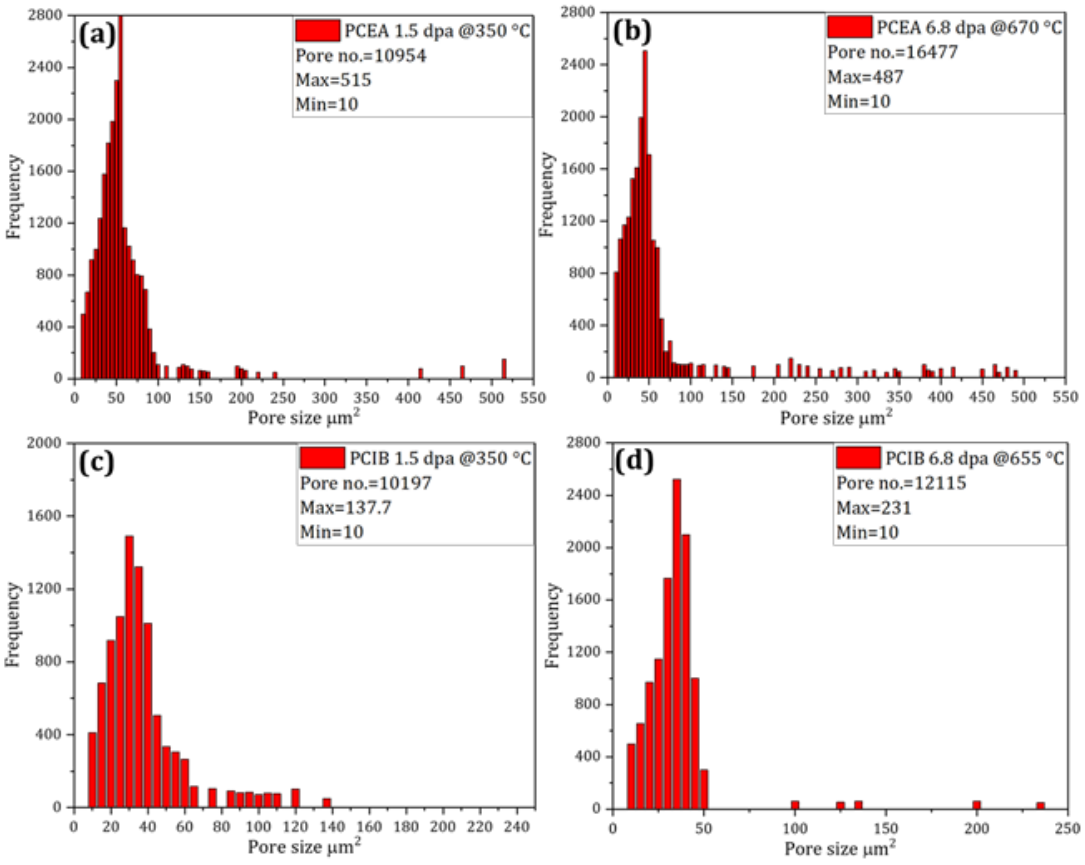

Figure 5.24: Histograms of the frequency of pore size distribution measured from 10 PLM images for each irradiated nuclear graphite grades.

To conclude, nuclear graphite has three main components; filler particles, binder phase, and porosity. Porosity is a significant component in ensuring the physical integrity of graphite components in the reactor. Porosity evaluation of nuclear graphite grades candidate for Generation-IV reactors is critical due to three reasons; (1) it can accommodate thermal expansion (Marsden et al., 2017; Zhou et al., 2017a), (2) absorbing dimensional changes caused by neutron irradiation (Fugallo et al., 2014), and (3) withstanding large internal crystallite strains without severely weakening the properties (Kelly, 1981).

The results here confirmed that neutron-irradiation induced damage to the structure of nuclear graphite. This was evident due to the crystal fragmentation and the formation of new pores. This is because the neutron irradiation graphite leads to the crystallites experiencing an expansion along c-axis, which is accommodated by the closing of large pores and contraction along a-axis (Kelly. 1981; Neighbour, 2000). This finding supported by the XRD measurements discussed later in chapter 7.

The contraction in the a-axis causes the overall bulk contractions of graphite artifacts, which increases in magnitude as the irradiation dose increases. The accommodation pores (Mrozowski cracks) are filled as a result of swelling on the c-axis leading to thermal expansion. The continuous expansion along the c-axis passes the a-axis shrinkage, resulting in a recovery of the previous shrinkage and even swelling beyond the initial volume, which is described by Telling and Heggie (2007) as the crystallites point of turnaround. However, the results of this Thesis do not show the point of turnaround.

With regards to the porosity, it is present in the graphite filler particles, in the binder matrix, and at the filler/binder interface. In line with Kane et al., (2011) and Hagos (2013), the volume percentage of the pores for both virgin and neutron-irradiated graphite, as well as their shape, size distribution, and orientation depend fundamentally on the raw materials used, the manufacturing process, and thermal history of each graphite billet.

5.2.2 SEM results

Figure 5.25 shows SEM micrographs from PCEA graphite samples dosed at 1.5 dpa. The microstructure of binder (Figure 5.25 (a)) and a filler particle (Figure

5.25 (c)). Figure 5.25 (a) shows that the binder region exhibits a wide range of shapes and a significant size distribution (the calculated average size from SEM is 65.4 ± 20μm^2), which was also observed in the virgin samples. Filler regions can be identified by both their high crystallinity and micro-cracks parallel to the basal planes. The average size of filler particles was identified by PLM. These micro-cracks are formed during the manufacturing process because of thermal contraction that induces the delamination of basal planes. As seen in Figure 5.25 (c), the micro-cracks are, on average, 5 μm to 180 μm in length and 100 nm to 10 μm in width. In addition, the SEM micrographs reveal open pores (~13%) and closed pores (~8 %) in both the filler and binder regions, which are difficult to distinguish in the PLM images.

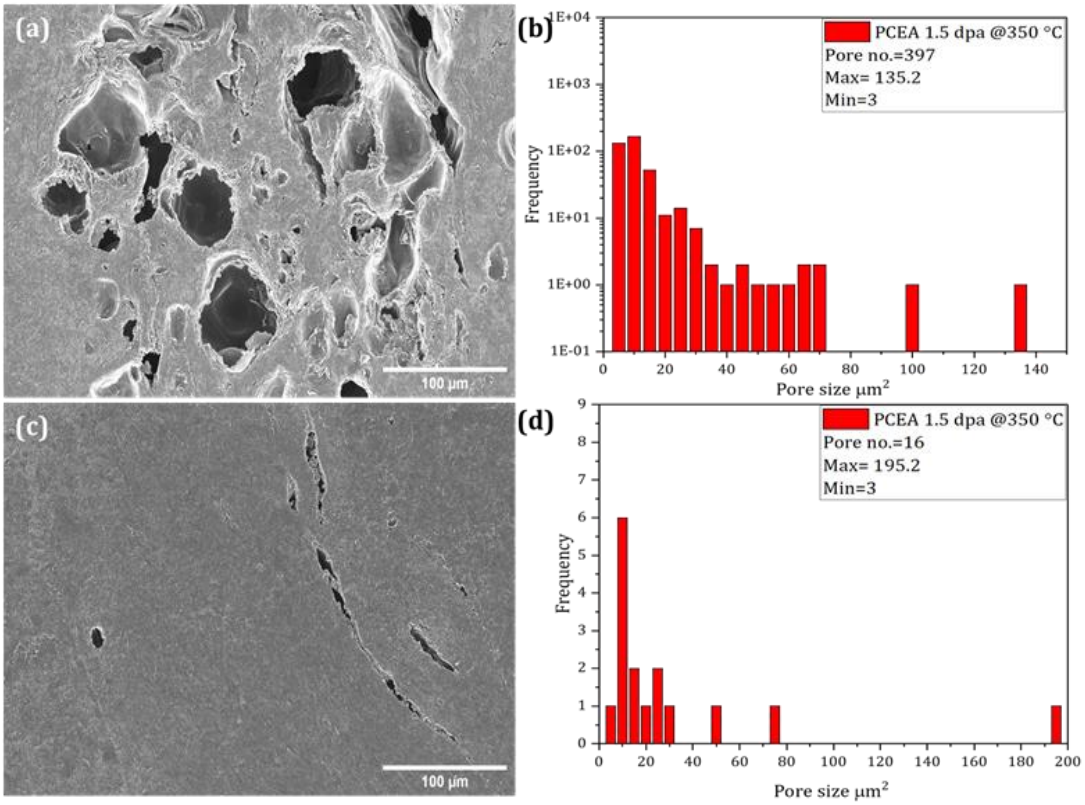

Figure 5.25: SE-SEM micrographs of irradiated PCEA; (a) showing pores within binder phase; (c) crack-like pores within filler particle; (b) and (d) are histograms of the respective pore size distributions.

Figure 5.26 shows the SEM micrographs of both filler and binder regions of PCEA graphite samples dosed at 6.8 dpa. Figure 5.26 (a) reveals the porosity in the binder region, showing a similar shape and size distribution to that observed in virgin samples and lower-dose samples (1.5 dpa). However, the pore size is

slightly smaller than it was in lower dose samples. Figure 5.26 (c) demonstrates neutron-induced changes to the microstructure of filler particles that appear as a notable reduction in the size of micro-cracks to ~1 μm and to 75 μm in length and from 100 nm to 10 μm width.

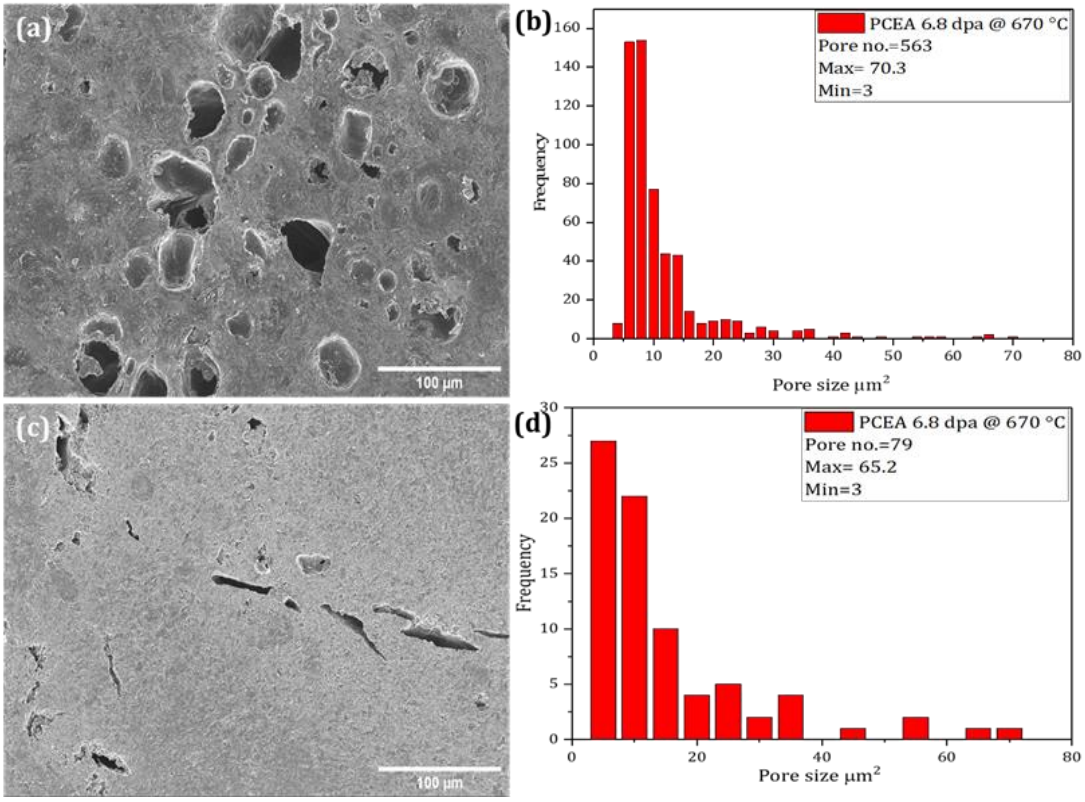

Figure 5.26: SE-SEM micrographs of irradiated PCEA; (a) showing pores within binder phase; (c) crack-like pores within filler particle; (b) and (d) are histograms of the respective pore size distributions.

In Figure 5.27, (a) and (b) show the microstructural features of PCIB samples irradiated to 1.5 dpa and 6.8 dpa, respectively. As can be seen from SEM, images were not possible to estimate the radiation damage to the pores structure of the PCIB graphite samples. This is due to the imperfect surface finish; the pores are not as clear as they are in the images of the virgin samples.

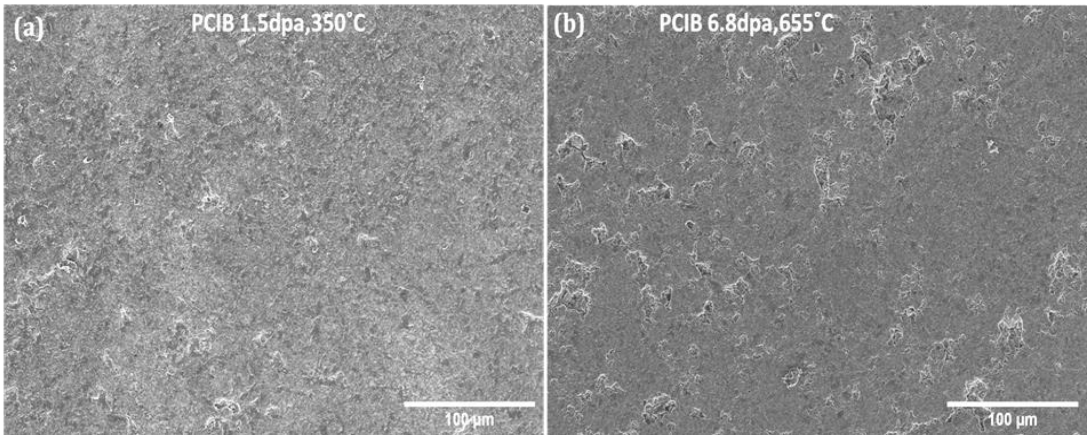

Figure 5.27: SE-SEM micrographs of irradiated PCIB; (a) showing porosity at lower dose/ temperature; (b) at higher dose/ temperature.

Overall, the irradiated samples were less homogeneous than the virgin sample, which agrees with Hagos (2013), who reported that after irradiation, the graphite crystals are fragmented and are smaller. Similarly, a high degree of cracking inside the pores was observed in both virgin and irradiated nuclear graphite in Hagos's work. Also, the frequency and size of these cracks change after irradiation, which agrees with the data at the lower dose/temperature of this work. The findings also in line with Mironov (2014), who study similar grades used in this Thesis but unpolished specimens. Mironov's results showed that after neutron irradiation, significant changes in the surface morphology and an increase in total porosity, with no preferential pore shape and orientation. However, Mironov's analysis is more qualitative rather than quantitative analysis. Furthermore, the presence of heavily porous regions does not observe by Mironov (2014). A possible reason is the limited size of the image dataset (10 images) may not be a representative of generalisable trends of porosity within PCIB graphite.

5.3 Summary

The understanding of the nuclear graphite microstructure is critical in order to later determine how microstructural features affect properties. Therefore, this chapter first studied the microstructure of filler particles and porosity in four different types of virgin nuclear graphites (PGA, Gilsocarbon, PCEA, and PCIB) using PLM and SEM. The variation between grades is ultimately dependent on the method of manufacture and the raw materials used. A comparison between

virgin and neutron-irradiated PCEA and PCIB nuclear graphites were then made using PLM and SEM. The main results are summarised below:

- Image analysis of the microstructure of nuclear graphite and the types and distribution of porosity seems to be the best method in quantitatively determining these parameters.
- The shape of the filler particles varies between the needle and spherical shapes between grades. As expected, the PGA had anisotropic needle-shaped filler particles of a mean length of 697±20 μm. The more isotropic Gilsocarbon grade had spherical filler particles with an average size of 356± 21 μm. The filler particles of PCEA grade had a wide variation; almost 60% of the filler particles were needle-shaped with an average length size of 565±12μm and spherical filler particles with an average diameter of ca. 322±20 μm. The needle-shaped particles in PCEA are slightly smaller than those in PGA. In contrast, due to the fine microstructure of PCIB, it was more difficult to distinguish whether an area contained filler or binder particles.
- The PLM images also help to qualitatively and quantitatively measure domains in virgin nuclear graphite grades tested. The isochromatic regions range in size from <0.1 μm to 500 μm; 'mosaics' of size <0.1– 5 μm and 'domains' of size <5– 500 μm. Separate domains have large angles of misorientation, while within domains, the corresponding crystallites are connected with low angles of misorientation. This comparison between different virgin nuclear graphite using PLM has not yet been discussed in the literature; hence, these conclusions further the understanding of nuclear graphite.
- The porosity also varies due to differences in the manufacturing processes and starting materials. This work reported three major pore types in nuclear graphite: gas-evolution pores, shrinkage cracks, and micro-cracks of different shapes and dimensions observed using PLM and SEM.
- An examination of two neutron-irradiated graphites was made; PCEA and PCIB nuclear graphites subjected to neutron irradiation doses ranging from 1.5 - 6.8 dpa with the irradiation temperature varied between 350

˚C – 670 ˚C. The data illustrates that neutron irradiation causes significant damage to the structure of PCEA nuclear graphite, albeit the sample surface finish is not ideal. After irradiation, the graphite crystals are fragmented and become smaller as the dose increases. In irradiated specimens, due to poor surface finish, only the spherical filler particles were easily observable at higher dose/temperature conditions (6.8 dpa/670 ˚C, which had an average diameter of about 288 ± 18 μm.

- The irradiated PCEA and PCIB specimens showed no significant changes in the average pore size distribution when compared to their virgin specimens. However, the overall porosity did increase than the original values at both low and high temperatures and doses insert which may be a consequence of a limited population size.
- Overall, the importance of measurements derived from the 2D images of virgin specimens provides a good qualitative and quantitative basis for comparison with neutron-irradiated graphite specimens. To the authors' knowledge, the results of the present quantitative study of porosity in virgin and neutron-irradiated PCIB graphite has not been done using PLM and SEM. Similarly, the conclusions made from the comparison of the virgin PCEA and PCEA irradiated PCEA graphite is a novel contribution to the literature. The novel contributions to the literature continue in the following chapter, in which a 3D analysis is made using the serial sectioning method.

Chapter 6

6.1 Serial sectioning methods for the 3D reconstruction of the microstructure of nuclear graphite

PLM and SEM images were discussed in chapter 5 to investigate the 2D pore structure images of nuclear graphite in both virgin and neutron-irradiated samples. This chapter discusses for the first time the 3D images of pore structure of two types of virgin nuclear graphite (PCEA and PCIB) constructed via manually compiled stacks of PLM images and also via FIB-SEM tomography. The extension of PLM technique to 3D allows the analysis of the pore structure in the interior of the materials to be achieved. The yields data from both techniques is very useful to the study of graphite moderator materials. In principle, this work could be extended to irradiated samples; however, this was not possible in the present work due to health and safety considerations.

6.1.1 Image analysis

Two different software packages were used for image processing and analysis; Fiji was used for processing and analysing images, and Amira was used to provide a 3D reconstruction of pore structure. PLM allows the distinction of the distribution of various constituents within the sample, such as binder and filler particles, and the types and distribution of pores within the microstructure. PLM was also used in this work with serial-sectioned samples to assemble 3D data from a series of 2D images, often referred to as stereology. Each section was polished to different depths below the surface to achieve a slice thickness of ~1 µm. The general analysis procedure is summarised in the following steps:

- The images obtained from PLM were pre-processed in Fiji software in sequential steps: images were stacked linearly; calibrated in 3 dimensions; cropped to remove unwanted areas because during imaging the selected area slightly drifted as the process of alignment was done manually; contrast-enhanced; aligned using the StackReg and TurboReg registration plugins in Fiji, and finally, images were segmented in terms

of contrast. Segmentation is the central procedure in image analysis, by which the digital image is partitioned. Segmentation enables the extraction of objects from each image using multiple algorithms. However, the labelling of pixels on a numbered object such as the pores in nuclear graphite is sometimes difficult to achieve automatically with Fiji. Thus, both automatic and manual approaches were adopted to compare results. This done by first defining an upper and lower limit by eye for each image in an image stack, which is a similar method followed in the analysis of 2D image described in chapter 4. This is because there are very significant contrast differences between individual images within an image stack, and automated thresholding does not work particularly well in this case.

- Then an additional automatic analysis was performed using the 3D object counter plugin to count the pores in the image, which was developed by Bolte and Cordelieres (2006). Pores at the edges were excluded for more accurate measurement; however, as one can see, many pores were located around the edges of the images of both samples particularly images obtained from FIB-SEM. Figure 6.1 and 6.2 display a montage of four slices of PCEA and PCIB.
- Fiji software was used to reconstruct a 3D image of the samples. A total of 10 slices were taken for both virgin PCEA and PCIB graphite. The resulting total dimensions of the PLM bounded box reconstruction volumes are 1012160.12 μm^3 and 1841429.89 μm^3 for PCEA and PCIB, respectively.

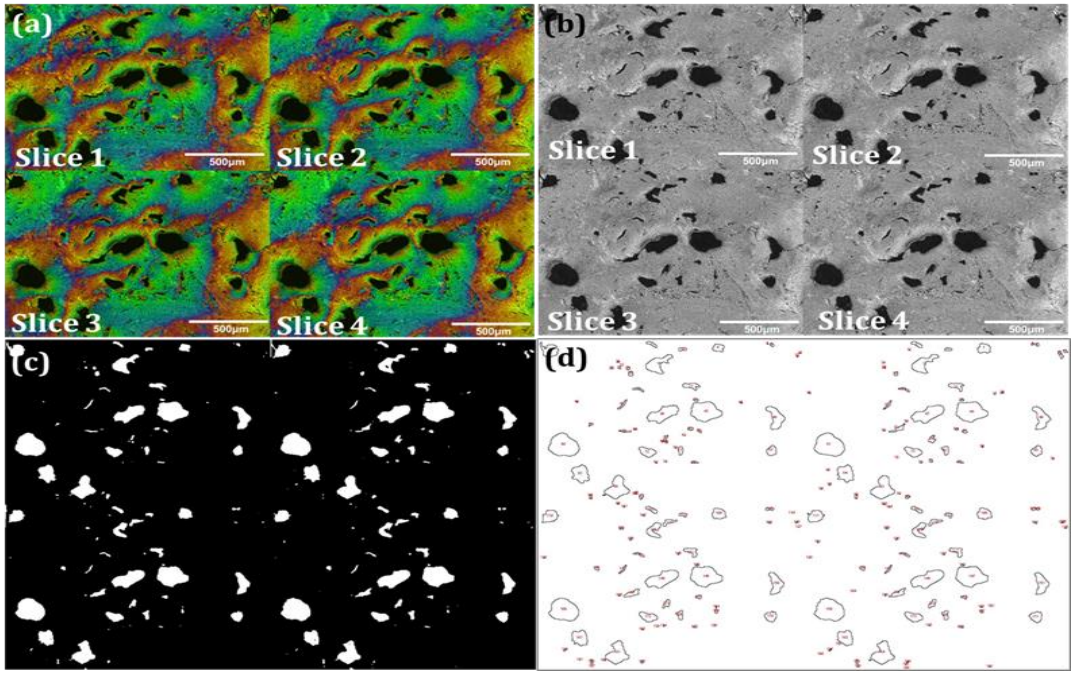

Figure 6.1: PLM images-montage of PCEA nuclear graphite, showing the analysis process of four slices obtained through progressive polishing: (a) original micrograph, (b) grayscale micrograph of original micrograph after removing the saturation and hue, (c) final segmented image used to extract a quantitative analysis of pores within the microstructure of nuclear graphite (d) the outlines of measured pore areas.

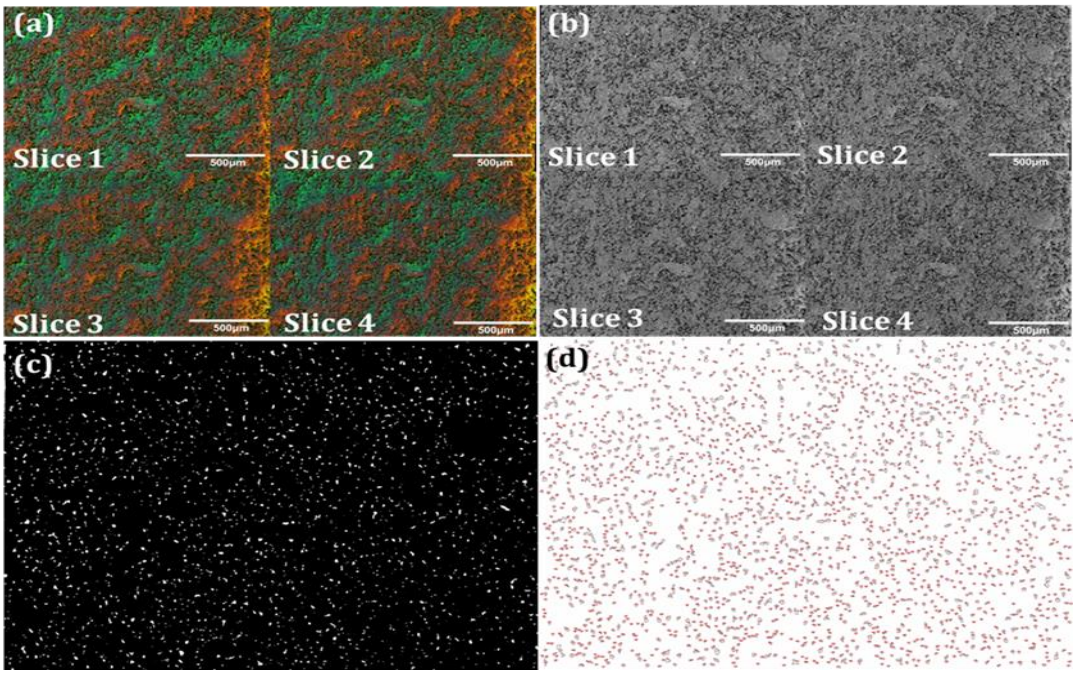

Figure 6.2: PLM images-montage of PCIB nuclear graphite, showing analysis process of four slices obtained through progressive polishing: (a) original micrograph, (b) grayscale micrograph of original micrograph after removing the saturation and hue, (c) final segmented image used to extract a quantitative analysis of pores within the microstructure of nuclear graphite (d) the outlines of measured pore areas.

In contrast, the analysis of FIB-SEM images was quite challenging, and each series of images in this work required special treatment due to the presence of vertical striping artefacts, including FIB curtaining caused by the ion beam milling step, as well as shading and charging defects and open pores filled with platinum (Pt); all of which affect the quality of the automated thresholding (Figure 6.3). The subtle variations in the stability of the FIB-SEM cryo-stage (e.g. temperature changes/gradients) and electrostatic effects of the sample (e.g. charging) can cause also a slight drift of the sample during milling. As a result of this, some ions can hit the front edge during lamella preparation, causing progressive degradation of the front side by ion beam erosion. To prevent ion beam erosion at the front side and to obtain a homogenous surface texture (e.g., to avoid curtaining), a thick protective layer of organometallic platinum for subsequent milling operations was deposited, and a large area was selected. The curtaining effect also increases with lower acceleration voltages during milling which was used for high-quality samples. Therefore, 30 kV was chosen for this purpose during the milling process. As for the shading and charging issue, they appeared when the scan speed of 20µs and the line of integration were chosen. To overcome these issues, the scan speed of 10µs, and two lines of integration with lower current (0.8 nA) were used. While, the issues related to some open pores filled with a deposited layer of platinum (Pt) were not overcome, as shown in Figure 6.3.

The general procedure in analysing the material is summarised in the following steps and is illustrated in Figure 6.4:

- A single region of interest was investigated in each sample; 22.3 × 23.1× 73 µm for PCEA graphite and 40.4× 23.4× 16 µm for PCIB graphite. A total of 730 and 160 slices were taken for PCEA and PCIB graphite respectively, with each milling step removing 100nm of material. The resulting voxels resolution are 0.021 µm×0.027 µm×0.03 µm for PCEA and 0.033 µm×0.041 µm×0.1 µm for PCIB.
- During FIB-SEM imaging, the scale of images is shortened dramatically because of the angle of image acquisition. Therefore, the images were corrected by stretching in the y-direction using the following correction factor that is multiplied by the pixel length in the y-direction (6.1):

$$\frac{1}{\sin\theta} \times y_h \qquad (6.1)$$

Where θ is the angle between the FIB and SEM columns (54°), and y_h is the voxel height.

- The images obtained from FIB-SEM were pre-processed in Fiji using similar image processing procedures described for PLM. FIB-SEM images also had to be aligned because slices drifted left and right during the slice and view process. However, after segmentation, noise reduced (smoothing) with a 3D-median filter, which is important to avoid counting noise (white dots) in images as pores, consequently resulting in inaccurate results analysis (see Figure 6.5).
- Amira software was used to reconstruct 3D images of the two samples. The resultant dimensions of the bounded box reconstruction volume were 22.89×10.18×7.39 μm^3 (1724.33 μm^3) for PCEA and 19.07× 21.93 × 6.47 μm^3 (2703.8 μm^3) for PCIB. Table 6.1 summarises the number of measurements undertaken using serial sectioning method. Note the same samples were used for both PLM and FIB-SEM.

Table 6.1: A summary of the number of samples from each graphite type analysed using PLM and FIB-SEM.

Samples	No. of specimens	PLM measurement	FIB-SEM
PCEA	1	One Region (filler- binder)	One Region (filler- binder)
PCIB	1	One region	One region

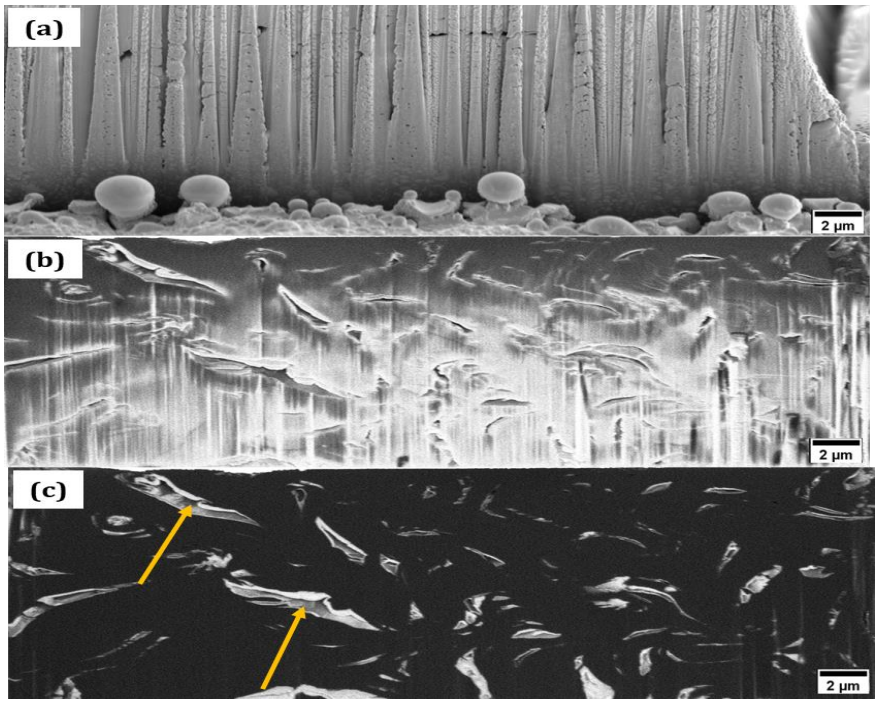

Figure 6.3: FIB-SEM images showing: (a) vertical striping (curtaining) artefacts caused by the milling; (b) shading defects and charging; (c) some open pores filled with platinum during deposition of the platinum protective strap.

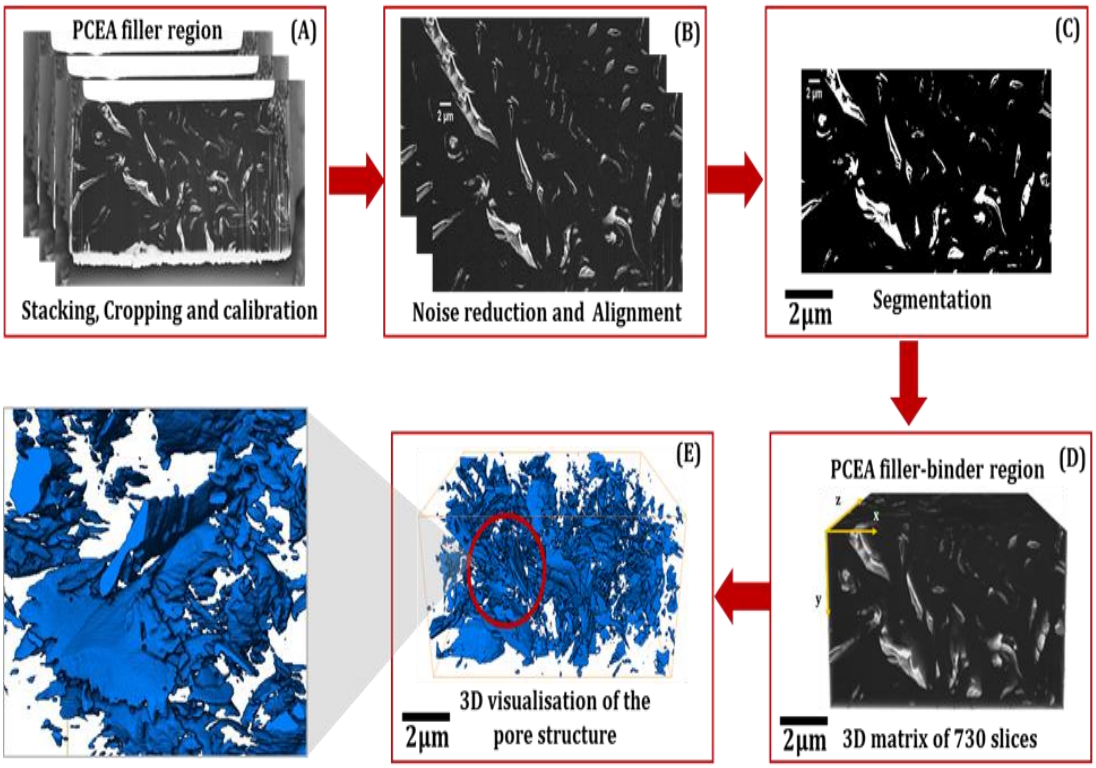

Figure 6.4: The general procedures followed for image processing and segmentation of FIB-SEM images; the zoomed area in (E) shows more details of pores connectivity.

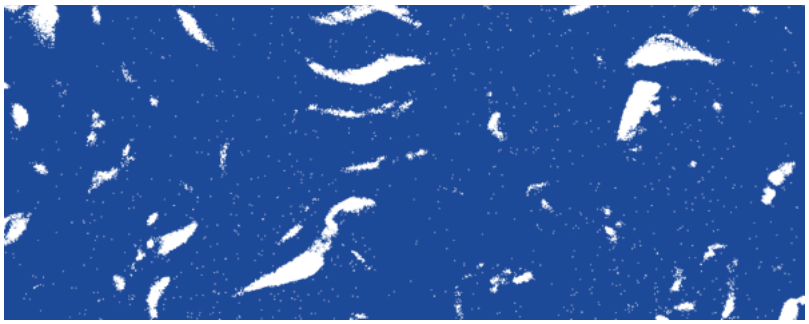

Figure 6.5: FIB-SEM image; showing noise (small dots) after segmentation. Note the colour of the image has been changed for illustration.

6.1.2 PLM serial sectioning

6.1.2.1 Results and discussion

Porosity structure plays a critical role in determining the mechanical behaviour of nuclear graphite. In order to accurately predict the mechanical performance of a material, it is important to understand the size, shapes, and distribution of porosity in 3D. Three-dimensional characterisation of porosity also can provide critical input to develop a microstructural model. Classical stereological method using PLM allowed to extrapolate information about porosity from two-dimensional images. This analysis was undertaken to compare the 2D analysis of the pore size, shape and distribution. Also, the 3D analysis allowed the examination of the connectivity and changes to the structure of pores through the body of nuclear graphite, as a result of progressive polishing.

Table 6.2 and 6.3 summarise the overall porosity of virgin PCEA and PCIB virgin graphite, respectively, calculated from the 3D reconstruction. PCEA sample has a volume of porosity lying between 10–1500 μm^3, whereas PCIB has volume lying between 10-550 μm^3. Each graphite has a characteristic pore structure due to different manufacturing processes used. PCEA micrographs show cracks and pores structures of different sizes, shapes (including near-circular, elliptical, and acicular shapes) and distribution depending on the region of interest in PCEA (e.g. filler or binder regions). In contrast, the PCIB micrographs exhibit an almost uniform structure with random shaped pores and different size distributions. The volume fraction of porosity obtained from serial sectioning of one region for each graphite sample was approximately 13 % and 15 % for PCEA and PCIB, respectively.

Comparing these values to the data in chapter 5, which were calculated from random 2D regions, PCEA 3D appears to be slightly less porous by 2.9%, as the 2D image calculation was 15.9%, while the 3D image calculation was 13%. The estimated percentages of 2D and 3D PCIB were nearly the same; 15.3% and 15%, respectively. The calculated volume fractions for both samples were less than theoretical porosity; ~20% for PCEA and 19% for PCIB. The finding of PCEA graphite in 2D analysis agrees with Kane et al., (2011), who found that PCEA nuclear graphite has an average porosity of ~16%. Figure 6.6 shows the histograms of pores size distribution within PCEA and PCIB nuclear graphites. Finally, no significant differences were observed in the total porosity for PCEA and PCIB graphite

Table 6.2: Summary of porosity structural data of virgin PCEA graphite using PLM, computed from the 3D reconstruction of serial sectioning.

Volume range (μm^3)	No. of pores	Volume (μm^3)	Area (μm^2)	Volume Fraction %
10-50	22	3613.5	2291.9	0.36
50-100	10	1729.2	690.1	0.17
100-150	9	1403.8	2148.3	0.14
150-200	7	700.3	1993.1	0.07
200-550	4	1549.9	5287.5	0.15
550-1500	8	118839.9	245785.5	11.74
Total	60	127836.6	258196.2	12.63

Table 6.3: Summary of porosity structural data of virgin PCIB graphite using PLM, computed from the 3D reconstruction of serial sectioning.

Volume range (μm^3)	No. of pores	Volume (μm^3)	Area (μm^2) [10^4]	Volume Fraction %
10-50	426	17542.6	114255.6	0.95
50-100	535	43263.7	219907.3	2.35
100-150	319	39267.2	144453.6	2.13
150-200	218	27849.6	109617.5	1.51
200-250	168	25531.2	92099.4	1.39
250-300	135	23158.3	50605.9	1.26
300-350	110	21561.7	43346.4	1.17
350-400	77	21355.9	56181.2	1.16
400-450	65	20546.4	34728.8	1.12
450-500	44	19896.9	43966.8	1.08
500-550	30	16687.3	36480.1	0.91
Total	2127	276660.8	945642.4	15.12

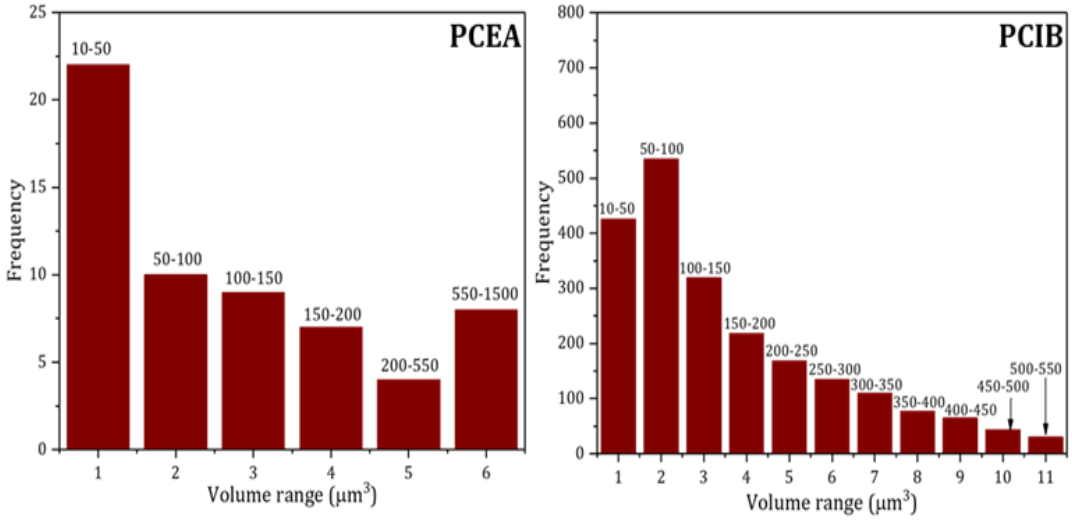

Figure 6.6: histograms of PCEA (left) and PCIB (right) graphites showing the distribution of pore sizes.

Figure 6.7 and 6.8 show 3D volume reconstructions of PCEA and PCIB porosity, respectively, which shows 3D slabs with pores indicated within that volume. These figures show that PCEA has more big pores than PCIB graphite grade. In PCEA, some pores in the binder phase appear to be separated from the large pores, while other pores are joined. In the filler particles, the long thin pores were closed and then were separated and merged with the large pores; these pores were more likely to connect through slices. However, the porosity of the PCIB nuclear graphite did not appear to change through the thickness, as it has smaller pores, making the connections between slices difficult to see. This limitation may be due to an inadequate number of slices, and because the thickness of each slice (~1µm) was small to show changes to the pores through the body of graphite samples.

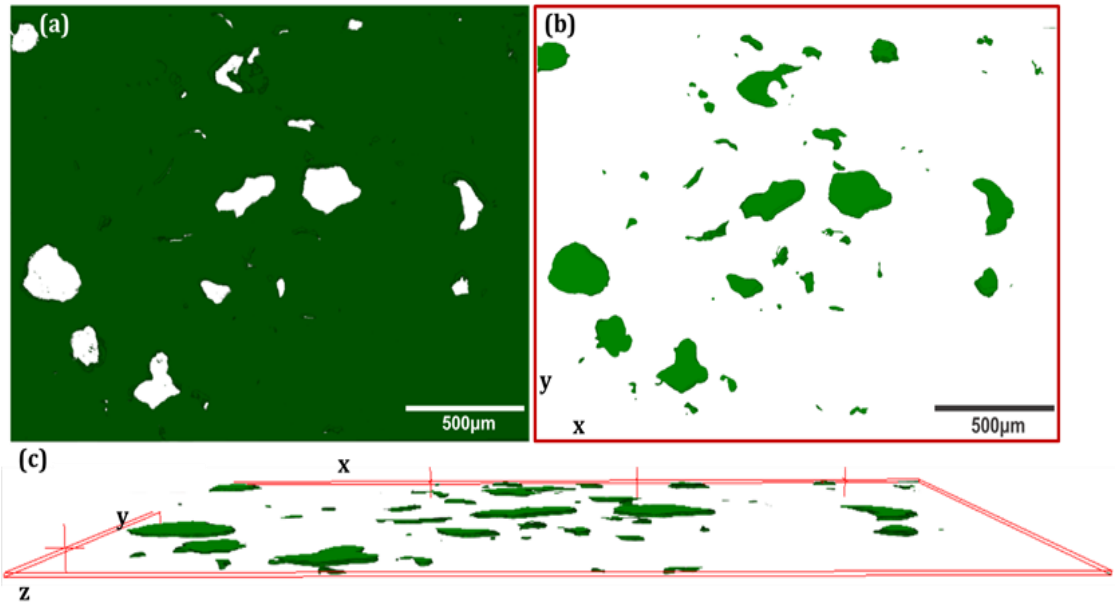

Figure 6.7: PLM images show (a) stacks of 10 images showing sample surface area; revealing open pores in white (large pores connected through the whole slices) and the cracks (closed or partially closed), (b) is the 3D pore reconstruction of slices of PCEA nuclear graphite (c) the 3D pore reconstruction from a different view.

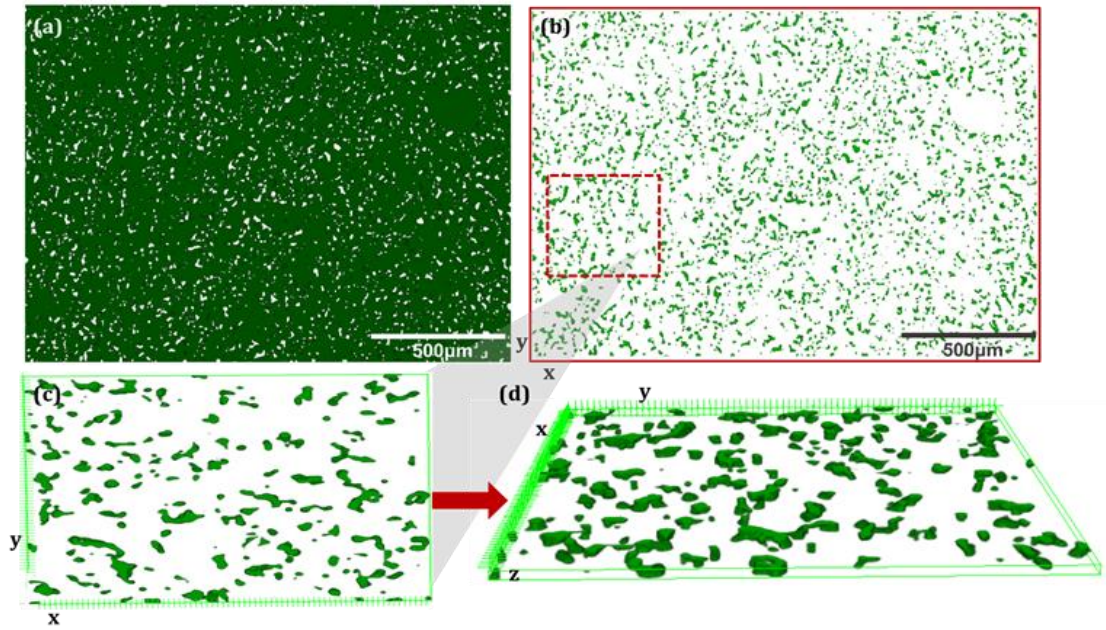

Figure 6.8: PLM images (a) and (b) 3D pore reconstruction of 10 slices of PCIB nuclear graphite using PLM; (c) and (d) shows an example of pores connected in 3-D volume from different views.

Figure 6.9 and 6.10 exhibit 3D surface plots of pixel intensity (0-255) through the stack of 10 thresholded and segmented images of PCEA and PCIB nuclear graphite, respectively. Interconnected pores are apparent as high-intensity regions that span the z-axis. The colour scales on the z-axis simply refer to the contrast level (0-255).

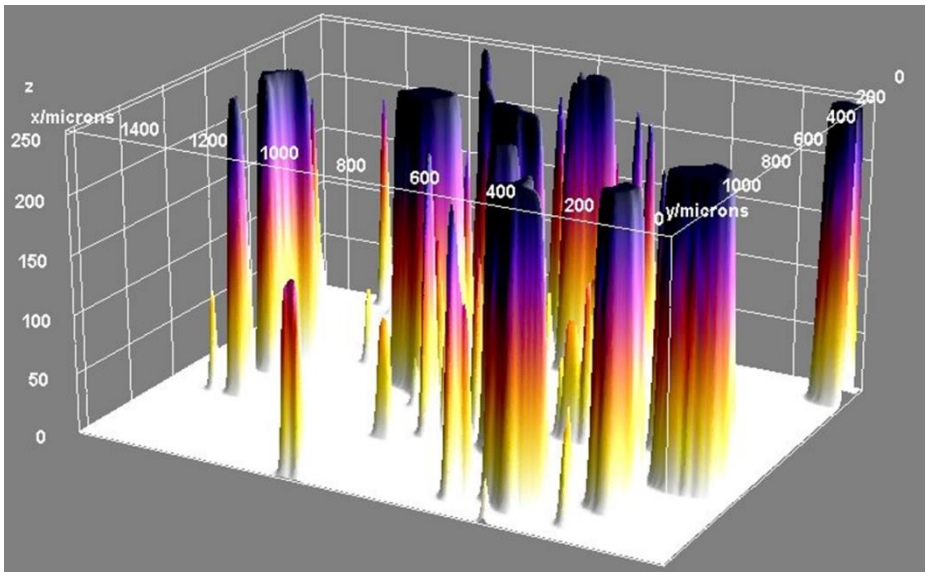

Figure 6.9: 3D surface plot of the 10 thresholded and segmented images of PCEA nuclear graphite.

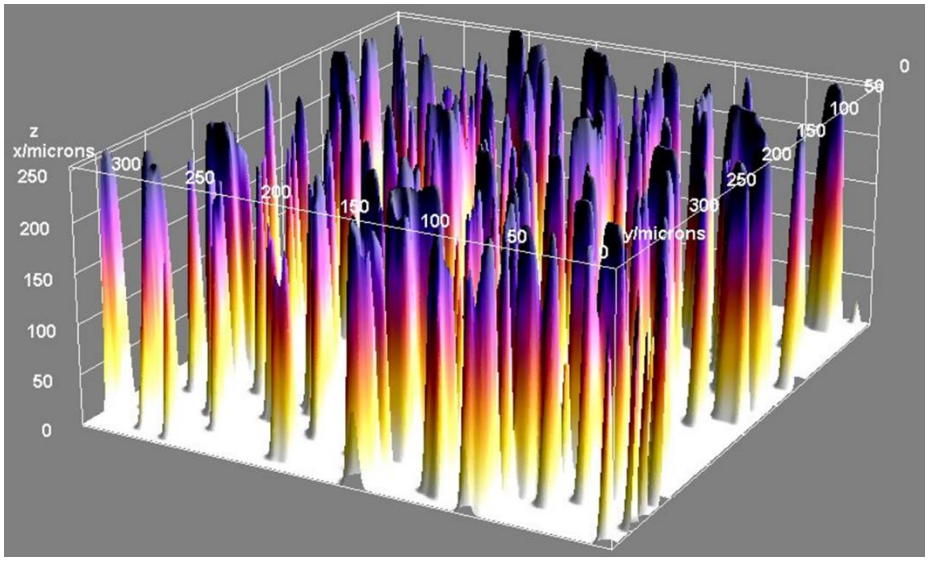

Figure 6.10: 3D surface plot of the 10 thresholded and segmented images of PCIB nuclear graphite.

6.1.3 FIB-SEM serial sectioning

6.1.3.1 Results and discussion

Table 6.4 and 6.4 summarise the FIB-SEM data used in this study, and Figure 6.11 and 6.11 give examples of images slices taken from each sample image stack. Figure 6.11 shows some examples of unstacked images of multiple micro-cracks and pore structures of different size, shape, and distribution across the region of interest in PCEA (filler-binder), which were observed in most of the SEM images and were discussed in chapter 5. In contrast, Figure 6.12 displays the pore structure in PCIB, which has more-homogeneous pores compared to PCEA; some are large pores, and only a few micro-cracks are evident. In the case of PCIB, it is hard to distinguish whether an area contained filler or binder particles due to the fine microstructure; therefore, the two regions of interest were chosen randomly to be representative of the overall microstructure.

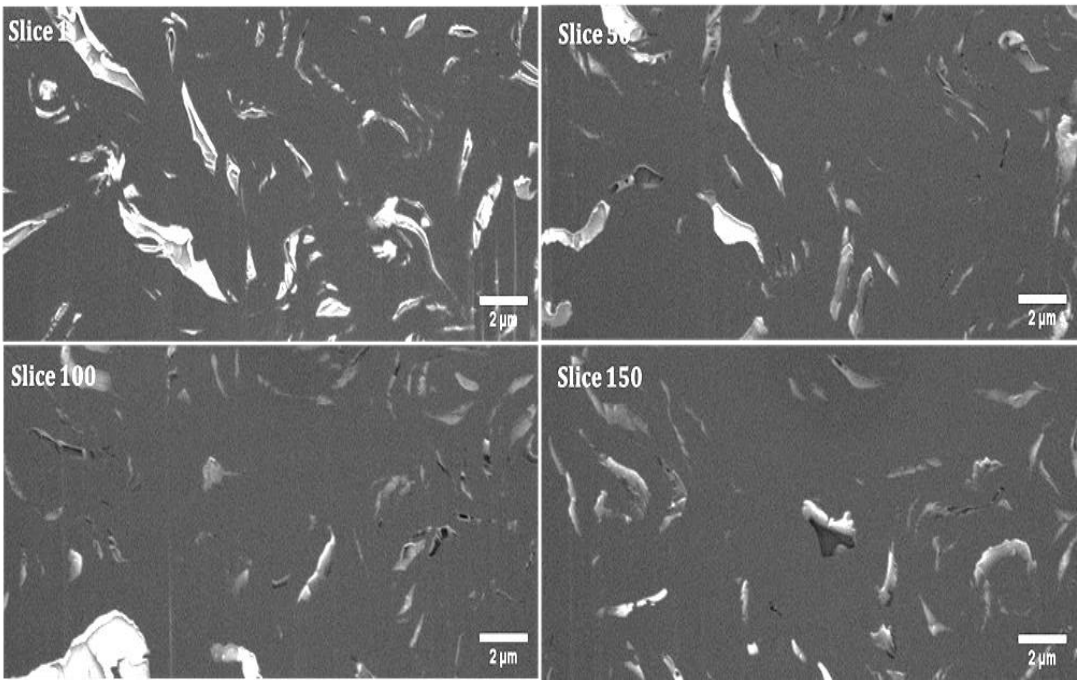

Figure 6.11: Examples of single images from PCEA images stack; showing the changes to the structure of pores. Scale bar for each image is 2µm.

Table 6.4: Summary of porosity structural data of virgin PCEA graphite, computed from the 3D FIB-SEM reconstruction.

Volume range (μm^3)	No. of pores	Volume (μm^3)	Area (μm^2)	Volume Fraction %
0.001-0.005	960	2.9	141.9	0.17
0.005-0.01	362	2.6	130.7	0.15
0.01-0.05	593	11.1	434.3	0.64
0.05-0.1	132	9.2	296.7	0.53
0.1-0.5	221	49.5	1290.2	2.87
0.5-1.0	54	36.9	812.1	2.14
1.0-1.5	36	29.7	603.7	1.72
1.5-2.0	14	23.4	431.1	1.36
2.0-25	44	109.9	3003.2	6.37
Total	**2416**	**275.2**	**7143.9**	**15.9**

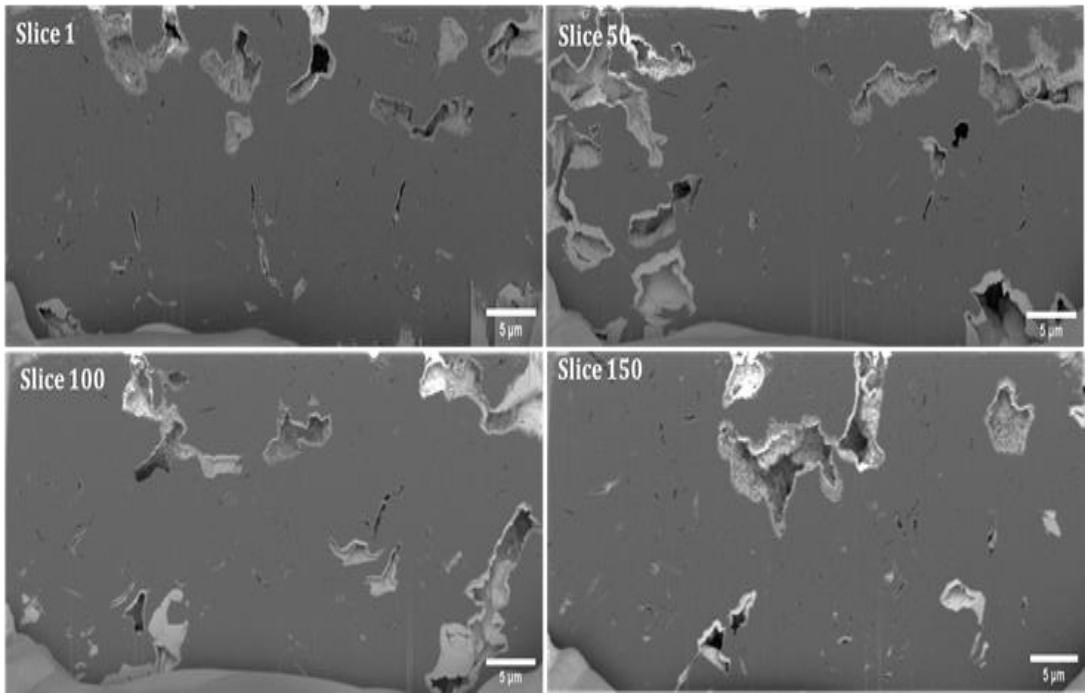

Figure 6.12: Examples of single images from PCIB images stack; showing changes to the structure of pores. Scale bar for each image is 5µm.

Table 6.5: Summary of porosity structural data of virgin PCIB graphite, computed from the 3D FIB-SEM reconstruction.

Volume range (μm^3)	No. of pores	Volume (μm^3)	Area (μm^2)	Volume Fraction %
0.001-0.005	0	0	0	0
0.005-0.01	105	0.89	34.5	0.033
0.01-0.05	314	7.21	213.9	0.267
0.05-0.1	117	8.11	196.5	0.300
0.1-0.5	109	26.9	515.1	0.995
0.5-1.0	34	16.5	272.2	0.610
1.0-1.5	6	5.8	81.4	0.215
1.5-2.0	5	8.8	108.6	0.325
2.0-25	8	79.3	773.6	2.933
Total	**698**	**153.51**	**2195.8**	**5.678**

Table 6.4 and 6.2 show the pore distribution in both samples, which are in the range of 0.005– 25μm^3. The minimum pore size, however, resolved was 0.001–0.005 μm^3 for PCEA and 0.005–0.01 μm^3 for PCIB nuclear graphite. The total volume fraction of porosity in PCEA was ~15.9%, which are in agreement with total porosity calculated by PLM in chapter 5 considering pore areas and volumes investigated are significantly different. In PCIB, larger pores account for most of the volume, where the pores are located around the edge of images. However, initially, these pores were first excluded during the analysis as, for these pores, the whole pore is not visible in the image which could give an inaccurate measurement of the pore size and overall porosity. As a result, the total porosity of PCIB was calculated to be ~6%, which is significantly less than the percentages measured by PLM of around 15%. This limitation was also observed in the results of Arregui-Mena et al. (2018). Including, pores around the sample edges increase the overall porosity to ~19%, more than the total porosity reported by PLM (Table 6.6). This value (14-years) old (however agreed well with the total porosity (19.13%) given by the manufacturer. Figure 6.13 and 6.12 show histograms of pore size distribution within both samples. Moreover, 3D volume reconstructions revealed the pore connectivity, particularly between large voids (Figure 6.15 to 6.16). Figure 6.16 and 6.16 shows a 3D visualisation

of both PCEA and PCIB samples from different views, showing the variation of pore connectivity through the slices.

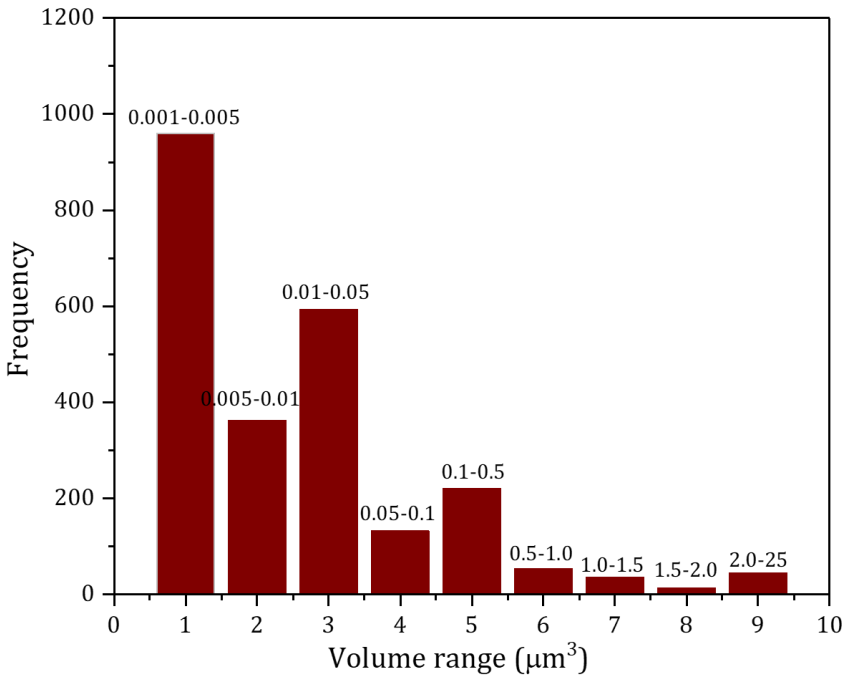

Figure 6.13: A histogram of PCEA graphite showing the distribution of pore sizes.

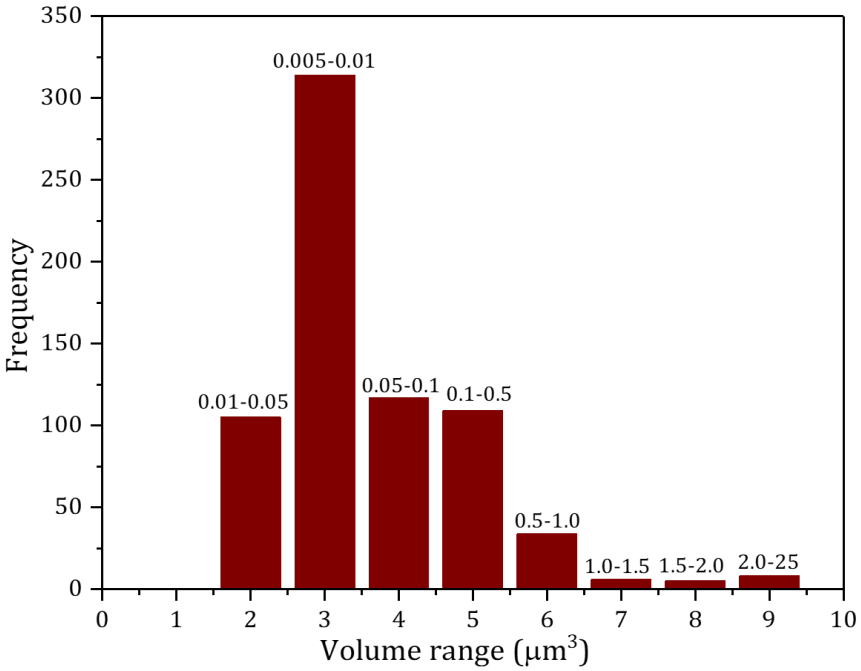

Figure 6.14: A histogram of PCIB graphite showing the distribution of pore sizes.

Table 6.6: Summary of porosity structural data of virgin PCIB graphite

Edge Pores	Volume range (μm^3)	No. of pores	Volume (μm^3)	Area ($\mu m^{2)}$	Volume Fraction %
Excluded	0.005-25	698	153.51	2195.8	5.69
Included	0.005-75	1103	512.69	5421.3	18.96

The structure of the porosity was investigated using the 3D reconstructions generated from the FIB-SEM 2D image stacks. Figure 6.15 to 6.16 illustrate the porosity structure of PCEA and PCIB nuclear graphite samples. The pore structure in the filler-binder region of PCEA exhibits a greater number and larger volume of voids that are composed of long and narrow cracks and a more-complex network of different-sized pores and smaller cracks. In contrast, the PCIB nuclear graphite pore structure has fewer and smaller pores.

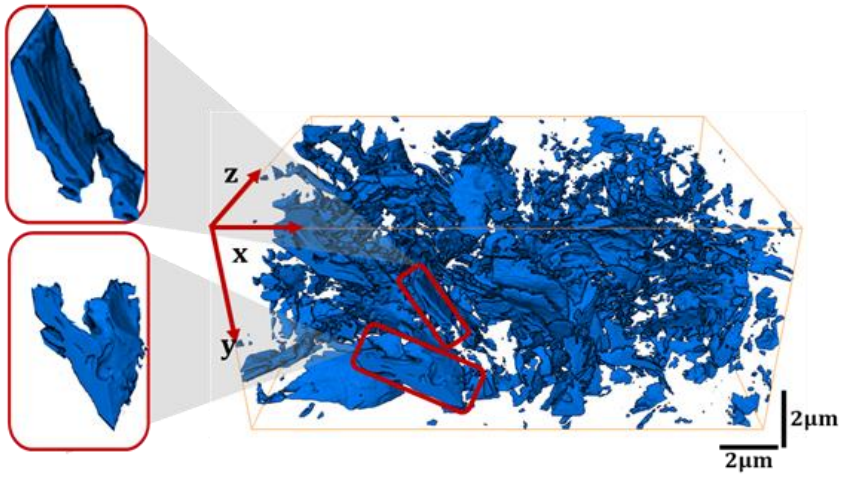

Figure 6.15: 3D pore reconstruction of PCEA nuclear graphite; the insets show an example of pores connected in 3D; top pore found connected through 78 slices; bottom pore connected through 86 slices.

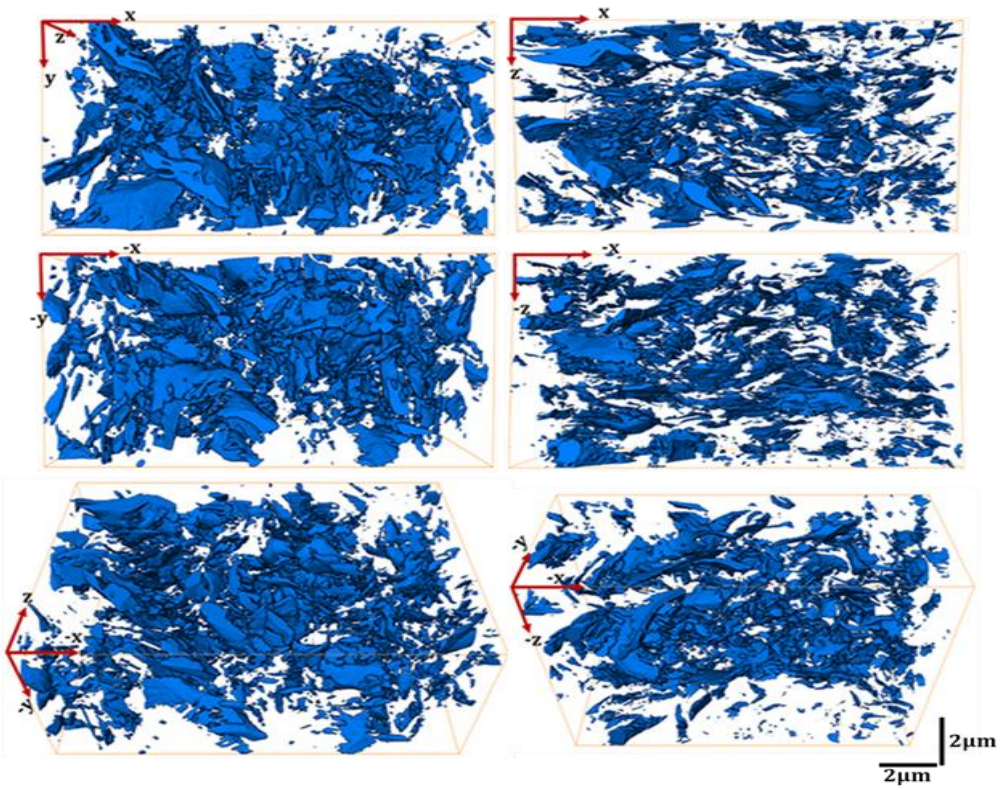

Figure 6.16: 3D visualisation of the pore structure of 730 slices of PCEA, showing the variation of pore connections from different views.

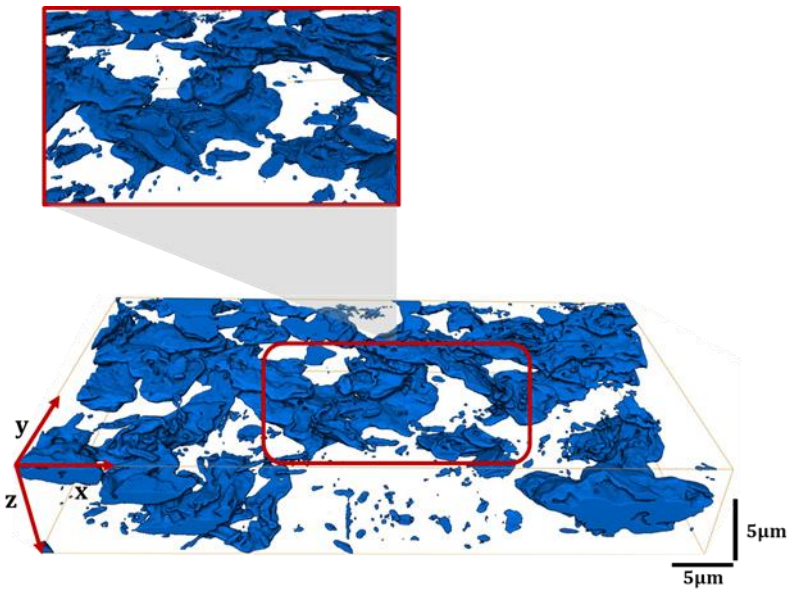

Figure 6.17: 3D pore reconstruction of PCEA nuclear graphite; the inset shows an example of pores connected in 3D.

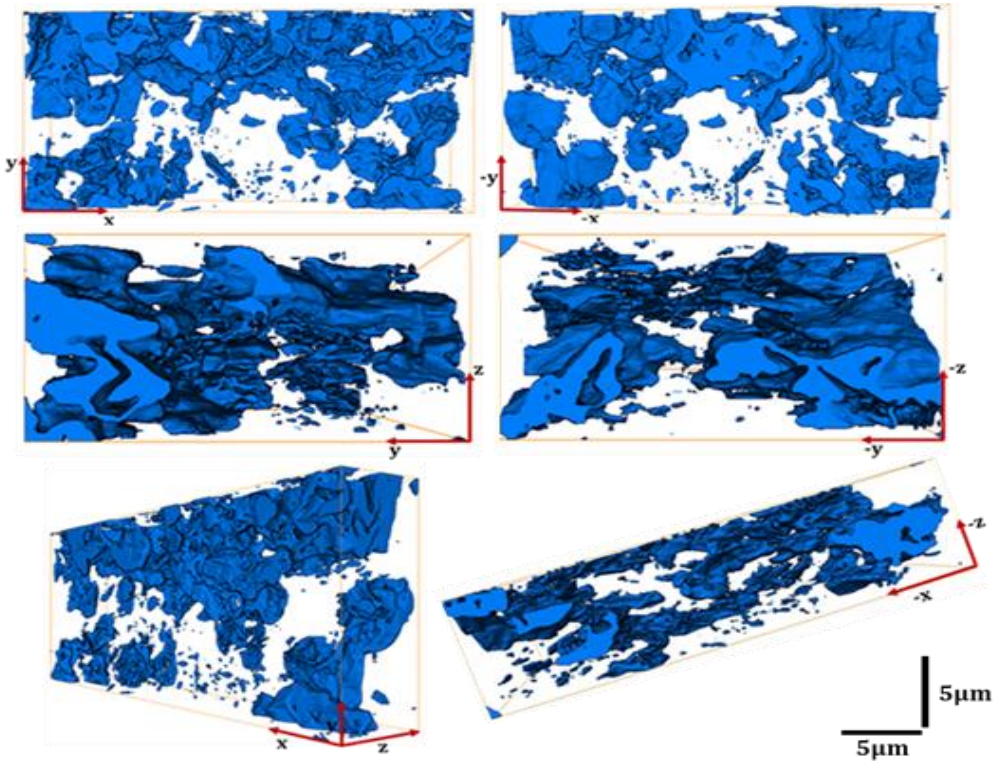

Figure 6.18: 3D visualisation of the pore structure of 160 slices of PCIB, showing the variation of pore connectivity through slices from different views.

FIB-SEM tomography reconstructions were used to study the structure of porosity within nuclear graphite, showing a wide range of pore structures. FIB-SEM gave both qualitative and quantitative information: size, shape, type (open or closed), connectivity, and distribution within the samples. This high-resolution imaging technique has some limitations. Firstly, the field of view is limited compared to PLM and other techniques such as X-ray tomography. FIB-SEM is also affected by sample preparation; mechanical polishing, milling of fiducial marks, and deposition of a platinum layer to protect the samples from any charging effects. During image acquisition, many issues were raised, such as the presence of artefacts (curtaining by the ion beam) and shading and charging defects. Charging effects are caused by a large number of secondary electrons being emitted from the sample due to local topological effects, and the lack of a conductive path by which excess electrons can be removed, causing bright areas in the images (Arregui-Mena et al., 2018).

Moreover, the milling steps and the positioning of the stage to image the same area are time-consuming. The process is fully automated; therefore, it was difficult to ensure that the same number of slices were taken from each sample.

Samples tended to drift slightly, and some open pores filled with platinum, making image thresholding difficult. Therefore, the combination of FIB-SEM with other imaging techniques is recommended to overcome these limitations, allowing us to obtain multiscale data acquisition and to validate the measurements. In general, FIB-SEM provides useful information about features smaller than one μm, which are especially important to understand the fine structure of PCIB nuclear graphite.

In conclusion, FIB-SEM can be used to evaluate the damage caused by neutron irradiation if the area of interest is selected carefully. Our experience with using FIB-SEM to characterise the porosity of nuclear graphite agrees well with Arregui-Mena et al. (2018), who tested nuclear AGX graphite (Gilso grade).

6.2 Summary

The finding of this chapter provides a novel and useful information on the structure of pores in two virgin nuclear graphite grades (PCEA and PCIB). PLM and FIB-SEM micrographs showed distinct changes in the pore structure of virgin nuclear graphites. The pore shape, size distribution, and connectivity vary through the thickness.

PLM stacked images of the virgin samples were all taken at the same magnification for PCEA and PCIB to allow easy comparison. FIB-SEM images of the virgin graphite samples were taken at different magnifications to capture the differences in the porous structure. 3D volume reconstruction of the images was performed with Fiji and Amira software. FIB-SEM is more useful than PLM because FIB-SEM allows greater magnification and has a longer depth of focus. These features allow pores to be measured at scales from 100 nm to 100 μm. Also, the automatic measurements produced a large volume of data. Though PLM images were recorded manually, furthermore, because of sample size and sample handling in easier, FIB-SEM could give insight into the effect of neutron irradiation on nuclear graphite via its ability to more easily serial section 'active' graphite samples.

Overall, the three-dimensional analyses performed in this chapter is important because these analyses gave significant information of pores structure

of nuclear graphite grades candidate for Generation-IV reactors at two different length scales (micro and nanoscale). Since microstructural deformation in nuclear graphite is a 3D mechanism, the benefits of using PLM and FIB-SEM for data collection are clear. Despite the fact there is an undeniable benefit of utilising 3D techniques to analyse 3D processes, there are cases where 2D techniques provide data that is just as useful. Subsequently, there is more existing literature such as Kane et al. (2011), Bodel (2013) that uses 2D techniques than 3D techniques for graphite microstructural analysis. This is due to that PLM analysis is easier, quicker and requires less specialised equipment.

Chapter 7

7.1 Characterisation of the crystalline structure of virgin and irradiated nuclear graphite specimens

In this chapter, the crystalline structures of different coke sources of nuclear graphite (PGA, Gilsocarbon, PCEA, and PCIB) have been investigated by X-ray diffraction and Raman spectroscopy, both are common techniques used to gain a good understanding of the radiation effects in nuclear graphite (Babu and Seehra, 1996; Freeman et al., 2017; Goggin et al., 1964; Hagos et al., 2010; Henson et al., 1968; Howe et al., 2007; Krishna et al., 2015; Krishna et al., 2017; Mironov, 2014; Zheng et al., 2014; Zhou et al., 2014). In the following sections, results will be discussed and compared with data from previous studies.

7.1.1 Interpretation of X-Ray diffraction patterns of virgin (nuclear) graphite

7.1.1.1 Results and discussion

Figure 7.1 displays the indexed peaks of the analysed virgin graphites (PGA, Gilsocarbon, PCEA and PCIB) that initially indicate no significant differences between them. All Bragg peaks with Miller indices of (002), (100), (101), (102), (004), (103), (110), (112) and (006) were present for PGA nuclear graphite, with other types of nuclear graphite demonstrating similar peaks, except for (102), which was not apparent. The peaks from all samples were in good agreement with the literature data (JCPDS 00-056-0159). However, the insert (b) shows the variation of the (002) peaks width and position between PGA, Gilsocarbon, PCEA, PCIB, and HOPG. The (002) peak of HOPG occurs at a higher diffraction angle than the nuclear graphites. However, the (002) diffraction angle differs slightly between nuclear graphite, which confirmed the suggestion that 'no two graphite samples would ever have identical X-ray diffraction patterns in every details' (Zhou et al., 2014). Consequently, at least four samples for each type of virgin nuclear graphites were examined to obtain more reliable XRD measurements.

The XRD pattern from PGA showed similar characteristics, particularly in their tendency of peak to broaden and decrease in intensity due to lattice strain, such as (100), (101), (102) and (103). In contrast, only (100), (101) and (103) peaks were observed for Gilsocarbon, PCEA, and PCIB nuclear graphites. However, PGA nuclear graphite demonstrated higher peak intensities (e.g. (002), (004), (110)) than the three other nuclear grades; similar observations were reported by (Krishna et al., 2017; Zhou et al., 2014).

Table 7.1 summarises the important parameters extracted from XRD data, which influence the performance of any nuclear graphite moderator in reactors, which are the <c> lattice parameter, the in-plane lattice parameter <a> and the coherence lengths L_c and L_a. The total data collected for all virgin samples was 80 measurements (20 measurements per graphite sample, see chapter 4 (section 4.1.2.3)). The study of these parameters especially the coherence lengths are of great interest since there is a considerable body of evidence that more highly crystalline graphites with low interlayer spacings $d_{(002)}$ and hence small value of <c>, have larger values of coherence lengths and there appears to be a direct correlation between the "crystallinity" of graphites and the stability of their dimension under neutron irradiation (Kelly et al., 1966; Wen et al., 2008; Zheng et al., 2014).

For all samples, <c> was higher than the single crystal graphite values but <a > were close to single crystal graphite (c = 0.6708 and a=0.2456 nm) at room temperature and in agreement with previous studies such as (Mironov, 2014; Zheng et al., 2014; Zhou et al., 2014; Krishna et al., 2017). The fluctuation of <a > is less than in $<d_{(002)}>$ values, which is expected due to strong covalent in-plane bonding. The c-lattice parameters for all measured nuclear graphite samples were, in comparison, slightly larger for than Highly oriented pyrolytic graphite (HOPG), which had a good degree of graphitisation compared to the virgin nuclear graphites. Therefore, nuclear graphite grades have more imperfect structures (Nightingale, 1962; Simmons, 1965; Zheng et al., 2014; Zhou et al., 2017a).

Coherence lengths L_c and L_a for nuclear graphites are other important factors that decrease with an increase of the interlayer spacing, increasing the disorder (defects), and a smaller crystal size (Nightingale, 1962; Simmons, 1965; Thrower and Nagle, 1973). The L_a crystallite size for the virgin nuclear graphites

was larger than L_c, as shown in Table 7.1. However, by using W-H plot, L_c values are higher than values obtained by the Scherrer equation and similar to the uncorrected L_a values owing to the presence of micro-strain and shown in Table 7.1. Therefore, these results are in agreement with the findings of nuclear graphite (Mironov, 2014; Zhou et al., 2014) and HOPG in (Gallego et al., 2013). The measured strain broadening of virgin nuclear graphite seems to be negligible but the (002) peak in HOPG showed higher values of lattice strain accounts for as much as 20% of the peak width. A similar observation of HOPG lattice strain conducted by Thrower and Nagle (1973), who reported a little higher lattice strain of 30% of the peak width in HOPG. Note micro-strain calculated only for L_c as there are not enough useable peaks for L_a.

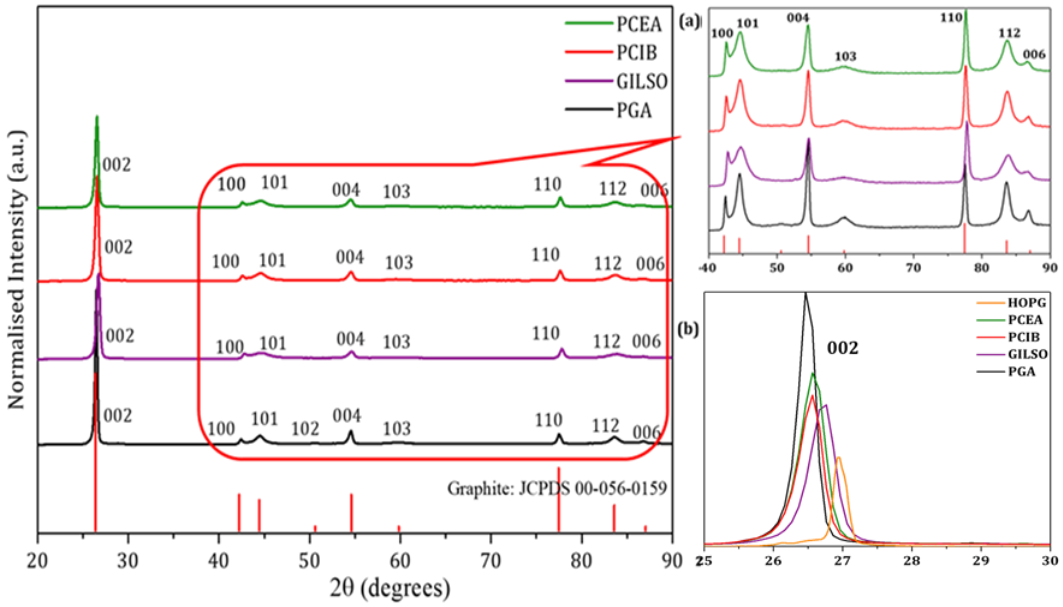

Figure 7.1: XRD patterns of four different types of virgin nuclear graphite. The inset (a) is zoomed to show details of XRD peaks from 2θ= 40° to 90°. While (b) shows the variation of 002 peaks shapes and positions of the measured graphites compared HOPG.

It can be summarised that L_c increases as the c-lattice parameter decreases, while L_a increases as a-lattice parameter increases, see Table 7.1 and Figure 7.2. It is important to mention that the coherence lengths (crystallite size) are often confused with the term grain size in such graphites, which is typically several orders of magnitudes larger than the coherence lengths. This was demonstrated by employing optical and electron microscopy in this Thesis. Each

grain comprises of several small coherent crystalline volumes distinguished by the mean sizes L_a and L_c.

In comparison, PGA graphite showed larger crystallite size compared to other types of nuclear graphite analysed in this Thesis with smaller c-lattice parameters indicating its higher degree of perfection. The measurements of the filler size also showed that PGA has a larger filler size compare to Gilsocarbon, PCEA, and PCIB graphite grades. In terms of porosity, the 2D analysis in chapter 5 exhibited that both PCEA and PCIB graphite grades are less porous compared to PGA and Gilsocarbon graphite and demonstrating small average pore size. This observation also confirmed from the 3D analysis, which was made in chapter 6 using PLM and FIB-SEM techniques. The 3D analysis showed a similar measurement of total porosity in PCEA and PCIB graphite grades to those obtained from random 2D measurements using PLM and SEM techniques.

Table 7.1: Summaries, the average of unit cell constants and coherence lengths for different samples of virgin nuclear graphite, collected from 20 measurements for each sample, obtained using the Scherrer equation.

NG	lattice parameter (nm)		L_c (nm) **	L_c	Micro-strain	L_a (100) (nm)	L_a (110) (nm)
	(002)	(100)					
	<c >	<a >		(nm) ***	%		
HOPG	0.6702(2)	-*	85.2 (12)	107.3	0.5±0.1	-*	-*
PGA	0.6750 (4)	0.2466(1)	30.5(2)	70(5)	0.002±0.01	60.8 (8)	70.6(2)
GILSO	0.6755 (3)	0.2457(4)	19.2(3)	53(4)	0.004±0.01	48.8(6)	50.9(8)
PCEA	0.6760 (1)	0.2461(3)	25.7(4)	51(2)	0.003±0.01	43.4 (5)	64.3 (2)
PCIB	0.6754 (2)	0.2461(2)	23.1(2)	47(3)	0.003±0.01	42.0 (3)	60.0 (5)

*(-) there are no values presented here as the peaks were very weak. However, Gallego et al. (2013) reported the value of L_a equals to 54.4nm calculated from (110) peak.
** values obtained using the Scherrer equation (size includes strain).
*** values obtained using the Williamson-Hall plot to determine size and strain in <002>.

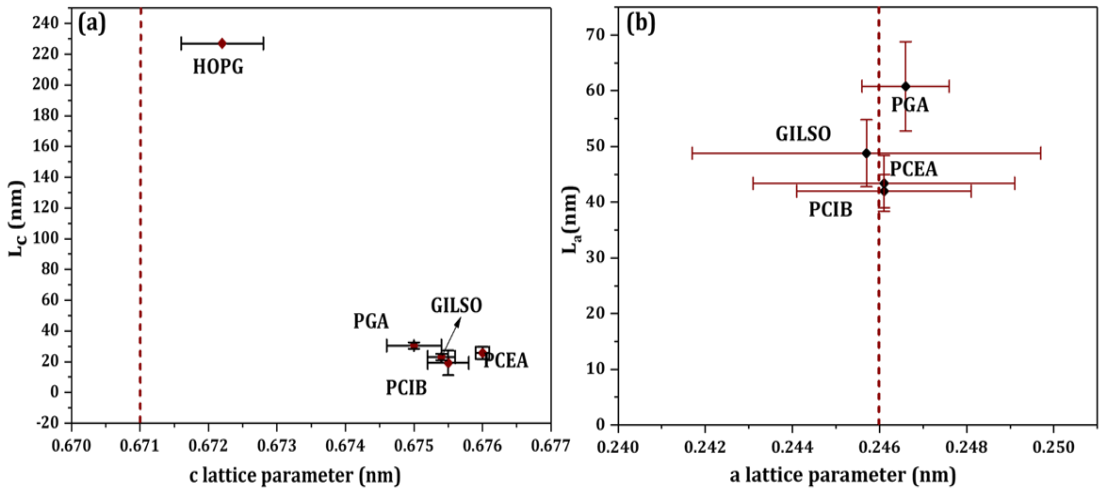

Figure 7.2: plots show the variation in the crystallographic properties of four different virgin nuclear graphite and HOPG in: (a) Coherent lengths inter-plane length L_c (002) and (b) in-plane L_a (100) versus the average interlayer spacing c and a-lattice parameters. The dashed lines represent the respective values for the perfect single crystalline graphite structure.

7.1.1.2 Summary of XRD results of virgin graphites

This section has provided a qualitative and quantitative analysis of different types of nuclear graphite that have been used in old and current nuclear reactors (PGA and Gilsocarbon) and the two possible candidates for VHTRs (Generation-IV), namely PCEA and PCIB graphites. Therefore, the microstructure of virgin nuclear graphites was studied in this Thesis using XRD, by analysing the d_{002} interlayer spacing along the c direction, the in-plane lattice parameter along a direction, and crystallite coherence lengths along the c and a directions.

The measurements obtained from refined parameters discussed in the previous section displays that the interlayer spacing $d_{(002)}$ is the main indicator for the degree of perfection of the nuclear graphite structure. The average $d_{(002)}$ interlayer spacings of all measured nuclear graphite samples were found to be close to 0.3377 nm. PGA nuclear graphite had a smaller average $d_{(002)}$ than the nuclear graphites, which confirms that PGA has a higher degree of perfection. The smaller the interlayer spacing $d_{(002)}$, the larger the crystallite size (L_a and L_c), as shown in Table 7.1. Consequently, the fraction of stacking faults and random shifts is smaller in PGA than in other tested nuclear graphite grades. However, no significant differences among other nuclear graphites were observed in the c

and a- axes lattice parameters. In general, the coherence lengths vary and range from 23-31nm, 33-64 nm and 42-70 nm for L_c (002), L_a (100), and L_a (110), respectively. The L_c values of nuclear graphites were much smaller compared to HOPG which is >200 nm. The small values of L_a and L_c attained in this work suggest that PCEA and PCIB nuclear graphite grades are highly disordered graphites compared to PGA and Gilsocarbon samples.

The findings were in agreement with previous studies (Zhou et al., 2014; Krishna et al., 2017; Freeman et al., 2017). However, it is noticeable that the measured L_c values appear to be lower than the values reported in the literature. This is because L_c values extracted using only the Scherrer equation are lower than those reported in the literature. However, when strain is considered using the W-H plot for L_c, values are given which are close to those found in the literature, by around 86% for PGA, 92% for Gilsocarbon, 78% for PCEA. However, for PCIB, no values have previously been reported, which are not considered a strain, as there have been few studies investigating this type of graphite (e.g., Mironov, 2014). The findings of virgin PCEA and PCIB nuclear graphites agree with Mironov (2014), who also examined the same samples (PCEA and PCIB) in her work. However, new measurements and analysis were applied in the present work.

In addition, the significant consistency between the results obtained in this section using Rietveld refinement analysis and previous studies indicate that the data obtained by this approach is universal. Although samples are made from different raw materials and manufactured using different processing methods, the microstructural properties revealed by XRD follow a generic behaviour.

Comparing the XRD findings to results from chapter 5, both virgin PCEA and PCIB graphite grades are less porous than PGA and Gilsocarbon graphite and demonstrating small average pore size. This observation of porosity also confirmed from the 3D analysis that was made in chapter 6 using PLM and FIB-SEM techniques. This analysis showed a similar measurement of total porosity in PCEA and PCIB graphite grades to those obtained from random 2D measurements using PLM and SEM techniques.

7.1.2 The influence of neutron irradiation on nuclear graphite analysis by XRD

7.1.2.1 Results and discussion

Five neutron-irradiated samples were reanalysed in this study; the XRD raw data of irradiated specimens were collected and analysed by Mironov (2014) (the work of irradiated samples was not possible to be performed by the author of Thesis due to health and safety considerations). However, the raw data was independently reanalysed and interpreted by the author of this work. Although the software program X´pert High Score Plus was used in both this work and in Mironov (2014), the analysis procedure was different. Mironov used a line profile refinement to analyse virgin and irradiated materials, however, few specific details can be found in her work on this, while the full Rietveld refinement method was adopted in this work, which is a statistical-based modelling approach. Therefore, the experimental diffraction profiles were modelled using a Pseudo-Voigt (pV) shape function. In accordance with the Rietveld refinement, fitting involved a non-linear least-squares refinement of deconvoluted theoretical line profiles until they matched a measured diffraction line profile. The d-spacings, crystallite size, and micro-strain were then measured using the fitted peak parameters.

Figure 7.3 shows XRD plots for both PCEA and PCIB nuclear graphite samples virgin and neutron-irradiated graphites. The calculated unit-cell parameters and coherence lengths are listed in Table 7.2 (collected from a total of 20 measurements for all irradiated samples) and micro-strain Table 7.3. The data presents changes following irradiation. For instance, the (002) and (004) peaks appear to broaden, and as the dose increases, the (103) and (006) peaks become more diffuse and finally disappear. This can be seen in the results from samples treated with the highest dose levels and temperatures. Also, some peaks, such as the (100) peak, were shifted to a higher 2θ angle indicating a decrease in the a-lattice parameter; the opposite was true for the (002) peak and hence the c-axis. Compared to virgin specimens of the same grade, XRD diffractograms of the two nuclear graphite samples illustrated that crystallite sizes L_c and L_a decreased by roughly 55% and 42%, respectively, for PCEA sample at low-dose, low-temperature (1.5 dpa and 350 ˚C), while in the high-dose, high-temperature

sample (6.8 dpa and 670 ˚C), the crystallite sizes were reduced by roughly 46% and 48% for L_c and L_a, respectively. In contrast, for PCIB samples L_c and L_a decreased by approximately 64% and 47% at low-dose, low-temperature (1.5 dpa and 350 ˚C), while in the high-dose, high-temperature sample L_c was reduced by 60% and L_a by 52%. Figure 7.4 shows changes in the (002) Peak widths and positions with increasing doses and temperatures of PCEA and PCIB nuclear graphites.

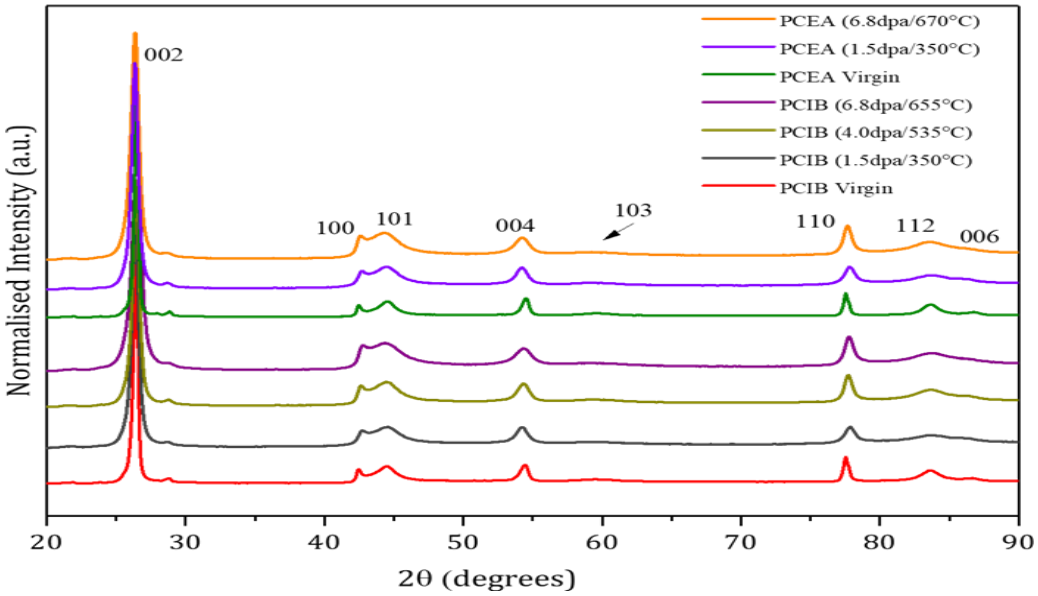

Figure 7.3: Measured XRD patterns of virgin and irradiated PCIB and PCEA.

Table 7.2: Summaries the average of unit cell constants and coherence lengths for different samples of virgin and irradiated nuclear graphite.

NG	Dose	Irr. Temp.	c lattice parameter from (002)	a lattice parameter from (100)	L_c	L_c W-H	L_a (100)	L_a (110)
	dpa	˚C	nm	nm	nm	nm	nm	nm
PCEA	-	-	0.6760 (1)	0.2461 (3)	25.7 (4)	51(2)	64.3 (2)	43.4 (54)
	1.5	350	0.6776 (2)	0.2442 (1)	14.0	28.6	26.7	14.8
	6.8	670	0.6779 (2)	0.2433 (2)	11.8	25.6	30.6	29.1
PCIB	-	-	0.6754 (2)	0.2461 (2)	23.1 (20)	47(3)	60.0 (45)	42.0 (29)
	1.5	350	0.6766 (2)	0.2445 (2)	14.7	28.7	28.4	25.4
	4.0	535	0.6769(3)	0.2435 (3)	15.1	26.3	29.3	23.2
	6.8	655	0.6771(3)	0.2433(1)	14.0	25.4	31.2	20.4

Table 7.3: A summary of the measured micro-strain using Williamson-Hall Plot.

Specimen	Dose	Irr.Temp.	Micro-Strain
	dpa	˚C	%
PCEA	-	-	0.21±0.02
	1.5	350	0.42±0.11
	6.8	670	0.56±0.13
PCIB	-	-	0.19±0.01
	1.5	350	0.41±0.12
	4.0	535	046.±0.32
	6.8	655	0.53±0.21

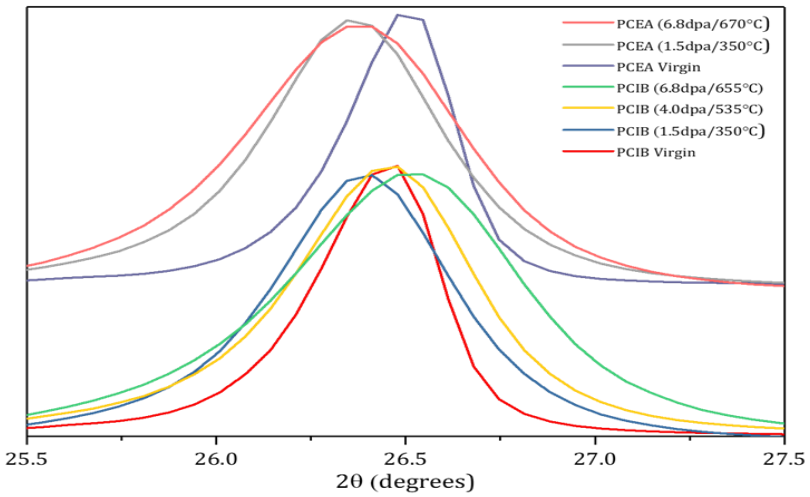

Figure 7.4: Changes in the (002) Peak with Irradiation of the measured Nuclear graphites PCEA and PCIB.

Comparing the findings of this work to Mironov's (2014) findings, it was revealed that Mironov did not demonstrate any general trends with increasing doses. However, the reanalysed data here shows a clear trend of expansion in the c-axis and a reduction in a-axis as the dose increased, as seen in Figure 7.5 and 7.6.

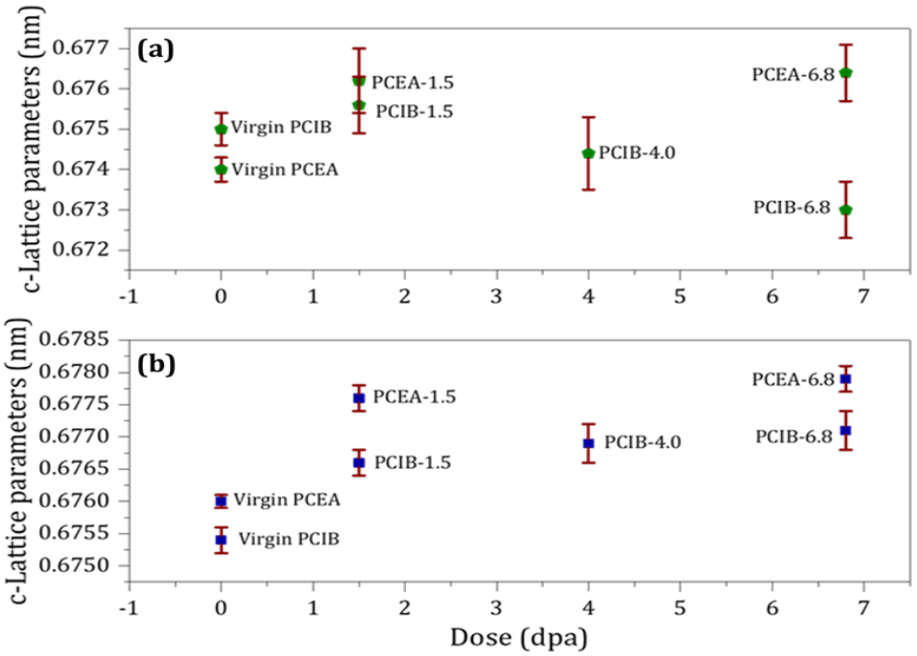

Figure 7.5: A comparison of the change of the c-lattice parameters (a) data from (Mironov, 2014) and (b) values obtained in this work for virgin and irradiated (nuclear) graphite with the variation of dose(/temperature).

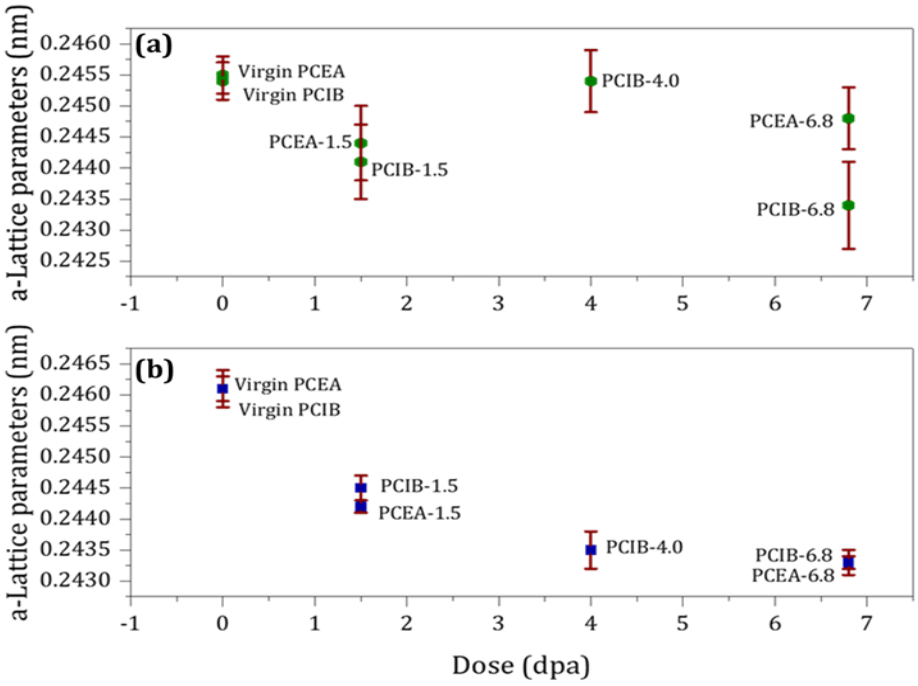

Figure 7.6 A comparison of the change of the a-lattice parameters (a) data from (Mironov, 2014) and (b) values obtained in this work for virgin and irradiated (nuclear) graphite with the variation of dose(/temperature).

Figure 7.7 and 7.8 also show comparisons between the values of the crystallite sizes, L_c and L_a obtained from Mironov (2014), and values measured in this work. In comparing Figure 7.7 (a) and Figure 7.7 (b) to the virgin

specimens of the same grade, XRD measurements of the two nuclear graphite samples illustrated that crystallite sizes L_c decreased as the irradiation dose and temperature increased. The reduction in the $L_{a\ (110)}$ crystallite sizes was also evident for PCEA samples, which is in line with Mironov's work. In contrast, the PCIB samples showed a different trend to Mironov's work; it had a clear decreased trend of 23% (compared to the PCIB virgin samples) as the dose increased, while Mironov's trend increased by 8% (compared to the PCIB virgin samples), as the dose increased.

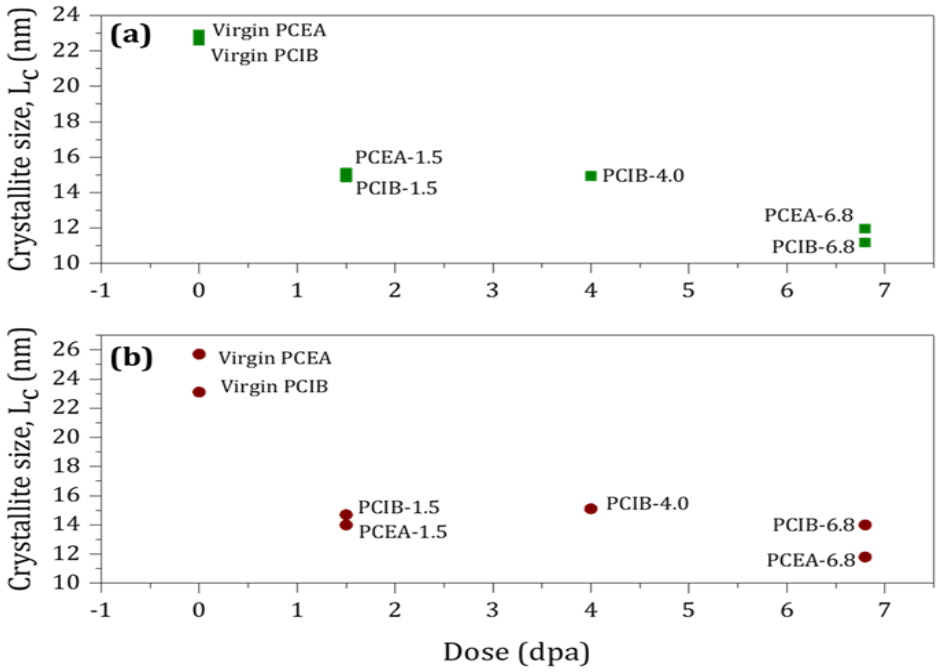

Figure 7.7: A comparison of the change of the crystallite size L_c (a) from (Mironov, 2014) and (b) values obtained in this work for virgin and irradiated (nuclear) graphite with the variation of dose(/temperature).

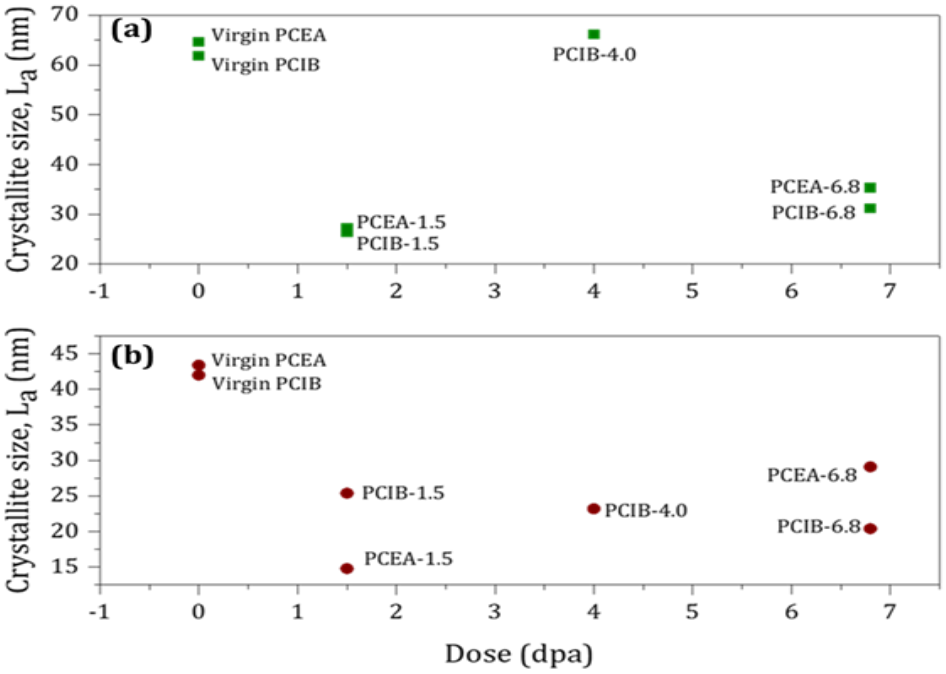

Figure 7.8: A comparison of the change of the crystallite size, $L_{a\,(110)}$ (a) from (Mironov, 2014), and (b) values obtained in this work for virgin and irradiated (nuclear) graphite with the variation of dose(/temperature).

The results also agree broadly with the findings of Gallego et al. (2013) on HOPG, but with a rather smaller reduction in crystallite size observed in this study. Vreeling et al. (2008) reported a bulk dimensional change of PCEA and PCIB graphite irradiated similarly, between 6 and 10 dpa at 750 °C. They found more shrinkage in the direction of the grain (parallel to the extrusion direction) than against the direction of the grain. The present results show a similar trend, but PCEA was given a higher irradiation dose (6.8 dpa) is more affected against the grain, showing a significant reduction in the crystallite size in agreement with the results of Krishna et al., (2017). The preferred crystallite orientation is likely to be along the direction of the grain, which can be utilised to relate polycrystalline properties to crystalline properties (Marsden et al., 2008).

7.1.2.2 Summary of XRD results of irradiated graphites

To conclude, five neutron-irradiated samples were reanalysed in this work ranged from 1.5 to 6.8 dpa and irradiation temperatures varied between 350 °C and 670 °C using X-ray diffraction. This enables to determine how the crystal structure varies between virgin and neutron irradiation graphite. Thus, XRD

measurements were used to acquire quantitative data regarding various properties of the crystal lattice.

The main findings of this work are as follows:

- As the irradiation doses and temperatures increased, both PCEA and PCIB nuclear graphites showed an expansion in the c-lattice parameter and a shrinking in the a-lattice parameter.
- XRD measurements of neutron-irradiated samples exhibit a decrease in the crystallite sizes L_c and L_a for both PCEA and PCIB samples at lower dose and temperature and therefore have higher structural damage. At higher dose and temperature, the reduction in crystallite sizes (L_c and L_a) varied between samples; the crystallite size L_c for PCEA 6.8dpa/670 ˚C continues to decrease to some degree, while the crystallite size L_a showed a slight increase from the values of the sample irradiated at 1.5 dpa. Nevertheless, the increased value is still lower in comparison to the virgin value. Whereas for PCIB samples irradiated to 4.0 dpa/535 ˚C, the crystallite sizes L_c and L_a appeared to be first constant, and then it started to reduce slightly as the irradiation dose and temperature increased (PCIB 6.8 dpa/655 ˚C). Overall, the results were shown to be in line with Mironov (2014), with the exception of the L_a crystallite size of PCIB (4.0 dpa/535 ˚C); this size decreased in the present analysis, while it increased in Mironov's analysis.
- The final conclusion is based on the extracted XRD data; micro-strain of both virgin and irradiated nuclear graphites (Table 7.3). It was shown that irradiated graphites exhibit higher micro-strain values compared to virgin graphites. The latter confirmed the significant changes to the structure of the materials post-neutron irradiation, and therefore crystallite size loses much of its physical significance.

7.1.3 Raman scattering of various types of defects in virgin nuclear graphite

7.1.3.1 Results and discussion

Figure 7.9 compares Raman spectra for the different types of polycrystalline virgin graphite and the reference graphite, HOPG. Nuclear graphite is characterised by its two first order prominent lines: the disorder-induced D band or defect (A_{1g} mode) observed at ~1356 cm^{-1} and the active G band (E_{2g} mode) at ~1583 cm^{-1}. The latter arises from the stretching of sp^2 bonded carbon atoms in both chains and rings. The D band is very sensitive to structural change, and most of the literature attributes the D band to the presence of defects in the lattice. As the quantity of defects rises, there are more transitions giving rise to the D band. Therefore, the intensity ratio I_D/I_G is used as an indicator of the defect density in nuclear graphite. Moreover, polycrystalline graphite (PGA, GILSO, PCEA, and PCIB) spectra show a distinct weak D' band at ~1623 cm^{-1}.

The first-order Stokes-Raman spectrum of HOPG specimen shows a relatively near-perfect graphite crystallographic geometry, and the I_D/I_G ratio is zero because there is no D band observed in the spectrum (Figure 7.9). This is because the A_{1g} mode is forbidden in perfect graphite (HOPG) and only becomes active in the presence of disorder. In addition to the G peak, a band is observed at 2700 cm^{-1}, which in agreement with Ferrari and Robertson (2000), McDermott (2012), and Krishna et al. (2016) for HOPG. These studies also reported that the Raman G peaks of HOPG show almost negligible residual stresses.

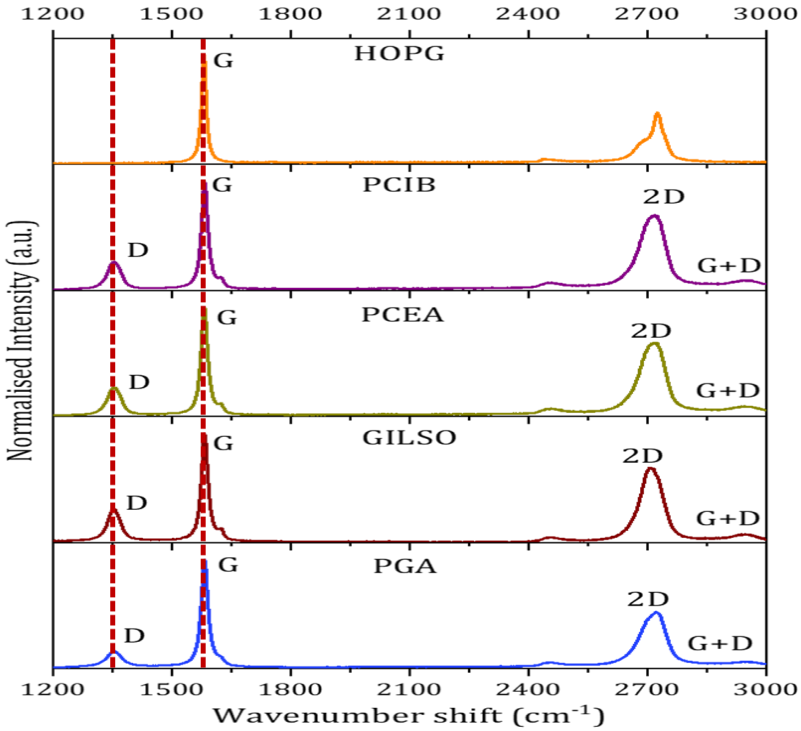

Figure 7.9: The normalised room temperature Raman spectra of different virgin nuclear graphites.

Figure 7.10 shows comparisons between Raman spectra of filler and binder regions for PGA, GILSO, and PCEA nuclear graphite as the filler particle sizes were large enough to be analysed under the optical microscope associated with the Raman spectrometer. For PCIB, it was difficult to distinguish filler particles due to the fine microstructure. As can be noticed, PGA, Gilsocarbon and PCEA binder regions tend to have a larger FWHM of the G peak and a higher I_D/I_G ratio than observed in filler particles (Table 7.4). This is due to the differences in defect population, and also the fact that there are many more crystallite boundaries as the crystallite size is smaller in the binder than in filler particles. Furthermore, PGA, Gilsocarbon, PCEA and PCIB nuclear graphites reveal the presence of residual stresses that developed during the manufacturing process, causing polarisation-dependent shifts. These shifts are detected to be dependent on internal stress values (Krishna et al., 2015). Table 7.4 and 7.5 list the shifts in the Raman G peaks due to the presence of internal stresses in the virgin nuclear graphite grades and list L_a values, which have been derived from equation (4.14) in chapter 4 (section 4.1.4.3.1).

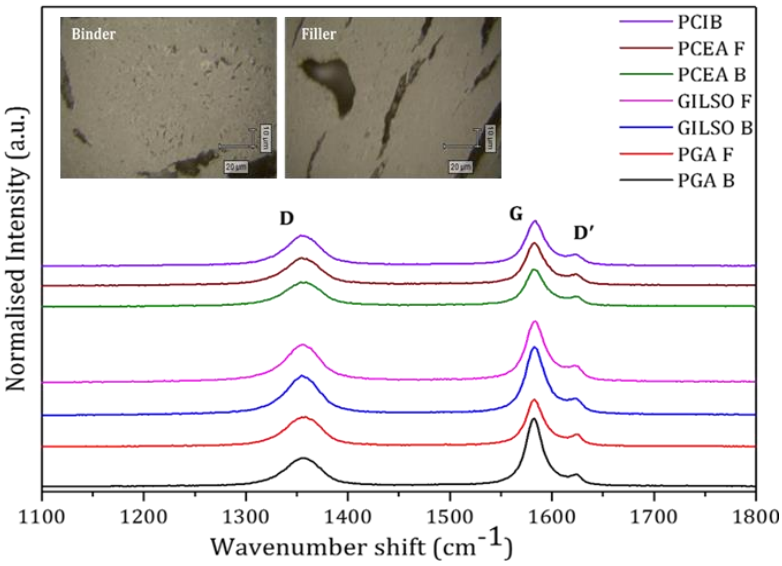

Figure 7.10: The normalised room temperature Raman spectra of virgin nuclear graphite collected from both binder regions (B) and filler particles (F) in different nuclear graphite. Example micrographs of Gilsocarbon graphite show both filler and binder areas which are easily distinguishable.

Table 7.4: The average Raman spectra of virgin nuclear graphite collected from both binder (B) and filler (F) particle samples (collected from 60 spectra per nuclear graphite sample). L_a values have been measured from an empirical equation (4.14), see chapter 4.

Nuclear Graphite	I_D/I_G	L_a nm	FWHM of G peak [cm^{-1}]	Raman shift [cm^{-1}]		
				D	G	D'
PGA-Binder	0.18(9)	93.4(1)	21.1(4)	1352.4(1)	1581.4(9)	1621.1(2)
PGA-Filler	0.11(6)	152.9(1)	18.5(6)	1353.4(1)	1581.7(7)	1620.9(3)
GILSO-Binder	0.27(5)	62.3(2)	21.2(2)	1353.4(6)	1581.9(5)	1622.6(4)
GILSO-Filler	0.20(2)	84.1(1)	18.1(5)	1353.9(1)	1582.6(9)	1622.7(1)
PCEA-Binder	0.25(4)	67.3(3)	20.1(5)	1354.3(5)	1581.7(3)	1622.4(1)
PCEA-Filler	0.22(2)	76.4(2)	19.2(6)	1354.4(4)	1581.8(4)	1622.7(3)

Table 7.5 summarises the averages of the analysed data of Raman spectra collected from both binder and filler particles of virgin nuclear graphite samples: the Raman intensity ratio (I_D/I_G) and the FWHM of the G band ($FWHM_G$). The

intensity ratios for Gilsocarbon, PCEA, and PCIB graphites are higher than in PGA graphite moderators, but all specimens show similar values for the $FWHM_G$. PGA has much lower values for filler and binder regions due to the larger crystallite size (L_c and L_a), which is confirmed by XRD measurement (see Table 7.1) and Raman measurement of L_a, which have been measured from an empirical equation (4.14), see chapter 4. The L_a values obtained from Raman are strongly dependent on laser excitation energy (Zheng et al., 2014), and thus, the values are only for sample-to-sample comparison. The smaller value of L_a in PCIB results from a more homogeneous structure compared to PGA, Gilsocarbon, and PCEA. The calculated crystallite sizes L_a using the Scherrer equation (Table 7.1) are significantly smaller than L_a calculated from Raman spectra based on the intensity ratio of D band to G band. This is because the XRD L_a values are uncorrected for the strain, which would mean that they are potentially an underestimate. This data agrees with numerous literature sources, such as (Ferrari, 2007; Freeman et al., 2017; Krishna et al., 2015; Krishna et al., 2017; Knight and White, 1989; Mcdermott, 2012; Tuinstra and Koenig, 1970).

Table 7.5: Averages of analysed data of a total of 280 Raman spectra collected from HOPG samples and both binder and filler particles of virgin nuclear graphite samples. L_a values have been measured from an empirical equation (4.14), see chapter 4.

Grades	I_D/I_G	L_a	FWHM of G peak	First-order characteristics (Raman shift) [cm^{-1}]		
		nm	[cm^{-1}]	D	G	D'
HOPG	-	-	14.6(4)	-	1580.41(3)	-
PGA	0.14(1)	120.1(2)	19.8(8)	1353.07(1)	1581.54(8)	1621.05(1)
GILSO	0.24(7)	70.07(2)	19.6(8)	1353.75(9)	1582.18(8)	1622.62(1)
PCEA	0.23(5)	73.12(3)	19.6(7)	1354.31(4)	1581.79(4)	1622.60(2)
PCIB	0.26(1)	64.68(2)	19.9(8)	1354.20(3)	1582.21(4)	1623.11(4)

Figure 7.11 shows the negative linear relationship between the Raman intensity ratio and L_a, where the crystallite size L_a is obtained from XRD suggesting the presence of edge effects. However, the width of the G peaks in the virgin graphites exhibit no correlation with the crystallite size L_a and the slopes vary between grades due to their different microstructural characteristics. The

G peaks positions show less correlation, which decreases as the crystallite size L_a increase (PGA samples exhibited more strain than other types of nuclear graphite grades). Figure 7.12 allows a visual comparison of 60 measurements averaged over both filler and binder regions collected for each grade of graphite materials researched in this work. This was done to investigate the correlation between the disorder in the lattice, and the crystallite size L_a. Figure 7.12 reveals a positive linear correlation between I_D/I_G ratios and the $FWHM_G$ (G peak broadening), suggesting that defects also arise from lattice defects formed during processing. However, the slopes are different due to the differences in the microstructure of nuclear graphite grades with R-squared values that are 0.54, 0.59, 0.41, and 0.37 for PGA and Gilsocarbon, PCEA and PCIB graphites respectively. The broadening of the G peak is related to defects within the sp^2-bonded lattice. These defects contribute to the D band intensity. However, an additional important contribution arises from edge effects and defects associated with crystallite grain boundaries. The higher the correlation between $FWHM_G$ and I_D/I_G suggests the dominance of in-plane lattice defects. Whereas, a lower correlation would suggest the dominance of grain boundaries. As can be seen, all samples show a positive linear correlation between the $FWHM_G$ and the I_D/I_G intensity ratios (all have similar slope). However, PGA graphite has a higher correlation than other types (bigger slope and r^2 values), indicating the dominance of in-plane lattice defect with less edge effects at crystallite boundaries due to large crystallite size in PGA relative to other graphites. Whereas, Gilsocarbon, PCEA, and PCIB show a lower correlation indicating an increased contribution from crystallite grain boundaries due to their smaller crystallite sizes.

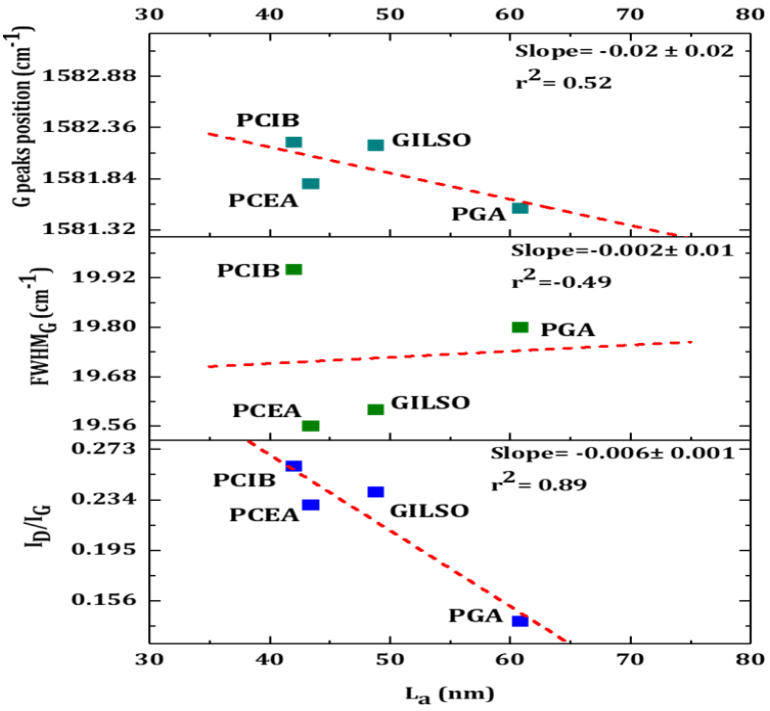

Figure 7.11: The variation of the I_D/I_G intensity ratios; $FWHM_G$ and G peak position from Raman spectra of different virgin graphite samples versus crystallite size L_a obtained from XRD.

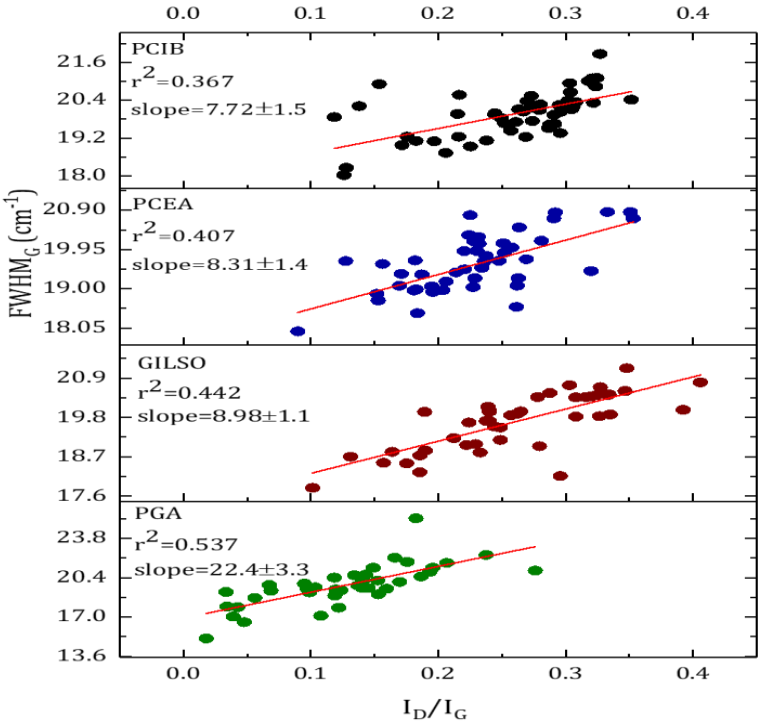

Figure 7.12: The intensity ratio I_D/I_G estimated by Raman spectra versus $FWHM_G$ for several nuclear graphite grades.

7.1.3.2 Summary of Raman results of virgin graphites

Raman spectroscopy was used to observe and quantify the microstructure of four different graphite grades; PGA, Gilsocarbon, PCEA, and PCIB. Different parameters were compared; in-plane crystallite size L_a, the intensity ratio I_D/I_G, and $FWHM_G$ to characterise the structural disorder in graphite grades. Raman spectroscopy helped to do separate measurements in filler and binder regions of different nuclear graphites. The findings showed that binder reign is more disordered. The main results for this section are summarised below:

- The Raman spectra of highly oriented pyrolytic graphite (HOPG) showed only one mode at 1582.6 cm^{-1} because the A_{1g} D breathing mode in perfect graphite (HOPG) is forbidden, while nuclear graphites exhibit a D band at ~1583 cm^{-1}. The I_D/I_G intensity ratio of the latter is inversely proportional to the effective crystallite size L_a measured by XRD. Thus, the D band intensity is partially attributed to disorder at crystallite boundaries, which can be used to measure L_a. However, the positive correlations between I_D/I_G ratios and the $FWHM_G$ suggest that lattice defect also contributed significantly to the D band intensity.

7.1.4 Raman scattering of various types of defects in neutron-irradiated nuclear graphite

7.1.4.1 Results and discussion

The Raman spectra of irradiated specimens were collected by Mironov (2014). However, in depth analysis was followed in this work. While, Mironov outlined a few specific details about the fitting procedure, in this work, non-linear fitting of the peaks was done manually by fitting each peak centre. In addition, a Lorentzian function was used to fit D′ bands. The analysed Raman peak profiles were then used to investigate the intensity ratios of D and G bands, the FWHM of G peak, the lateral crystallite size (L_a), internal stresses and lattice disorder.

Figure 7.13 displays the Raman spectra for both virgin and irradiated PCEA and PCIB samples. Table 7.6 lists the averages of the examined data extracted from the Raman spectra by peak fitting. The dashes in Figure 7.13 compare the virgin and irradiated graphite samples and confirm that damage has occurred to the microstructure of PCEA and PCIB samples after neutron irradiation. This damage is evident because the D peak becomes broader and intensifies after irradiation as compared to the virgin samples. The FWHM of the G peak increases, due to the accumulation of irradiation-induced defects and their clusters in the lattice. This accumulation of defects causes the crystallites to fragment (Krishna et al., 2015; Ferrari and Robertson, 2000). The intensity ratio (I_D/I_G) and FWHM of the G peak are associated with the concentrations of interstitials/vacancies and their clusters. The I_D/I_G ratio is significantly higher for irradiated graphite samples than for virgin samples, as presented in Table 7.6. The clearest changes occurred to PCEA and PCIB, when both were subjected to low dose irradiation (1.5 dpa) and low temperature (350˚C), confirming the XRD results discussed earlier. As irradiation dose and the temperature are raised, some increase in the I_D/I_G ratio is still apparent (PCEA: 6.8 dpa / 670 ˚C and PCIB: 6.8 dpa / 655 ˚C).

Conversely, following irradiation, the average lateral crystallite size L_a of the two graphites tested was found to decrease in agreement with XRD results. Distinct but faint D′ peaks are another indication of increased disorder and can be assigned to the micro-crystallinity of the graphite. At low doses and temperatures (1.52 dpa / 350.9 ˚C), this peak exhibits a similar tendency to

broaden and weaken or is subsumed under the G peak that has increased in wavenumber. However, at higher doses and temperatures (6.8 dpa / 670.7 ˚C and 656.9 ˚C) the G peak broadens less, and the D′ peak is again observed at approximately1625 cm^{-1}.

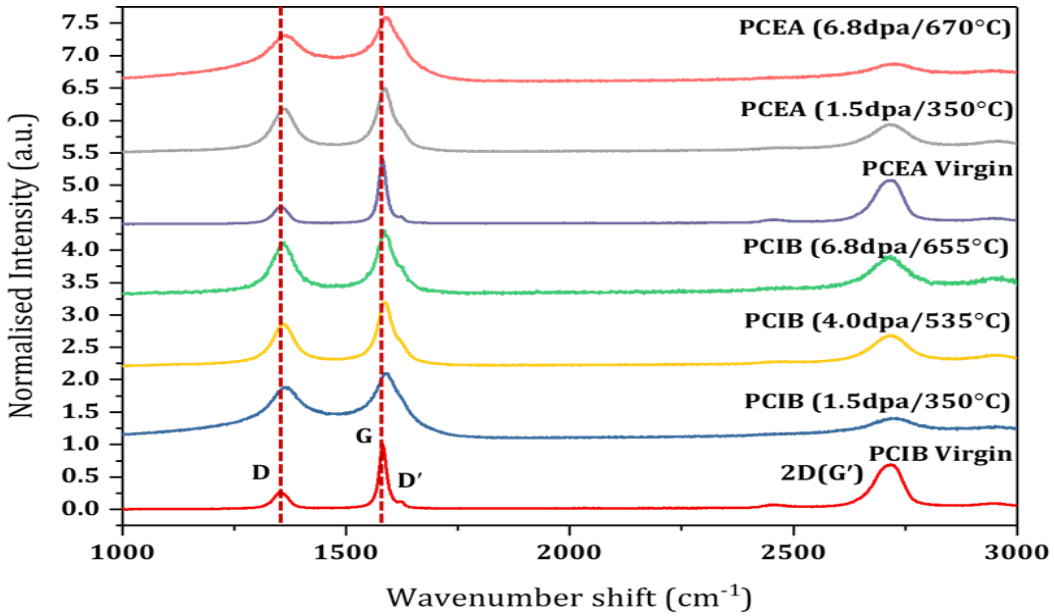

Figure 7.13: Raman spectra in the 1000-3000 cm^{-1} wavenumber range of raw of nuclear graphite grades, both virgin and irradiated.

Figure 7.14 shows the Raman G line in virgin and irradiated graphites. The G peaks in irradiated graphites shifted to a higher frequency particularly at lower dose/ temperature due to the presence of internal stresses, as shown in Figure 7.14 and Table 7.6. This agrees with XRD results. Raman spectroscopy also can be used to evaluate internal stress distribution in the filler and binder regions of nuclear graphite. It was difficult to estimate the stress in cracks and pores in the filler and binder phases separately as the measurement of the specimens had been taken randomly by (Mironov, 2014). Krishna et al. (2015) investigated residual stresses in PGA, Gilsocarbon, and NBG-18 graphite and then authors concluded that the filler is always under tensile forces, while the binder is mostly under compression.

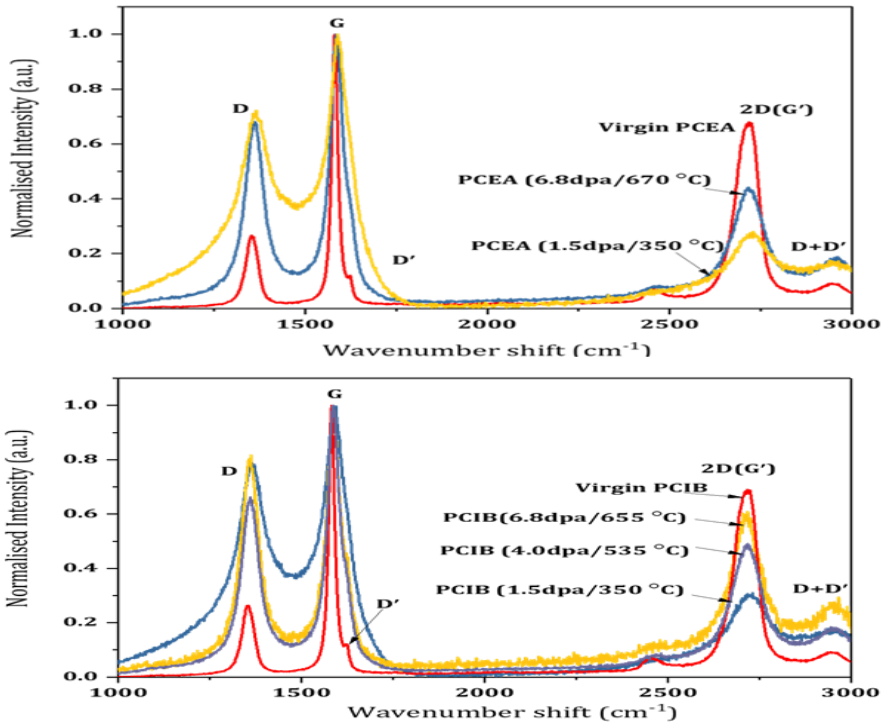

Figure 7.14: Raman spectra of raw virgin and irradiated nuclear graphite grades, showing filler–binder region of PCEA (top) and PCIB (bottom). The shifting of G peak towards the left and right directions indicates compressive residual and tensile stresses in the structure respectively.

Table 7.6: Total averages (across filler and binder regions) of analysed data of Raman spectra of virgin and irradiated nuclear graphites.

Nuclear graphite	Dose	Temp.	I_D/I_G	L_a	FWHM of G peak [cm^{-1}]	First-order characteristics (Raman) [cm^{-1}]		
	dpa	°C		nm		G	D	D'
PCEA	-	-	0.23(5)	73.12	20(7)	1583(7)	1354(1)	1623(1)
	1.5	350	0.70(1)	24.02	89(7)	1592(2)	1365(2)	-
	6.8	670	0.73(1)	23.04	56(4)	1595(1)	1363(1)	1625(2)
PCIB	-	-	0.26(1)	64.68	20(8)	1582(4)	1354(3)	1623(4)
	1.5	350	0.81(1)	19.78	69(6)	1590(2)	1362(3)	-
	4.0	535	0.84(1)	21.02	48(3)	1588(1)	1359(2)	-
	6.8	655	0.87(1)	19.33	51(3)	1589(1)	1360(1)	1624(2)

Figure 7.15 and Figure 7.16 shows the correlation between FWHM of the G peak and the I_D/I_G ratios for virgin and irradiated samples. Virgin samples show a significant correlation, which indicates crystal edge effects are reduced as the crystallite size is larger and disorder predominantly arises from lattice defects such as interstitials and vacancies and their clusters, which results in the

disordering of the basal planes. With increasing irradiation, this correlation is reduced as the crystallites fragment. Although PCEA still shows some remaining correlation, which may indicate less grain fragmentation. This could be due to the fact that PCEA is extruded and has around 60% needle-like filler particles. In general, all obtained findings agree with XRD data and are in line with other studies, such as Freeman et al. (2017), Krishna et al. (2015), Krishna et al. (2017), Gallego et al. (2013) and Vreeling et al. (2012). The specific trends identified here are consistent with the general trends identified by Mironov (2014), although the improved fitting procedure and deeper data analysis provide additional insight into the microstructural changes.

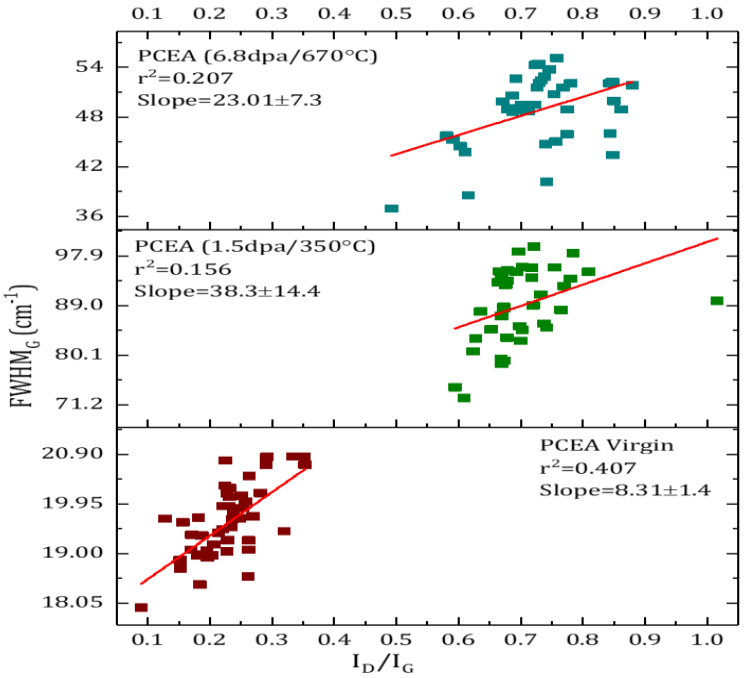

Figure 7.15: The $FWHM_G$ versus I_D/I_G intensity ratio for virgin and irradiated PCEA.

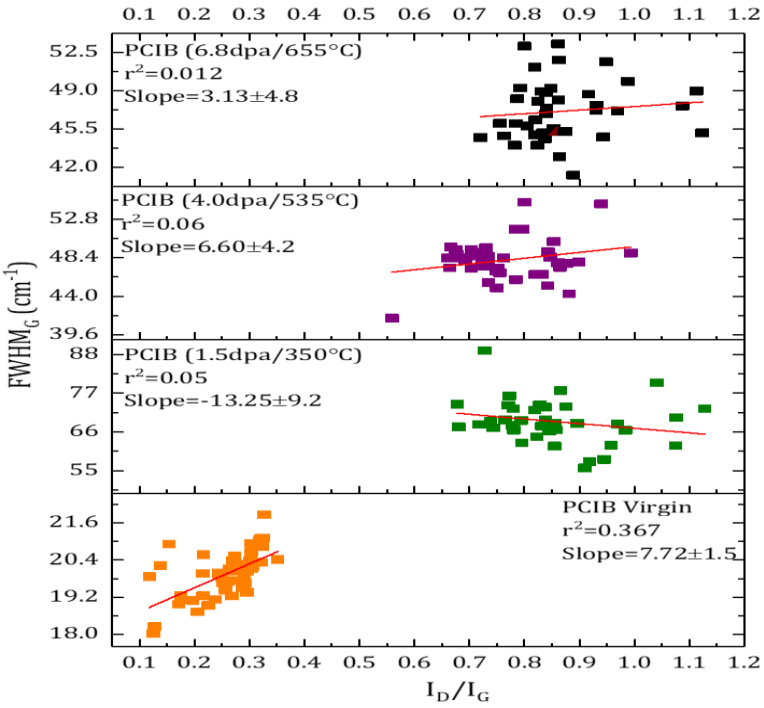

Figure 7.16: The $FWHM_G$ versus I_D/I_G intensity ratio for virgin and irradiated PCIB.

Figure 7.17 shows the negative linear relationship between the Raman I_D/I_G ratio and L_a, where the crystallite size L_a is obtained from Raman for both virgin and irradiated graphites. As can be seen, PCIB graphites show a better correlation than PCEA graphite (Figure 7.17 (a)). Conversely, Figure 7.17 (b) shows the crystallite size L_a versus the change in the FWHM of G peaks that clearly increases at lower doses/temperatures for both PCEA and PCIB graphites and at higher doses/temperatures start to decrease the width of G peaks. Figure 7.18 (a) shows the variation of the intensity ratio of both samples PCIB and PCEA graphites as a function of the irradiation dose, whilst Figure 7.18 (a) illustrates the corresponding change of the FWHM of G peaks. At low dose/ low temperature both I_D/I_G and $FWHM_G$ increase. At higher dose/higher temperature, the I_D/I_G remains relatively constant; however, the $FWHM_G$ decreases significantly as lattice defects are annealed out.

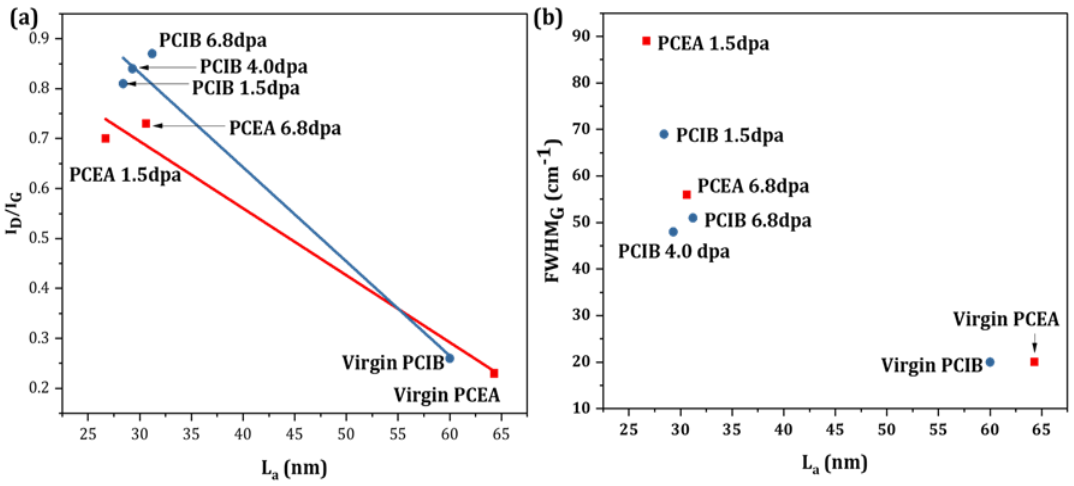

Figure 7.17: Plots of the crystallite size (L_a) obtained from XRD versus (a) the intensity ratios from Raman spectra of virgin and irradiated graphite samples; (b) the FWHM of G peaks.

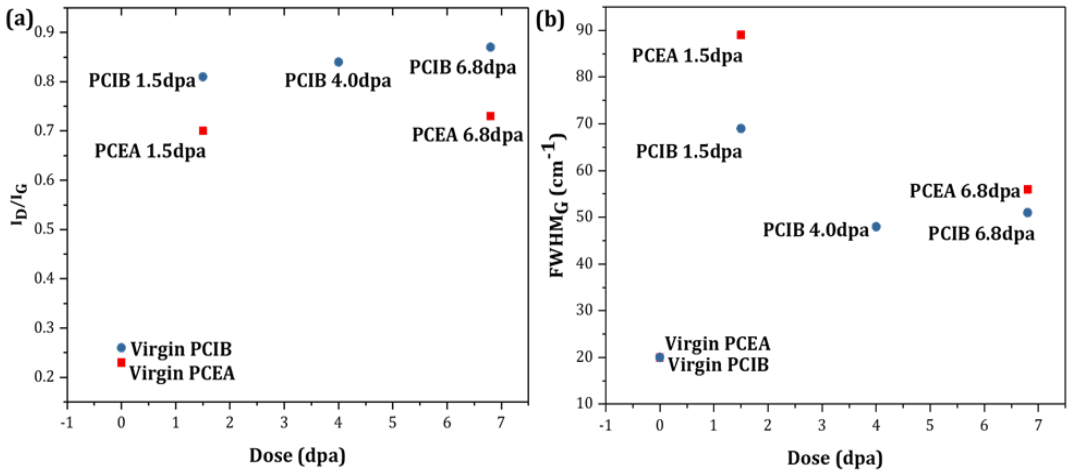

Figure 7.18: (a) the of intensity ratio of virgin and irradiated graphite samples and (b) the FWHM of the G peaks versus irradiation dose.

To summarise, Figure 7.19 presents an overall comparison of the average values estimated for the crystallite size of both virgin and neutron-irradiated samples (PCEA and PCIB) obtained by both XRD and Raman spectral analysis. These results correlated well with one another (note that XRD $L_{a\,(100)}$ values here have not been corrected for strain, so L_a values are low). Calculations of variation revealed the limits of variability to be approximately 11%, 13%, and 37%, for virgin PCEA, PCEA 1.5, and PCEA 6.8 respectively and 8%, 30%, 28%, and 38%, for virgin PCIB, PCIB 1.5, PCIB 4.0 and PCIB 6.8 respectively. The virgin PCEA and PCIB graphite exhibited the lowest differences between the Raman and XRD derived values, while the steady changes in the neutron-irradiated PCEA and

PCIB graphites exposed to higher irradiation doses and temperatures were found to present larger differences. Figure 7.16 also shows that this behaviour is almost universal and independent of these samples, which suggests a universal mechanism.

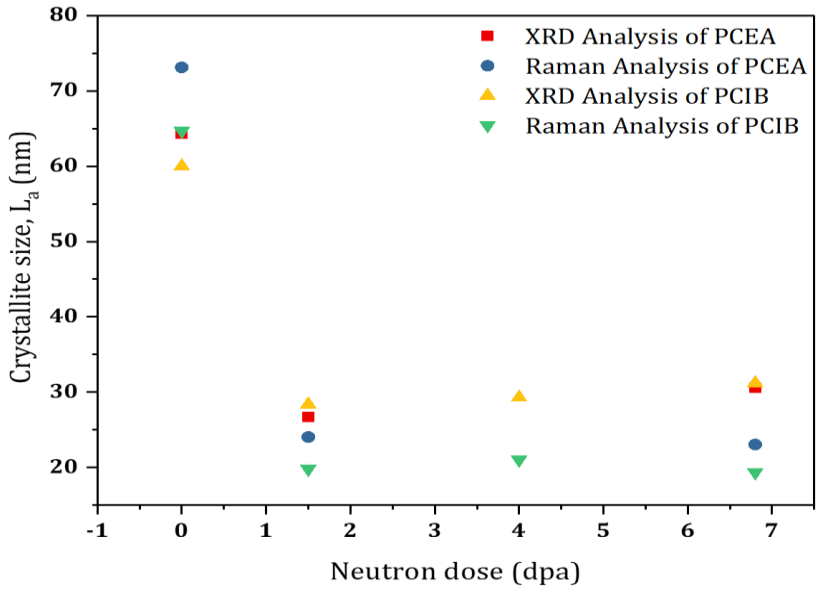

Figure 7.19: Comparison of results from XRD and Raman spectroscopy show variation for crystallite size, $L_{a\,(100)}$.

Moreover, the micro-strain obtained by XRD (Table 7.3) showed a significant increase in the irradiated samples compared to their virgin values for both PCEA and PCIB graphite samples. This was evident also from shifts in the Raman G peak, which indicated the strain produced in the irradiated neutron samples. In the PCEA and PCIB graphite, the micro-strain became more apparent with increasing irradiation doses and temperatures.

Although there are differences between Raman and XRD derived values, both techniques showed the damage to be more evident in samples exposed to lower neutron irradiation doses and temperatures. These results seem to agree with the PLM and SEM images analysis in chapter 5, where the examination of PCEA and PCIB nuclear graphites illustrated that neutron irradiation causes significant damage to the structure of irradiated samples. After irradiation, the graphite crystals were fragmented and became smaller with increased porosity. At higher irradiation doses and temperatures, the statistical analysis of porosity exhibited no significant differences compared to lower doses and temperatures.

Although the variation in the XRD and Raman derived values, these findings proved that both techniques are complementary and are highly sensitive to small changes in the microstructure.

7.1.4.2 Summary of Raman results of irradiated graphites

Raman spectra were used to quantitatively calculate the characteristic crystallite size (L_a), stress, and the lattice disorder across sub-surface areas of the graphite samples. Raman spectra confirmed that neutron irradiation induces structural damage to the nuclear graphite, indicating the formation of lattice defects and the fragmentation of crystallites. The most significant finding is that low dose and temperature samples showed more damage compared to higher irradiation doses and temperatures, which is most likely because defects are less mobile at low temperatures. By increasing irradiation dose and temperature, the average crystallite size (L_a) of the PCEA and PCIB graphite decreased with significant increases in both the intensity ratio of D and G peaks and the G-peak width.

Nevertheless, no significant difference in Raman features was observed between PCEA and PCIB graphite. Although there is a limitation in these results because the analysis of specimens was taken randomly, thus proved difficult to distinguish stresses in cracks and pores in both filler and binder regions. One of the main implications of the findings is that the quantitative analysis of both virgin and irradiated PCIB further the literature, as there is limited quantitative analysis on the same graphite grade.

Chapter 8

This chapter summarises the experimental work on virgin and neutron-irradiated nuclear graphite discussed earlier in the Thesis by analysing the findings and stating their important and novel observations and interpretations. That is, the present chapter summarises the main findings of chapters 5, 6, and 7 and provides a comparison of their observations from each technique used with reference to the existing literature and current understanding of irradiation damage. The final section concludes the Thesis by suggesting future experimental work that can extend or enhance the understanding of the irradiation-induced damage in nuclear graphite.

8.1 Concluding remarks

To begin, this Thesis attempted to address the following questions:

2. How does neutron irradiation affect the structure of nuclear graphite grades at micro and nanoscale? How are these changes affected by neutron radiation dose and temperature?
2. What measurement techniques help to quantitatively evaluate these changes for both virgin and irradiated nuclear graphite?

Overall, the findings of chapters 5, 6, and 7 confirmed that the combination of PLM, SEM, XRD, Raman, and FIB-SEM techniques facilitate an assessment of the crystallinity and porosity of both virgin and neutron-irradiated graphites at different length scales. A more detailed summary of these findings is provided below.

8.1.1 Structural classification of nuclear graphite

The aforementioned techniques were used in this Thesis to determine the structure of the nuclear graphite at different length scales. Based on the results obtained from using these techniques in chapters 5, 6, and 7, there are three dominant structural characteristics in all types of nuclear graphite; the amount of the coke filler used, pitch-based binder, and porosity, which are supported by

many previously published studies and papers (e.g., Aitkaliyeva, 2017; Heijna et al., 2017; Kane et al., 2011; Zhou et al., 2017a). Understanding these components can be used to develop a model for structure-property predictions, particularly under irradiation, because the nuclear graphite is still considered to be a neutron moderator and structural support material for Generation-IV nuclear reactors.

Although several models regarding this subject have been published, still there are no full multi-scale models, particularly for those grades suggested for Generation-IV reactors. The measurements of this Thesis enabled to distinguish and evaluate four virgin nuclear graphites at different length scales; macro, micro, and nanoscale. Hence, Figure 8.1 depicts a structure-based full multi-scale model from the macroscale to the nanoscale level. This Figure describes the overall structure of [PGA, Gilsocarbon, and PCEA] the nuclear graphite qualitatively. However, as the main interest of this Thesis was the analysis of PCEA and PCIB nuclear graphite grades suggested for (V)HTRs, Figure 8.1 also provides quantitative characteristics of the PCEA nuclear graphite, which can be used to study the effect of neutron irradiation further. Figure 8.2 shows a schematic view of the structure of virgin PCEA nuclear graphite ((V)HTRs candidates). The following sections have attempted to define the structure of nuclear graphite at macro, micro, and nanoscale.

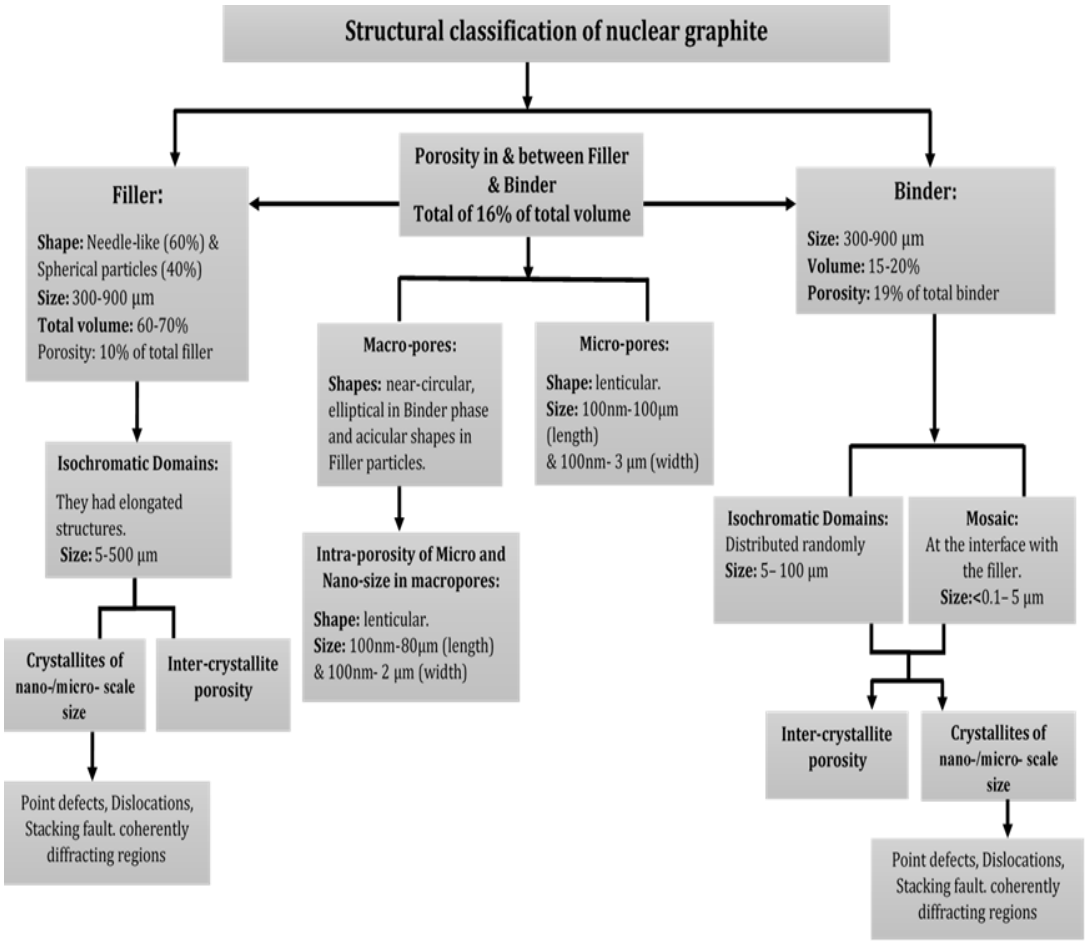

Figure 8.1: The structure of [PCEA] nuclear graphite at multi-scale levels.

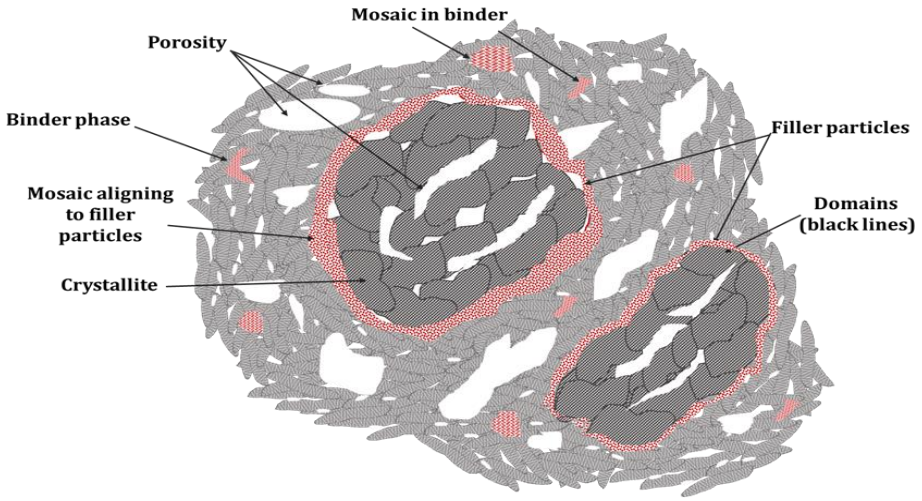

Figure 8.2: A schematic representation of the structure of PCEA nuclear graphite at a multi-scale level.

8.1.1.1 Structure at Macro-Scale

At the macro-scale, the nuclear graphite was divided into three main components: filler particle, binder phase, and porosity. The filler particles of PGA, Gilsocarbon, PCEA, and PCIB grades ranged from medium filler particles (PGA, Gilsocarbon, and PCEA) to ultrafine particles (PCIB). The shape of the filler particles also varied between grades: PGA had anisotropic needle-shaped filler particles, the quasi-isotropic Gilsocarbon grade had spherical filler particles, and the filler particles of PCEA grade varied, as almost 60% were needle-shaped, while 40% were spherical. The needle-shaped particles in PCEA were slightly smaller than those in PGA. These findings are in line with Bodel (2013), Kane et al. (2011), Marsden et al. (2008), and Taylor (2016), Wen et al. (2008).

By contrast, the fine microstructure of PCIB made it difficult to distinguish whether an area contained filler or binder particles. The binder phase also varied between grades (e.g., PGA has more finely-ground filler, which was mixed with coal tar or petroleum pitch residues (binder), compared to other grades). Porosity also varies at the macro-scale which was observed within the filler particles and binder phase (the maximum pore size found in this Thesis was ~1mm). These pores formed due to incomplete local packing, shrinkage of the binder-coke mix on carbonisation stage, and large-scale gaseous evolution channels arising from the release of gas and vapour decomposition products, during the manufacturing process. (Freeman et al., 2016; Hagos et al., 2010; Kane et al., 2011; Taylor 2016).

8.1.1.2 Structure at Micro-Scale

The understanding of nuclear graphite at the domain level is of significant interest because at micro-scale, both the filler particles and binder phase are shown to have separate domains and porosity. The domain texture is different for the filler particle and the binder phase, such as the intra-domain porosity, the orientation of porosity, and preferred orientation of layer planes within the domains. These parameters are critical as they have a connection with the structural parameters at the nanoscale, as shown in this Thesis; crystallite sizes decreased by neutron irradiation damage, which led to changes to local orientations within the domains.

PLM image analysis, therefore, was used to facilitate a qualitative and quantitative analysis of domains in different grades of virgin nuclear graphite. The analysis showed that isochromatic regions range in size from <0.1 μm to 500 μm, which was divided into two parts; (1) 'mosaics' of size <0.1– 5 μm, and (2) 'domains' of size <5– 500 μm. Separate domains have large angles of misorientation, while within domains, the corresponding crystallites have low angles of misorientation. The findings showed that the overall porosity at microscale of the PGA samples was ~20%, higher than in Gilsocarbon, PCEA, and PCIB graphite. However, the porosity within filler particles was higher in Gilsocarbon than in PGA or PCEA nuclear graphite (11.3%, 12.5%, and 9.5%, respectively).

8.1.1.3 Structure at Nano-Scale

At the nano-scale, domains in nuclear graphite were further sub-divided into crystallites and porosity using XRD, SEM, and FIB-SEM. The crystallite size obtained from XRD was shown to be larger than the PGA graphite crystallite size. Also, PGA was found to have a smaller interlayer spacing ($d_{(002)}$) compared to Gilsocarbon, PCEA, and PCIB. These crystallites were regarded as a large region of dislocations that were subdivided at an additional level corresponding to point defects, dislocations, and coherently diffracting regions.

Raman was used in order to characterise the structural disorder in graphite grades using the following parameters: the intensity ratio (I_D/I_G) and the FWHM of the G band ($FWHM_G$). The main conclusion was that the intensity ratios for Gilsocarbon, PCEA, and PCIB graphites are higher than in PGA graphite moderators, but all specimens showed similar values for the $FWHM_G$. PGA had much lower values for filler and binder regions due to the larger crystallite size (L_c and L_a), which was confirmed by the XRD measurement, as mentioned above.

8.1.2 Results of porosity analysis

For the first time using serial sectioning methods that employed different techniques (PLM and FIB-SEM), the porosity in nuclear graphite was further studied. The analysis of porosity from each of the aforementioned scales found to have different shape and size distribution. These techniques were adopted to

develop a 3D microstructural model of porosity in two forms of virgin nuclear graphite: PCEA and PCIB (Generation-IV candidates). Fiji software was used to analyse the stacks of PLM and FIB-SEM images, and the overall results are summarised in Table 8.1. This Table shows that the volume fraction of porosity obtained from progressive polishing using the PLM of one region for each graphite sample was 13% and 15% for PCEA and PCIB, respectively. Compared to the data in chapter 5, which used PLM from the same samples calculated from random 2D regions, PCEA was slightly less porous, falling by 2.9% from a level of 15.9%. The estimated percentages of PCIB were almost the same (15.3%). These findings agree with the existing literature (Evans, 1978; Kane et al., 2011). Furthermore, the FIB-SEM analysis of volume fraction of porosity in PCEA was ~15.9%, which aligns with the total porosity calculated by PLM in chapter 5, even though the pore areas and volumes investigated were significantly different. In PCIB, the overall porosity was ~19%, greater than the total porosity reported from 2D and 3D analysis using PLM. However, this aligns closely with the total porosity (19.13%) given by the manufacturer.

Table 8.1: A summary of the overall porosity in PCEA and PCIB nuclear graphite grades from 2D and 3D analysis.

Nuclear Graphite	**Porosity (%) from PLM at the microscale**		**Porosity (%) in 3D from FIB-SEM at the nanoscale**
	2D	**3D**	
PCEA	15.9%	13%	15.9%
PCIB	15.3%	15%	19%

Both techniques revealed distinct structural differences in pore shape, size, distribution, and pore connectivity between PCEA and PCIB. Hence, PLM and FIB-SEM techniques were found to be valuable and confirmed their capabilities. They are, therefore, useful for studying the effects of neutron irradiation in nuclear graphite and provide data that complements X-ray tomography.

Although PLM technique gave a large field view that helped to distinguish filler particles and binder regions within the microstructure, it was shown to have a limited resolution (the smallest pore size detected was 3 μm^2), lower

magnification, and porosity detection is limited by the need to polish the sample surface. Another limitation when using PLM is that image alignment between serial sections was very difficult. Conversely, FIB-SEM provided a small field of view, but a much better resolution (smaller by an order of magnitude compared to PLM). However, serial sectioning using FIB-SEM was also limited by several factors, which included the conditions used (e.g., accelerating voltages and FIB current); the use of high energy gallium ions for milling can lead to the formation of damaged layers such as the curtaining effect; open pores filling with sputtered platinum which used as a protective layer, and making image thresholding difficult.

Consequently, a combination of FIB-SEM with other imaging techniques is recommended to overcome these limitations. This will facilitate the acquisition of multiscale data and thus validate the measurements. In general, FIB-SEM provides useful information on features significantly smaller than 1 μm, which are especially important in understanding the fine structure of PCIB nuclear graphite. While this 3D measurement derived only from virgin samples in this Thesis, the observational changes made at 3D level of the microstructure of the virgin material serve as a fundamental base for future work on the microstructure of the nuclear graphite. These findings can be used to establish a better understanding of the fundamental mechanisms and provide a good quantitative basis for comparison with irradiated samples.

The limitation associated with XRD is that the need for rotating the samples manually; this is to ensure that the same area of filler or binder was not collected. Further limitations are the limited number and size of the irradiated samples used in this work, and there were no resources available to collect the data of irradiated samples at the University of Leeds.

8.1.3 Summary and discussion: structural changes of nuclear graphite induced by neutron irradiation conclusions and further analysis

PLM, SEM, XRD, and Raman spectroscopy were used to observe and quantify the effects of neutron irradiation-induced damage on two nuclear-grade graphites (PCEA and PCIB, both based on petroleum coke). The neutron irradiation doses

ranged from 1.5 to 6.8 dpa and irradiation dose and temperatures between 350°C and 670°C, which affected the structure of the nuclear graphite.

A comparison of the microstructural information extracted from these techniques showed that neutron irradiation of graphite induces fragmentation of the basal planes and crystallites when the sample is irradiated at lower doses and temperatures. These samples exhibited relatively greater structural damage than those subjected to higher doses and temperatures due to annealing of the structural damage at higher temperatures. These changes to the structure have been associated with a notable change in the total porosity (at the micro-scale) of both samples (PCEA and PCIB) compared to virgin samples, as found by using PLM and SEM image analysis.

Conversely, irradiated samples showed no significant changes in the pore size compared to their virgin values. The irradiated PCIB sample compared to the virgin PCIB sample showed a relatively inhomogeneous structure with heavily porous regions observed at both lower and higher doses and temperatures. Despite such variation, the microstructural changes in PCEA and PCIB graphite grades (Generation-IV candidates) exhibited certain commonalities. They behaved in a similar way to the PGA and Gilsocarbon graphite used in the UK Magnox and AGRs, respectively, as shown in this work [of virgin and irradiated samples] and the irradiated work reported in the literature review (Gallego et al., 2013; Goggin et al.,1964; Haag, 2005; Heijna et al., 2017; Henson et al., 1968; Krishna et al., 2017; Marsden et al., 2017; Vreeling et al., 2012; Zhou et al., 2017a; Zhou et al. 2017b), as discussed in chapters 2 and 3. These studies showed a reduction in crystallite size due to neutron irradiation and the introduction of crystallite fragmentation following neutron irradiation.

The findings also align with the work of Mironov (2014), who examined identical samples using XRD and Raman. However, Mironov (2014) did not identify any general trends with an increasing dose. By contrast, the reanalysed data shows a clear trend in that the crystallite size decreased as the dose increased. Hence, the XRD patterns of nuclear graphites need to be correctly interpreted due to their inherent disorder, as this can significantly influence the shape of the diffracted peaks. Overall, the effects of neutron irradiation in nuclear graphites were confirmed in this study using XRD, Raman, PLM, and SEM (discussed in chapters 5 and 7).

Damage mechanisms associated with the aforementioned structural changes were described in detail in chapter 2. The microstructural changes of graphite upon neutron irradiation were driven by displacement damage cascades. A single collision cascade caused the creation of interstitial atoms and vacancies, referred to as Frenkel pairs. The accumulation of these defects resulted in the aforementioned structural changes, which were found to be dependent on the irradiation dose.

With increasing irradiation dose, the generation of defects was shown to progressively impact on the lattice periodicity of the hexagonally arranged crystal structure of graphite, which lead to an increase in internal strain, as confirmed by XRD measurements and from Raman peaks shifting. Freeman et al. (2017) reported changes in virgin and irradiated samples, which were similar to those used in this Thesis using high-resolution transmission electron microscopy (HRTEM), as can be seen in Figure 8.3. Here, Freeman et al.'s (2017) work showed that (002) basal layers in the virgin PCEA and PCIB samples displayed long-range order. Their findings demonstrate an increase in d-spacing as the dose increases, causing an expansion in c-direction. However, XRD findings here showed lower values, ranging between 0.337 to 0.338 nm, compared to Freeman et al.'s (2017) data. This Thesis showed that as irradiation dose increases, the basal planes of the irradiated PCEA specimens begin to exhibit higher concentrations of crystal defects, which were particularly evident at higher doses (6.8 dpa).

The case in PCIB was slightly different, demonstrating that the damage at lower doses is more evident and exhibits regions of near-perfect basal layers surrounded by "pockets" of the higher disorder. This disorder caused a reduction in the crystallinity of the irradiated samples as the irradiation dose increased, as confirmed by the XRD measurements of this work. At larger length scale, PCIB showed heavily porous regions of large pores than other regions of the same sample, which appeared as the dose and temperatures increased. However, these regions were found to have close average pore size at both lower and higher doses and temperatures.

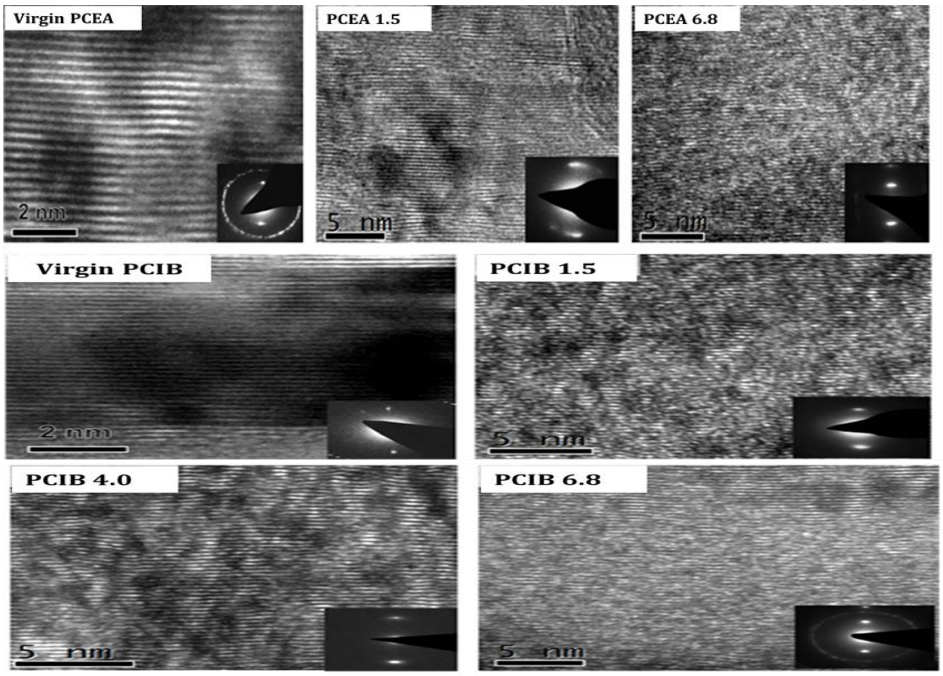

Figure 8.3: HRTEM micrographs and SAED patterns of PCEA and PCIB virgin and irradiated graphite samples. Reprinted from (Freeman et al., 2017).

Moreover, the disorder of these stacked layers led to an expansion in c-lattice parameters (or the interplanar $<d_{002}>$ spacing) and reduction in a-lattice parameters, which XRD and Raman data have revealed. Kelly (1971) proposed a model to describe this occurrence, irrespective of irradiation temperature or dose, which involves the aggregation of displaced interstitial carbon atoms to form additional basal layers, which were discussed in detail in chapter 2. This leads to the pre-existing basal planes to open for the purpose of accommodating the new interstitial atomic planes, as well as their corresponding defects, such as di-vacancies and spiro-interstitials. Subsequently, the corresponding shrinkage parallel to the layer plane results from the vacancy lines collapse.

However, this notion has recently been challenged by Heggie et al., (2011), who claimed that: (1) at low temperatures, interstitials are immobile and are unable to aggregate to generate new graphene sheets. This means that the standard model is insufficient for neutron irradiation at <250 °C; (2) the potential formation of small interstitial defect clusters would be unable to have a major impact on the interlayer spacing, and (3) the standard model fails to consider the movement and nucleation of basal dislocations, which are shown to be dominant during neutron irradiation by X-ray diffraction experiments.

Therefore, Heggie suggests that the accumulation of Frenkel pairs and the combination of interlayer defects (for example, interplanar di-vacancies, di-interstitials, and spiro-interstitials), which fix the graphene layers in place, resulting in a stress build-up and ultimately buckling of the graphitic planes. Such buckling is the cause of the c-axis expanding at irradiation temperatures of <250 °C. However, at irradiation temperatures >250 °C, these interlayer defects disappear when the buckling of the graphite layers is superseded by the folding of the planes to form "ruck and tuck" defects.

The Raman and XRD spectroscopy results, in which the concluding irradiation-induced microstructural transformation was reported, led to a decreased crystallite size (see Table 7.2 and Table 7.6 in chapter 7). Conventionally, this has been linked with strain-induced bending and breaking of crystal planes in the course of the irradiation process, which was seen in the graphitic planes of the irradiated PCEA and PCIB samples. The quantitative analysis of micro-strain confirms this (see Table 7.3 in chapter 7).

A mechanism of this kind appears to be an insufficient explanation for the reduction in crystallite size which was observed in these irradiated graphite specimens. Furthermore, if Heggie's "ruck and tuck" defect model is to be accepted, the breaking of planes as a result of strain-induced bending is an irreconcilable concept. Although it is correctly depicted in Figure 7.3 (chapter 7) that the lattice distortion may cause a broadening of the XRD (002) peak and the Raman G-peaks, it is shown in Figure 7.6 that this has no physical meaning regarding any reduction in crystallite size as stated by Nightingale (1962). However, the examination of the HRTEM images in Figure 7.17, it is likely to assume that the reduction in crystallite size, occurring with irradiation is a direct consequence of the expanding "pockets" of disorder which disturb the areas of pristine graphite. Most of the measurements of the crystallite site are comprised the average size of these pristine regions.

It has previously been comprehensively described that, with continuous neutron damage, the number of disordered regions reduces (Chartier et al., 2018; Yi et al., 2016). However, the disorder generally grows and percolates over the whole of the graphite microstructure. Following the collapse of the disordered pockets to generate less graphitic graphite, all that remains are the pristine graphene layers. Therefore, virgin and irradiated PCEA and PCIB

samples were compared by using different methods, as well as using data from previous literature, which gave a glimpse into this progressive process. These methods and data from previous literature also gave an indication that a change from easily distinguishable areas of pristine graphite to a microstructure is almost exclusively disordered, in which it is not easy to resolve the regions of pristine graphite.

Telling and Heggie (2007) discuss the effect of temperature during irradiation and state that at high temperatures, there is a simultaneous "annealing" process that competes with the continual neutron irradiation damage. This behaviour was found in PCEA and PCIB at higher irradiation dose and temperature (PCEA (6.8 dpa/655 ˚C) and PCIB (6.8 dpa/670 ˚C)) from PLM and SEM results. This showed some annealing of the structure at higher temperatures, which potentially partially repaired the damage. This annealing process includes the recombination of the interstitial atoms and vacancies that are formed during irradiation (Krishna et al., 2017).

Overall, the findings showed that crystallite size decreases, and pores do not change significantly in size; however, new pores are formed. From the literature review, it is clear that the properties of the graphite, such as thermal conductivity, coefficient of thermal expansion, mechanical strengths, modulus, and electrical resistivity change during neutron irradiation. Neutron irradiation-induced damage can negatively affect the properties of graphite, which results in the failure of graphite components.

Consequently, this work attempted to examine and evaluate the microstructural changes in both virgin and irradiated graphite because the properties of nuclear graphite are strongly dependent on several parameters, such as grain size, microstructural orientation, defects, and manufacturing methods (Zhou et al., 2017b). The changes in nuclear graphite properties are highly temperature-dependent, as reported in the literature by Heijna et al. (2017), Zhou et al. (2017b), and Marsden et al. (2017). Heijna et al. (2017) reported the changes in PCEA and PCIB nuclear graphites properties due to neutron irradiation. The authors found that although both PCEA and PCIB graphites are classified as isotropic materials based on their CTE values, the dimensional changes are highly anisotropic in all directions, and this is more pronounced in PCIB graphite during irradiation. This anisotropic behaviour

leads to different dimensional changes in each direction, which is dependent on the graphite components' location and orientation in the graphite billet. These differences in dimensional changes and the properties of the graphite can lead to increase local stresses in contact between graphite bricks, resulting in failure. The thermal expansion also can induce stress to the graphite component. Based on the literature review discussed in chapter 2, CTE values and the behaviour of neutron irradiation are comparable for all nuclear graphite grades.

Similarly, Young's modulus does not exhibit large differences between PCEA and PCIB graphite grades. With increasing dose and temperature, the strength of the graphite, such as the compressive, tensile, and flexural strength, increase. This is mainly attributed to the thermal closure of Mrozowski cracks and other micro-cracks induced within the graphite during manufacture. Although the failure mode for PCIB graphite is more energetic as reported in the literature, measurements of tensile strengths of the PCEA and PCIB graphite showed that PCIB graphite is stronger than PCEA graphite (Heijna et al., 2017).

Although the findings of this Thesis showed similarity in the behaviour of both PCEA and PCIB samples under neutron irradiation, the changes to the porosity of PCIB exhibited more damage than PCEA samples compared to the virgin samples, because of the presence of more heavily porous regions. Therefore, based on this conclusion and from the discussion above PCEA graphite grades could be generally more favourable for application in (V)HTR systems. This is due to two reasons: (i) PCEA graphite has low dimensional anisotropy and (ii) resilience of pores aggregation compared to PCIB graphite grades.

8.2 Future work

The limitations of the experimental work carried out during the completion of this Thesis have been discussed. These limitations can be overcome by extending the work of this Thesis. The measurements derived from 2D images of virgin specimens provide a strong qualitative and quantitative basis for comparison with neutron-irradiated graphite specimens. SEM and PLM are, therefore, useful techniques for developing a mechanistic understanding of the graphite behaviour, but remain limited by the polishing process.

Suggested further work to complement the results on irradiated materials should develop a better process to produce a highly polished scratch-free surface under the constraints of working with an active material. This will facilitate a better observation of the microstructure and ensure accurate measurement of the total porosity of the material after neutron irradiation. Furthermore, studying the material at one dose with variable temperatures and vice versa will give more consistent results. Moreover, FIB-SEM could also provide an insight into the effect of neutron irradiation on nuclear graphite through its ability to easily serial section 'active' graphite samples. Conducting an analysis of pores in the filler and binder of virgin and irradiated graphite separately will allow the behaviour of porosity under neutron irradiation to be predicted more accurately

Appendix A

The information presented in this section is extracted from Idaho National Laboratory (INL), United State, reports (Swank, 2011; Windes, 2012; Windes et al., 2013) comprising irradiation parameters data along with the description of the irradiation facility.

The irradiated materials used in this Thesis were obtained from Idaho National Laboratory (INL), United State as a part of the Next Generation Nuclear Plant (NGNP) Graphite Radiation and Development R&D program. This program aims to measure irradiated material property changes for a wide variety of nuclear graphites to predict their behaviour and operating performance within the core of new very high-temperature reactor (VHTR) designs (Swank, 2011). VHTR reactors are seen as an outstanding source of reliable base load power, which promise enhanced features such as operating at a high level of fuel efficiency, safety, proliferation-resistance, sustainability and cost. Hence the performance and reliability of materials when exposed to the higher neutron doses and extremely corrosive higher temperature environments which will be found in VHTR (Generation-IV) reactors are critical areas of study, as key considerations for the successful development of VHTR reactors are suitable structural materials for both in-core and out-of-core applications (Yvon, 2016).

This program includes an Advanced Graphite Creep (AGC-1) experiment, comprising six irradiation capsules which were irradiated in the Advanced Test Reactor (ATR). As reported by Swank (2011), the AGC-1 experiment is designed to determine the changes to specific material properties, i.e. thermal expansion, elastic modulus, mechanical strength, irradiation-induced dimensional change rate, and irradiation creep for several grades of nuclear graphite types over a range of moderate doses and high temperatures. The six capsules comprise graphite test specimens (~500 graphite samples) which were exposed to a dose range from 0.5 to 7 dpa at three different temperatures (600, 900, and 1200°C) (Windes, 2012). Due to irradiation-induced creep within graphite components which is critical to determining the operational life of the graphite core, some of the samples were also exposed to an applied load to control the creep rate for

each graphite type under both neutron dose and temperature (Windes et al., 2013).

The AGC-1 capsule was irradiated in the south flux trap of the ATR from September 5, 2009 to January 8, 2011 crossing seven irradiation cycles (approximately 378 effective full-power days). After the irradiation was completed on January 8, 2011, the AGC-1 capsule was stored in the ATR Canal for approximately 60 days to allow the activity of the steel pressure tube section of the capsule to decay to lower levels, following the disassembly of the capsules (Swank, 2011).

For the purpose of guaranteeing that the same dose is given to similar samples, it was necessary to match the stacking of the sample with the ATR flux profile. This is asymmetrical (see Figure A.1) because the core components change the profile. This request which ensures that similar samples receive similar doses was attained by loading more “piggyback” samples in the bottom of the capsule couple nearest to the core centreline. Nevertheless, further samples were irradiated from the new designed ones (e.g. PCEA) in comparison with the older generation H451. The purpose of this was to guarantee a greater variety of irradiation doses and temperatures (Windes et al., 2013).

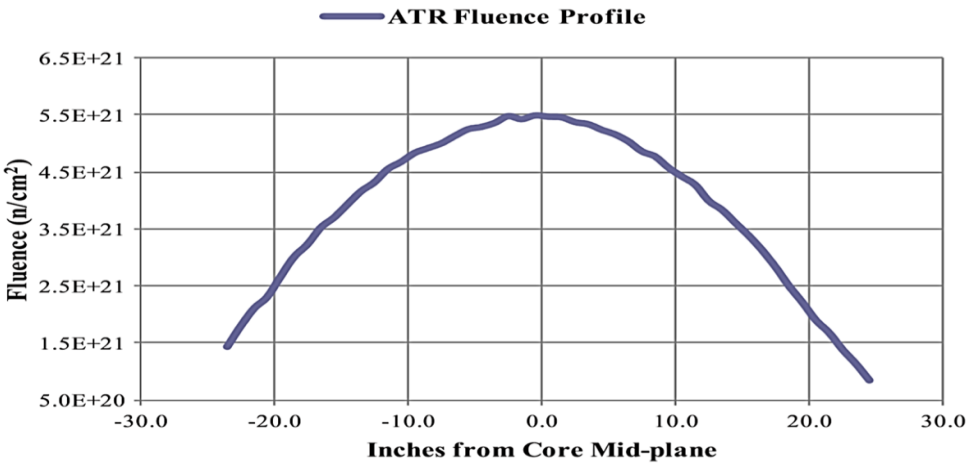

Figure A. 1: ATR fluence profile during AGC-1 capsule irradiation (Windes, 2012).

Additionally, during the stacking of the samples, the grain size orientation, relative to the irradiation load, was considered, due to the fact that the orientation of the grain affects the irradiation creep. This is of greater importance than the measurements where the applied load is parallel to the

grain. The experiment guaranteed that every capsule was irradiated at a constant temperature, and that variation applied only to the load and the dose (Swank, 2011).

In January 2011, the AGC-1 samples completed their irradiation cycle, and their accumulated dose was between ~1-7 dpa, the significant figures are best estimates. Since this was the first experiment undertaken as a part of AGC, there were software problems in temperature control in the way in which the temperature was not uniform (see Figure A.2) throughput the capsule, and in that the irradiation temperature was raised to about 675 °C. Throughout the irradiation process, the temperature variation in the whole capsule was 350 °C, and the doses ranged from 1.82 to ~7dpa. The variation in temperature between these matched pair samples in the central region was between a 30 °C low and a 68 °C high. Although these temperature variations between sample pairs are higher than anticipated, they are inside the acceptable uncertainty levels (Windes et al., 2013). It is important to mention that the irradiated graphite samples examined in this Thesis, were a part of the central capsule, and no load was applied.

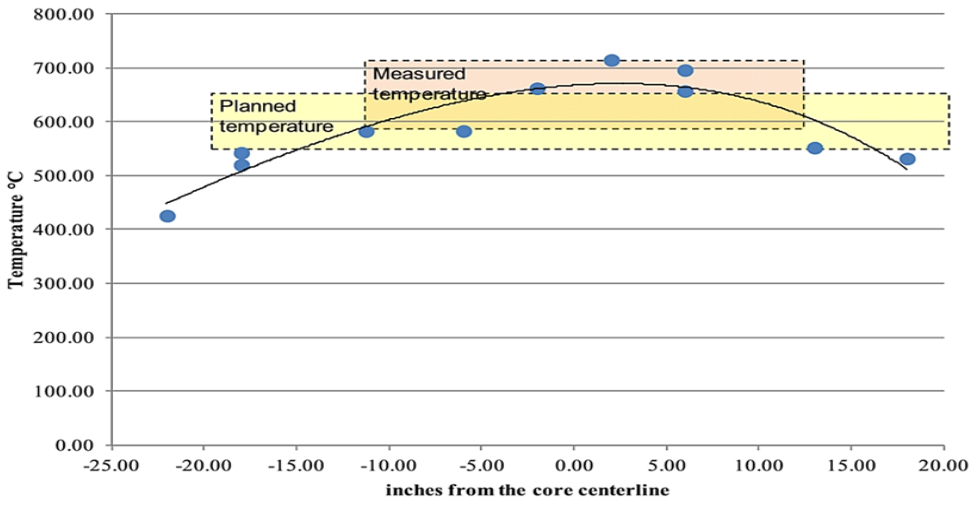

Figure A. 2: Initial estimation of attained temperature profile in the AGC-1 capsule (Windes, 2012).

Appendix B

Publication, conferences, meetings and awards

Publication

- Freeman, H.M., Mironov, B.E., Windes, W., Alnairi, M.M., Scott, A.J., Westwood, A.V.K. and Brydson, R.M.D., 2017. Micro to nanostructural observations in neutron-irradiated nuclear graphites PCEA and PCIB. *Journal of Nuclear Materials*, *491*, pp.221-231.

Conferences and meetings

Date	Conference/Meeting	Contribution
April 2015	EdF Annual Graphite Meeting, Manchester, UK	Attendee
July 2015	Microscience Microscopy Congress 2015, Manchester, UK	Attendee
September 2015	International Nuclear Graphite Specialist Meeting, Nottingham, UK	Attendee
April 2017	EdF Annual Graphite Meeting, Manchester, UK	Attendee
July 2017	Microscience Microscopy Congress 2017, Manchester, UK	Attendee
November 2017	Topical Research Meeting on Physics. Innovation. Nuclear Manchester, UK	Poster
December 2017	Nuclear Waste Management & Decommissioning Frontiers conference, Leeds, UK	Poster
January 2018	Internal Research Exchange Event Leeds, UK	Poster
October 2018	The 6th EDF energy Nuclear Graphite Conference Kendal, UK	Presentation with a paper

Award

- Nuclear Waste Management & Decommissioning Frontiers conference, December 2017, Leeds, UK award for best poster deployment, see the link: https://nda.blog.gov.uk/2018/02/08/one-stop-shop-for-sharing-research

References

Aitkaliyeva, A., He, L., Wen, H., Miller, B., Bai, X. M. and Allen, T. 2017. Irradiation effects in Generation-IV nuclear reactor materials. *structural materials for Generation-IV nuclear reactors.* Elsevier, pp.253-283.

Andor. 2016. Raman micro-spectroscopy. [Online]. Available from: https://www.oxinst.com/learning/view/article/raman-micro-spectroscopy

Anon. 1956. Calder hall power station. *The Engineer.*

Arai, Y. 1993. Structure and properties of pitch-based carbon fibres. *Nippon Steel Technical Report.* **59**(0).

Arregui-Mena, J.D., Edmondson, P.D., Campbell, A.A. and Katoh, Y. 2018. Site specific, high-resolution characterisation of porosity in graphite using FIB-SEM tomography. *Journal of Nuclear Materials.* **511**, pp.164-173.

Asthana, A., Matsui, Y., Yasuda, M., Kimoto, K., Iwata, T. and Ohshima, K.I. 2005. Investigations on the structural disordering of neutron-irradiated highly oriented pyrolytic graphite by X-ray diffraction and electron microscopy. *Journal of Applied Crystallography.* **38**(2), pp.361-367.

Babout, L., Marsden, B., Mummery, P. and Marrow, T. 2008. Three-dimensional characterisation and thermal property modelling of thermally oxidised nuclear graphite. *Acta Materialia.* **56**(16), pp.4242-4254.

Babu, V.S. and Seehra, M. 1996. Modelling of disorder and X-ray diffraction in coal-based graphitic carbons. *Carbon.* **34**(10), pp.1259-1265.

Bacon, G. and Warren, B. 1956. X-ray diffraction studies of neutron-irradiated graphite. *Acta Crystallographica.* **9**(12), pp.1029-1035.

Baker, D. 1971. Graphite as a neutron moderator and reflector material. *Nuclear Engineering and Design.* **14**(3), pp.413-444.

Banhart, F. 2002. The role of lattice defects in the formation of new carbon structures under electron irradiation. *Journal of Electron Microscopy.* **51**(suppl_1), pp.S189-S194.

Bansal, R., Kubis, A., Hull, R. and Fitz-Gerald, J. 2006. High-resolution three-dimensional reconstruction: A combined scanning electron microscope and focused ion-beam approach. *Journal of Vacuum Science & Technology B: Microelectronics and Nanometer Structures Processing, Measurement, and Phenomena.* **24**(2), pp.554-561.

Barros, E., Sato, K., Samsonidze, G.G., Souza Filho, A., Dresselhaus, M. and Saito, R. 2011. D band Raman intensity calculation in armchair edged graphene nanoribbons. *Physical Review B.* **83**(24), p245435.

Baskin, Y. and Meyer, L. 1955. Lattice constants of graphite at low temperatures. *Physical Review.* **100**(2), p544.

Basko, D. 2009. Boundary problems for Dirac electrons and edge-assisted Raman scattering in graphene. *Physical Review B.* **79**(20), p205428.

Beams, R., Cançado, L.G. and Novotny, L. 2011. Low-temperature Raman study of the electron coherence length near graphene edges. *Nano Letters.* **11**(3), pp.1177-1181.

Berre, C., Fok, S., Marsden, B., Babout, L., Hodgkins, A., Marrow, T. and Mummery, P. 2006. Numerical modelling of the effects of porosity changes on the mechanical properties of nuclear graphite. *Journal of Nuclear Materials.* **352**(1), pp.1-5.

Berre, C., Fok, S., Marsden, B., Mummery, P., Marrow, T. and Neighbour, G. 2008. Microstructural modelling of nuclear graphite using multi-phase models. *Journal of Nuclear Materials.* **380**(1-3), pp.46-58.

Bodel, W. 2013. *The relationship between Young's modulus and microstructure of nuclear graphite*. Ph.D. Thesis, The University of Manchester.

Bolte, S. and Cordelieres, F. 2006. A guided tour into subcellular colocalization analysis in light microscopy. *Journal of Microscopy.* **224**(3), pp.213-232.

Brocklehurst, J. and Kelly, B. 1993. Analysis of the dimensional changes and structural changes in polycrystalline graphite under fast neutron irradiation. *Carbon.* **31**(1), pp.155-178.

Burchell, T., Clark, R., Stephens, J., Eto, M., Haag, G., Hacker, P., Neighbour, G., Janev, R. and Wickham, A. 2000. IAEA international database on irradiated nuclear graphite properties.

Burchell, T., Yahr, T. and Battiste, R. 2007. Modelling the multiaxial strength of H-451 nuclear grade graphite. *Carbon.* **45**(13), pp.2570-2583.

Burchell, T.D. 2012. *Radiation effects in graphite.* Oak Ridge National Laboratory (ORNL).

Butz, B., Dolle, C., Niekiel, F., Weber, K., Waldmann, D., Weber, H.B., Meyer, B. and Spiecker, E. 2013. Dislocations in bilayer graphene. *Nature.* **505**, p533.

Béghein, P., Berlioux, G., du Mesnildot, B., Hiltmann, F. and Melin, M. 2012. NBG-17–An improved graphite grade for HTRs and VHTRs. *Nuclear Engineering and Design.* **251**, pp.146-149.

Cancado, L., Takai, K., Enoki, T., Endo, M., Kim, Y., Mizusaki, H., Speziali, N., Jorio, A. and Pimenta, M. 2008. Measuring the degree of stacking order in graphite by Raman spectroscopy. *Carbon.* **46**(2), pp.272-275.

Cançado, L., Takai, K., Enoki, T., Endo, M., Kim, Y., Mizusaki, H., Jorio, A., Coelho, L., Magalhaes-Paniago, R. and Pimenta, M. 2006. General equation for the determination of the crystallite size L a of nanographite by Raman spectroscopy. *Applied Physics Letters.* **88**(16), p163106.

Cervi, E., Cammi, A. and Di Ronco, A. 2018. Stability analysis of the Generation-IV nuclear reactors by means of the root locus criterion. *Progress in Nuclear Energy.* **106**, pp.316-334.

Chartier, A., Van Brutzel, L. and Pageot, J. 2018. Irradiation damage in nuclear graphite at the atomic scale. *Carbon.* **133**, pp.224-231.

Contescu, C.I., Mee, R.W., Wang, P., Romanova, A.V. and Burchell, T.D. 2014. Oxidation of PCEA nuclear graphite by low water concentrations in helium. *Journal of Nuclear Materials.* **453**(1-3), pp.225-232.

Crouse, B. 2011. Linear defects: Dislocations. (21, 22).

Cuesta, A., Dhamelincourt, P., Laureyns, J., Martinez-Alonso, A. and Tascon, J.M. 1998. Comparative performance of X-ray diffraction and Raman microprobe techniques for the study of carbon materials. *Journal of Materials Chemistry.* **8**(12), pp.2875-2879.

Daniels, H.R. 2003. *Novel characterisation techniques for carbonaceous materials in the FEGTEM*. Thesis, University of Leeds.

Dekdouk, B., Chapman, R., Brown, M. and Peyton, A.J. 2012. Evaluating the conductivity distribution in isotropic polycrystalline graphite using spectroscopic eddy current technique for monitoring weight loss in advanced gas-cooled reactors. *NDT & E International.* **51**, pp.150-159.

Delannay, L., Yan, P., Payne, J. and Tzelepi, N. 2014. Predictions of inter-granular cracking and dimensional changes of irradiated polycrystalline graphite under plane strain. *Computational Materials Science.* **87**, pp.129-137.

Dillon, R., Woollam, J.A. and Katkanant, V. 1984. Use of Raman scattering to investigate disorder and crystallite formation in as-deposited and annealed carbon films. *Physical Review B.* **29**(6), p3482.

Dunn, D. and Hull, R. 1999. Reconstruction of three-dimensional chemistry and geometry using focused ion beam microscopy. *Applied Physics Letters.* **75**(21), pp.3414-3416.

Eiichi Fujita, F. and Izui, K. 1961. Observation of lattice defects in graphite by electron microscopy, part I. *Journal of the Physical Society of Japan.* **16**(2), pp.214-227.

Evans, M. 1978. *Porosity in graphites*. Ph.D. Thesis, University of Newcastle Upon Tyne.

Fang, X., Wang, H., Yu, S. and Li, C. 2012. The various creep models for irradiation behaviour of nuclear graphite. *Nuclear Engineering and Design.* **242**, pp.19-25.

Ferrari, A. and Robertson, J. 2001. Resonant Raman spectroscopy of disordered, amorphous, and diamondlike carbon. *Physical Review B.* **64**(7), p075414.

Ferrari, A.C. 2007. Raman spectroscopy of graphene and graphite: disorder, electron-phonon coupling, doping and nonadiabatic effects. *Solid State Communications.* **143**(1), pp.47-57.

Ferrari, A.C. and Robertson, J. 2000. Interpretation of Raman spectra of disordered and amorphous carbon. *Physical Review B.* **61**(20), p14095.

Fletcher, A. 2008. Carbon. [Online]. [Accessed 19 sep.]. Available from: http://personal.strath.ac.uk/ashleigh.fletcher/carbon.htm

Freeman, H. 2016. *Radiation Damage in Nuclear Graphite*. Ph.D. Thesis, University of Leeds.

Freeman, H., Jones, A., Ward, M., Hage, F., Tzelepi, N., Ramasse, Q., Scott, A. and Brydson, R. 2016. On the nature of cracks and voids in nuclear graphite. *Carbon.* **103**, pp.45-55.

Freeman, H., Mironov, B., Windes, W., Alnairi, M., Scott, A., Westwood, A. and Brydson, R. 2017. Micro to nanostructural observations in neutron-irradiated nuclear graphites PCEA and PCIB. *Journal of Nuclear Materials.* **491**, pp.221-231.

Fugallo, G., Cepellotti, A., Paulatto, L., Lazzeri, M., Marzari, N. and Mauri, F. 2014. Thermal conductivity of graphene and graphite: collective excitations and mean free paths. *Nano Letters.* **14**(11), pp.6109-6114.

Gallego, N., Meisner, R. and Burchell, T. 2013. Annealing studies of irradiated HOPG using X-ray measurements. *Present. Int. Nucl. Graph. Spec. Meet., Seattle: Oak Ridge National Laboratory.*

Gallego, N.C., Burchell, T.D. and Klett, J.W. 2006. Irradiation effects on graphite foam. *Carbon.* **44**(4), pp.618-628.

Gill, J. 2014. *An investigation into the decontamination of carbon-14 from irradiated graphite*. Thesis, University of Central Lancashire.

Goggin, P., Henson, R., Perks, A. and Reynolds, W. 1964. Dimensional changes in the irradiated graphite lattice. *Carbon.* **1**(2), pp.189-200.

Gogotsi, Y. 2006. *Nanotubes and nanofibers.* CRC Press.

Gouadec, G. and Colomban, P. 2007. Raman Spectroscopy of nanomaterials: How spectra relate to disorder, particle size and mechanical properties. *Progress in Crystal Growth and Characterisation of Materials.* **53**(1), pp.1-56.

Grebennikova, T. 2018. *Interview at the University of Manchester.*

Groeber, M.A., Haley, B., Uchic, M.D., Dimiduk, D.M. and Ghosh, S. 2006. 3D reconstruction and characterisation of polycrystalline microstructures using a FIB-SEM system. *Materials Characterisation.* **57**(4-5), pp.259-273.

Gulans, A., Krasheninnikov, A.V., Puska, M.J. and Nieminen, R.M. 2011. Bound and free self-interstitial defects in graphite and bilayer graphene: A computational study. *Physical Review B.* **84**(2), p024114.

Haag, G. 2005. *Properties of ATR-2E graphite and property changes due to fast neutron irradiation.* Forschungszentrum Jülich GmbH, Zentralbibliothek.

Hacker, P.J., Neighbour, G.B. and McEnaney, B. 2000. The coefficient of thermal expansion of nuclear graphite with increasing thermal oxidation. *Journal of Physics D: Applied Physics.* 33(8), p991.

Hagos, B., Jones, A., Marrow, T. and Marsden, B. 2010. Microstructural analysis of irradiated nuclear graphite waste. *Diamond.* **10**.

Hagos, B.A. 2013. *Microstructural and chemical behaviour of irradiated graphite waste under repository conditions*. Ph.D. Thesis, The University of Manchester.

Hall, G., Marsden, B. and Fok, S. 2006. The microstructural modelling of nuclear grade graphite. *Journal of Nuclear Materials.* **353**(1), pp.12-18.

Harris, P.J. 2005. New perspectives on the structure of graphitic carbons. *Critical Reviews in Solid State and Materials Sciences.* **30**(4), pp.235-253.

Hay, B., Anhalt, K., Chapman, L., Boboridis, K., Hameury, J. and Krenek, S. 2011. High-temperature thermophysical properties of advanced materials for nuclear design. In: *Joint IMEKO TC11-TC19-TC20 Int. Symp. Metrological Infrastructure,*

Environmental and Energy Measurement and Int. Symp. of Energy Agencies of Mediterranean Countries, pp.71-76.

Heggie, M., Suarez-Martinez, I., Davidson, C. and Haffenden, G. 2011. Buckle, ruck and tuck: A proposed new model for the response of graphite to neutron irradiation. *Journal of Nuclear Materials.* **413**(3), pp.150-155.

Heijna, M., de Groot, S. and Vreeling, J. 2017. Comparison of irradiation behaviour of HTR graphite grades. *Journal of Nuclear Materials.* **492**, pp.148-156.

Hennig, G. 1962. Vacancies and dislocation loops in graphite. *Applied Physics Letters.* **1**(3), pp.55-56.

Henson, R., Perks, A. and Simmons, J. 1968. Lattice parameter and dimensional changes in graphite irradiated between 300 and 1350 C. *Carbon.* **6**(6), pp.789-806.

Holt, M. 2008. *Issues of scale in nuclear graphite components*. Ph.D. Thesis, University of Hull.

Holzer, L., Indutnyi, F., Gasser, P., Münch, B. and Wegmann, M. 2004. Three-dimensional analysis of porous BaTiO3 ceramics using FIB nanotomography. *Journal of Microscopy.* **216**(1), pp.84-95.

Howe, J.Y., Cavin, B.O., Drakeford, A.E., Peascoe, R.A., Zontek, T.L. and Miller, D.J. 2007. Influence of bulk graphite thickness on the accuracy of X-ray diffraction measurement. *Academia.* pp.1-5.

Huang, Q. and Tang, H. 2019. Porosity analysis of superfine-grain graphite IG-110 and ultrafine-grain graphite T220. *Materials Science and Technology.* **35**(8), pp.962-968.

Hull, D. and Bacon, D.J. 2011. *Introduction to dislocations.* Elsevier.

IAEA. 2019. Gas-cooled reactors. *International Atomic Energy Agency*. [Online]. [Accessed 20 March 2019]. Available from: https://www.iaea.org/topics/gas-cooled-reactors

Ishiyama, S., Burchell, T., Strizak, J. and Eto, M. 2008. The effect of high fluence neutron irradiation on the properties of a fine-grained isotropic nuclear graphite. *Journal of Nuclear Materials.* **230**(1), pp.1-7.

Jensen, S. and Nonbøl, E. 1999. *Description of the Magnox type of gas-cooled reactor (MAGNOX).* NKS.

Jing, S.P., Zhang, C., Pu, J., Jiang, H.Y., Xia, H.H., Wang, F., Wang, X., Wang, J.Q. and Jin, C. 2016. 3D microstructures of nuclear graphite: IG-110, NBG-18 and NG-CT-10. *Nuclear Science and Techniques.* **27**(3), p66.

Johns, S., Shin, W., Kane, J.J., Windes, W.E., Ubic, R. and Chinnathambi, K. 2018. A new oxidation based technique for artefact-free TEM specimen preparation of nuclear graphite. *Journal of Nuclear Materials.*

Jones, A., Hall, G., Joyce, M., Hodgkins, A., Wen, K., Marrow, T. and Marsden, B. 2008. Microstructural characterisation of nuclear grade graphite. *Journal of Nuclear Materials.* **381**(1), pp.152-157.

Kane, J., Karthik, C., Butt, D.P., Windes, W.E. and Ubic, R. 2011. Microstructural characterisation and pore structure analysis of nuclear graphite. *Journal of Nuclear Materials.* **415**(2), pp.189-197.

Keane, K. 2019. Hunterston B: Pictures show cracks in Ayrshire nuclear reactor. *BBC News.* [Online]. [Accessed 10 March 2019]. Available from: https://www.bbc.co.uk/news/uk-scotland-47485321

Kelly, B. 1971. A simple model of the effect of interstitial atoms on the interlayer properties of a graphite crystal. *Carbon.* **9**(5), pp.627-631.

Kelly, B., Marsden, B., Hall, K., Martin, D., Harper, A. and Blanchard, A. 2000. Irradiation damage in graphite due to fast neutrons in fission and fusion systems. *IAEA Tecdoc.* **1154**.

Kelly, B., Martin, W. and Nettley, P. 1966. Dimensional changes in polycrystalline graphites under fast-neutron irradiation. *Phil. Trans. R. Soc. Lond. A.* **260**(1109), pp.51-71.

Kelly, B.T. 1981. *Physics of graphite*. Applied Science LTD.15, 20, 50.

Kelly, B.T. 1982. Graphite-the most fascinating nuclear material. *Carbon.* **20**(1), pp.3-11.

Kelly BT, B.J.a.G.J. 1972. Irradiation damage in graphite. In: *Graphite Structures for Nuclear Reactors*, *Conference Organised by the Nuclear Energy Group of The Institution of Mechanical Engineers*.

Klein, D.R. 2010. *Organic chemistry.* Chichester: John Wiley & Sons. 20,35.

Knight, D.S. and White, W.B. 1989. Characterisation of diamond films by Raman spectroscopy. *Journal of Materials Research.* **4**(02), pp.385-393.

Kodsi, C. 2017. *Computational framework for fracture of graphite bricks in an AGR core*. Ph.D. Thesis, University of Glasgow.

Kragh, H. 2002. *Quantum generations: A history of physics in the twentieth century.* Princeton University Press.

Krishna, R., Jones, A.N., Edge, R. and Marsden, B.J. 2015. Residual stress measurements in polycrystalline graphite with micro-Raman spectroscopy. *Radiation Physics and Chemistry.* **111**, pp.14-23.

Krishna, R., Unsworth, T.J. and Edge, R. 2016. Raman spectroscopy and microscopy. *Reference module in materials science and materials engineering.* Elsevier.

Krishna, R., Wade, J., Jones, A.N., Lasithiotakis, M., Mummery, P.M. and Marsden, B.J. 2017. An understanding of lattice strain, defects and disorder in nuclear graphite. *Carbon.* **124**, pp.314-333.

Larkin, P. 2011. *Infrared and Raman spectroscopy; principles and spectral interpretation.* Elsevier.

Latham, C., Heggie, M., Gámez, J., Suarez-Martinez, I., Ewels, C. and Briddon, P. 2008. The di-interstitial in graphite. *Journal of Physics: Condensed Matter.* **20**(39), p395220.

Latham, C., McKenna, A., Trevethan, T., Heggie, M., Rayson, M. and Briddon, P. 2015. On the validity of empirical potentials for simulating radiation damage in graphite: a benchmark. *Journal of Physics: Condensed Matter.* **27**(31), p316301.

Lewis, E.E. 2008. *Fundamentals of nuclear reactor physics.* Elsevier/ Academic Press.

Li, L., Reich, S. and Robertson, J. 2005. Defect energies of graphite: Density-functional calculations. *Physical Review B.* **72**(18), p184109.

Lin, J., Fang, W., Zhou, W., Lupini, A.R., Idrobo, J.C., Kong, J., Pennycook, S.J. and Pantelides, S.T. 2013. AC/AB Stacking boundaries in bilayer graphene. *Nano Letters.* **13**(7), pp.3262-3268.

Liu, Z. and Zhou, X. 2014. *Graphene: Energy Storage and Conversion Applications.* CRC Press.

Ma, Y. 2007. Simulation of interstitial diffusion in graphite. *Physical Review B.* **76**(7), p075419.

Ma, Y., Lehtinen, P., Foster, A.S. and Nieminen, R.M. 2004. Magnetic properties of vacancies in graphene and single-walled carbon nanotubes. *New Journal of Physics.* **6**(1), p68.

Malard, L., Pimenta, M., Dresselhaus, G. and Dresselhaus, M. 2009. Raman spectroscopy in graphene. *Physics Reports.* **473**(5), pp.51-87.

Marsden, B., Jones, A., Hall, G., Treifi, M. and Mummery, P. 2017. Graphite as a core material for Generation-IV nuclear reactors. *Structural Materials for Generation-IV Nuclear Reactors.* Elsevier, pp.495-532.

Marsden, B.J., Hall, G.N., Wouters, O., Vreeling, J.A. and van der Laan, J. 2008. Dimensional and material property changes to irradiated Gilsocarbon graphite irradiated between 650 and 750 °C. *Journal of Nuclear Materials.* **381**(1–2), pp.62-67.

Marsh, H. and Reinoso, F.R. 2006. *Activated carbon.* Elsevier.

Mcdermott, L. 2012. *Characterisation and chemical treatment of irradiated UK graphite waste*. Thesis, University of Manchester.

Mernagh, T.P., Cooney, R.P. and Johnson, R.A. 1984. Raman spectra of graphon carbon black. *Carbon.* **22**(1), pp.39-42.

Metcalfe, M. and Tzelepi, N. 2014. Application of optical microscopy to study changes in graphite microstructure. In: *Engineering Challenges Associated with the Life of Graphite Cores, 6-9 May, The National College, Nottingham*.

Mileeva, Z., Ross, D. and King, S. 2013. A study of the porosity of nuclear graphite using small-angle neutron scattering. *Carbon.* **64**, pp.20-26.

Milev, A., Wilson, M., Kannangara, G.K. and Tran, N. 2008. X-ray diffraction line profile analysis of nanocrystalline graphite. *Materials Chemistry and Physics.* **111**(2), pp.346-350.

Mironov, B.E. 2014. *Nuclear graphite: structural characterisation and effects of irradiation*. Ph.D. Thesis, University of Leeds.

Mogire, E. 2015. *Nuclear graphite polishing rout,* 19 October.

Mrozowski, S. 1954. Mechanical strength, thermal expansion and structure of cokes and carbons. In: *Proceedings of the Conferences of Carbon*: Buffalo Univ.

Mukhopadhyay, P. and Gupta, R.K. 2012. *Graphite, Graphene, and their polymer nanocomposites.* CRC Press.

NDT. 2014. Linear defects. [Online]. [Accessed 20 December]. Available from: https://www.ndeed.org/EducationResources/CommunityCollege/Materials/Structure/linear_defects.htm

Neighbour, G.B. 2000. Modelling of dimensional changes in irradiated nuclear graphites. *Journal of Physics D: Applied Physics.* **33**(22), p2966.

Neighbour, G.B. 2012. *Modelling and measuring reactor core graphite properties and performance.* Royal Society of Chemistry.

Nemanich, R. and Solin, S. 1979. First-and second-order Raman scattering from finite-size crystals of graphite. *Physical Review B.* **20**(2), p392.

Nightingale, R.E. 1962. *Nuclear graphite.* Academic Press. 3, 6, 10, 31, 35, 54, 100.

NPTEL. 2009. High strength high modulus fibres: Manufacturing of carbon fibres from pan precursors, viscose and pitch fibres. *The National Programme on Technology Enhanced Learning.* [Online]. [Accessed 9 December 2016]. Available from: http://nptel.ac.in/courses/116102006/module2/chapter%202.4.htm

Oku, T. and Ishihara, M. 2004. Lifetime evaluation of graphite components for HTGRs. *Nuclear Engineering and Design.* **227**(2), pp.209-217.

Panyukov, S. and Subbotin, A. 2008. Theory of radiation-induced shape-change of graphite. *Atomic energy.* **105**(1), pp.32-41.

Paul, R.M. and Morral, J.E. 2018. A 3D random pore model for the oxidation of graphite with open porosity. *Journal of Nuclear Materials.* **499**, pp.344-352.

Pierson, H.O. 2012. *Handbook of carbon, graphite, diamonds and fullerenes: processing, properties and applications.* William Andrew.

Pimenta, M.A., Dresselhaus, G., Dresselhaus, M.S., Cancado, L.G., Jorio, A. and Saito, R. 2007. Studying disorder in graphite-based systems by Raman spectroscopy. *Physical Chemistry Chemical Physics.* **9**(11), pp.1276-1290.

Preston, S.D. and Marsden, B.J. 2006. Changes in the coefficient of thermal expansion in stressed Gilsocarbon graphite. *Carbon.* **44**(7), pp.1250-1257.

Radovic, L.R. 2004. *Chemistry and physics of carbon.* CRC Press. 5, 10, 33.

Reich, S. and Thomsen, C. 2004. Raman spectroscopy of graphite. *Philosophical Transactions of the Royal Society of London A: Mathematical, Physical and Engineering Sciences.* **362**(1824), pp.2271-2288.

Reynolds, W. and Thrower, P. 1965. The nucleation of radiation damage in graphite. *Philosophical Magazine.* **12**(117), pp.573-593.

Rietveld, H. 1969. A profile refinement method for nuclear and magnetic structures. *Journal of Applied Crystallography.* **2**(2), pp.65-71.

Roche, E., Lavin, J. and Parrish, R. 1988. The mosaic nature of the graphite sheet in pitch-based carbon fibres. *Carbon.* **26**(6), pp.911-913.

Schaffer, M., Wagner, J., Schaffer, B., Schmied, M. and Mulders, H. 2007. Automated three-dimensional X-ray analysis using a dual-beam FIB. *Ultramicroscopy.* **107**(8), pp.587-597.

Schindelin, J., Arganda-Carreras, I. and Frise, E.e.a. 2012. "Fiji: an open-source platform for biological-image analysis". *Nature methods* ***9****(7).* [Online]. Available from: https://imagej.net/Fiji

Schneider, C.A., Rasband, W.S. and Eliceiri, K.W. 2012. NIH Image to ImageJ: 25 years of image analysis. *Nature methods.* **9**(7), p671.

Shen, K., Huang, Z.-H., Shen, W., Yang, J., Yang, G., Yu, S. and Kang, F. 2015. Homogenous and highly isotropic graphite produced from mesocarbon microbeads. *Carbon.* **94**, pp.18-26.

Shi, L., Li, H., Zou, Z., Fok, A.S., Marsden, B.J., Hodgkins, A., Mummery, P.M. and Marrow, J. 2008. Analysis of crack propagation in nuclear graphite using three-point bending of sandwiched specimens. *Journal of Nuclear Materials.* **372**(2), pp.141-151.

Simmons, J. and Reynolds, W. 1962. Uranium and graphite. *Monogr. Inst. Metals, London.* (27), p75.

Simmons, J.H.W. 1965. *Radiation damage in graphite.* Oxford: Pergamon Press Ltd.3-8,96, 112.

Song, J., Zhao, Y., Zhang, J., He, X., Zhang, B., Lian, P., Liu, Z., Zhang, D., He, Z. and Gao, L. 2014. Preparation of binderless nanopore-isotropic graphite for inhibiting the liquid fluoride salt and Xe135 penetration for molten salt nuclear reactor. *Carbon.* **79**, pp.36-45.

Sparky. 2013. Introduction to crystal structure. *Sparkys word science.* [Online]. [Accessed 20 December]. Available from: https://sparkyswordscience.blogspot.com/2013/12/introduction-to-crystal-structure.html

Spicer, J.B., Olasov, L.R., Zeng, F.W., Han, K., Gallego, N.C. and Contescu, C.I. 2016. Laser ultrasonic assessment of the effects of porosity and microcracking on the elastic moduli of nuclear graphites. *Journal of Nuclear Materials.* **471**, pp.80-91.

Sun, K., Stroscio, M.A. and Dutta, M. 2009. Graphite C-axis thermal conductivity. *Superlattices and Microstructures.* **45**(2), pp.60-64.

Swank, D. 2011. *AGC-1 post-irradiation examination status.* Idaho National Laboratory (INL).

Taylor, J.E.L. 2016. *Investigating the effects of stress on the microstructure of nuclear grade graphite*. Ph.D. Thesis, University of Manchester.

Telling, R. and Heggie, M. 2007. Radiation defects in graphite. *Philosophical Magazine.* **87**(31), pp.4797-4846.

Telling, R.H., Ewels, C.P., Ahlam, A. and Heggie, M.I. 2003. Wigner defects bridge the graphite gap. *Nature Materials.* **2**(5), p333.

Telling, R.H. and Heggie, M.I. 2003. Stacking fault and dislocation glide on the basal plane of graphite. *Philosophical Magazine Letters.* **83**(7), pp.411-421.

Teobaldi, G., Tanimura, K. and Shluger, A. 2010. Structure and properties of surface and subsurface defects in graphite accounting for van der Waals and spin-polarisation effects. *Physical Review B.* **82**(17), p174104.

Thomsen, C. and Reich, S. 2000. Double resonant Raman scattering in graphite. *Physical Review Letters.* **85**(24), p5214.

Thrower, P. 1964. Interstitial and vacancy loops in graphite irradiated at high temperatures. *British Journal of Applied Physics.* **15**(10), p1153.

Thrower, P. and Nagle, D. 1973. The importance of strain in crystallite size determinations in graphite. *Carbon.* **11**(6), pp.663-664.

Tipler, P.A. and Mosca, G. 2007. *Physics for scientists and engineers.* Macmillan.

Trefilov, V.I. 2012. *Ceramic-and carbon-matrix composites.* Springer Science & Business Media.

Trevethan, T., Latham, C.D., Heggie, M.I., Briddon, P.R. and Rayson, M.J. 2014. Vacancy diffusion and coalescence in graphene directed by defect strain fields. *Nanoscale.* **6**(5), pp.2978-2986.

Tuinstra, F. and Koenig, J.L. 1970. Raman spectrum of graphite. *The Journal of Chemical Physics.* **53**(3), pp.1126-1130.

Uchic, M.D. 2006. 3D microstructural characterisation: Methods, analysis, and applications. *JOM Journal of the Minerals, Metals and Materials Society.* **58**(12), pp.24-24.

Uchic, M.D. 2011. Serial sectioning methods for generating 3D characterisation data of grain-and precipitate-scale microstructures. *Computational methods for microstructure-property relationships.* Springer, pp.31-52.

Uchic, M.D., Holzer, L., Inkson, B.J., Principe, E.L. and Munroe, P. 2007. Three-dimensional microstructural characterisation using focused ion beam tomography. *Mrs Bulletin.* **32**(5), pp.408-416.

Uskoković-Marković, S., Jelikić-Stankov, M., Holclajtner-Antunović, I. and Đurđević, P. 2013. Raman spectroscopy as a new biochemical diagnostic tool. *Journal of Medical Biochemistry.* **32**(2), pp.96-103.

Vaughan, A. 2018. Cracks in nuclear reactor will hit EDF Energy with £120m bill. *The Guardian*.

Venezuela, P., Lazzeri, M. and Mauri, F. 2011. Theory of double-resonant Raman spectra in graphene: Intensity and line shape of defect-induced and two-phonon bands. *Physical Review B.* **84**(3), p035433.

Vreeling, J., Wouters, O. and Van der Laan, J. 2008. Graphite irradiation testing for HTR technology at the high flux reactor in Petten. *Journal of Nuclear Materials.* **381**(1-2), pp.68-75.

Vreeling, J.A., Smit-Groen, V.M. and Staveren, T.O.V. 2012. X-ray diffraction experiments on irradiated graphite. In: *Presentation to the 3rd Research Coordination Meeting*, *April, Vienna*.

Wen, K., Marrow, J. and Marsden, B. 2008. Microcracks in nuclear graphite and highly oriented pyrolytic graphite (HOPG). *Journal of Nuclear Materials.* **381**(1-2), pp.199-203.

Wen, K., Marrow, T. and Marsden, B. 2008. The microstructure of nuclear graphite binders. *Carbon.* **46**(1), pp.62-71.

Williamson, G. 1960. Electron microscope studies of dislocation structures in graphite. *Proc. R. Soc. Lond. A.* **257**(1291), pp.457-463.

Willmott, P. 2011. *An introduction to synchrotron radiation: techniques and applications.* John Wiley & Sons.

Windes, W. 2012. *Data report on post-irradiation dimensional change of AGC-1 samples.* Idaho National Laboratory (INL).

Windes, W., Swank, W.D., Rohrbaugh, D. and Lord, J. 2013. *AGC-2 graphite pre-irradiation data analysis report.* Idaho National Laboratory (INL).

Wirth, B.D. 2007. How does radiation damage materials? *Science.* **318**(5852), pp.923-924.

WorldNuclearAssociation. 2018. Nuclear power in the United Kingdom. *World Nuclear Association.* [Online]. [Accessed 10 April 2019]. Available from: www.world-nuclear.org/information-library/country-profiles/countries-t-z/united-kingdom.aspx

WorldNuclearNews. 2015. World's last operating Magnox reactor closes. *World Nuclear News.* [Online]. [Accessed 20 November 2018]. Available from: www.world-nuclear-news.org/WR-Worlds-last-operating-Magnox-reactor-closes-31121501.html

Yi, C., Chen, X., Zhang, L., Wang, X. and Ke, C. 2016. Nanomechanical z-shape folding of graphene on flat substrate. *Extreme Mechanics Letters.* **9**, pp.84-90.

Yvon, P. 2016. *Structural materials for Generation-IV nuclear reactors.* Woodhead Publishing.

Zaefferer, S., Wright, S. and Raabe, D. 2008. Three-dimensional orientation microscopy in a focused ion beam–scanning electron microscope: A new dimension of microstructure characterisation. *Metallurgical and Materials Transactions A.* **39**(2), pp.374-389.

Zankel, A., Wagner, J. and Poelt, P. 2014. Serial sectioning methods for 3D investigations in materials science. *Micron.* **62**, pp.66-78.

Zhang, H., Zhao, M., Yang, X., Xia, H., Liu, X. and Xia, Y. 2010. Diffusion and coalescence of vacancies and interstitials in graphite: A first-principles study. *Diamond and Related Materials.* **19**(10), pp.1240-1244.

Zheng, G., Xu, P., Sridharan, K. and Allen, T. 2014. Characterisation of structural defects in nuclear graphite IG-110 and NBG-18. *Journal of Nuclear Materials.* **446**(1), pp.193-199.

Zhou, X.W., Tang, Y.P., Lu, Z.M., Zhang, J. and Liu, B. 2017. Nuclear graphite for high-temperature gas-cooled reactors. *New Carbon Materials.* **32**(3), pp.193-204.

Zhou, Z., Bouwman, W., Schut, H. and Pappas, C. 2014. Interpretation of X-ray diffraction patterns of (nuclear) graphite. *Carbon.* **69**, pp.17-24.

Zhou, Z., Bouwman, W., Schut, H., Van Staveren, T., Heijna, M. and Pappas, C. 2017. Influence of neutron irradiation on the microstructure of nuclear graphite: An X-ray diffraction study. *Journal of Nuclear Materials.* **487**, pp.323-330.

Zickler, G.A., Smarsly, B., Gierlinger, N., Peterlik, H. and Paris, O. 2006. A reconsideration of the relationship between the crystallite size La of carbons determined by X-ray diffraction and Raman spectroscopy. *Carbon.* **44**(15), pp.3239-3246.